

SCALING LAWS IN ORIFICED THERMIONIC HOLLOW CATHODES

PIERRE-YVES CAMILLE RÉGIS TAUNAY

A DISSERTATION
PRESENTED TO THE FACULTY
OF PRINCETON UNIVERSITY
IN CANDIDACY FOR THE DEGREE
OF DOCTOR OF PHILOSOPHY

RECOMMENDED FOR ACCEPTANCE
BY THE DEPARTMENT OF
MECHANICAL AND AEROSPACE ENGINEERING
ADVISER: EDGAR YAHZID CHOUAIRI

SEPTEMBER 2020

© Copyright by Pierre-Yves Camille Régis Taunay, 2020.

All rights reserved.

Abstract

Scaling laws for the total pressure, attachment length, and electron temperature within thermionic orificed hollow cathodes, an essential source of electrons for industrial and scientific applications, are developed. Total pressure, electron temperature, and attachment length are critical as they control the operational life of thermionic hollow cathode inserts, and, therefore, of the hollow cathode.

The scaling laws are derived from first principles for the total pressure, and from a semi-analytical approach for the electron temperature and attachment length. The model presented herein addresses critical issues of past, zero-dimensional models that are reviewed in this work. The model, which combines a zero-dimensional approach to the conservation of energy and momentum for the combined plasma-neutral fluid and a charge-exchange-limited ambipolar diffusion model, allows for the computation of all plasma quantities, including the total fluid pressure. The assumptions on which the model relies are partially informed by an empirical analysis of the total pressure. The model depends on the operating conditions (discharge current and mass flow rate), cathode geometry, and the gas species, along with two non-controllable parameters: the neutral gas temperature and the sheath potential. Total pressure data at up to 300 A of cathode discharge current was obtained experimentally and was used, along with data from the literature, to verify the model. Good agreement is obtained for all quantities.

The total pressure is found to scale both with the square of the mass flow rate multiplied by a weak function of discharge current, and with the square of the discharge current. This scaling can be physically interpreted as due to the relative importance of the magnetic pressure and the gasdynamic pressure. Both electron temperature and attachment length are found to vary inversely with the neutral gas pressure-cathode diameter product. The predicted emission length is found to be between 0.8–1.2 times the insert radius, to scale weakly with the pressure-diameter

product, and to be nearly independent of the orifice diameter. The analysis suggests that the diffusion-dominated nature of the insert plasma can account for the scaling of the emission length. Cathode design rules are formulated based on the results of the analysis: insert length and radius should be similar to optimize the usage of the thermionic emitter, and the mass flow rate can be bounded such that the pressure-insert diameter product is close to the empirically determined value of 3.7 Torr-cm.

Acknowledgements

It would never have been possible to pass this finish line without the help of many others. I would like first to thank my advisor Prof. Edgar Choueiri. Eddie, thank you for accepting me into the Princeton EP family and for giving me the foundation on which I built and honed my skills for both the cathode experiment and other interests. You have shown me what great science and writing is about and have pushed me to become not only an engineer, but also a physicist.

The cathode experiment was possible largely because of the help of Bob Sorenson. Bob, thank you for teaching me about electronics, HAM radio, machining, how to “think,” and so much more. Thank you also for putting up with us “hacks” and for being available to extensively discuss some black magic RF problems, even during your well-deserved retirement. The Smith chart should more aptly be called the Sorenson chart.

I would like to thank my committee and readers who took the time to guide me through my doctoral work and provide me with valuable feedback: Dr. Yevgeny Raitses, Dr. Mikhail Shneider, Prof. Samuel Cohen, Dr. Dan Lev, and Prof. Michael Littman.

Thank you to my EPPDyL and 3D3A colleagues and friends: Chris, Matthew, Mike, Sebastián, Will, Joe, and Rahul. You have all made this time in the lab/dungeon much more enjoyable than it would have been otherwise. Chris (my lab partner), I don’t think I could have finished this dissertation without your help and your original work on the cathode. You’ve been extremely patient in dealing with my cathode-physics musings, editing papers, and teaching me about machining and LabView. I have decided that I won’t hold a grudge against you for breaking the first cathode. Matt, you have made sure that I was ready to stand for generals. After hearing my response a 1001 times, I hope that you will remember what a plasma is. Mike, thank you for your all-around enthusiasm and the great evenings with a

homemade pizza around a fire. Sebastián, your eclectic music selection (thanks in part to WPRB) was always a treat when walking into and through the lab. Thank you also for always being available to discuss a math or physics question and for being the lab's grammarian who knows how to properly use hyphens. Will, you have shown me that sometimes the brute-force approach (both numerical and physical) is the correct approach. I will never forget the momento you left on my desk after I got married. Joe and Rahul, you brought a different and welcome perspective from the audio lab. Thank you for all of your helpful discussions. Finally, thank you to the undergraduate researchers Jordan, David, and Sydney. Your helping with the cathode diagnostics pod was invaluable and your questions made me a better teacher.

Dave, Jim, and Matthew, a big thank you for keeping the E-Quad from collapsing. Thank you especially for your help in dealing with sub-basement equipment and the (never-ending) issues with the cooling water (a.k.a. sludge). Glenn and Al, your expertise and help in machining cathode materials was greatly appreciated. I promise we are done with breaking drill bits and dulling end-mills on RA-253MA! A particular thank you to Jon Prévost, a colleague and a friend. You have helped me with all of the custom-made electronics circuits that were used for the cathode experiment. Thank you, too, to Jill Ray, the ever-amazing graduate program administrator. You were a never-ending source of useful information and unwavering support through all of the ups and downs.

I would like to thank the many Princeton friends that I have made along the way. From first year homework sessions to FPO by way of preparation for generals, you have made my time at Princeton memorable. Thank you to the D-Bar trivia team for the great deal of fun in crushing opposition every other week. The snack prizes (especially ¡Sponch!) and debates about last-round jokers will never be forgotten. Thank you also to the MAE friends for a fantastic ski trip in Vermont.

I want to thank my family and friends around the globe for their constant support and for not questioning my never-ending schooling. À mes parents: le travail sur les “fusées” est différent de ce que j’imaginais quand j’étais petit, mais c’est tout aussi amusant. Merci de vous être assurés que je termine mon doctorat. To my wife Stevie, thank you for putting up with me while I was getting “another piece of paper” and for putting things in perspective during the most trying times of the PhD. Last, but not least, thank you to my son Nico for always making me smile and feel like the world’s best comedian.

The research in this dissertation was carried out with the support of the Program in Plasma Science and Technology from the Princeton Plasma Physics Laboratory. This dissertation carries T#3399 in the records of the Department of Mechanical and Aerospace Engineering.

Contents

Abstract	iii
Acknowledgements	v
List of Tables	xii
List of Figures	xiv
List of Symbols	xx
List of Acronyms	xxviii
1 Introduction	1
1.1 Background and motivation	1
1.2 Dissertation focus	9
1.3 Previous work	9
1.4 Dissertation outline and methodology	11
2 Review of 0-D cathode models	12
2.1 Siegfried and Wilbur [69]	15
2.2 Siegfried and Wilbur [52, 63, 65, 71, 72] — a refined approach	17
2.3 Mandell and Katz [75–78]	24
2.4 Capacci <i>et al.</i> [82]	29
2.5 Domonkos [64, 73]	35
2.6 Goebel and Katz [42, 92]	55
2.7 Mizrahi <i>et al.</i> [95, 96]	63

2.8	Albertoni et al. [49, 55]	68
2.9	Model comparisons	78
2.10	Critical issues	85
2.11	Summary	95
3	Experimental configuration and data analysis	97
3.1	Cathode configuration	97
3.2	Facilities	103
3.3	Measurement system	106
3.4	Additional dataset	108
3.5	Data analysis	109
3.6	Total pressure measurements	112
4	Empirical analysis of the total pressure	114
4.1	Π -products	115
4.2	Qualitative evidence of a simple scaling relationship	118
4.3	Power law approach	121
4.4	Randomized selection	125
4.5	Predictive capabilities	127
4.6	Summary	129
5	Zero-dimensional cathode model	130
5.1	Assumptions	132
5.2	Fluid model	137
5.3	Plasma model	143
5.4	Implementation	149
5.5	Results	151
5.6	Summary	156

6	Scaling laws	159
6.1	Pressure-diameter product	159
6.2	Total pressure	162
6.3	Electron temperature and attachment length	169
6.4	Summary	172
7	Practical applications	174
7.1	Implications on cathode design	174
7.2	Lifetime calculation	176
8	Conclusion	180
8.1	Summary of main findings	181
8.2	Future work	182
A	Π-product derivation	184
B	Cathodes reviewed	186
C	Coefficients for the total pressure, electron temperature, and attachment length	190
C.1	Total pressure	190
C.2	Electron temperature and attachment length	191
D	Summary of scaling laws	193
E	Associated electronics	195
E.1	High-voltage, high-current sense board	195
E.2	Pirani gauge power	198
F	Mean and variance of functions of normally-distributed random variable	200

List of Tables

1.1	Work function and Richardson coefficient of a few materials.	7
2.1	Dimensions of the benchmark cathodes. Dimensions are from [65,72], [42,83,92,105–108], and [42,60,107,109,110] for Siegfried and Wilbur’s cathode, the NSTAR discharge cathode, the NEXIS cathode, respec- tively.	78
2.2	Operating conditions and average experimental data required for model input. The definition of the TH8 and TH15 operating points is taken from [108]. The average plasma potentials and electron temperatures are computed from [111] — the reported measurement error is ± 1 V for the potential, and ± 0.5 eV for the electron temperature.	82
2.3	Results from the insert models applied to the NSTAR discharge cath- ode. The experimental data is spatially averaged from data reported in [111]. Plasma potential accuracy is ± 1 V, and electron temperature ± 0.5 eV. No information about accuracy of density measurements is reported.	84
2.4	Results from the orifice models applied to the NSTAR discharge cathode.	84
2.5	Comparison of pressure predictions (in Torr) of multiple flow mod- els applied to the NSTAR cathode. Empirical correlation from [65] (pp.127–129). Experimental data is taken from [117] for TH4, TH8, and TH15, and from [118] for TH12.	87

3.1	Characteristics of the resistor shunts (without temperature derating).	105
4.1	R-squared value and average error for the studied flow models and empirical relationship.	125
4.2	R-squared value and average error for the linear fit with a randomized Π -product. The data for the unperturbed fit is shown on the “Reference” line.	126
B.1	Dimensions and operating conditions of the benchmark cathodes. . .	187
B.2	Comprehensive list of dimensions (in mm) of the benchmark cathodes.	189
C.1	Π -product exponents and constant.	190
C.2	The coefficients used for the insert electron temperature and attachment length correlations (Equations 5.25 and 5.27).	191
C.3	The coefficients used for the orifice electron temperature (Equation 5.26).	192
D.1	List of derived scaling laws.	193

List of Figures

1.1	Schematic of typical orificed hollow cathode	1
1.2	Demonstrated (solid) and estimated (open) lifetime of hollow cathodes for given discharge currents. None of the cathodes for which lifetime testing was conducted reached end-of-life.	5
1.3	Comparison of material evaporation for different emitter materials. For a given current density, the emitter temperature is calculated with Richardson-Dushman equation and the work function from Table 1.1. Evaporation data from [33] for IrLa, IrCe, Ta, and LaB ₆ at low current density, and from [42] (p.255) for BaO-W, W, and LaB ₆ at high current density.	8
2.1	Ratio of thermal electron current backstreaming to ion current for varying sheath voltage and electron temperature.	20
2.2	Ratio of the contribution to the insert surface power balance from thermal electrons backstreaming to ions for varying sheath voltage and electron temperature.	22
2.3	Comparison of Katz's fit (Equation 2.31) to Hayashi's recommended data for total electron-neutral cross section, and to the electron-neutral elastic collisions cross section from [79]. Momentum transfer cross sections are from [79] and [80].	27

2.4	Ratio of electron-ion to electron-neutral collision frequencies, for increasing ionization fraction $\alpha = n_e/n_n$. The Coulomb logarithm is assumed to be equal to 7.1 — the average value for electron temperatures between 0.1 to 10 eV, and electron densities between 10^{18} and 10^{22} m^{-3}	31
2.5	0-D cell representation of the orifice currents.	39
2.6	Region of multi-step ionization.	47
2.7	Comparison of the distribution-averaged collision cross sections. (a) Beam-distribution-averaged excitation cross section computed with Equation 2.69 (dashed line), and Equation 2.70 (solid line). The excitation cross section for a monoenergetic beam is shown with a dotted line. (b) Ratio of the distribution-averaged excitation cross sections for two electron beam temperatures.	48
2.8	0-D cell representation of the insert currents.	50
2.9	(a) Electron temperature and (b) edge-to-axis density ratio as a function of pressure-diameter product.	62
2.10	Comparison of different viscosity models for xenon gas. Experimental fit from [102].	74
2.11	Comparison of emission length empirical relationship (Equation 2.135) for $K = 5, 10, 15 \text{ Pa}\cdot\text{m}$ to experimental data from [65] for (a) xenon and (b) argon.	76
2.12	Comparison of cathode insert models for Siegfried and Wilbur's xenon cathode. Experimental data and original model results are from [65].	80
2.13	Comparison of cathode orifice models for Siegfried and Wilbur's xenon cathode.	81

2.14	Total pressure for two pressure models applied to the NEXIS cathode as functions of (a) discharge current with constant mass flow rate ($\dot{m} = 5.5$ sccm) and (b) mass flow rate with constant discharge current ($I_d = 22$ A). Experimental data from [115, 116].	86
2.15	Viscosity of mercury vapor computed with the Chapman-Enskog method applied to a Lennard-Jones 12-6 potential. Experimental data from [119].	88
2.16	Orifice Knudsen number, range of Reynolds number for both insert and orifice, and orifice entrance length (as a fraction of total orifice length).	91
3.1	Exploded view of the cathode assembly without heater, fasteners, and heat shields.	99
3.2	CAD rendering of the cathode without heater, fasteners, and heat shields. Dimensions are in cm.	100
3.3	Cutaway view of the cathode assembly showing the location of the installed inserts and gas inlet.	101
3.4	Schematic of the cathode apparatus (top view) showing the location of temperature measurements.	101
3.5	Princeton large hollow cathode.	102
3.6	Cathode operating on argon at 300 A of discharge current.	102
3.7	Vacuum vessel.	103
3.8	Diagram of the vacuum system, inspired by [125]. The pumping system is not to scale.	104
3.9	Electrical diagram of the experiment.	106
3.10	Calibration curve for the Pirani gauge.	107
3.11	Example of the derivation of the attachment length from an electron density profile. Experimental data from [111] for the NSTAR discharge cathode operating at 15 A.	109

3.12	Total pressure measurements: (a) with cold gas only (300 K); (b) during cathode operation with argon. Filled and empty markers indicate measurements made with the Pirani and Baratron gauge, respectively.	113
4.1	Correlation matrix of the Π -products.	119
4.2	Explained variance for the dataset.	120
4.3	Local Linear Embedding applied to the Π -products.	121
4.4	Proposed power law (Equation 4.21) applied to the entire data set: $\Gamma(\Pi) = 1.2 \times 10^7 \Pi_2^{0.79} \Pi_3^{0.23} \Pi_4^{-0.27} \Pi_5^{0.82} \Pi_6^{0.25} \Pi_7^{0.41}$. Data from [111, 116, 122] for the NSTAR cathode, [60, 105, 111, 115] for the NEXIS cathode, [47] for Salhi's cathode, [64] for the AR3, EK6, and SC012, [112] for Friedly's cathode, [113, 121] for the T6 cathode, [65, 72, 120, 126] for Siegfried's cathode, and [29, 30] for the JPL 1.5 cm cathode.	123
4.5	Error histogram for the proposed fit (Equation 4.21).	124
4.6	Applied power law to the NEXIS cathode for the case of (a) constant mass flow rate of 5.5 sccm, and (b) constant discharge current of 22 A.	128
4.7	Sensitivity of the proposed empirical law to the gas temperature, applied to the NEXIS cathode.	128
5.1	Ratio of (a) mean free path to orifice length for total inelastic electron-neutral collisions, (b) inter-collision time to neutral gas residency time.	134
5.2	Fluid control volume considered in the analysis.	137
5.3	(a) Peak insert temperature of the NSTAR cathode. (b) Cathode external wall temperature of Salhi's cathode. Experimental data from [116] and [47], respectively. Gray area on the model indicate the minimum and maximum values obtained for the indicated mass flow rates, with sheath voltage and gas temperature with values between 1–10 V and 2000–4000 K, respectively.	152

5.4	(a) Attachment length normalized by the cathode insert diameter and (b) electron temperature as functions of discharge current. Experimental data for the JPL lanthanum hexaboride (LaB_6) cathode and Salhi's cathode from [30] and [47], respectively.	155
5.5	Comparison of pressure models used for the calculation of the total pressure inside hollow cathodes. (a,b) NSTAR cathode. Experimental data from [111, 116, 122]. (c,d) NEXIS cathode. Experimental data from [105, 115]. (e,f) PLHC.	157
6.1	Distribution of total pressure-diameter product for a large number of cathodes. (a) Pressure-diameter product calculated using the insert diameter for all cathodes. (b) Pressure-diameter product calculated using the orifice diameter for only those cathodes presented in [64]. .	161
6.2	Ratio of the total to magnetic pressure (P/P_{mag}) as a function of the ratio of discharge current to mass flow rate (I_d/\dot{m}) for the following cathodes: (a) Friedly's, (b) the NSTAR, (c) the NEXIS, (d) Salhi's operating with argon and an orifice diameter of 1.21 mm, and (e) our own hollow cathode. The shaded area bounds the results of the range of the free parameters of the numerical algorithm.	163
6.3	Approximation of the quantities that are necessary to find a scaling relationship for the total pressure. (a) Computed insert ionization fraction, (b) term $\langle\sigma_{iz}v\rangle T_{eV}^{1/2}$, (c) computed orifice neutral density, and (d) term $\sqrt{1 + \alpha_o T_e/T_n}$. Results for (a), (c), and (d) are shown for the NSTAR cathode operating at 3.7 sccm only. However, all other cathodes follow similar trends (although fitting values are different). .	166
6.4	Theoretically-derived correlation applied to the entire experimental dataset.	170

6.5	(a) Attachment length and (b) electron temperature as functions of the neutral pressure-diameter product ($P_n d_c$). Symbols for (b) are the same as (a). The horizontal error bars bounds the results of the range of the free parameters of the numerical algorithm. Experimental data from [30, 47, 60, 65, 110, 111]. Scaling law for the attachment length for Albertoni <i>et al.</i> from [49] with the corresponding value of K in the range of 5–15 Pa-m.	173
7.1	Estimated and demonstrated range of mass flow rate for select cathodes.	175
7.2	Effect of (a) orifice-to-insert diameter ratio, (b) mass flow rate, (c) discharge current on the computed lifetime.	179
E.1	Schematic of the electronics used to sense current on all shunts. . . .	196
E.2	Shunt board implementation. Red: top PCB layer. Blue: bottom PCB layer.	197
E.3	Schematic of the electronics used to power the PVC1000 Pirani gauge.	198
E.4	PVC1000 board implementation. Blue: bottom PCB layer.	199

List of Symbols

Constants

ϵ_0	Permittivity of vacuum	8.85×10^{-12} F/m
λ_{01}	First zero of 0-th Bessel function of the first kind	2.404826
μ_0	Permeability of vacuum	$4\pi \times 10^{-7}$ H/m
B	Lafferty's constant for the evaporation rate of lanthanum hexaboride 36850 K	
C	Lafferty's constant for the evaporation rate of lanthanum hexaboride	13
C_0	Double sheath factor	1.8516
C_{ei}	Electron-ion collision constant	2.9×10^{-12}
e	Elementary charge	1.602×10^{-19} C
h	Planck's constant	6.62×10^{-34} J·s
k_θ	Constant to calculate the linear conductance weight θ	28
k_B	Boltzmann's constant	1.38×10^{-23} J/K
m	Electron mass	9.1×10^{-31} kg

Geometry

A_{emit}	Emitter area	m^2
-------------------	--------------	--------------

d_c	Cathode (insert) diameter	m
d_o	Orifice diameter	m
L_{emit}	Emission length	m
L_o	Orifice length	m
L_{ck}	Cathode tip to keeper length	m
r_c	Cathode (insert) radius	m
r_o	Orifice radius	m
r_{ds}	Spherical double sheath radius	m

Collisions

λ_{ex}	Mean free path for excitation	m
λ_{pr}	Energy exchange mean free path	m
ν_{ei}	Electron-ion collision frequency	s
ν_{en}	Electron-neutral collision frequency	s
ν_{in}	Ion-neutral collision frequency	s
σ_{CEX}	Charge-exchange cross section	m ²
σ_{inel}	Total inelastic cross section	m ²
σ_{en}	Electron-neutral collision cross section	m ²
σ_{ex}	Excitation cross section	m ²
σ_{iz}	Ionization cross section	m ²

Energy and power

\dot{q}_{conv}	Convection power	W
\dot{q}_{Ω}	Resistive power	W
\dot{q}_{coll}	Power lost to plasma volume by random electron flux	W
\dot{q}_{ori}	Power deposited in plasma volume by orifice ions	W
\dot{q}_{dx}	Power deposited at insert surface by de-excitation of excited states	W/m ²
\dot{q}_{em}	Power deposited in plasma volume by thermionic electrons	W
\dot{q}_{ex}	Excitation power	W
\dot{q}_{iz}	Ionization power	W
\dot{q}_{ph}	Power deposited at insert surface by emitted photons	W/m ²
\dot{q}_{th}	Thermal power lost from the insert	W
ϵ_{ex}	Excitation energy	eV
ϵ_{iz}	Ionization potential	eV

Thermionic emission

ϕ_{eff}	Effective work function	eV
ϕ_w	Surface work function	eV
D_{RD}	Richardson-Dushman constant	A/(m ² ·K ²)
E_c	Cathode surface electric field	V/m
T_c	Insert temperature	K
T_o	Orifice plate temperature	K

Gas flow

\dot{m}	Mass flow rate	kg/s
\dot{m}_A	Mass flow rate	eqA
\dot{Q}	Flow throughput	Pa·m ³ ·s
γ	Ratio of heat capacities	
\mathbf{v}_i	Ion fluid velocity	m/s
\mathbf{v}_n	Neutral fluid velocity	m/s
\mathbf{v}	Mean fluid velocity	m/s
μ	Dynamic viscosity	Pa·s
ρ	Mean mass density	kg/m ³
Kn	Knudsen number	
Ma	Mach number	
Re	Reynolds number	
θ	Linear conductance weight	
a	Speed of sound	m/s
C_a	Thin orifice conductance	m ³ /s
C_m	Molecular flow aperture conductance	m ³ /s
C_v	Viscous (continuum) flow aperture conductance	m ³ /s
d_m	Diameter of gas particles in the hard-sphere approach	m
L_{fd}	Entrance length	m
M	Ion or neutral particle mass	kg

P	Total pressure	Pa
P_n	Neutral gas pressure	Pa
P_{exit}	Static pressure at the orifice outlet	Pa
$P_{\text{ionization}}$	Orifice ionization energy density	Pa or J/m ³
P_{gd}	Gasdynamic pressure	Pa
P_{mag}	Magnetic pressure	Pa
P_{mf}	Momentum flux towards the orifice plate	Pa
R_g	Gas constant	J/(kg·K)

Plasma parameters

α	Ionization fraction	
\bar{n}_e	Average electron density	m ⁻³
$\underline{\underline{\beta}}$	Magnetic stress tensor	
η_p	Plasma resistivity	$\Omega \cdot \text{m}$
$\ln \Lambda$	Coulomb logarithm	
ϕ_p	Plasma potential	V
ϕ_s	Sheath potential	V
ϕ_{ds}	Double sheath potential	V
ϕ_{ps}	Pre-sheath potential	V
$\underline{\mathbf{B}}$	Magnetic flux density	T
$\underline{\mathbf{E}}$	Electric field	V/m

D	Diffusion coefficient	m^2/s
D_a	Ambipolar diffusion coefficient	m^2/s
f_s	Sheath-edge ratio	
I_d	Discharge current	A
I_e	Electron current	A
I_i	Ion current	A
I_r	Random electron current	A
I_{em}	Thermionic current	A
J_e	Electron current density	A/m^2
J_r	Random electron current density	A/m^2
J_{em}	Thermionic current density	A/m^2
J_i	Ion current density	A/m^2
n_e	Electron density	m^{-3}
n_e^s	Sheath-edge electron density	m^{-3}
n_i	Ion density	m^{-3}
n_n	Neutral gas density	m^{-3}
R_p	Plasma resistance	Ω
R_{or}	Orifice plasma resistance	Ω
T_e	Electron temperature	K
T_i	Ion temperature	K

T_n	Neutral gas temperature	K
T_{eV}	Electron temperature	eV
T_{iV}	Ion temperature	eV
T_{nV}	Neutral gas temperature	eV
v_B	Bohm velocity	m/s
v_{scat}	Neutral scattering velocity	m/s

Other Symbols

δ	Free parameter for Mizrahi <i>et al.</i> model	
Σ_0	Internal partition function for the neutral state	
Σ_i	Internal partition function for the singly ionized state	
τ_{ij}	Ratio of the temperature T_i to T_j	
θ	Heaviside function	
$H(T)$	Heat loss in Goebel and Katz's model	W
J_0	Zero-th order Bessel function of the first kind	
J_1	First order Bessel function of the first kind	
K	Empirical constant for the attachment length in the model of Albertoni <i>et al.</i> 5–15 Pa·m	
N_i	Total number of ions	
N_{ex}	Total number of excited atoms	

p_{ex}	Percentage of primary excitation events that yield ions through multi-step ionization in Domonkos's model	
W	Material evaporation rate	kg/m ² /s

List of Acronyms

AF-MPDT	applied-field magnetoplasmadynamic thruster
BaO	barium oxide
C12A7	calcium-aluminate electride $[\text{Ca}_{24}\text{Al}_{28}\text{O}_{64}]^{4+}(\text{e}^{-})_4$
DAQ	data acquisition system
EEDF	Electron Energy Distribution Function
IrCe	iridium-cerium
IrLa	iridium-lanthanum
JPL	Jet Propulsion Laboratory
LaB₆	lanthanum hexaboride
LLE	Local Linear Embedding
MPDT	magnetoplasmadynamic thruster
NI	National Instruments
PCA	Principal Component Analysis
PLHC	Princeton large hollow cathode
Ta	tantalum
W	tungsten

Chapter 1

Introduction

1.1 Background and motivation

Thermionic, orificed hollow cathodes serve as plasma sources of electrons and have been used for a variety of applications, such as surface processing [1–3], neutral beam injectors for fusion devices [4–6], and electric space propulsion [7,8]. The cross section of a typical orificed hollow cathode is shown in Figure 1.1.

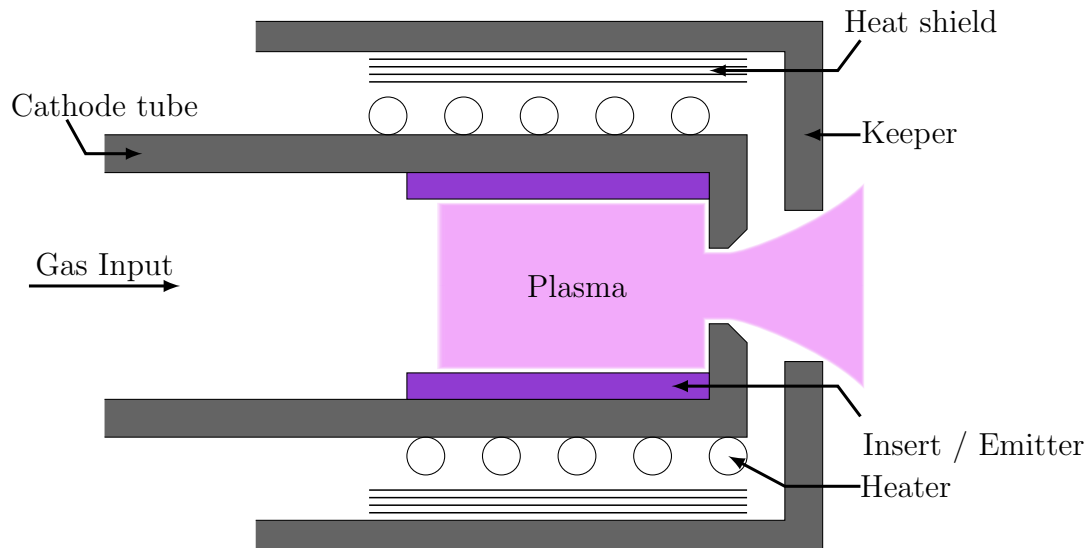


Figure 1.1: Schematic of typical orificed hollow cathode

Hollow cathodes feature a hollow tube (made of either a refractory metal or graphite) which is capped by an orifice plate and in which a low-work-function thermionic material is inserted. A keeper electrode is placed around and/or in front of the cathode to initiate the discharge and to protect the orifice plate from high-energy ions (hypothesized to be generated by ion acoustic instabilities in the plume [9]) that are accelerated towards the cathode. An external heater is used to bring the insert material to emitting temperatures. It is surrounded by heat shields to ensure that heat is efficiently transferred to the emitter. A neutral gas (*e.g.*, xenon) is then introduced in the tube and a discharge is established with an external anode.

Once steady-state is achieved, hollow cathodes operate in a self-heating mode and the heater is unnecessary. In this mode, the emitter is heated both by electrons and ion impact. Heat is lost through radiative and conductive processes, and through thermionic cooling. The ratio of power deposited by electrons to that deposited by ions depends on the plasma condition (electron temperature and sheath potential). The cathode can be split into three distinct regions:

- the *insert* region,
- the *orifice* region, and
- the *plume*.

The insert region is of particular interest because the plasma processes in that region influence the total lifetime of the emitter. The orifice constriction ensures that the plasma in the insert region stays highly collisional by keeping the insert total pressure high ($\sim 1\text{--}10$ Torr) and constant. The study of the plume region can be entirely decoupled from that of the rest of the cathode because of the existence of a Mach 1 surface at or near the orifice exit. This sonic condition is due to the expansion of the ionized gas into vacuum.

1.1.1 Scope of this work

Emission process While electrons can be emitted from a material through other physical processes (*e.g.*, secondary or photoelectric emission), we restrict the scope of this work to cathodes that emit electrons through thermionic emission.

Applications We will consider only applications to electric space propulsion. Examples of space propulsion thrusters that require a cathode are Hall-effect thrusters, ion thrusters, and magnetoplasmadynamic thrusters (MPDTs). Orificed hollow cathodes are typically used for the former two, though exploratory work has been conducted with MPDT [10–14] at low current (< 200 A).

Cathode type Other types of cathodes for space propulsion include solid (rod), tube, and multi-channel cathodes. Tungsten rod cathodes are typically used in both arcjets and high-power MPDT (Megawatt-level) that operate with noble gases or hydrogen. The high temperature required for emission with pure tungsten ($\propto 2,700^\circ\text{C}$ for a current density of 10 A/cm^2) shortens the lifetime of rod cathodes because of evaporation, localized melting, and embrittlement. The latter is due to recrystallization of refractory metals at high temperatures: tungsten undergoes recrystallization at or below a temperature of $1,500^\circ\text{C}$ [15].

Tube and multi-channel cathodes are also “hollow” and operate with a neutral gas introduced in a single or multiple channels that is then ionized. Tube cathodes do not have an orifice plate and are therefore subject to large pressure gradients within the internal plasma region. Because of the low internal pressure, the electron temperature is higher than that of orificed hollow cathodes. In turn, the sheath potential of the plasma inside the tube cathode is also higher, and so is the energy of ions that impact the thermionic emitter. This contributes to material sputtering and increases the temperature of operation of the emitter, and, therefore, its evaporation

rate. Both increased sputtering and evaporation contribute to the reduction of the operational lifetime of tube cathodes.

The low internal pressure of tube cathodes is circumvented by either capping the cathode tube or using multiple channels. Both orificed hollow cathodes and multi-channel hollow cathodes are able to deliver higher currents than solid or tube cathodes and have a longer lifetime than tube cathodes for similar operating conditions. Multi-channel cathodes have been demonstrated both with condensible propellant (*e.g.*, lithium) in applied-field magnetoplasmadynamic thrusters (AF-MPDTs) [16] and with noble gases. Orificed hollow cathodes operate at a lower temperature than multi-channel ones because they typically use a low-work-function thermionic emitter which provides cooling through electron emission. The lower operating temperature also leads to a lower evaporation rate of the emitter and increases the lifetime of the cathode.

Range of operation of hollow cathodes Because orificed hollow cathodes are the most promising type of cathodes for future missions, their reliable operation is critical. In the context of space propulsion, proposed missions require operational lifetimes of up to 100,000 hours (100 kh) [17,18] without servicing, with estimated total discharge powers in the range of 100–200 kW [19], or, equivalently, for up to 800 A of current for a typical Hall-effect thruster (assuming an efficiency of 100%, a specific impulse of 2,000 s, and xenon gas). Existing thrusters are starting to approach or exceed this power level [20–22]. Alternative thrusters such as the AF-MPDT are attractive alternatives to Hall-effect and ion thrusters for high-power, manned missions to Mars and beyond because of their high thrust density, specific impulse, and thrust efficiency. However, they also require long lifetimes with even higher discharge currents of 1 kA or more.

To date, only cathodes that operate at low current (< 20 A) have undergone life testing and the lifetime of high-current (> 100 A) cathodes has only been estimated to be in the tens of kilo-hours (see Figure 1.2). There is a clear need for technological improvements to increase cathode performance to a combined range of discharge current and lifetime that can enable next-generation missions. High discharge currents can be achieved by scaling the cathodes to larger sizes. It is unclear, however, how the cathode lifetime is affected by an increase in discharge power.

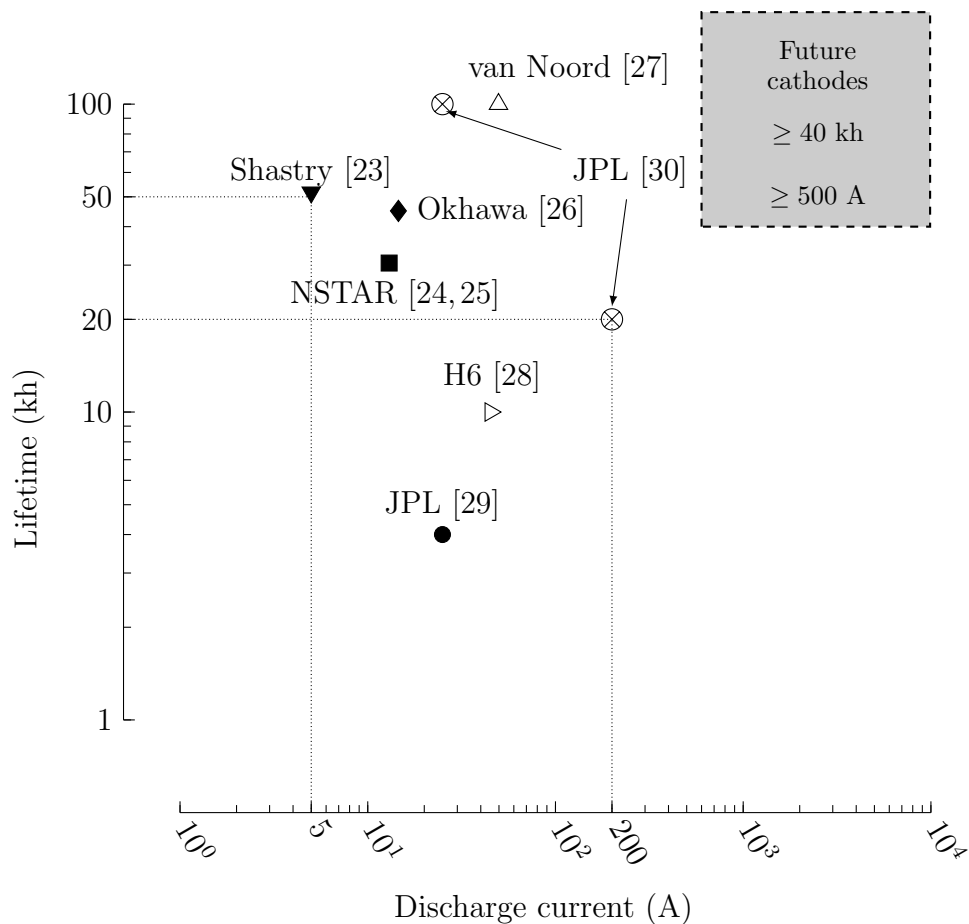


Figure 1.2: Demonstrated (solid) and estimated (open) lifetime of hollow cathodes for given discharge currents. None of the cathodes for which lifetime testing was conducted reached end-of-life.

1.1.2 Lifetime-limiting factors

The lifetime of a thermionic orificed hollow cathode is limited by the erosion of external surfaces, by its heater failing prematurely, and by the evaporation and material sputtering of the thermionic emitter.

Surface erosion

The erosion of the orifice plate and keeper is due to high-energy plume ions that are accelerated towards the cathode and sputter the electrode. The orifice plate is protected by the keeper electrode so that only the latter can be considered as the lifetime-limiting factor. A possible solution to extend the lifetime of both surfaces is to either quench the energy of the high-energy ions with external gas injection or to simply use a thicker keeper electrode. The former has been demonstrated in high-current cathodes [31]. We use the latter in our experimental work for simplicity.

Heater failure

Large hollow cathodes require an external heater to start the thermionic emission process. Heaters based on refractory metals (*e.g.*, swaged tantalum) suffer from grain growth, embrittlement, and are difficult to manufacture. Graphite-based heaters, on the other hand, are only limited by the sublimation of their carbon surface and are easily fabricated. Their expected lifetime is well over 100 kh [32], and are therefore not a critical component, though they remain to be demonstrated in space.

Emitter failure

Evaporation and sputtering Both evaporation and sputtering of the emitter depend on the behavior of the plasma in the insert region and on the choice of emitter material. Emitter material include pure or thoriated refractory metals (*e.g.*, tungsten and thoriated tungsten), refractory metals impregnated with a low-work function

Table 1.1: Work function and Richardson coefficient of a few materials.

Material	Work function	Richardson coefficient ($\text{A}\cdot\text{cm}^{-2}\text{K}^{-2}$)	Reference
BaO-W	$1.67 + 2.87 \times 10^{-4} T_c$	120	[42] (p.252)
C12A7	0.5–3.5	N/A	[37, 38, 40, 41]
IrCe	2.57	120	[33]
IrLa			
LaB ₆	2.70	29	[42] (p.252)
Ta (polycrystalline)	4.25	37	
W (polycrystalline)	4.55	70	[43]

material (*e.g.*, barium oxide (BaO)-impregnated tungsten), borides (*e.g.*, LaB₆), and less-common compounds such as iridium-cerium (IrCe) [33–36] or calcium-aluminate electride $[\text{Ca}_{24}\text{Al}_{28}\text{O}_{64}]^{4+}(\text{e}^-)_4$ (C12A7) [37–41]. Table 1.1 shows the work function of select emitter materials. It is preferable to use a thermionic emitter with a low work function, as it reduces the temperature of operation and therefore material evaporation for a given target emission current density. We show in Figure 1.3 the evaporation rate and emitter temperature as a function of current density. For a given current density J_{em} the emitter temperature T_c is obtained with the Richardson-Dushman equation:

$$J_{em} = D_{RD} T_c^2 \exp\left(-\frac{e\phi_w}{k_B T_c}\right), \quad (1.1)$$

where D_{RD} is a material-dependent constant, e is the electron charge, k_B is the Boltzmann constant, and ϕ_w is the work function of the emitter, in eV. To limit evaporation low-temperature ($\sim 1000^\circ\text{C}$) operation of the emitter is preferable. This requires the thermionic emitter to be efficiently used so that the total current density is low. The attachment length, or length over which the plasma is dense enough to “absorb” all emitted electrons, is a direct measure of the plasma coupling to the emitter. For efficient operation, the attachment length should match the length of the thermionic insert. Sputtering can be limited by reducing the plasma sheath potential to limit ion acceleration in the sheath. Low sheath potentials can be achieved at

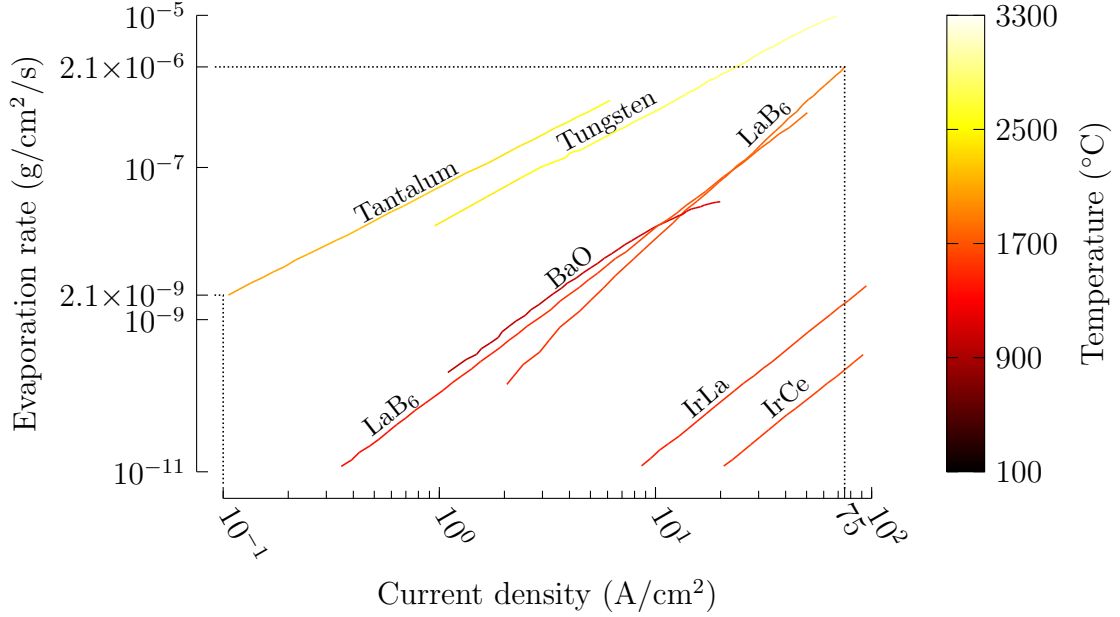


Figure 1.3: Comparison of material evaporation for different emitter materials. For a given current density, the emitter temperature is calculated with Richardson-Dushman equation and the work function from Table 1.1. Evaporation data from [33] for IrLa, IrCe, Ta, and LaB₆ at low current density, and from [42] (p.255) for BaO-W, W, and LaB₆ at high current density.

low electron temperature (less than 2 eV) for typical cathode plasma densities (10^{18} – 10^{21} m⁻³).

We note that the C12A7 electrider has a theoretical work function in the range of 0.5–3 eV [37, 38, 40, 41] and can also be an excellent candidate for orificed hollow cathodes. However, it is unclear if plasma-wall interactions may damage the structure that enables low-temperature emission.

Poisoning Impurities in the operating gas may increase the work function of a material (“poisoning” of the material). Both BaO dispenser materials and iridium-based compounds are attractive because of their low work function and evaporation rate, respectively. However, they do suffer from poisoning [35, 44] and therefore require the use of high-purity gases for space applications. While lanthanum hexaboride has a larger work function (and therefore operating temperature) than both of those

materials it is a robust material that does not suffer as much from poisoning [45]. Its characteristics make it an excellent emitter material for orificed hollow cathodes.

1.2 Dissertation focus

Our goal is to provide tools that enable the design of cathodes for given performance targets (discharge current and lifetime) without any prior experimental quantities. Because the lifetime of the cathode is intimately tied to the behavior of the internal cathode plasma, we seek to quantify the variation of plasma quantities with controllable parameters (*e.g.*, cathode geometry and discharge current).

The core idea of this work is that the fundamental quantities dictating the lifetime of cathodes can be derived from simplified fluid models for a partially-ionized plasma. In this approach, we will:

1. perform a dimensional analysis on experimental data and determine which parameters are relevant to the flow regime in which cathodes operate,
2. use a fluid theoretical framework based on the results of the dimensional analysis to formulate scaling relationships, and
3. apply and verify the developed correlations to a cathode regime that has never been tested.

1.3 Previous work

Previous scaling relationships have been proposed to quantify the lifetime of a cathode [46], to establish the operating envelope of cathodes [47,48], or to evaluate the plasma attachment length [49].

Kaufman *et al.* [46] Kaufman empirically developed some of the first scaling relationships for the lifetime of hollow cathodes under the assumption that it is limited by the erosion of the cathode tip:

$$\frac{I_d}{d_o} \leq 12 \text{ A/mm}, \quad (1.2)$$

where I_d is the total discharge current in amperes, and d_o is the orifice diameter.

Because the empirical correlations were developed from mercury hollow cathode data they are not applicable to modern cathodes which operate on noble gases. The life-limiting process of tip erosion is also mitigated by the presence of a keeper in a modern cathode.

Salhi *et al.* [47,48] Salhi *et al.* find that the plasma effective length is proportional to the internal diameter of the cathode ($L_{\text{emit}} \propto d_c$) by solving the Laplace equation in the insert region. The authors also find that the maximum discharge current that can be drawn by a cathode is proportional to the cathode inner diameter ($I_d \propto d_c$) by arguing that resistive heating is balanced by convection losses. The use of the Laplace equation to solve for the potential distribution within a plasma, however, is not justified because the assumption of quasineutrality does not imply that the charge density in Poisson's equation must vanish [50].¹ The fact that Salhi *et al.* obtain the correct scaling for the attachment length is likely due to the exponential nature of the potential distribution decay in the axial direction. We have found that our cathode (whose experimental setup will be described in the following chapter) can operate above the maximum current suggested by Salhi *et al.*, which implies that including only resistive heating and convection losses limits the domain of applicability of the relationship for the maximum discharge current that can be drawn by a cathode.

¹To correctly obtain the potential distribution from the plasma density in a collisional and weakly-ionized plasma the current continuity may be used [51].

Albertoni *et al.* [49] The empirical analysis performed by Albertoni *et al.* suggests that the attachment length L_{emit} is inversely proportional to the total pressure P in hollow cathodes:

$$L_{\text{emit}} = K/P, \tag{1.3}$$

where K is a constant between 5–15 Pa-m. This result is similar to that found in [52] for sheath voltages less than 8 V for xenon. However, the observed scaling of attachment length cannot be captured by the electron transport phenomena suggested in [52], nor by the purely empirical relationship given in [49] (which does not offer a mechanistic explanation).

1.4 Dissertation outline and methodology

In the next chapter, we review past attempts at a theoretical model of the cathode insert plasma. We then present the experimental setup we developed and derive empirical scaling relationships based on experimental data measured with our setup and from the literature. In the following two chapters, we derive our own cathode model based on the lessons learned from our review and empirical study, and we apply the theoretical model to the derivation of rigorous scaling laws. We discuss the physical meaning of those scaling laws and provide design rules for future cathodes.

Chapter 2

Review of 0-D cathode models¹

Several approaches have been used to model the physical processes within orificed hollow cathodes, often restricting their focus to the “active zone” or insert plasma region [42, 52, 55] where significant electron emission is supplied to the plasma by the emitter. In turn, sufficient ion current is generated from the plasma for the discharge to be self-sustaining and to avoid space-charge-limited emission. The insert plasma is usually modeled with either zero-dimensional (0-D) or two-dimensional (2-D) axisymmetric approaches, either including the orifice as a coupled region or using a separate model implemented as a boundary condition.

While there exists several elaborate 2-D fluid [56, 57], hybrid-particle in cell (PIC) [58], and full PIC models [59] to describe the behavior of the plasma inside hollow cathodes, none have been applied or used to elucidate the underlying physics governing hollow cathodes over a wide range of operating conditions. All existing two-dimensional models require experimental data as an input and are therefore lim-

¹This chapter is based on work presented in References

- [53]: Wordingham, C. J., Taunay, P.-Y. C. R., and Choueiri, E. Y., “A Critical Review of Orificed Hollow Cathode Modeling: 0-D Models,” *53rd AIAA/SAE/ASEE Joint Propulsion Conference & Exhibit*, 2017, AIAA-2017-4888, and
- [54]: Taunay, P.-Y. C. R., Wordingham, C. J., and Choueiri, E. Y., “An Empirical Scaling Relationship for the Total Pressure in Hollow Cathodes,” *AIAA Propulsion and Energy Forum*, 2018, AIAA-2018-4428.

ited to cathodes for which such data exist. Moreover, in the case of existing fluid models, the treatment of the sheath is inconsistent with the physics involved. The latest iterations [56] of the “OrCa2D” code [60] use the work of Prewett and Allen [61] to compute the wall electric field in order to calculate emission enhancement due to the Schottky effect when the field is non-zero at the wall. The OrCa2D code relies on the assumptions made in [61], which limit it to cases where the emitter does not feature a virtual cathode and does not operate at the sheath space-charge limit, which is a possibility in thermionic hollow cathodes. Sary *et al.* [57] use the image-charge approach developed for vacuum emission by Lin and Eng [62] to treat the emitter wall boundary condition and add the fluxes of ions and random electrons from the bulk plasma. However, Sary *et al.* only include the image-charge created by the emitted electrons and ignore the one generated by both plasma ions and electrons. This likely does not enforce the zero-potential boundary condition at the wall and it is unlikely that results from vacuum emission can be directly applied to thermionic emission in the presence of a plasma. Because they require experimental data and, in the case of fluid models, inconsistently treat the sheath, two-dimensional models in their current form cannot be used for predictive purposes or to formulate scaling laws.

The 0-D approach relies on a control volume with volume-averaged plasma properties. While important processes such as the variation of the plasma density along the cathode axis or the plasma potential along its radial direction may be neglected, 0-D models can still provide useful results and scaling relationships. Any choice of simulation dimension requires the inclusion of plasma-wall interactions for a comprehensive model, ideally implemented in the form of a double- or emitting-sheath model at the surface of the emitter. The emission mechanism is typically assumed to be field-enhanced thermionic emission [49, 63, 64], governed by the Richardson-Dushman equation. The work function is often modified to account for the Schottky effect due to the sheath electric field (though this correction is sometimes neglected [42]). In

order to estimate the electric field at the emitter surface, the double-sheath analysis of Prewett and Allen [61] is typically employed, although other authors use the plasma potential in place of the sheath potential in the equations from [61]; the effect of this simplification will be discussed in later sections. Other important emission processes, such as space-charge-limited emission, are often ignored or implicitly handled through the use of the emission length or “active zone” where the plasma density is assumed to be sufficient to avoid limitation of the extracted thermionic current.

One of the primary difficulties associated with the assumption of uniform plasma properties is that it requires a description of the appropriate boundaries of the active zone in order to model the insert emission region. The calculation of the emission length, L_{emit} , or active zone length, in the axial direction typically requires a separate model, as the 1-D axial variation of the plasma and neutral densities appears to govern the formation of this region.

Approaches for calculating the attachment length include: 1) using a fixed multiple of the mean free path for energy exchange [52,65] of the emitted electrons, 2) assuming ambipolar-diffusion-dominated density decay [42], 3) using empirical correlations that yield L_{emit} as a function of the cathode internal pressure [49], 4) iterative calculations of the discharge power (selecting L_{emit} such that the power is minimized) [55], 5) using L_{emit} as a free parameter to fit experimental data [49], or 6) taking L_{emit} from experimental data [42].

While various models have been proposed, few are completely self-consistent or self-contained and readily available to extend the domain of operation of hollow cathodes. This chapter will review 0-D models developed since the advent of the orificed hollow cathode and provide critical insight on their quality and validity. Comparisons between the various 0-D model results and experimental data for two benchmark cathodes are given in Section 2.9. When possible, the algorithm of the original authors are re-implemented using Python and its Numpy [66] and Scipy [67] packages. Non-linear

systems of equations are solved in a least squares approach with Scipy’s `root` solver configured with the Levenberg-Marquardt algorithm [68]. The critical modeling issues we identified in our review are discussed in Section 2.10.

2.1 Siegfried and Wilbur [69]

A simple first-principles approach was initially chosen by Siegfried and Wilbur to model orificed hollow cathodes operating on mercury, employing tantalum-foil inserts coated with the low-work-function material R-500 (ϕ_w of approximately 2.3–2.4 eV). Their work follows modeling efforts from Bessling [70]. Plasma-wall interactions are entirely neglected in this model, but it allows for the calculation of the local plasma density and ionization fraction as a function of the measured electron temperature and the — calculated or measured — cathode pressure. The cathode stagnation pressure, P , is estimated assuming choked-sonic flow at the orifice,

$$P = \frac{\dot{m}\sqrt{T_n}}{\pi r_o^2} \left[\frac{\gamma}{R_g} \left(\frac{2}{\gamma + 1} \right)^{\frac{\gamma+1}{\gamma-1}} \right]^{-1/2}, \quad (2.1)$$

where the neutral gas temperature T_n is a stagnation quantity. \dot{m} , γ , R_g , and r_o are the input mass flow rate, ratio of heat capacities, specific gas constant, and orifice radius, respectively. Using the set input mass flow rate for \dot{m} in Equation 2.1 implicitly assumes that 100% of the propellant gas leaves the cathode in a neutral state, and therefore neglects ionization processes that decrease the total number density of neutrals as well as any pressure contributions from plasma ions or electrons. It also neglects viscous effects within the orifice and insert region and the heating of the neutral gas by the plasma, as the derivation of Equation 2.1 relies on the assumption of isentropic flow. The effect of the discharge current on the pressure is also neglected, though the authors note that the variation was only 15% of the total over the range of discharge currents examined. Siegfried and Wilbur also report good agreement

between measured and calculated pressures, despite the apparent inapplicability of the flow model used.

The ionization fraction α is determined based on a two-temperature Saha model,

$$\frac{\alpha^{1+\tau_{ge}}}{(1-\alpha)^{\tau_{ge}}(1+\alpha/\tau_{ge})} = \frac{1}{P} \frac{(2\pi m)^{3/2}}{h^3} e^{5/2} T_{nV} T_{eV}^{3/2} \left(\frac{\Sigma_i}{\Sigma_0} \right)^{\tau_{ge}} \exp \left(-\frac{\epsilon_{iz}}{T_{eV}} \right), \quad (2.2)$$

where $\alpha = n_e / (n_e + n_n)$. n_e and n_n are the electron and neutral densities, respectively. m , e , h designate the mass and charge of the electron, and the Planck constant, respectively. ϵ_{iz} is the ionization energy of the gas considered, in eV. Both the neutral gas temperature, T_{nV} , and electron temperature, T_{eV} are here in eV. Σ_i and Σ_0 are the partition functions of the ions and of the neutral gas, respectively. τ_{ge} is the ratio of the neutral gas temperature to the electron temperature. The total pressure is expressed in Pascals in Equation 2.2, and the ions/neutrals are assumed to be in thermal equilibrium with one another, but not with the electrons, which are further assumed to have equilibrated amongst themselves.

The total pressure is linked to the heavy particle density and plasma density using the perfect gas law, under the assumption that the densities and temperatures are uniform within the cathode:

$$P = e (n_e T_{eV} + n_n T_{nV} + n_i T_{iV}), \quad (2.3)$$

where n_i and T_{iV} are the ion density and temperature in eV, respectively. The neutral temperature is also assumed to be equal to the ion temperature and is calculated as the average of the estimated internal cathode temperature and the orifice plate temperature (≈ 0.1 eV for Siegfried and Wilbur's experiment).

Evaluation

The authors demonstrate good agreement between calculated and experimental data for their mercury cathode operating in spot mode ($I_d = 6.0$ A at $\dot{m} = 100$ mA). In plume mode ($I_d = 2.0$ A at the same \dot{m}), the authors experimentally measured a flat electron temperature profile, but chose to use a linear fit for the electron temperature when implementing their model as it gives better agreement with the experimental data. Siegfried and Wilbur also demonstrate that the model results are sensitive to the chosen neutral gas temperature. They compare the results of the algorithm for two values of T_{nV} : $T_{nV} = 0.1$ eV and $T_{nV} = T_{eV}$. The latter value results in an increase in the ionization fraction, and therefore the plasma density, of several orders of magnitude.

2.2 Siegfried and Wilbur [52, 63, 65, 71, 72] — a refined approach

Siegfried and Wilbur refined their original model in a series of articles and reports [52,63,65,71,72]. In this refined model, the authors assume that the plasma properties are uniform within an “ion production region” that coincides with the insert emission length (or attachment length, L_{emit}). An early version of the new model is described in [63] and [71]. It consists of a current balance and insert power balance, with the assumption that ions are either collected at the emitter or the orifice plate, leave the cathode through the orifice, or travel toward the upstream region of the cathode at the Bohm velocity. The sheath electric field is described using Child’s law and an assumed sheath thickness of one Debye length (thereby assuming a single-species, space-charge-limited sheath). The unknowns of this system are the plasma potential, electron temperature, emitter temperature, and plasma density. This version of the model requires two measured quantities (electron temperature and plasma potential), the

emission length, and the heat loss from the emitter (through conduction, radiation, and convection) in order to solve for the two other quantities of interest. This model is still a notable improvement over the initial one, as it does not rely on a Saha-type equation for the ionization fraction, the use of which is generally not justified [49].

A later, improved approach introduces a flow model, a double-sheath approach to treat the electric field at the cathode surface, and a plasma volume power balance. The emission length is linked to the energy-exchange mean free path of the emitted electrons. The introduction of two additional physical constraints allows for four physical quantities to be computed — the plasma density, plasma potential, neutral gas density, and emitter temperature. The electron temperature remains a free parameter. This improved version is described and critiqued below.

Total pressure The cathode pressure upstream of the orifice is assumed to be equal to the stagnation pressure, which is roughly constant along the cathode length. It is given by an empirical relationship,

$$P = \left(\frac{\dot{m}_A}{4r_o^2} \right) (c_1 + c_2 I_d) \times 10^{-3}, \quad (2.4)$$

where P is in Torr, \dot{m}_A in mA-equivalent, and r_o in mm. The constants c_1 and c_2 depend on the gas of interest. Equation 2.4 addresses the shortcomings of Equation 2.1, as it is empirically derived and does not neglect the effects of the plasma on the flow.

Current balance The ion and electron currents, I_i and I_e , are related to the total discharge current through a net current balance:

$$I_d = I_e + I_i = J_{em} A_{\text{emit}} + J_i (A_{\text{emit}} + 2\pi r_c^2), \quad (2.5)$$

where A_{emit} is the total emission area and r_c is the (inner) radius of the insert. Ions are lost from the plasma volume at the emitter and orifice boundaries and in the upstream portion of the cathode. Siegfried and Wilbur assume that the ions are lost upstream at the Bohm velocity, as opposed to the ion thermal velocity. This leads to an ion current contribution approximately 2 times higher at the upstream boundary as compared to the ion thermal current (using $T_{eV} = 0.8$ eV and $T_{iV} = 0.1$ eV). The ion current is obtained with the Bohm velocity, which is assumed to be valid even with a boundary emitting electrons, a common assumption that yields reasonable results but that is not entirely justified. We discuss this assumption in more details in Chapter 5. The effect of the pre-sheath on the ion density is also neglected in the expression for the ion current density, J_i :

$$J_i = en_e \left(\frac{eT_{eV}}{M} \right)^{1/2}, \quad (2.6)$$

where M is the ion mass. It is assumed that no electrons return to the insert from the plasma so that only thermionic electrons contribute to the total current, in sharp contrast with later models [42, 49, 73]. This assumption does not hold under all conditions encountered in orificed hollow cathodes. Assuming that the collection areas for back-streaming electrons and ions are the same, the ratio of back-streaming electrons, I_r , to ion current, I_i , at the insert surface may be calculated as:

$$\frac{I_r}{I_i} = \left(\frac{M}{2\pi m} \right)^{1/2} \exp(-\phi_s/T_{eV}), \quad (2.7)$$

where ϕ_s is the sheath potential. Figure 2.1 illustrates this ratio for common operating conditions found in orificed hollow cathodes, for both mercury and xenon as propellant. For the case where the sheath potential is taken to be equal to the plasma potential, this assumption may be valid at low electron temperatures (1–1.5 eV).

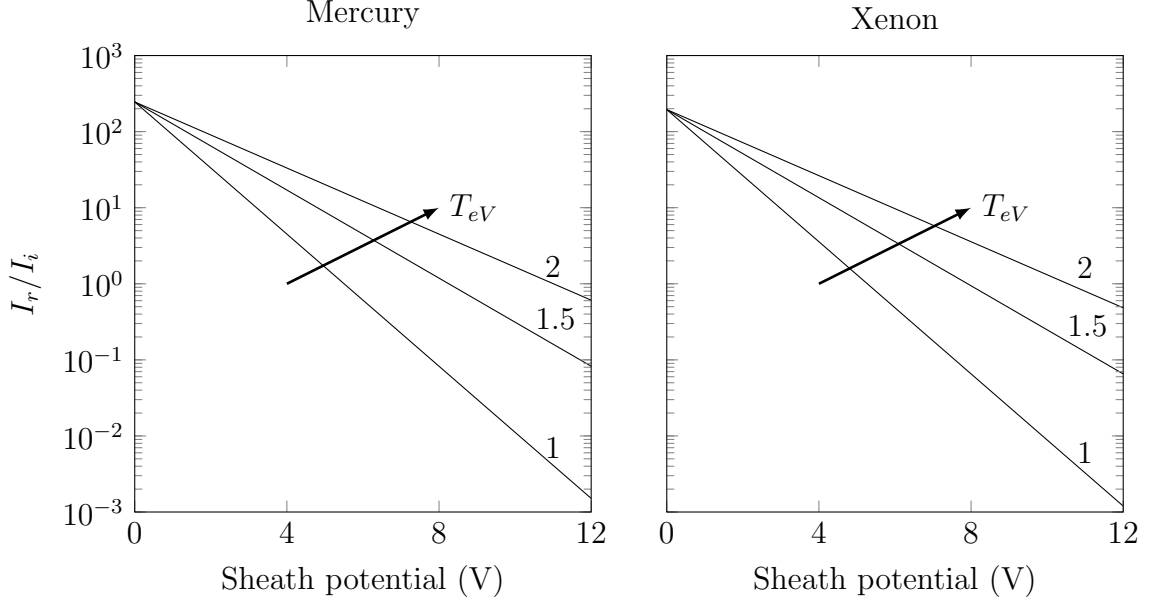


Figure 2.1: Ratio of thermal electron current backstreaming to ion current for varying sheath voltage and electron temperature.

The Richardson-Dushman relationship is used to calculate the thermionic current,

$$J_{em} = D_{RD} T_c^2 \exp \left(-\frac{e\phi_{\text{eff}}}{k_B T_c} \right), \quad (2.8)$$

with an effective work function, ϕ_{eff} , modified to take into account the finite electric field at the cathode surface, E_c :

$$\phi_{\text{eff}} = \phi_w - \left(\frac{e|E_c|}{4\pi\epsilon_0} \right)^{1/2}. \quad (2.9)$$

ϵ_0 designates the permittivity of vacuum. The cathode surface electric field can be calculated using an approximate form of the surface electric field expression from Prewett and Allen's double sheath model [61]:

$$E_c \approx \left(\frac{n_e e T_{eV}}{\epsilon_0} \right)^{1/2} \left(2 \left(1 + 2 \frac{\phi_p}{T_{eV}} \right)^{1/2} - 4 \right)^{1/2}. \quad (2.10)$$

Siegfried and Wilbur use the plasma potential, ϕ_p , instead of the sheath potential in Equation 2.10. The correction to the work function is not affected by this change, as the plasma potential only appears to the 1/4-th power in Equation 2.9.

Power balance The model includes power balances for both the insert surface and plasma volume, given by Equations 2.11 and 2.12, respectively:

$$J_i A_{\text{emit}} (\phi_p + \epsilon_{iz} - \phi_w) + \underbrace{\dot{q}_{dx} A_{\text{emit}} + \dot{q}_{ph} A_{\text{emit}}}_{\text{neglected}} = \dot{q}_{th} + I_{em} \phi_{\text{eff}}, \text{ and} \quad (2.11)$$

$$\phi_p I_e = \epsilon_{iz} I_i + \frac{5}{2} T_{eV} I_d. \quad (2.12)$$

\dot{q}_{th} and I_{em} are the total heat loss (through conduction, convection, radiation) and total thermionic current, respectively. Power deposition to the insert by de-excitation (\dot{q}_{dx}) and photon absorption (\dot{q}_{ph}) are neglected. Ohmic heating in the plasma is ignored, which becomes more significant with increasing discharge current. The electrons back-streaming to the surface are neglected here as well. The power contribution of the backstreaming electrons may be compared to the ion contribution:

$$\frac{P_r}{P_i} = \left(\frac{M}{2\pi m} \right)^{1/2} \exp(-\phi_s/T_{eV}) \frac{2T_{eV} + \phi_w}{\epsilon_{iz} + \phi_s - \phi_w}. \quad (2.13)$$

Figure 2.2 illustrates the power ratio for common operating conditions found in orificed hollow cathodes, for mercury and xenon propellants. Similar conclusions to those drawn from Figure 2.1 can be reached: assuming a sheath potential equal to the plasma potential (usually 8–12 V) and low electron temperature justifies neglecting the random electron flux.

Attachment length The plasma attachment length is taken to be proportional to the energy-exchange mean free path of the thermionically emitted electrons (primary

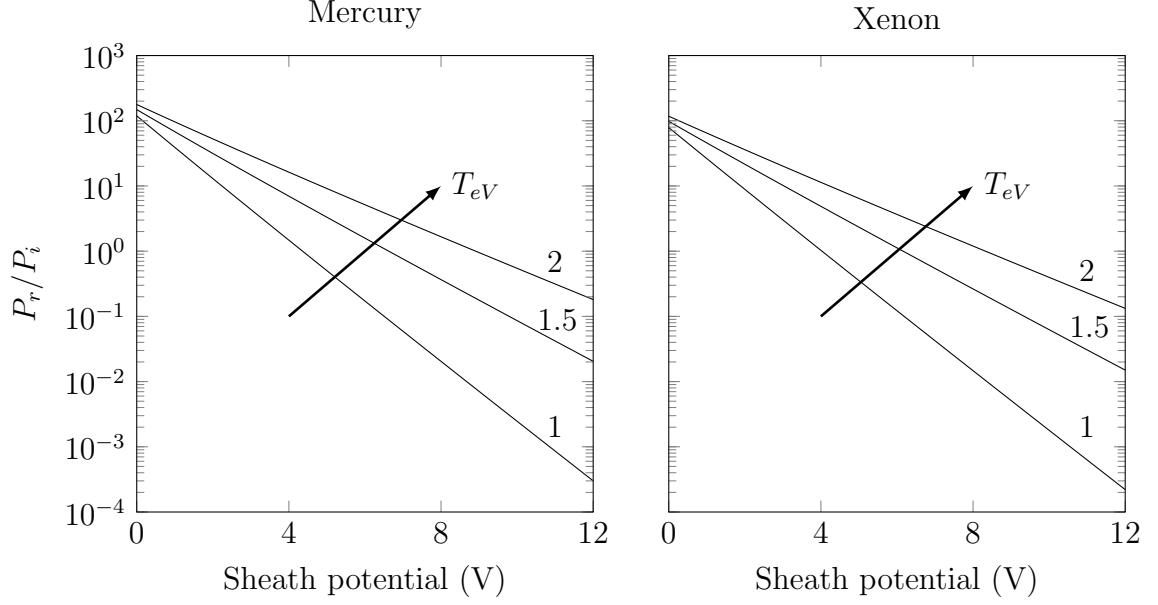


Figure 2.2: Ratio of the contribution to the insert surface power balance from thermal electrons backstreaming to ions for varying sheath voltage and electron temperature.

electrons), λ_{pr} :

$$L_{\text{emit}} = c_3 \lambda_{pr}, \quad (2.14)$$

where c_3 varies with the gas species [65]. The energy-exchange mean free path is the mean free path of the primary electrons. For mercury, it may be estimated with:

$$\lambda_{pr} = \left(\frac{6.5 \times 10^{-17} n_e}{\phi_p^2} + \frac{10^3 n_n \phi_p}{2.83 \times 10^{23} - 1.5 n_n} \right)^{-1}, \quad (2.15)$$

where the first term corresponds to elastic collisions, while the second approximates inelastic collisions. Only electron-electron collisions are retained for elastic collisions, as they dominate over electron-atom and electron-ion elastic collisions [72]. In Equation 2.15, the second term is a fit to the collisional-radiative model of Peters and Wilbur [74], as the knowledge of the density of every gas state needs to be known. For other species, the inelastic mean free path can be estimated using its usual defi-

dition with the electron beam energy set equal to the plasma potential:

$$\lambda_{pr} = \left(\frac{6.5 \times 10^{-17} n_e}{\phi_p^2} + n_n \sigma_{\text{inel}}(\phi_p) \right)^{-1}. \quad (2.16)$$

The total inelastic collision cross section, σ_{inel} , includes excitation and direct ionization reactions, both from ground states, but step-wise ionization is ignored. The system is closed with the perfect gas law (Equation 2.3).

Additional details The final version of the model still relies on experimental data, as it does not include any prediction of the electron temperature. The heat loss is calculated by considering surface-to-ambient radiation and conduction through the cathode back to the cathode base. Several other noteworthy assumptions and simplifications exist in all versions of the model, including:

- Except in the calculation of the energy-exchange mean free path for mercury, excitation and stepwise ionization are ignored. This is a common assumption [42, 49] that appears to produce decent results despite being generally unjustified.
- As a result of the assumption that plasma and sheath potentials are equal, the energy of the primary electrons for use in calculating the energy-exchange mean free path is assumed equal to the plasma potential, which may differ from the energy the electrons would actually gain in the sheath.

Evaluation For a mercury cathode, the model shows relatively good agreement for the evolution of the emitter temperature as a function of discharge current, and plasma density as a function of internal pressure. However, the model predicts a non-linear trend for the plasma density as a function of discharge current, in contradiction with experimental data. The predicted plasma density evolves linearly as a function of the internal pressure and does not capture the saturation of the plasma density for

pressures above 3 Torr. The model also tends to under-predict the plasma potential for the mercury cathode, with the caveat that it is only compared to a single value for a different experiment. Calculations for the xenon cathode are shown later in comparisons with other models.

In summary, the various incarnations of Siegfried and Wilbur’s model can produce good agreement with experimental data, but cannot predict the electron temperature and require an additional model for the insert heat loss, in addition to relying upon a number of assumptions that may not hold for other cathode operating conditions.

2.3 Mandell and Katz [75–78]

Mandell and Katz offer a model of the orifice plasma only. It relies on the balance of ion production and losses, a neutral gas flow model, and a plasma power balance.

Neutral gas flow From mass conservation, the total mass flow rate is equal to the sum of the gas and ion mass flow rates:

$$\dot{m} = \dot{m}_g + \dot{m}_i. \quad (2.17)$$

In units of equivalent-Ampères, the mass flow rates have the following form:

$$\dot{m}_g = \pi r_o^2 n_n e \sqrt{\frac{e T_{nV}}{2\pi M}}, \text{ and} \quad (2.18)$$

$$\dot{m}_i = \pi r_o^2 J_i. \quad (2.19)$$

The ion current density is defined using the average velocity of a Maxwellian distribution:

$$J_i = n_e e \sqrt{\frac{e T_{iV}}{2\pi M}}. \quad (2.20)$$

Ion balance The ion production through direct electron-impact ionization is balanced by the losses to the boundaries of the system

$$\left(\frac{dN_i}{dt}\right)_{\text{iz}} = \left(\frac{dN_i}{dt}\right)_{\text{out}}, \quad (2.21)$$

where N_i is the total number of ions. The ionization rate is estimated using a Maxwellian-averaged cross section:

$$\left(\frac{dN_i}{dt}\right)_{\text{iz}} = (\pi r_o^2 L_o) n_e n_n \sigma_{iz}(T_{eV}) \sqrt{\frac{8eT_{eV}}{\pi m}}, \quad (2.22)$$

where L_o and σ_{iz} are the orifice length and ionization cross section, respectively. For xenon, the ionization cross section is calculated with a fit to Hayashi's experimental data [79]:

$$\sigma_{iz}(T_{eV}) = (3.97 + 0.643T_{eV} - 0.0368T_{eV}^2) \exp\left(\frac{-12.127}{T_{eV}}\right) \times 10^{-20}. \quad (2.23)$$

Ion losses occur through the boundaries of the orifice. Mandell and Katz assume that the ion losses are uniform at the orifice entrance, exit, and walls. Neglecting the density and potential drop due to the pre-sheath, and using the thermal flux for ion loss, the ion outflow is given by:

$$\left(\frac{dN_i}{dt}\right)_{\text{out}} = 2\pi r_o (r_o + L_o) \sqrt{\frac{eT_{eV}}{2\pi M}} n_e. \quad (2.24)$$

Plasma power balance Ohmic heating, \dot{q}_Ω , is balanced by ionization, radiation/excitation, and convection losses (\dot{q}_{iz} , \dot{q}_{ex} , \dot{q}_{conv}):

$$\begin{aligned} \dot{q}_\Omega &= \dot{q}_{iz} + \dot{q}_{ex} + \dot{q}_{\text{conv}} \\ \Leftrightarrow R_p I_d^2 &= \left(\frac{dN_i}{dt}\right)_{\text{iz}} \langle \epsilon_{iz} \rangle + \left(\frac{dN_i}{dt}\right)_{\text{ex}} \langle \epsilon_{ex} \rangle + I_d (T_{eV} - T_{eV}^{\text{ins}}), \end{aligned} \quad (2.25)$$

where $\left(\frac{dN_i}{dt}\right)_{\text{ex}}$ has the same expression as $\left(\frac{dN_i}{dt}\right)_{\text{iz}}$, with the excitation cross section substituted for the ionization cross section. R_p and ϵ_{ex} designate the plasma resistance and the excitation energy, respectively. For xenon, the excitation cross section can be fit to Hayashi's experimental data:

$$\sigma_{ex}(T_{eV}) = 1.93 \times 10^{-19} T_{eV}^{-1/2} \exp\left(\frac{-11.6}{T_{eV}}\right). \quad (2.26)$$

The average ionization and excitation energies are estimated as 12.2 eV and 10 eV, respectively. The authors have omitted the factor of 5/2 for the convection losses in Equation 2.25.

The plasma resistivity, η_p , contains contributions from both electron-ion and electron-neutral collisions, and is given by:

$$\eta_p = \frac{m}{n_e e^2} (\nu_{ei} + \nu_{en}), \quad (2.27)$$

where ν_{ei} and ν_{en} are the electron-ion and electron-neutral collision frequencies, respectively. The plasma resistance is obtained from the resistivity and the orifice geometry assuming axial current conduction:

$$R_p = \eta_p \frac{L_o}{\pi r_o^2}. \quad (2.28)$$

The electron-ion collision frequency is obtained using:

$$\nu_{ei} = C_{ei} n_e \ln \Lambda T_{eV}^{-3/2}, \quad (2.29)$$

where $C_{ei} = 2.9 \times 10^{-12}$. The Coulomb logarithm, $\ln \Lambda$, is expressed as:

$$\ln \Lambda = 30 - \frac{1}{2} \ln (n_e T_{eV}^{-3}). \quad (2.30)$$

The electron-neutral collision frequency may be defined with a hard-sphere model with a constant collision cross section, σ_{en} , equal to $5 \times 10^{-19} \text{ m}^2$ (see, *e.g.*, [75]). Alternatively, it may be calculated based on the momentum transfer cross section. The authors propose a fit to experimental cross section data [78]:

$$\sigma_{en} = 6.6 \times 10^{-19} \frac{T_{eV}/4 - 0.1}{1 + (T_{eV}/4)^{1.6}}, \quad (2.31)$$

but use the total electron-neutral collision cross section, which also includes inelastic collisions, instead of the momentum transfer cross section. Figure 2.3 features a comparison of the fit to the total, Maxwellian-averaged, experimental cross section, and to the Maxwellian-averaged momentum-transfer cross section, both from Hayashi's experimental data [79].

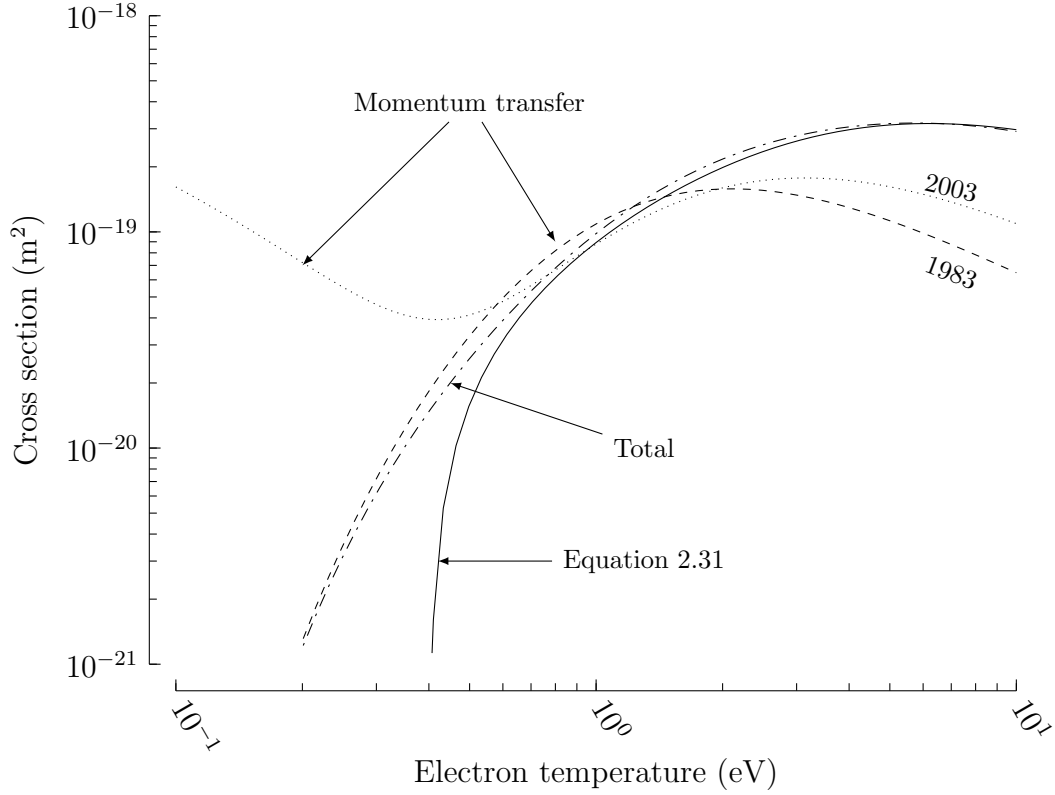


Figure 2.3: Comparison of Katz's fit (Equation 2.31) to Hayashi's recommended data for total electron-neutral cross section, and to the electron-neutral elastic collisions cross section from [79]. Momentum transfer cross sections are from [79] and [80].

Equation 2.31 approximates Hayashi’s recommended data for the total electron-neutral collision cross section for electron temperatures between 1 and 10 eV. The numerical fit also approximates the momentum-transfer cross section for electron temperatures between 0.8 and 2 eV. However, the fit overestimates momentum-transfer data by a factor of 2 for electron temperatures above 2 eV. More recent elastic electron-neutral cross section data also indicates that Equation 2.31 underestimates the electron-neutral cross section at low electron energies. We retrieved the elastic cross section data from the LXCAT website [81] (originally from [80]). We recommend using the more recent elastic cross section data from Hayashi to estimate the electron-neutral collision frequency.

Further assumptions are required to compute the plasma density, neutral gas density, and electron temperature. The authors assume that:

- The ion temperature is equal to the electron temperature. This is in sharp contrast with both earlier [52, 63, 69, 72] and later models [42], where the ion temperature is set equal to the neutral gas temperature, a consequence of frequent charge-exchange collisions in the plasma volume. The authors relax this assumption in [78], and set T_{iV} equal to 0.1 eV.
- The electron temperature from the insert T_{eV}^{ins} is known.
- The neutral gas temperature is known.

Evaluation Because of the lack of experimental data in the orifice region of hollow cathodes it is difficult to estimate the accuracy of orifice models. We compare this model to other orifice models in a later section.

2.4 Capacci *et al.* [82]

Capacci *et al.* propose a complete model of a hollow cathode, consisting of an independent insert model, a simple orifice model, and a plume model. The plume is considered to extend from the cathode tip to the keeper plate. The goal of the model is to predict the performance of new hollow cathode designs by calculating the current-voltage characteristic of a cathode along with the cathode temperature.

2.4.1 Insert

The insert model is solved for the plasma and gas densities, the wall temperature, the plasma potential, and the electron temperature. It follows the latest revision of Siegfried and Wilbur outlined in [52], with an additional equation required to close the system. Capacci *et al.* suggest the addition of a two-temperature Saha equation (Equation 2.2), or an ion conservation equation (Equation 2.21). Additional modifications are introduced in the determination of the pressure in the insert region, evaluation of the emission length, and estimation of the heat loss in the insert surface power balance.

Neutral flow Much like Siegfried and Wilbur, Capacci *et al.* use an empirical relationship for the pressure in the insert region,

$$P = \frac{\dot{m}}{4r_o^2} (c_1 + c_2 I_d + c_3 I_d^2), \quad (2.32)$$

where c_1 , c_2 , and c_3 are empirical constants. The expression differs from Equation 2.4 with the addition of a quadratic dependency on the current. We were not able to compare the two empirical relationships, as the empirical constants are not specified in [82].

Emission length The emission length is defined without a thorough analysis of the collision processes present in the insert region. It is posited that the emission length is directly proportional to the insert radius, and is given by:

$$L_{\text{emit}} = c_4 r_c, \quad (2.33)$$

where c_4 is another empirical constant. The authors indicate that c_4 should take into account the non-uniformity of the thermionic process — suggesting this term should be evaluated with a separate model or experimental data. Capacci *et al.* set c_4 to a value of 0.5 in their study. This approach does not take into account any of the processes that influence the emission length. For example, higher mass flow rates and discharge currents typically reduce the emission length.

Heat loss The authors estimate the heat loss \dot{q}_{th} from a separate thermal analysis of the insert region:

$$\dot{q}_{th} = 2r_c (c_5 + c_6 T_c) L_{\text{emit}}^{0.2}, \quad (2.34)$$

where c_5 and c_6 vary based on cathode geometry.

The remaining insert model equations are identical to those of Siegfried and Wilbur’s refined model.

2.4.2 Orifice

The orifice model serves as a bridge between the insert and keeper regions. It is also used to estimate the voltage drop across the orifice. No plasma processes (*e.g.*, ionization) are considered. Only electron-ion collisions are implemented in the finite plasma resistance, in effect considering the plasma to be fully ionized. While the approximation $\nu_{ei} \gg \nu_{en}$ may be true at low electron temperatures for sufficient ionization fractions (less than 1 eV and 1%) or for high ionization fractions (greater

than 10%), the electron-neutral collisions cannot be neglected for a typical cathode orifice operational point ($T_{eV} \approx 1 - 3 \text{ eV}$, $\alpha \approx 1 - 10\%$) as shown on Figure 2.4 for xenon.

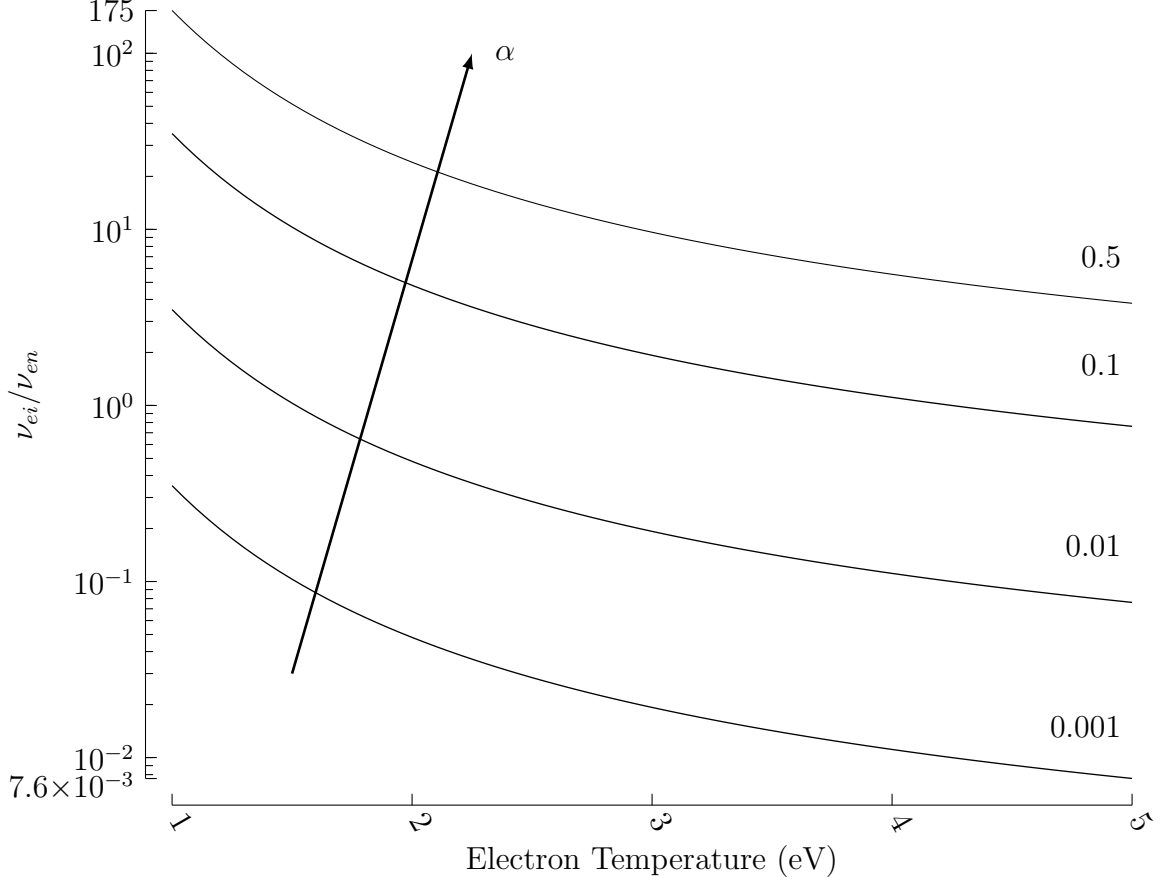


Figure 2.4: Ratio of electron-ion to electron-neutral collision frequencies, for increasing ionization fraction $\alpha = n_e/n_n$. The Coulomb logarithm is assumed to be equal to 7.1 — the average value for electron temperatures between 0.1 to 10 eV, and electron densities between 10^{18} and 10^{22} m^{-3} .

The temperature of the electrons in the orifice is a free parameter, and is assumed to be equal to 1 eV in the calculations of Capacci *et al.*. The electron density is obtained by considering that the current is entirely carried by the electrons, with the fluid velocity of the electrons assumed to be equal to their thermal velocity:

$$I_d = en_e^{\text{orifice}} \left(\frac{eT_{eV}}{2\pi m} \right)^{1/2} \pi r_o^2. \quad (2.35)$$

This assumption ignores the ions entrained outside of the orifice, and overestimates the fluid velocity of the electrons. For a given cathode, with only electrons carrying current, the fluid (or drift) velocity may be obtained as:

$$u_e = \frac{I_d}{n_e e \pi r_o^2}. \quad (2.36)$$

For the NSTAR neutralizer cathode ($r_o = 0.14$ mm), 2-D simulations [83] have shown a maximum orifice plasma density of $2.2 \times 10^{22} \text{ m}^{-3}$, and an electron temperature of 2.2 eV for a mass flow rate of 3.6 sccm and discharge current of 3.26 A. This amounts to an electron fluid velocity of $1.5 \cdot 10^4$ m/s, while the electron thermal velocity is equal to $6.2 \cdot 10^5$ m/s. Capacci *et al.* clearly overestimate the fluid velocity of the electrons, and, as a consequence, underestimate the plasma density in the orifice.

Neutral flow The orifice neutral density is estimated by assuming adiabatic and isentropic flow conditions:

$$n_n^{\text{orifice}} = n_n \left(\frac{\gamma + 1}{2} \right)^{-1/(\gamma-1)}. \quad (2.37)$$

Double sheath The authors assume the existence of a planar double sheath at the entrance of the orifice, though they ignore any ion contribution from the orifice in their insert model. A rigorous derivation of the double-sheath potential, ϕ_{ds} , in the space-charge limited case over a distance d is described in [84] by Langmuir. Langmuir's result can be rewritten as [85]:

$$\phi_{ds} = \left(\frac{9 (J_e + J_i) d^2}{4 \epsilon_0 C_0} \sqrt{\frac{m}{2e}} \left(1 + \sqrt{\frac{m}{M}} \right)^{-1} \right)^{2/3}. \quad (2.38)$$

Capacci *et al.* consider the distance between the two planar sources of charged species to be the Debye length, and introduce the approximations $m/M \ll 1$, $C_0 \approx 7.5/4$,

and $J_e + J_i \approx I_d/\pi r_o^2$. By conservation of current, the latter assumption amounts to ignoring ion and electron currents to the orifice wall. The double sheath potential can now be computed in terms of electron temperature, density, and total discharge current:

$$\phi_{ds} = \left(\frac{9I_d T_{eV}}{7.5\pi r_o^2 n_e e} \sqrt{\frac{m}{2e}} \right)^{2/3}. \quad (2.39)$$

Ohmic heating An additional voltage contribution across the orifice comes from the plasma resistance:

$$V_\Omega = I_d R_{or}. \quad (2.40)$$

The expression for the plasma conductivity of Capacci *et al.* artificially inflates the contribution of the orifice to the total voltage drop from anode to cathode. The scaling constant is off by multiple orders of magnitude.

The assumptions of adiabatic and isentropic flow are also contradicted by introducing Ohmic contributions in the orifice region — the power deposited by Joule heating will clearly heat the neutral gas before it expands in vacuum. The existence of a double-sheath at the entrance of the orifice region is also disputed.

2.4.3 Keeper

Spherical double sheath Capacci *et al.* consider the existence of an additional double-sheath in the plume region, which has been observed by Siegfried and Wilbur in the keeper region in the plume mode [69]. The authors assume that the double-sheath is located at the tip of the cathode. This assumption implies the existence of ions streaming towards the orifice region, which have been ignored in both the orifice and insert models. The authors use a spherical model to estimate the current through the double-sheath as described in [86], which assumes a space-charge-limited process.

Assuming that $I_d \approx I_e$, the ion current and double sheath voltage are:

$$I_i^{\text{tip}} = \alpha \left(r_o / r_{ds}^{\text{tip}} \right) I_d \sqrt{\frac{m}{M}}, \text{ and} \quad (2.41)$$

$$\phi_{ds}^{\text{tip}} = \left(\frac{I_i^{\text{tip}}}{4\pi\epsilon_0 j_0 \left(r_o / r_{ds}^{\text{tip}} \right)} \sqrt{\frac{M}{2e}} \right)^{2/3}, \quad (2.42)$$

respectively. Both $\alpha \left(r_o / r_{ds}^{\text{tip}} \right)$ and $j_0 \left(r_o / r_{ds}^{\text{tip}} \right)$ are tabulated as functions of $r_o / r_{ds}^{\text{tip}}$ in [86].

The authors propose to calculate the external double sheath radius at the cathode tip by assuming that the Bohm criterion applies to the ions. This is in direct contradiction with the assumption of [86], where the ions are considered to be cold at the sheath entrance. The proposed surface area over which the ions flow is incorrectly assumed to be a circle. To be consistent with the assumption of a hemispherical double sheath, it should be the area of a sphere, of radius r_{ds}^{tip} . The ion current is given by:

$$I_i^{\text{tip}} = e n_e^{\text{tip}} 2\pi \left(r_{ds}^{\text{tip}} \right)^2 \sqrt{\frac{e T_{eV}^{\text{tip}}}{M}}. \quad (2.43)$$

Neutral flow The neutral gas density, electron density, and temperature in this region are estimated assuming a spherical expansion and a simple two-temperature Saha equation model (see Equation 2.2), respectively. The resulting expression for the neutral density in the plume is:

$$n_n^{\text{tip}} = n_n^{\text{orifice}} \left(\frac{\psi r_o / \sin \psi}{(r_o / \sin \psi + L_{ck}/2) \psi} \right)^2 \quad (2.44)$$

This approach is similar to Siegfried and Wilbur's first attempt at hollow cathode modeling presented in [69], with the choked flow (Equation 2.1) being replaced by Equation 2.44.

2.4.4 Evaluation

The authors apply their solver to three cathodes — NCC A300, A5000, and A10000. The model seems to be insensitive to changes in the mass flow rate, and is unable to reproduce the discharge characteristic of the cathode. The overall shape of the characteristic seems qualitatively correct, but the model underpredicts the discharge voltage by 8–45%, even though the orifice plasma resistivity is overestimated.

The results for the A300 cathode suggest that the majority of the discharge voltage comes from the plasma potential drop. The electron temperature obtained in the insert region is also quite low — around 0.7 eV. Capacci *et al.* do note that the wall temperature is very sensitive to the effective work function. The introduction of a simple constant value for the calculation of the effective length also decreases the accuracy of the wall temperature prediction. The specific contributions of the orifice and keeper models are not discussed, and no comparison with previous models is offered. The approach is promising and reuses key elements of Siegfried and Wilbur’s successful low-current approach, but some assumptions are questionable, and the spherical double-sheath model is not implemented correctly. The plasma resistivity is also overestimated in the orifice region, and the model relies on experimental data (*e.g.*, empirical pressure relationship). These factors combined render the approach unreliable in its current form.

2.5 Domonkos [64, 73]

Domonkos models cathode performance by considering the orifice and the insert regions separately. The model for the orifice region is based on that of Mandell and Katz [64, 75] (with the addition of a current balance equation), and requires the orifice wall temperature, mass flow rate, and discharge current as input. The full model is comprised of current, ion, and energy conservation equations in each volume. The

insert and orifice region models are coupled through the electron/ion exchange at the orifice entrance and the insert electron temperature. The latter appears in the electron convection term for the orifice.

Each of the coupled models has its own set of free parameters needed to approximate the excitation and ionization processes taking place and to describe the electron emission and power deposition in the insert. Unfortunately, Domonkos's model description contains typographical or physical errors in many of the equations (repeated in all references for the model, and in later models citing his work [49,87]), making it difficult to implement without ambiguity. We have attempted to correct typographical errors in the equations that follow, pointing out inconsistencies in the physical treatment when they appear.

2.5.1 Orifice model

The orifice model uses ion conservation, current continuity, and conservation of energy in the plasma volume to solve for the plasma density and electron temperature. In order to evaluate the neutral density, the gas flow through the orifice is assumed to occur at the sonic velocity characteristic of the orifice wall temperature.

Ion conservation The ion balance in the orifice region equates the gains of ions through both electron-impact ionization and the influx from the insert region to the ion losses through the orifice inlet, outlet, and walls:

$$\left(\frac{dN_i}{dt}\right)_{\text{iz}} + \underbrace{\left(\frac{dN_i}{dt}\right)_{\text{in}}}_{\text{neglected}} - \left(\frac{dN_i}{dt}\right)_{\text{out}} = 0. \quad (2.45)$$

The second term in Equation 2.45 is neglected due to the assumption that a double sheath exists at the constriction of the orifice entrance, preventing the flow of ions from the insert region. The ionization rate coefficient is calculated by integrating the

product of the velocity-dependent ionization cross section and the electron velocity over a Maxwellian Electron Energy Distribution Function (EEDF). Domonkos considers only direct electron-impact ionization and neglects step-wise ionization in the orifice:

$$\left(\frac{dN_i}{dt}\right)_{\text{iz}} = (\pi r_o^2 L_o) \left(\frac{m}{2\pi e T_{eV}}\right)^{3/2} 4\pi n_e n_n \int_0^{+\infty} v^3 \sigma_{iz}(v) \exp\left(-\frac{mv^2}{2eT_{eV}}\right) dv. \quad (2.46)$$

The ions leaving the volume exit through either the sheath surrounding the orifice surfaces (assumed to include the orifice inlet) or through thermal efflux at the orifice outlet, towards the keeper and anode. The Bohm condition is used to calculate the flux of ions towards the wall and through the double sheath:

$$\left(\frac{dN_i}{dt}\right)_{\text{out}} = \underbrace{0.61 n_e \sqrt{\frac{eT_{eV}}{M}} (2\pi r_o L_o + \pi r_o^2)}_{\text{sheaths}} + \underbrace{\frac{1}{4} n_e \sqrt{\frac{8eT_{iV}}{\pi M}} \pi r_o^2}_{\text{thermal}}. \quad (2.47)$$

Using the Bohm criterion to calculate the ion flux to the orifice surfaces is justifiable, due to the assumption that the orifice walls are not emitting. The ion acceleration in the pre-sheath should therefore be unmodified [61]. However, applying the Bohm criterion to the double sheath is questionable. The electrons and ions are counter-streaming in the case of the double sheath, rather than traveling in the same direction, as is the case for the wall sheath. The ion current should instead be solved for in a manner consistent with the double sheath model used (*e.g.*, using the Langmuir ratio $\sqrt{m/M}$ to find the ratio of ion to electron currents [84]).

Mass conservation The neutral gas density in the orifice is calculated using mass conservation, assuming sonic flow:

$$n_n = \frac{\dot{m}}{M \pi r_o^2 \sqrt{\gamma R_g T_n}}. \quad (2.48)$$

The (static) neutral gas temperature is assumed to be equal to the orifice plate temperature, which must be obtained from experimental data. In using this equation for the *neutral* density, Domonkos implicitly assumes that 100% of the neutral gas input exits the cathode in the same state, disregarding ionization processes and the electron pressure contribution. Domonkos seems to imply at various points within the coupled models that n_n instead refers to the density of *heavy* particles — both ions and neutrals — which is more reasonable from a mass conservation standpoint. However, Domonkos then uses this value as the neutral density for the purposes of calculating the ionization rate, reducing it by the plasma (ion) density when calculating the excitation rate. The target species in both cases should have the same density, unless excited ions or multiple ionization events are considered.

In addition, it is unclear whether the appropriate velocity for the ions leaving the volume through the orifice outlet is that of the fluid (which would be required for continuity if the density calculated above is the *heavy* particle density) or the ion thermal velocity. The difference between these values is relatively small, however, given that the ratio of the neutral sound speed to the ion thermal velocity is $\sqrt{\frac{5\pi}{24}} \approx 0.81$ for a monatomic propellant. Domonkos uses the ion thermal velocity to calculate the ion flux through the orifice outlet, but the overall contribution from the exiting ion current is small regardless of the flow velocity used.

Current continuity Current continuity in the orifice region is used to find the electron current entering the orifice from the insert region plasma. A simplified picture of the orifice currents is shown in Figure 2.5. Ions leave the orifice at the thermal velocity through the outlet (I_i^{emit}), at the Bohm velocity through the double sheath (I_i^{ds}) at the orifice inlet, or recombine at the orifice walls (I_i^{walls}), having been accelerated to the Bohm velocity by the orifice wall sheath. No ion current flows from the insert region into the orifice due to the double sheath.

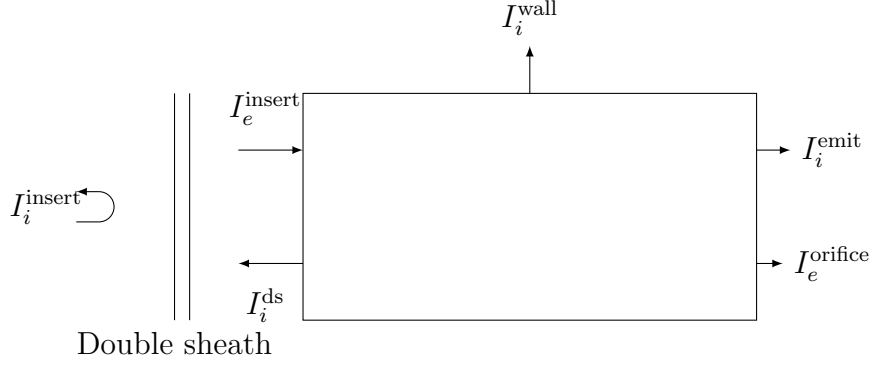


Figure 2.5: 0-D cell representation of the orifice currents.

The total discharge current can be calculated at the downstream end of the orifice as the difference between the electron and ion currents leaving the orifice:

$$I_d = I_e^{\text{orifice}} - I_i^{\text{emit}}, \quad (2.49)$$

which, along with the ion flux terms in the orifice, can be used to calculate the electron current from the insert. Domonkos gives the following expression for the insert electron current:

$$I_d = I_e^{\text{insert}} + I_i^{\text{wall}} + I_i^{\text{ds}} - I_i^{\text{emit}}. \quad (2.50)$$

Domonkos's proposed relationship (Equation 2.50) at the downstream end of the orifice features an unnecessary term, I_i^{emit} , and consequently violates conservation of charge. Because no electrons are lost in the orifice, the electron current at the outlet should be equal to the sum of the electron current at the inlet and the electron current generated by ionization in the orifice volume:

$$I_e^{\text{orifice}} = I_e^{\text{insert}} + I_e^{\text{created}}. \quad (2.51)$$

Because electrons and ions are created in pairs, and all ions created in the orifice must also leave the orifice (for steady-state conditions), we can express the electron current due to volume ionization in terms of the ion outfluxes:

$$I_e^{\text{created}} = I_i^{\text{wall}} + I_i^{\text{ds}} + I_i^{\text{emit}}. \quad (2.52)$$

Equations 2.49, 2.51, and 2.52 can be combined to yield the correct relationship:

$$I_d = I_e^{\text{insert}} + I_i^{\text{wall}} + I_i^{\text{ds}}. \quad (2.53)$$

The terms I_i^{wall} , I_i^{ds} , and I_i^{emit} are obtained as shown in Equation 2.47. They are expressed separately below:

$$I_i^{\text{wall}} = 0.61n_e e \sqrt{\frac{eT_{eV}}{M}} (2\pi r_o L_o), \quad (2.54)$$

$$I_i^{\text{ds}} = 0.61n_e e \sqrt{\frac{eT_{eV}}{M}} (\pi r_o^2), \text{ and} \quad (2.55)$$

$$I_i^{\text{emit}} = n_e e \frac{1}{4} \sqrt{\frac{8eT_{iV}}{\pi M}} \pi r_o^2, \quad (2.56)$$

respectively.

In Domonkos's approach, the two current continuity Equations 2.49 and 2.53 yield both the electron current coming from the insert, I_e^{insert} , and the electron current leaving the orifice, I_e^{orifice} . Because the discharge current increases along the length of the orifice, their determination is necessary for the calculation of the Ohmic losses in the orifice. We note that either I_e^{insert} or I_i^{ds} is a known quantity, as these quantities are tied together through the double sheath relationship [84],

$$I_e^{\text{insert}} = I_i^{\text{ds}} \sqrt{\frac{M}{m}}. \quad (2.57)$$

The double sheath ion current, I_i^{ds} , has been assumed to be known and set equal to the Bohm current in Domonkos's approach, which likely over-predicts the required electron current, I_e^{insert} , and, therefore, the double sheath voltage if calculated in a self-consistent manner.

Energy conservation Power deposition in the orifice volume is assumed to take place via Ohmic heating, balanced by losses due to ionization, excitation, and electron convection:

$$\dot{q}_\Omega = \dot{q}_{iz} + \dot{q}_{ex} + \dot{q}_{\text{conv}}. \quad (2.58)$$

Domonkos assumes that the electron current increases linearly along the orifice length due to the previously discussed ionization taking place in the orifice. The electron current is given by:

$$I_e(x) = I_e^{\text{insert}} + bx, \quad (2.59)$$

where $b = \frac{I_e^{\text{orifice}} - I_e^{\text{insert}}}{L_o}$. This assumption implies that the electron density increases along the length of the orifice if the drift velocity is constant (no electron losses are considered in the orifice). While this is inconsistent with the 0-D approach, it does make sense to attempt to account for the increase in electron current across the orifice, as volume ionization within the entire cathode has been estimated to account for up to 30% of the total discharge current [52]. The Ohmic heating term is calculated using the mean-square electron current over the length of the orifice:

$$\dot{q}_\Omega = R_{or} \langle I_e(x)^2 \rangle = \eta_p \frac{L_o}{\pi r_o^2} \left((I_e^{\text{insert}})^2 + I_e^{\text{insert}} b L_o + \frac{1}{3} b^2 L_o^2 \right), \quad (2.60)$$

where R_{or} is the resistance of the plasma in the orifice. Under the assumption of constant resistivity, the difference in Ohmic power deposition obtained using the mean-square current as opposed to using the outlet electron current is small. Even if

the electron current were to increase by 50% along the orifice length, the difference is only about 8%.

The orifice plasma resistivity is calculated using Equation 2.27, with the electron-ion collision frequency from the NRL plasma formulary [88],

$$\nu_{ei} = 3.9 \times 10^{-12} \frac{n_e}{T_{eV}^{3/2}} \ln \Lambda. \quad (2.61)$$

The electron-neutral collision frequency is evaluated using a calculated reaction rate based on experimental cross section data and a Maxwellian EEDF divided by the plasma density. The Coulomb logarithm differs slightly from Mandell and Katz's definition given earlier:

$$\ln \Lambda = 23 - \frac{1}{2} \ln \left(\frac{10^{-6} n_e}{T_{eV}} \right). \quad (2.62)$$

The ionization losses are calculated by multiplying the ionization rate in the volume by the ionization energy:

$$\dot{q}_{iz} = e\epsilon_{iz} \left(\frac{dN_i}{dt} \right)_{iz}. \quad (2.63)$$

The excitation losses are found in a similar manner:

$$\dot{q}_{ex} = e\epsilon_{ex} \left(\frac{dN_{ex}}{dt} \right). \quad (2.64)$$

The excitation rate, $\left(\frac{dN_{ex}}{dt} \right)$, is obtained by integrating over the total excitation cross section:

$$\left(\frac{dN_{ex}}{dt} \right) = (\pi r_o^2 L_o) \left(\frac{m}{2\pi e T_{eV}} \right)^{3/2} 4\pi n_e n_n \int_0^{+\infty} v^3 \sigma_{ex}(v) \exp \left(-\frac{mv^2}{2eT_{eV}} \right) dv. \quad (2.65)$$

In order to calculate the power loss due to excitation, the excited states are lumped with the average excitation energy, ϵ_{ex} , as a free parameter in the model. Its value

is set at 10 eV, though a more rigorous model would consider the different excitation levels in the gas of interest, and compute the average excitation energy. Doing so would require knowledge of the densities of each excited state in order to evaluate the contribution of stepwise excitations, which could be found using a collisional-radiative model similar to that implemented by Peters and Wilbur [74] for mercury.

Finally, convection losses are given by the difference between the power carried out of the orifice by the outgoing electron current and the power input from the insert electron current. Following Mandell and Katz, Domonkos neglects the factor of 5/2 that should be present in each of the convection terms:

$$\dot{q}_{\text{conv}} = (I_e T_{eV})_{\text{orifice}} - (I_e T_{eV})_{\text{insert}} . \quad (2.66)$$

2.5.2 Insert model

Similar balance equations are used to model the insert region: ion conservation, current continuity, and energy conservation are considered. The total pressure is calculated using a form of Poiseuille flow modified to take into account the pressure drop encountered at the flow constriction of the orifice.

Flow model

In order to calculate the pressure in the insert region, the pressure drop along the orifice length is estimated using Poiseuille flow and a correction due to the flow constriction:

$$P_{\text{insert}} = \sqrt{\dot{m} \frac{16\mu}{\pi r_o^4} R_g T_o L_o + P_{\text{sonic}}^2} + \frac{1}{2} \bar{\rho} \bar{u}^2 (1 + K_L) , \quad (2.67)$$

where P_{sonic} is the pressure calculated in the orifice model for the assumed choked-sonic flow through the orifice, $\bar{\rho}$ is the average density, \bar{u} is the average flow velocity, μ

is the dynamic viscosity, T_o is the orifice temperature, and K_L is the loss coefficient due to the constriction (≈ 0.5). The average density is evaluated as the arithmetic average of the pressures at each end of the orifice, using the upstream pressure without the correction as P_{insert} . The average velocity can be found using the linearized pressure gradient along the length of the orifice:

$$\bar{u} = \frac{r_o^2}{8\mu} \left(\frac{P_{\text{insert}} - P_{\text{sonic}}}{L_o} \right). \quad (2.68)$$

This flow model yields reasonable, but low, values of the pressure in Domonkos's experimental cathodes. This may be due to the pressure contribution from the discharge, or heating of the neutral gas by charge exchange [89]. A brief derivation of this model is given in Appendix C in [64].

Ion conservation

Domonkos considers ionization due to both primary (thermionically emitted) and plasma (thermalized/Maxwellian) electrons. Primary electrons contribute to the creation of excited states that are then ionized by the thermalized plasma electrons.

Primary electrons The primary electrons are emitted with a Maxwellian distribution at the emitter temperature, “shifted” to account for the acceleration of electrons by the sheath potential. The sheath potential is assumed to be equal to the plasma potential in this model. The distribution function used by Domonkos is given by:

$$f_b(v_e) = 4\pi \left(\frac{m}{2\pi e T_{eV}} \right)^{3/2} v_e^2 \exp \left(-\frac{m(v_e - v_b)^2}{2e T_{eV}} \right). \quad (2.69)$$

The proposed distribution is incorrect as the shift is applied directly to the *speed distribution*, as opposed to the *velocity in the direction of beam propagation*. The distribution given in Equation 2.69 is also not properly normalized. A more accurate

representation of the beam distribution is given by:

$$f_b(\mathbf{v}) = 2 \left(\frac{m}{2\pi e T_{eV}} \right)^{3/2} \exp \left\{ -\frac{m [v_x^2 + v_y^2 + (v_z - v_b)^2]}{2e T_{eV}} \right\} \theta(v_z - v_b). \quad (2.70)$$

In Equation 2.70, the velocity distribution is shifted only in the direction of the electron beam acceleration (taken to be the z -direction). The Heaviside θ ensures that no particle has a z -direction velocity less than that of the beam; such a particle would have a negative z -direction velocity at the emitter surface and would not leave the emitter. Equation 2.70 is more difficult to integrate than the original distribution. However, it can be transformed into a form more appropriate for integration by introducing the following definitions: $v_\perp = \sqrt{v_x^2 + v_y^2}$ and $|v| = \sqrt{v_\perp^2 + v_z^2}$. The integral becomes:

$$\iiint f_b(\mathbf{v}) d^3v = 4\pi \left(\frac{m}{2\pi e T_{eV}} \right)^{3/2} \int_{v_b}^{+\infty} \int_0^{+\infty} v_\perp \exp \left\{ -\frac{m [v_\perp^2 + (v_z - v_b)^2]}{2e T_{eV}} \right\} dv_\perp dv_z. \quad (2.71)$$

The corresponding reaction rate coefficient is therefore given by:

$$\langle \sigma v \rangle = 4\pi \left(\frac{m}{2\pi e T_{eV}} \right)^{3/2} \int_{v_b}^{+\infty} \int_0^{+\infty} |v| \sigma(|v|) v_\perp \exp \left\{ -\frac{m [v_\perp^2 + (v_z - v_b)^2]}{2e T_{eV}} \right\} dv_\perp dv_z. \quad (2.72)$$

Given the large disparity between the beam velocity induced by the emitter sheath and the thermal velocity characteristic of the emitter temperature, there seems to be little reason to introduce such a distribution unless the beam energy is close to the threshold energy for a process of interest. Typical sheath and plasma potentials for hollow cathodes are in the 3–12 V range, while emitter temperatures are 0.1–0.2 eV. Domonkos's choice of 8 V for the plasma potential (a free parameter in the model) is close to the first excitation energy of xenon, so the tail of the beam distribution

may contribute to excitation. However, the arbitrary nature of this plasma potential value makes it difficult to assess whether the finite beam temperature is important for a real cathode. The relatively low energy required (3.4 eV [90]) for ionization from xenon metastable states would make these events far more likely to contribute to stepwise ionization if a sufficient density of metastables exists within the mean free path of the beam electrons. Because the energy the electrons typically gain from the sheath potential is less than the threshold for direct ionization (at least in the case of xenon), Domonkos's approach of comparing the ionization and excitation mean free paths is likely unnecessary.

The density of primary electrons, n_e^{primary} , is the density of emitted electrons as they enter the bulk plasma, with a velocity, v_d , determined by the plasma potential. Domonkos uses the thermionic current density to calculate the density of primary electrons,

$$n_e^{\text{primary}} = \frac{J_{em}}{ev_d}, \quad (2.73)$$

where the velocity of electrons is obtained through energy conservation of ballistic electrons,

$$v_d = \left(\frac{2e\phi_p}{m} \right)^{1/2}, \quad (2.74)$$

and J_{em} is calculated in the same manner as for Siegfried and Wilbur's model, but the Richardson constant is set equal to 60 A/(cm² K²). The effective work function is evaluated using the expression for the electric field at the cathode surface from Prewett and Allen [61]. The emission length, L_{emit} , was introduced in Domonkos's equation for the ionization rate, and is set equal to the insert radius, r_c .

Multi-step ionization Domonkos modifies Equation 2.46 to account for multi-step ionization, which is assumed to occur in the region outlined in Figure 2.6. The mean

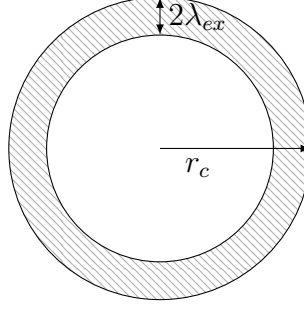


Figure 2.6: Region of multi-step ionization.

free path for excitation λ_{ex} is, by definition:

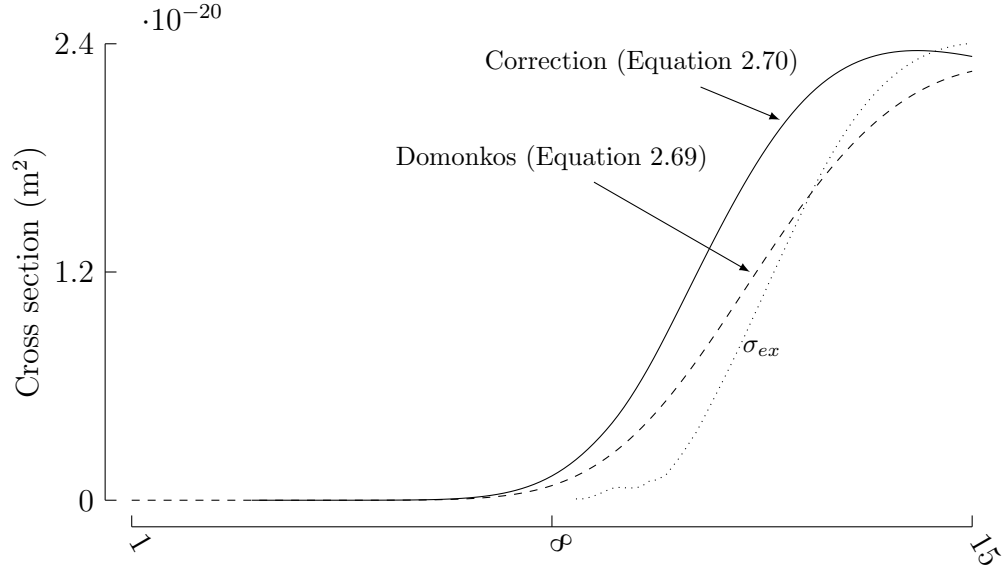
$$\lambda_{ex} = \frac{1}{n_n \sigma_{ex}}, \quad (2.75)$$

where σ_{ex} is the excitation cross section. In order to account for the effect of the finite-temperature beam of primary electrons, Domonkos uses the following expression:

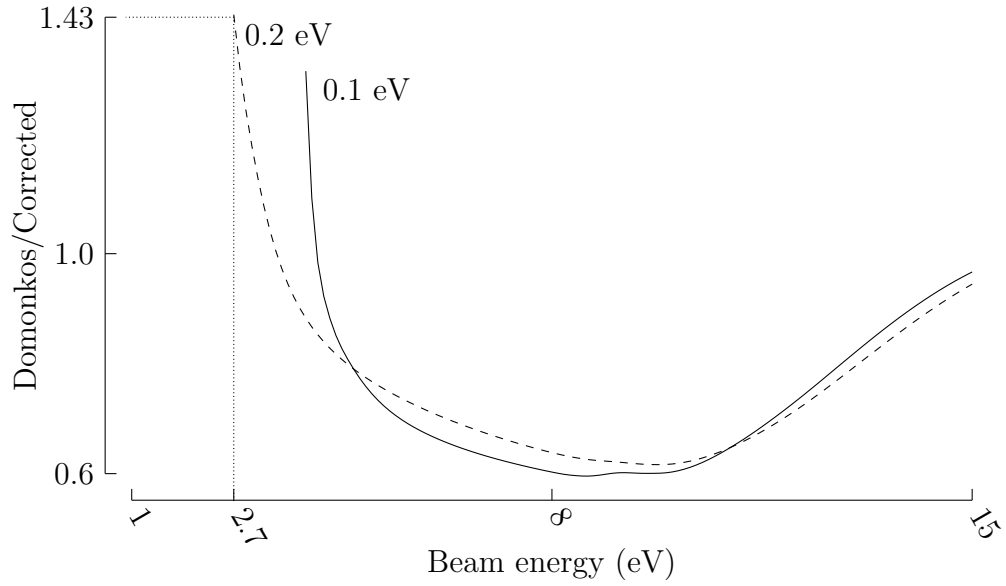
$$\lambda_{ex} = \frac{\langle v \rangle_{beam}}{n_n \langle \sigma_{ex} v \rangle_{beam}}. \quad (2.76)$$

This expression removes the effect of the normalization problems mentioned earlier. Even without the normalization issues, however, Domonkos's use of the distribution given by Equation 2.69 introduces significant error (approximately 40% at $\phi_p = 8$ V) in the effective cross section for excitation over most of the energy range of interest, as shown in Figure 2.7. The results shown were found by performing the integral in Equation 2.72 over all excitation cross sections in the LXCAT Hayashi database [81].

An arbitrary, fixed percentage of the primary excitation events, p_{ex} , is assumed to create ions through multi-step ionization. This percentage is a free parameter and attempts to account for the ions generated by stepwise ionization of beam-excited neutrals.



(a)



(b)

Figure 2.7: Comparison of the distribution-averaged collision cross sections. (a) Beam-distribution-averaged excitation cross section computed with Equation 2.69 (dashed line), and Equation 2.70 (solid line). The excitation cross section for a monoenergetic beam is shown with a dotted line. (b) Ratio of the distribution-averaged excitation cross sections for two electron beam temperatures.

Ionization rate The total ionization rate in the insert volume is given by:

$$\begin{aligned} \left(\frac{dN_i}{dt} \right)_{\text{iz}} = & \pi r_c^2 L_{\text{emit}} n_e n_n \langle \sigma_{iz} v_e \rangle_{\text{plasma}} \\ & + p_{ex} \pi L_{\text{emit}} \left(r_c^2 - (r_c - 2\lambda_{ex})^2 \right) n_e^{\text{primary}} n_n \langle \sigma_{ex} v_e \rangle_{\text{primary}}. \end{aligned} \quad (2.77)$$

The subscripts “plasma” and “primary” in Equation 2.77 for the rate coefficients indicate that those quantities are to be determined using the distribution-averaging appropriate for either the Maxwellian plasma electrons or the beam electrons, respectively.

Current conservation

The total discharge current is represented as the sum of the emitted electron current, the ion and electron fluxes collected on the cathode and orifice surfaces — including ions thermally diffusing upstream — and the ion flux towards the walls of the orifice. Domonkos gives the following relationship for the current continuity:

$$I_d = I_{em} + I_i^{\text{coll}} - I_e^{\text{coll}} - I_i^{\text{emit}}. \quad (2.78)$$

This expression, as for the case of the expression in the orifice, does not conserve charge. A correct approach considers either the insert control volume with an influx of ions from the double sheath, and outflux of electrons to the double sheath (see Figure 2.8), or the combination of both orifice and insert control volumes. Using the former approach, the current balance yields:

$$\begin{aligned} I_{em} - I_e^{\text{coll}} + I_i^{\text{coll}} + I_i^{\text{th}} &= I_e^{\text{insert}} + I_i^{\text{ds}} \\ \Leftrightarrow I_{em} - I_e^{\text{coll}} + I_i^{\text{coll}} + I_i^{\text{th}} &= I_d - I_i^{\text{wall}} \\ \Leftrightarrow I_d &= I_{em} - I_e^{\text{coll}} + I_i^{\text{coll}} + I_i^{\text{th}} + I_i^{\text{wall}}. \end{aligned} \quad (2.79)$$

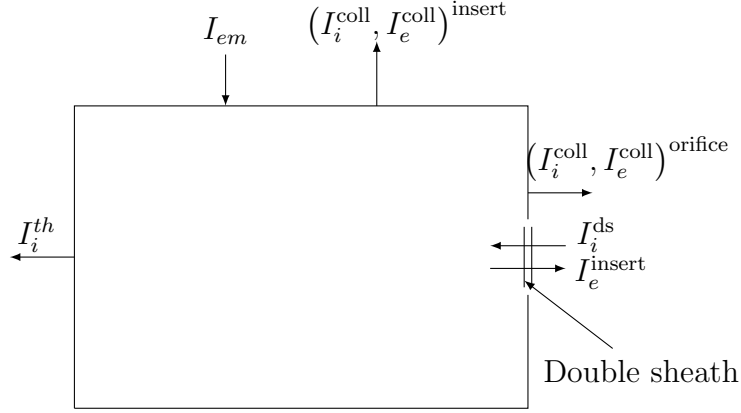


Figure 2.8: 0-D cell representation of the insert currents.

The ion current to the orifice wall, I_i^{wall} , is used to distinguish the ion current collected on the internal orifice walls from that collected on the insert and orifice plate surfaces, I_i^{coll} .

The thermionic current density is given by Equation 2.8. As mentioned earlier, Domonkos considers the plasma potential to be a free parameter, restricted to the range of 8 to 12 V, based on experimental data. The current density from the ions collected by the cathode and orifice surfaces is obtained using Equation 2.6 modified for the existence of a pre-sheath (assuming that the potential drop that is required to accelerate the ions to the Bohm velocity is unmodified by the electron emission in the insert):

$$I_i^{coll} = \underbrace{0.61en_e \sqrt{\frac{eT_{eV}}{M}} 2\pi r_c L_{emit}}_{\text{to inner cathode surface}} + \underbrace{0.61en_e \sqrt{\frac{eT_{eV}}{M}} \pi(r_c^2 - r_o^2)}_{\text{to orifice plate}}. \quad (2.80)$$

The current due to the backstreaming electrons is expressed in terms of the random electron current density as:

$$I_e^{coll} = J_r (2\pi r_c L_{emit} + \pi(r_c^2 - r_o^2)). \quad (2.81)$$

The random electron current density, J_r , is given by:

$$J_r = \frac{1}{4} \left(\frac{8eT_e V}{\pi m} \right)^{1/2} n_e e \exp \left(-\frac{e\phi_p}{k_B T_e} \right), \quad (2.82)$$

where the electron temperature, T_e , is here in Kelvin. The thermal ion current diffusing upstream, I_i^{th} , is accounted for using the expression for I_i^{emit} , with the orifice radius replaced by the cathode inner radius.

Conservation of energy

The insert plasma gains energy through Ohmic heating (\dot{q}_Ω), ion flux from the orifice (\dot{q}_{ori}), and sheath-accelerated thermionic electrons (\dot{q}_{em}). Losses are comprised by ionization (\dot{q}_{iz}), excitation of neutral particles (\dot{q}_{ex}), ion and electron convection (\dot{q}_{conv}), and electron backstreaming (\dot{q}_{coll}):

$$\dot{q}_\Omega + \dot{q}_{\text{ori}} + \dot{q}_{em} = \dot{q}_{iz} + \dot{q}_{ex} + \dot{q}_{\text{conv}} + \dot{q}_{\text{coll}}. \quad (2.83)$$

The boundaries of the control volume should be drawn carefully. We could include or exclude the pre-sheath in this approach. Domonkos chooses to ignore the pre-sheath potential, though includes its effect on the ion current due to the density decay.

Ohmic heating Domonkos considers that the electron current is the only driver for Ohmic heating. Ohmic heating is due to the net current, I_d , where we consider only electron-heavy collisions for resistivity. The resistivity is calculated in a similar fashion as in the previous section, though Domonkos here assumes that the current is conducted radially. To account for radial conduction, Domonkos introduces an average cross-sectional area, but misses a factor of π (shown in the corrected expression):

$$A_{\text{eff}} = \frac{\int_0^{r_c} (2\pi r L_{\text{emit}}) r dr}{\int_0^{r_c} r dr} = \frac{4}{3} \pi r_c L_{\text{emit}}. \quad (2.84)$$

The corrected expression for the Ohmic heating is given by:

$$\dot{q}_\Omega = I_d^2 \eta_p \frac{r_c}{(4/3) \pi r_c L_{\text{emit}}}. \quad (2.85)$$

Orifice ions Orifice ions carry both the average energy of (assumed) Maxwellian particles crossing a boundary surface and the potential energy obtained through the double sheath that is assumed to exist at the entrance of the orifice,

$$\dot{q}_{\text{ori}} = I_i^{ds} (\phi_{ds} + 2T_{iV}), \quad (2.86)$$

where the expression is in terms of the orifice quantities. The double sheath potential is estimated with the same expression as Capacci *et al.* (Equation 2.39). Domonkos uses the total discharge current in Equation 2.39. However, this is inconsistent with the definition of the net current through the double sheath, which is equal to $I_i^{ds} + I_e^{insert} \neq I_d$ (see Equation 2.53).

Thermionic electrons The thermionic electrons entering the volume carry the cathode fall voltage and a finite thermal energy due to the wall temperature. The characteristic energy of electrons leaving the wall is twice the wall temperature [91]. The cathode fall voltage is assumed to be equal to the plasma potential in Domonkos's approach. The thermal energy term should appear here with a factor of 2, as opposed to 3/2. However, the emitter temperature is typically negligible compared to the sheath potential and the term can simply be left out. The corrected expression for the emitted electron power is:

$$\dot{q}_{em} = I_{em} \left(\phi_p + 2 \frac{k_B T_c}{e} \right). \quad (2.87)$$

Ionization and excitation losses Generated ions contribute to ionization losses. This energy is lost from the plasma volume through the diffusion of ions upstream of the insert, and through the collection of ions at the insert and orifice walls:

$$\dot{q}_{iz} = (I_i^{th} + I_i^{coll})\epsilon_{iz}. \quad (2.88)$$

Both plasma and beam (also identified as “primary”) electrons participate in energy loss through excitation. Domonkos provides a relationship that is dimensionally inconsistent; we have corrected the equation below:

$$\dot{q}_{ex} = e\epsilon_{ex}(n_e n_n \langle \sigma_{ex} v_e \rangle_{\text{plasma}} + n_e^{\text{primary}} n_n \langle \sigma_{ex} v_e \rangle_{\text{primary}}) \pi L_{\text{emit}} r_c^2. \quad (2.89)$$

Particle and convection losses Particles are collected at the insert and orifice walls, and the power they carry is given by:

$$\dot{q}_{\text{coll}} = (I_i^{th} + I_i^{\text{coll}}) 2T_{iV} + I_e^{\text{coll}}(\phi_p + 2T_{eV}). \quad (2.90)$$

Though it is important to note that while the pre-sheath potential has been neglected, the energy of the ions leaving the plasma volume at the pre-sheath edge ($T_{eV}/2$, without any modification for electron emission) is likely of the same order of magnitude or greater than $2T_{iV}$. Finally, electrons leave the volume through the double sheath. Domonkos implicitly assumes that these electrons are the only charge carriers flowing through the sheath, and proposes that the convected current is equal to I_e^{insert} yielding the following expression for the convection power:

$$\dot{q}_{\text{conv}} = \frac{5}{2} I_e^{\text{insert}} T_{eV}. \quad (2.91)$$

2.5.3 Additional comments

The model requires the total discharge current, flow rate, cathode material, and cathode geometry as inputs. The four free parameters considered are the fixed percentage of the primary excitation events that create ions through multi-step ionization (p_{ex}), the excitation energy in both the orifice and insert regions, and the plasma potential in the insert region. Domonkos also mentions the work function as a free parameter in his model, though the values for most cathode materials are known and the parameter was constrained to a small range in his calculations.

Domonkos compares his results for the AR6, AR3, and SSPC cathodes, and performs a sensitivity analysis of his model. Both ϵ_{ex} and p_{ex} affect the number density and power consumption significantly, with more than 30% variation of plasma density over a 5%-range for p_{ex} . Domonkos chooses the values of $\epsilon_{ex} = 5$ eV and $p_{ex} = 5\%$ in the insert region in order to account for the reduction in effective excitation energy due to stepwise processes. Other authors choose a lumped value of 10 eV for the excitation energy of xenon as Domonkos uses in the orifice region.

Domonkos's model made an admirable attempt to be more comprehensive than other models, but in most cases the inclusion of complicating effects incurred the costs of increased sensitivity to free parameters and errors in implementation. Without a more complete characterization of the stepwise processes in xenon-fed orificed hollow cathodes, it is difficult to evaluate the efficacy of Domonkos's attempts to simplify their contribution. We were not able to re-implement or confirm the results of the original model as described in [64] and [73]. Domonkos gives intermediate calculations only for two different sets of operating conditions in the insert and orifice [64] and we could not find any combination of the original equations or our own corrections that would reproduce these values. It appears that the original implementation details have been lost.

2.6 Goebel and Katz [42, 92]

Goebel and Katz describe a 0-D model in their 2008 textbook [42] based on power balances for the insert plasma and the thermionic emitter, a current balance, and an ambipolar diffusion model (effectively an ion balance) for the electron temperature. A simplified power balance and the same ambipolar diffusion model are solved in the orifice in order to find the plasma density and electron temperature, respectively. Emission is assumed to be described by the Richardson-Dushman equation, with no modification due to the sheath electric field.

A Poiseuille flow model is used for the neutral gas pressure in both the orifice and insert, though the average pressure in each region is used for the 0-D model. The Poiseuille flow model is identical to that of Domonkos (Equation 2.67), excluding the correction due to the orifice constriction and the use of the sonic condition for the orifice outlet pressure, which must be specified separately. The pressure found is assumed to be that of the *neutral* species.

By assuming charge-exchange-limited ambipolar diffusion, constant temperature for the heavy species, and neglecting effects of the plasma on the flow, the axially-uniform electron temperature can be found solely as a function of the neutral gas pressure. The neutral temperature is usually taken to be 2–4 times the absolute wall temperature due to charge-exchange collisions between the ions and neutrals [42] (p.465), [89].

2.6.1 Insert model

Goebel and Katz’s insert model does not rely on inputs from the orifice model. Once the neutral pressure has been calculated from the Poiseuille flow model, the electron temperature can be found as a function of only pressure and cathode radius.

Ambipolar diffusion Unique to the approach of Goebel and Katz, modeling ion conservation using an ambipolar diffusion approach yields both an estimate of the spatial variation in plasma density within the insert region and the electron temperature. Using the electron and ion momentum equations, neglecting the electron current and neutral drift terms, and assuming that ion diffusion is limited by resonant charge exchange (due to the relatively large cross section $\propto 10^{-18} \text{ m}^2$ for the inert gases [93, 94]) the ambipolar diffusion coefficient, D_a , can be found:

$$D = D_a = \frac{e}{M} \frac{T_{iV} + T_{eV}}{n_n \sigma_{\text{CEX}} v_{\text{scat}}}, \quad (2.92)$$

where σ_{CEX} is the charge-exchange cross section. The neutral scattering velocity, v_{scat} , in Equation 2.92 is assumed to be the (1-D) ion thermal velocity. Goebel and Katz assume that the ionization rate coefficient, neutral density, and ambipolar diffusion coefficient are constant within the region being examined. By equating the diffusion losses with the ionization rate within the volume, the following equation for the plasma density is obtained:

$$\nabla^2 n_e + \left(\frac{n_n \langle \sigma_{iz} v_e \rangle}{D_a} \right) n_e = 0. \quad (2.93)$$

The solution to this equation is found using separation of variables. Assuming that there is no variation in the axial direction, the resulting plasma density is:

$$n_e(r) = n_e(0) J_0 \left(\sqrt{\frac{n_n \langle \sigma_{iz} v_e \rangle}{D_a}} r \right), \quad (2.94)$$

where J_0 is the zero-th order Bessel function of the first kind. In order to solve for the electron temperature, Goebel and Katz assume that the electron density is zero at the wall of the cathode. This yields the final relationship between the ambipolar diffusion

coefficient and the ionization rate coefficient in terms of the cathode geometry,

$$\left(\frac{r_c}{\lambda_{01}}\right)^2 n_n \sigma_{iz}(T_{eV}) \sqrt{\frac{8eT_{eV}}{\pi m}} = D_a, \quad (2.95)$$

where the ionization rate coefficient in Equation 2.95 has been replaced by the fit used by Mandell and Katz (Equation 2.23), and λ_{01} is the first root of the zeroth-order Bessel function of the first kind. This yields the radial variation in plasma density as well as the electron temperature. The average density, \bar{n}_e , needed for later calculations, is given by:

$$\bar{n}_e = \left[\frac{2J_1(\lambda_{01})}{\lambda_{01}} \right] n_e(0), \quad (2.96)$$

where J_1 is the first-order Bessel function of the first kind. In an earlier paper, Katz *et al.* [92] state that the electron temperature calculated using this approach is the maximum possible value, and that the correction in T_{eV} for finite values of the separation constant is, “less than one per cent.”

Current balance The current balance for the insert region equates the total discharge current to the sum of the emitted thermionic current and the generated ion current reduced by the random thermal electron current that returns to the emitter:

$$I_d = I_{em} + I_i - I_r \exp(-\phi_s/T_{eV}), \quad (2.97)$$

$$I_r = \frac{1}{4} \left(\frac{8eT_{eV}}{\pi m} \right)^{1/2} n_e^s e A_{\text{emit}}, \text{ and} \quad (2.98)$$

$$I_i = n_n \bar{n}_e e \langle \sigma_{iz} v_e \rangle V_{\text{emit}}. \quad (2.99)$$

Goebel and Katz also mention that the Bohm current is used to evaluate the ion current for the purposes of calculating the ion power deposition. This implies that the expression $I_i = en_e^s v_B A_{\text{emit}}$ should also be valid by virtue of ion conservation, where n_e^s is the electron density at the sheath edge and v_B is the Bohm velocity.

The introduction of n_e^s is a unique feature of this model, as it is the only model that attempts to calculate the sheath voltage independent of the plasma potential. The random electron current density should also be evaluated with the sheath edge density. The ion generation, by contrast, should be evaluated using the average electron density, \bar{n}_e .

Power balances The power balance for the insert plasma equates the power deposition from sheath-accelerated thermionic electrons and Ohmic heating to the losses due to ionization, electron convection, and random electron flux to the emitter:

$$I_{em}\phi_s + R_p I_e^2 = I_i \epsilon_{iz} + \frac{5}{2} T_{eV} I_e + (2T_{eV} + \phi_s) I_r \exp(-\phi_s/T_{eV}). \quad (2.100)$$

The energy characteristic of the random electrons, $(2T_{eV} + \phi_s)$, is necessary because the particles must have sufficient energy to overcome the sheath potential. The electrons would otherwise not leave the volume into the electron-repelling emitter sheath. A derivation of this term is also given in Appendix C in [42].

The power balance for the emitter sets the losses due to conduction, convection, and radiation ($H(T)$) and thermionic cooling equal to the power input due to ion and random electron bombardment. Ions must extract an electron at the cost of the work function from the material in order to recombine at the emitter surface and incident electrons are assumed to fall from the vacuum level to the Fermi level within the material, depositing ϕ_w at the wall, as shown below:

$$H(T) + I_{em}\phi_w = I_i \left(\epsilon_{iz} + \phi_s + \frac{T_{eV}}{2} - \phi_w \right) + (2T_{eV} + \phi_w) I_r \exp(-\phi_s/T_{eV}). \quad (2.101)$$

These equations cannot be readily solved as a system for the sheath voltage, plasma density, and wall temperature. They are instead combined to create simpler expressions that do not directly involve the wall temperature. This is achieved by as-

suming that the ion energy due to the pre-sheath can be neglected as compared to the ionization and sheath potentials. This assumption does not typically introduce significant error given the 1–2 eV electron temperature characteristic of the insert plasma. Algebraic manipulation of the remaining equations yields a system of equations that can be solved for the average neutral density and sheath voltage:

$$\phi_s = \frac{H(T)}{I_e} + \frac{5}{2}T_{eV} + \phi_w - R_p I_e, \quad (2.102)$$

$$\bar{n}_e = \frac{R_p I_e^2 - \left(\frac{5}{2}T_{eV} - \phi_s\right) I_e}{f_s T_{eV} \left(\frac{eT_{eV}}{2\pi m}\right)^{1/2} eA \exp(-\phi_s/T_{eV}) + n_n e \langle \sigma_{iz} v_e \rangle V (\epsilon_{iz} + \phi_s)}, \quad (2.103)$$

where f_s is the “edge-to-average” ratio that describes the ratio of the average plasma density to that at the sheath edge. The edge-to-average plasma density ratio is approximated by Goebel and Katz under the assumption that the plasma density in the region outside the sheath and pre-sheath can be described by a Boltzmann distribution:

$$f_s = \frac{n_e^s}{\bar{n}_e} \approx \exp(-(\phi_{\text{axis}} - \phi_s)/T_{eV}). \quad (2.104)$$

Because this value represents the ratio of the plasma density at the sheath edge to the average density over the volume, an additional factor should be used to convert the average density to that at the centerline (following Equation 2.96) when calculating f_s . The plasma resistivity is calculated using Equation 2.27. The electron-ion collision frequency is evaluated with Equation 2.29. The electron-neutral collision cross section is evaluated for xenon with a fit to Hayashi’s [79] recommended *total* electron-neutral cross section data (Equation 2.31). As mentioned earlier for Mandell and Katz’s use of this model, the elastic momentum-transfer collision cross section should be used instead. Goebel and Katz use Equation 2.62 as their definition of the Coulomb logarithm. In following the derivation of this model, we also found that the first term in the denominator of Equation 2.103 should be multiplied by a factor of 2.

These two equations must be solved iteratively or simultaneously for the average plasma density and the sheath potential, as the plasma resistance appears in the sheath potential equation and depends on the average plasma density. These values are both desirable, but because of the simplification, the model cannot predict the wall temperature directly. The dependence on the “edge-to-average” ratio requires the additional assumption that the plasma density follows a Boltzmann distribution (*i.e.*, the density decays exponentially with potential) as well as knowledge of the plasma potential from either experimental data or 2-D codes in order to close the system. In addition, the equations for the average density and sheath voltage depend on the emitter heat loss, which must be found from either a separate thermal model or experiment, and the plasma resistivity, which is itself a function of the average plasma density and the emission length, L_{emit} .

The authors present a model for the emission or attachment length based on the “e-folding distance” for the plasma density decay. Relaxing the assumption of zero axial variation in density, the decay is assumed to obey the earlier ambipolar diffusion model. To ensure uniform pressure and the validity of the ambipolar diffusion model, the cathode orifice must be relatively small compared to the insert diameter. An independent calculation of the ion current generated in the insert plasma is required. Goebel and Katz obtain the ion current through the use of a 2-D code, which means that this approach cannot be used in a self-contained fashion.

2.6.2 Orifice model

Goebel and Katz implement an additional power balance in a separate orifice model using the same flow and ambipolar diffusion models, and assume that the discharge current does not change within the orifice. It does not depend on experimental parameters as the attachment length is replaced with the orifice length, and emission from the orifice is ignored. This removes the need for the sheath potential in order

to calculate the plasma density and electron temperature. The orifice power balance equates the Ohmic heating in the orifice to the electron convection losses and to the ionization power loss in the orifice volume:

$$R_{or}I_d^2 = \frac{5}{2} (T_{eV} - T_{eV}^{ins}) I_d + en_n \langle \sigma_{iz} v_e \rangle \epsilon_{iz} (\pi r_o^2 L_o). \quad (2.105)$$

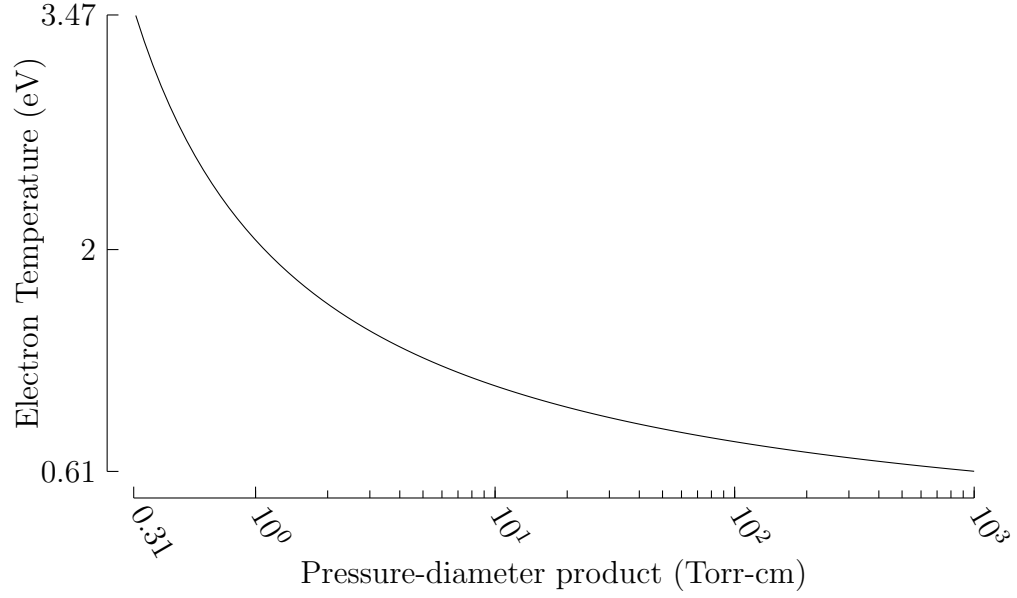
This equation can be solved easily for the orifice average plasma density after the insert model has been run:

$$\bar{n}_e = \frac{R_{or}I_d^2 - (5/2)I_d(T_{eV} - T_{eV}^{ins})}{en_n \langle \sigma_{iz} v_e \rangle \epsilon_{iz} \pi r_o^2 L_o}. \quad (2.106)$$

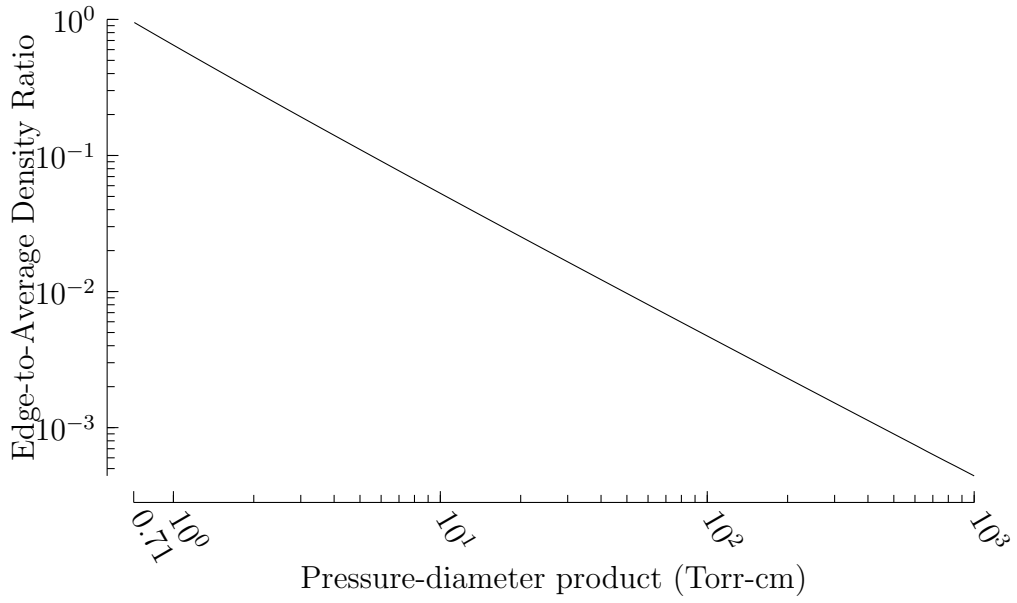
2.6.3 Evaluation

The model described above produces results that agree well with experiment when certain values of the input parameters are used. The model requires experimental/computational input in the form of the plasma potential and the attachment length (or the ion current, which can then be used to calculate L_{emit}). We note that for some operating conditions the global power balance method used to calculate the sheath voltage yields negative values of ϕ_s , or values of ϕ_s greater than the input ϕ_p .

Goebel's model has two independent equations for the ion current. This can be used to make a secondary calculation of the edge-to-axis density ratio and the insert electron temperature. Equating the volumetric ion generation to the Bohm ion current, we can solve for the electron temperature and f_s as functions of only the pressure-diameter product in the insert, as shown in Figure 2.9. Using this approach (not used by the original authors), we can remove the need for the plasma potential, as it is only used to calculate f_s . It is important to note that the ambipolar diffusion model as formulated breaks down at low pressure-diameter products or at high electron temperatures (typical for orifice plasma conditions), either because of the lack



(a)



(b)

Figure 2.9: (a) Electron temperature and (b) edge-to-axis density ratio as a function of pressure-diameter product.

of electron-ion collisions or due to the boundary conditions of the diffusion model. For orifice conditions, f_n approaches values of unity (or greater) and therefore the assumption of zero plasma density at the sheath edge cannot be justified.

2.7 Mizrahi *et al.* [95, 96]

The model of Mizrahi *et al.* focuses on the hollow cathode orifice. It is loosely based on Katz's model, and introduces the following modifications:

- There is a plasma flow in the orifice.
- The neutral gas temperature is equal to the ion temperature. Both heavy species temperatures are assumed to be much less than the electron temperature.
- Viscous effects on the neutral gas flow are introduced through a Poiseuille flow model.
- Ions may leave the cathode by being entrained by the neutral flow.

This approach relies on the continuity and momentum equations for charged particle flow, a plasma energy balance in the volume, and a neutral gas flow model. The superscripts $i \pm 1/2$ in this section refer to the physical quantities evaluated at the right- and left-hand sides of the volume, respectively.

Neutral flow A Poiseuille flow approach is used to evaluate the neutral gas density in the orifice. The Poiseuille equation is manipulated so as to introduce the arithmetic average density $\bar{n}_g = 1/2 \left(n_n^{i+1/2} + n_n^{i-1/2} \right)$:

$$\bar{u}_g = \frac{\Delta P r_o^2}{8\mu L_o} \Leftrightarrow \bar{u}_g = \frac{1 - \delta}{1 + \delta} \frac{k_B T_n \bar{n}_g r_o^2}{4\mu L_o}, \quad (2.107)$$

where

$$\Delta P = k_B T_n \left(n_n^{i-1/2} - n_n^{i+1/2} \right), \text{ and} \quad (2.108)$$

$$\delta = n_n^{i+1/2} / n_n^{i-1/2}. \quad (2.109)$$

This form of the Poiseuille equation removes the necessary knowledge of the upstream and downstream pressure, at the cost of the introduction of a free parameter, δ . The free parameter δ may be estimated if the neutral gas pressure and temperature are known downstream and upstream of the orifice:

$$\delta = n_n^{i+1/2} / n_n^{i-1/2} = T_{nV}^{i+1/2} P^{i+1/2} / T_{nV}^{i-1/2} P^{i-1/2}. \quad (2.110)$$

If the neutral temperature is further assumed to be constant along the orifice, then:

$$\delta = P^{i+1/2} / P^{i-1/2}. \quad (2.111)$$

The knowledge of the pressure downstream or upstream of the orifice, and the application of a Poiseuille flow model, yields the missing pressure, and δ .

Charged particle flow The momentum equations are written for both ions and electrons. The electron velocity is considered to be dominant over the ion and neutral velocities, and the ion-neutral collision term dominates over the ion-electron term in the ion momentum equation. Mizrahi *et al.* consider a steady-state system, and neglect the convective derivative. The neutral velocity is implicitly assumed to be the average neutral gas flow velocity in the channel from Equation 2.107. The combination of both the electron and ion momentum equations yields:

$$n_e u_i = n_e u_g - D_a \nabla n_e - \frac{m}{M} \frac{\nu_{ei} + \nu_{en}}{\nu_{in}} n_e u_e, \quad (2.112)$$

where ν_{in} is the ion-neutral collision frequency. Mizrahi *et al.* argue that the third term is negligible since $\frac{m}{M} \frac{\nu_{ei} + \nu_{en}}{\nu_{in}} \ll 1$, in direct contradiction with Katz *et al.* [97]. This assumption does not take into account the electron velocity as compared to the ion or neutral velocities. We can evaluate the first and third term on the right-

hand side of Equation 2.112. The neutral flow velocity is given by Equation 2.107. The electron flow velocity may be calculated by considering that all of the discharge current is carried by the electrons $I_d = en_e \pi r_o^2 u_e$. We used Equation 2.29 for the electron-ion collision frequency, and the Maxwellian-averaged momentum-transfer cross-section for electron-neutral collisions from [80] to calculate the electron-neutral collision frequency $\nu_{en} = n_n \langle \sigma v \rangle$. The charge-exchange collision cross section is assumed to be equal to 10^{-18} m^2 . Using the reported results of the model for xenon gas ($n_g = 1.1 \times 10^{23} \text{ m}^{-3}$, $n_e = 2.7 \times 10^{22} \text{ m}^{-3}$, $T_{eV} = 1.6 \text{ eV}$, $T_{iV} = 0.4 \text{ eV}$), both the third and first term on the right-hand side of Equation 2.112 may be evaluated:

$$\frac{m}{M} \frac{\nu_{ei} + \nu_{en}}{\nu_{in}} u_e \approx 170 \text{ m/s}$$

$$u_g \approx 181 \text{ m/s}$$

Clearly, the electron current term cannot be neglected based on the results of the model.

Density evaluation The density in the 0-D cell is considered to be constant and equal its average value. The cell-center density is also expected to be much greater than the density at the cell boundaries, due to significant ionization within the constricted orifice and expansion to vacuum at the outlet.

The density gradient in Equation 2.112 can be evaluated through a Taylor expansion from the center density to the boundary,

$$\nabla n_e = \left. \frac{\partial n_e}{\partial z} \right|_{i \pm 1/2} \approx \frac{\mp n_e^i \pm n_e^{i \pm 1/2}}{L_o/2} \approx \mp \frac{n_e^i}{L_o/2}. \quad (2.113)$$

Mizrahi *et al.* consider that the center density n_e^i is equal to the average density within the cell, \bar{n}_e . This gives:

$$\left. \frac{\partial n_e}{\partial z} \right|_{i \pm 1/2} \approx \mp \frac{\bar{n}_e}{L_o/2}. \quad (2.114)$$

A similar approach can be taken to evaluate the density gradient in the radial direction.

In the axial direction, by virtue of Bolzano's theorem, the gradient of the density must be zero at least once on the interval $[z_{i-1/2}, z_{i+1/2}]$. If this density maximum is achieved at the center of the cell, the density over the whole cell should be equal to \bar{n}_e to be consistent with the average density definition. This approach yields a discontinuity in density at the boundaries of the cell. For example, $n_e^{i-1/2,L} \neq n_e^{i-1/2,R}$ because $n_e^{i-1/2,L} \ll n_e^{i-1/2,R}$, where L and R designate the limit value when the boundary is approached from the left and right, respectively. Other cases require sharp density gradients in the first half or second half of the cell for consistency.

Continuity equation The mass flow rate for neutrals is obtained from the volumetric mass flow rate $Q = \bar{u}_g \pi r_o^2$ using:

$$\dot{m}_g = M n_n \pi r_o^2 \bar{u}_g. \quad (2.115)$$

The ion mass flow rate is obtained in a similar fashion:

$$\dot{m}_i = M n_e \pi r_o^2 u_i. \quad (2.116)$$

For both boundaries, we have

$$\dot{m} = \dot{m}_g + \dot{m}_i = M \pi r_o^2 (\bar{u}_g n_n^{i \pm 1/2} + (u_i n_i)^{i \pm 1/2}). \quad (2.117)$$

Averaging the value at left and right boundaries, and combining it with Equation 2.112 yields:

$$\dot{m} = M\pi r_o^2 \left(\bar{n}_g + \frac{1}{2} (n_e^{i+1/2} + n_e^{i-1/2}) \right) \bar{u}_g. \quad (2.118)$$

Mizrahi *et al.* are inconsistent with the density definition, and assume that $\bar{n}_e = \frac{1}{2} (n_e^{i+1/2} + n_e^{i-1/2})$, though the boundary plasma densities have previously been assumed to be negligible compared to the average density ($\bar{n}_e \gg n_e^{i\pm 1/2}$). The resulting mass conservation equation is:

$$\dot{m} = M\pi r_o^2 (\bar{n}_g + \bar{n}_e) \bar{u}_g. \quad (2.119)$$

Radial diffusion The radial diffusion of ions is assumed to be governed by charge-exchange collisions. The corresponding radial flux is evaluated in the same fashion as the axial boundary flux:

$$J_i = -eD_a \frac{\partial \bar{n}_e}{\partial r} \Big|_{r=r_o} \approx eD_a \frac{n_e}{r_o}. \quad (2.120)$$

This approach does not consider sheath physics and uses a linearized density gradient, in contrast with Goebel and Katz's model.

Ion balance Ions are considered to be created in the volume through direct-impact ionization with thermalized electrons, and are lost through diffusion to the boundaries. The ion balance is similar to that of all of the previously described authors. Using the axial and radial diffusion approach, the ion balance is given by:

$$\begin{aligned} \pi r_o^2 \left(J_i^{i+1/2} - J_i^{i-1/2} \right) + 2\pi r_o L_o J_i^{r=r_o} &= \pi r_o^2 L_o e \bar{n}_g \bar{n}_e \sigma_{iz} (T_{eV}) \sqrt{\frac{eT_{eV}}{m}} \\ \Leftrightarrow \bar{n}_g \sigma_{iz} (T_{eV}) \sqrt{\frac{eT_{eV}}{m}} &= \frac{2D_a}{r_o^2} (1 + 2(r_o/L_o)^2). \end{aligned} \quad (2.121)$$

Although Mizrahi *et al.* use the electron thermal velocity, Mandell and Katz’s fit uses the Maxwellian velocity for the electrons.

Power balance The power balance is similar to that of previously described authors. Mizrahi *et al.* do not consider a double sheath, but consider Ohmic heating balanced by ionization, excitation, and convection. Plasma resistance is provided through electron-ion and electron-neutral collisions. The cross sections for electron-neutral collisions, ionization, and excitation are estimated with numerical fits (Equations 2.31, 2.23 and 2.26, respectively):

$$R_p I_d^2 = \pi r_o^2 L_o \bar{n}_g \bar{n}_e e \sqrt{\frac{e T_{eV}}{m}} (\epsilon_{iz} \sigma_{iz} + \epsilon_{ex} \sigma_{ex}) + \frac{5}{2} (T_{eV} - T_{eV}^{\text{ins}}) I_d. \quad (2.122)$$

Evaluation Despite several fundamental inconsistencies, the model performs relatively well on the NSTAR neutralizer cathode as compared to other 0-D and higher-dimensional models. The model of Mizrahi *et al.* unfortunately relies on a free parameter, and on experimental data for the insert electron temperature. The study does not feature a sensitivity analysis. No comparison to experimental data is presented in [96], or available in the literature. The results of the model are consistent with that of Mandell and Katz from [75].

2.8 Albertoni et al. [49, 55]

Albertoni proposes a model for the insert and orifice plasma. The orifice is modeled as a separate 0-D volume. A free-standing double sheath at the orifice entrance is assumed to be present. The double sheath accelerates electrons towards the orifice while keeping ions within the emitter region. Albertoni’s orifice model includes an ion flux balance, plasma power balance, and a choked-flow calculation to compute plasma

density, electron temperature, and neutral density. Processes such as excitation — and therefore stepwise ionization — and radiation are neglected.

The emitter region model includes an ion flux balance, plasma and emitter power balances, a current density balance, and a pressure equation. Albertoni’s model considers thermal and emitted electrons as well as ions for the current balance. Volume ionization is again considered to originate from thermalized Maxwellian electrons, while stepwise ionization is neglected. The model must be coupled with a thermal simulation to obtain the temperature of the emitter, and, therefore, the emitted current. An early version of this model [55] that ignored the orifice showed good agreement for the peak emitter wall temperature for a single-channel hollow cathode. The current model predicts the variation of the plasma potential with mass flow rate and discharge current, but the author notes that these cannot be compared with readily-available experimental data.

Albertoni’s analysis neglects the emitted electrons, which participate in the stepwise ionization and neutral excitation processes, and suffers from the necessity of a coupled thermal model, which further complicates the solution process. The thermal model also considers that the emitter temperature is uniform, while experimental measurements have shown that emitter temperatures may vary by more than 10% of the peak temperature [98,99].

In an early version of his model, Albertoni carries out a separate evaluation of the plasma attachment length by invoking the “principle of minimum power,” which seeks to minimize the power deposited in the sheath $P_s = I_d \phi_s$, and, therefore, the sheath voltage ϕ_s for a given current. Albertoni solves the 0-D model by iterating through multiple plasma attachment lengths, and finds the corresponding minimum in the sheath voltage. For a given discharge current, minimizing the sheath voltage amounts to minimizing the net current density, which may bias this method towards the prediction of longer attachment lengths. Numerical results for the plasma at-

tachment length scale inversely with mass flow rate, as observed experimentally, but predict that L_{emit} increases with the discharge current, in contradiction with experimental results [42, 100].

2.8.1 Orifice model

Albertoni's approach is very similar to that of Domonkos: ion conservation and a plasma power balance are considered, achieving closure through a modified choked-flow pressure relation.

Ion conservation The ion conservation equation is identical to Equation 2.45. The author uses the Bohm criterion for the ion current density,

$$J_i = 0.61en_e \left(\frac{eT_{eV}}{M} \right)^{1/2}. \quad (2.123)$$

Plasma volume power balance Albertoni uses the total discharge current in the Ohmic heating term, and introduces a double-sheath power loss which is subsequently neglected. Power losses due to excitation of neutrals and radiation are also neglected:

$$\dot{q}_\Omega = \dot{q}_{iz} + \dot{q}_{ex} + \dot{q}_{\text{conv}} + \underbrace{\dot{q}_{ds}}_{\text{neglected}}. \quad (2.124)$$

The ionization power, \dot{q}_{iz} , is expressed as in Equation 2.12 and the ionization rate is found as in Domonkos's model (Equation 2.46).

Albertoni does not consider the current to vary along the length of the orifice, so the total discharge current is used in the Ohmic heating term:

$$\dot{q}_\Omega = R_p I_d^2. \quad (2.125)$$

The resistance of the plasma is obtained with both electron-ion and electron-neutral collisions. The electron-neutral collision cross section is estimated from Equation 2.31 (from [78]), while the collision frequency is estimated using the thermal velocity of the electrons, as opposed to the Maxwellian average velocity. The convection power is estimated as in Equation 2.66, but using a factor of 2 (which, once again, should be 5/2).

Pressure calculation Closure of the system is obtained through a choked-flow model of the orifice region, modified to account for the contribution of electrons to the flow:

$$P = \frac{\dot{m}}{\pi r_o^2} \sqrt{\frac{R_g}{\gamma} T_n \left(1 + \alpha \frac{T_e}{T_n} \right)}. \quad (2.126)$$

All quantities are considered to be static rather than stagnation properties. The gas temperature is assumed to be equal to that of the orifice plate. The total static pressure is equated to that given by the perfect gas law (Equation 2.3).

The correction for the electron pressure contribution is equivalent to calculating an effective gas constant for a mixture of heavy particles and electrons, assuming that T_e is constant and that all species expand isentropically through the orifice. For monatomic species, the total enthalpy of the fluid mixture may be expressed as [101]:

$$\begin{aligned} h_{\text{total}} &= \frac{n_e m}{n_e m + n_n M} \left(\frac{5}{2} \frac{k_B T_e}{m} + \frac{n_n M}{n_e m} \frac{5}{2} \frac{k_B T_n}{M} \right) \\ \Leftrightarrow h_{\text{total}} &\approx \alpha \frac{5}{2} \frac{k_B T_e}{M} + \frac{5}{2} \frac{k_B T_n}{M} \\ \Leftrightarrow h_{\text{total}} &\approx \underbrace{\frac{5}{2} \frac{k_B}{M} \left(1 + \alpha \frac{T_e}{T_n} \right)}_{\text{Effective gas constant}} T_n \end{aligned} \quad (2.127)$$

2.8.2 Insert model

The insert model features ion conservation, current conservation, plasma power balance, and pressure balance equations.

Ion conservation Albertoni considers that ions are brought into the control volume through direct ionization and from the orifice through the double sheath. Ions are lost through the sheaths, and thermally upstream. The resulting ion balance is given by:

$$e \left(\frac{dN_i}{dt} \right)_{iz} + J_i^{ds} \pi r_o^2 = J_i (2\pi r_c L_{\text{emit}} + \pi(r_c^2 - r_o^2)) + \frac{1}{4} n_e e \sqrt{\frac{8eT_{iV}}{\pi M}} \pi r_c^2. \quad (2.128)$$

Orifice and insert quantities are used to calculate J_i^{ds} and J_i , respectively. They are both given by Equation 2.123. The use of the Bohm current for the double sheath ion current leads to the previously discussed issues regarding the double sheath voltage and power predictions.

Current conservation Albertoni includes neither ion nor electron losses to the orifice plate, and neglects the thermal ions lost through the upstream boundary of the volume for current conservation. However, the contribution of these terms to the discharge current is likely small. The resulting current balance at the emitter surface is given by:

$$\frac{I_d}{2\pi r_c L_{\text{emit}}} = J_i + J_{em} - J_r \exp\left(-\frac{\phi_p}{T_{eV}}\right). \quad (2.129)$$

The thermionic current J_{em} is calculated with Equation 2.8. J_r is obtained with Equation 2.82. Using the total discharge current in this expression neglects the contribution of the orifice ions to the total current.

Plasma power balance The plasma power balance is similar to Equation 2.83, though Albertoni does not consider losses due to neutral excitation:

$$\dot{q}_\Omega + \dot{q}_{\text{ori}} + \dot{q}_{em} = \dot{q}_{iz} + \dot{q}_{\text{conv}} + \dot{q}_{\text{coll}}. \quad (2.130)$$

\dot{q}_Ω , \dot{q}_{ori} , \dot{q}_{em} , \dot{q}_{iz} are given by Equations 2.85, 2.86, 2.87, and 2.88, respectively. Albertoni's expression for \dot{q}_{coll} is similar to that of Equation 2.90, though the author does not include the plasma potential in the total energy of the collected electrons (electrons leaving the plasma in this case):

$$\dot{q}_{\text{coll}} = (I_i^{th} + I_i^{\text{coll}}) 2T_{iV} + I_e^{\text{coll}} 2T_{eV}. \quad (2.131)$$

This is a substantial omission for significant return electron currents. The power convected by the electron current is:

$$\dot{q}_{\text{conv}} = \frac{5}{2} T_{eV} I_d. \quad (2.132)$$

Neutral flow The system is closed with a pressure balance similar to that of Domonkos. Albertoni's formulation as reported in [49] is dimensionally inconsistent, as the radius should appear to the fourth power. Albertoni calculates the dynamic viscosity from kinetic theory, considering hard-sphere particles of diameter d_m and a mean-free-path approach:

$$\mu = \frac{1}{\pi d_m^2} \sqrt{\frac{M k_B T_o}{\pi}}. \quad (2.133)$$

A comparison of the viscosity calculations for the hard-sphere approach, the Chapman-Enskog method applied to the Lennard-Jones 12-6 potential with parameters $\sigma = 4.055 \text{ \AA}$ and $\epsilon/k_B = 229 \text{ K}$, and a derivation of viscosity from dimensional analysis from Stiel and Thodos [102] is shown for xenon in Figure 2.10. The van der Waals radius for xenon is considered to be equal to 216 pm for the hard-sphere model. The collision integrals for the Chapman-Enskog calculations are tabulated in [103] and originally from [104]. The hard sphere model under-predicts the viscosity at high-temperatures, which is especially important in the orifice. The Lennard-Jones 12-6 potential yields very close agreement to the experimental fit. We suggest using

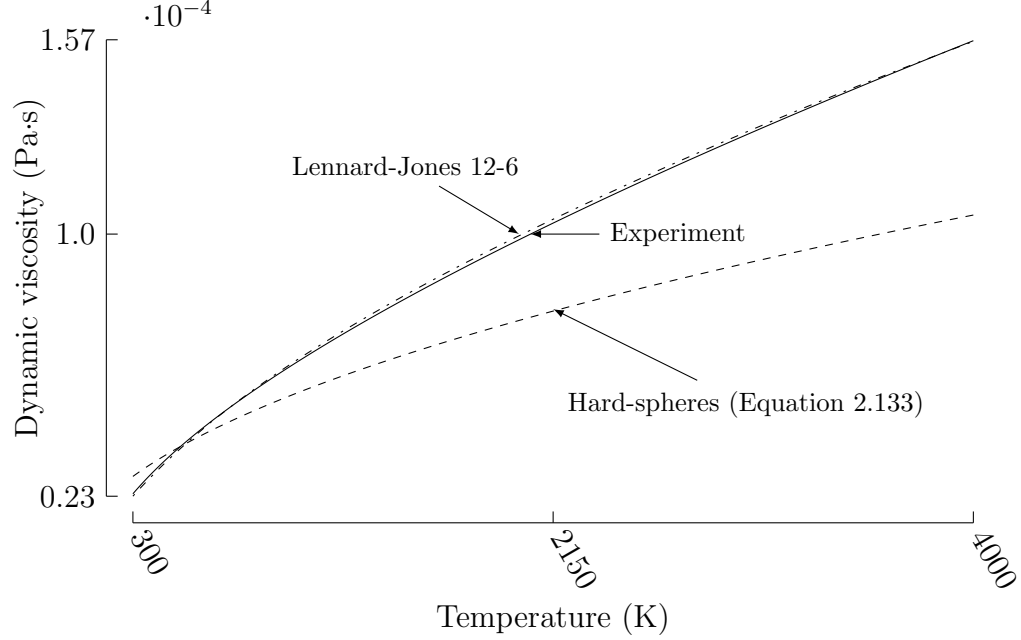


Figure 2.10: Comparison of different viscosity models for xenon gas. Experimental fit from [102].

either the fit to experimental data or the Lennard-Jones potential approach for accurate calculation of the viscosity.

Thermal model Albertoni includes a thermal model to predict the emitter temperature. Convection from the insert, conduction through the cathode tube, radiation from both the heat shield and orifice surfaces, and heat dissipation through evaporation of the insert are considered. The plasma processes at the insert surface deposit power through ion bombardment and electron backstreaming, and contribute to cooling through thermionic emission. Ohmic power deposition in the orifice plasma is assumed to be entirely transferred to the orifice plate. For radiation, a background temperature of 0 K is assumed. The base of the cathode is kept at an arbitrary value of 1000 K.

Albertoni represents the cathode as a radiative thermal network (see Figures 4 and 5 in [49]). The radiosities J_k are unknown, as are the node temperatures. The

thermal network requires the power inputs and outputs to the insert node, which are obtained from the insert power balance.

Insert power balance Albertoni’s insert power balance is similar to that of Goebel and Katz. The author does not consider the pre-sheath contribution to the ion power — though he uses the Bohm sheath criterion for the ion current — and adds the emitter temperature to the total energy of the emitted electrons:

$$\dot{q}_{th} + I_{em} \left(\phi_{\text{eff}} + \frac{3k_B}{2e} T_c \right) = I_i (\epsilon_{iz} + \phi_p - \phi_w) + (2T_{eV} + \phi_w) I_r \exp \left(-\frac{\phi_p}{T_{eV}} \right). \quad (2.134)$$

The emitter temperature contribution is negligible compared to the effective work function. The plasma model is coupled to the thermal model through the heat loss term, \dot{q}_{th} .

Emission length As discussed in the Introduction (Chapter 1, Section 1.3), Albertoni proposes to compute the plasma attachment length with the empirically-derived expression:

$$K \approx PL_{\text{emit}}, \quad K = 5 - 15 \text{ Pa} \cdot \text{m}. \quad (2.135)$$

We compared the emission length obtained from Equation 2.135 to experimental data from [65]. The cathode considered is Siegfried and Wilbur’s noble gas cathode operating on xenon and argon at mass flow rates of 92 and 287 mA, respectively, and an orifice diameter of 0.76 mm. For consistency, the pressure is calculated using Equation 2.4. The experimental emission length in [65] is determined from the insert temperature profile: it is the length that corresponds to the distance between the position of the maximum insert temperature and the position where the insert temperature is 90% of that maximum. While this definition is different from Albertoni’s (and also ours), it provides an upper-bound for the actual emission length. Results are shown in Figure 2.11. A value of K outside the specified range would clearly be

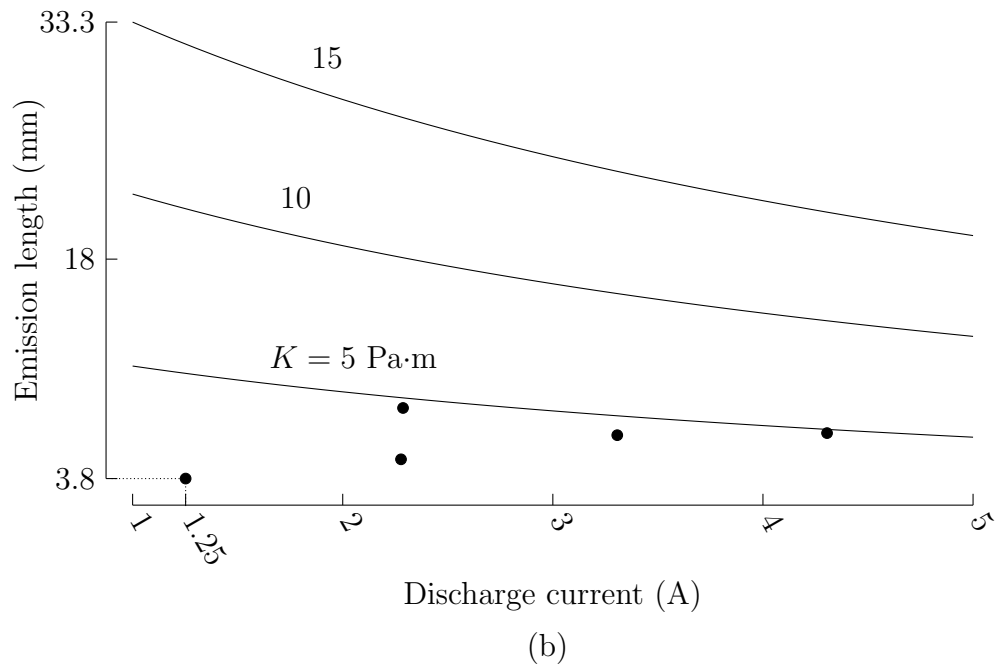
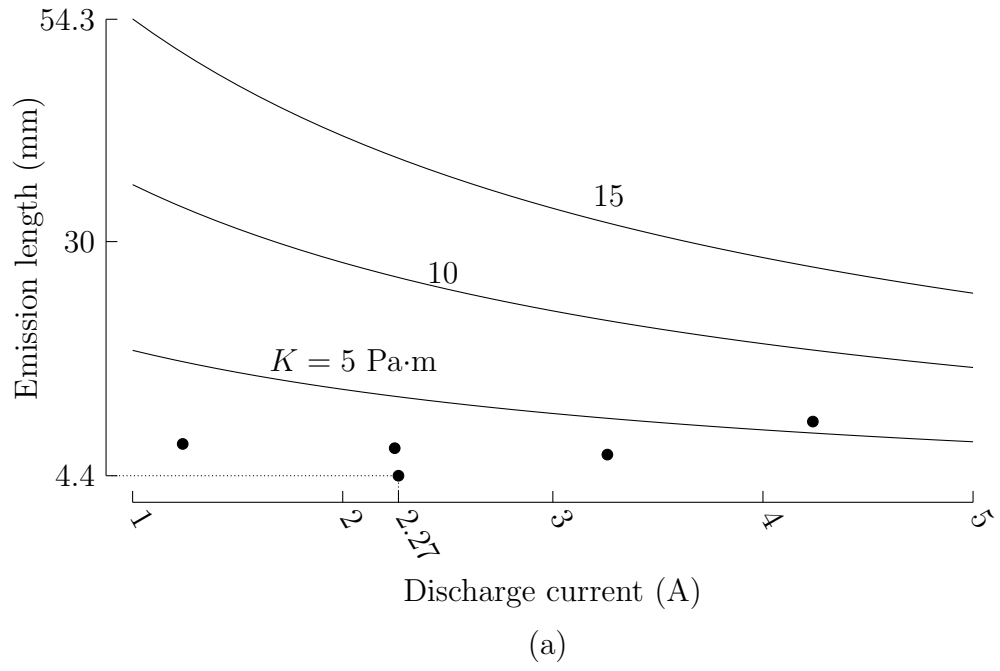


Figure 2.11: Comparison of emission length empirical relationship (Equation 2.135) for $K = 5, 10, 15$ Pa·m to experimental data from [65] for (a) xenon and (b) argon.

required to achieve agreement with experimental results.

2.8.3 Evaluation

The model does require additional information — material properties, further geometric data, and gas information. However, it is self-contained and does not require any experimental data other than collisional cross sections (unless L_{emit} is fit to the experimental data). It solves for the neutral and electron densities, plasma potential, and orifice and insert temperatures. Due to the complexity and detailed requirements for property input for Albertoni’s thermal model, we were not able to reimplement this model.

2.9 Model comparisons

We benchmarked the performance of the models on cathodes for which experimental data and a heat loss estimate are readily available, as it is a necessity for the insert models. This data is available for Siegfried and Wilbur’s original xenon cathode, and the NSTAR discharge cathode. Siegfried and Wilbur’s cathode uses a tantalum insert coated with R-500 (a barium-strontium-carbonate mixture [52]) as an emitter, while the NSTAR discharge cathode uses a porous tungsten insert impregnated with a mixture of barium, calcium, and aluminum oxides [42]. The dimensions for the different benchmark cathodes are shown in Table 2.1. We included the NEXIS cathode as it will be used in the next section for flow model comparisons.

Table 2.1: Dimensions of the benchmark cathodes. Dimensions are from [65, 72], [42, 83, 92, 105–108], and [42, 60, 107, 109, 110] for Siegfried and Wilbur’s cathode, the NSTAR discharge cathode, the NEXIS cathode, respectively.

Cathode	Dimension				
	L (cm)	Insert I.D. (cm)	O.D. (cm)	Orifice L (mm)	Orifice D (mm)
Siegfried and Wilbur	1.5 – 2.0	0.39	0.40	1.8	0.51 – 0.96
NSTAR Discharge	2.54	0.38	0.55	0.74	1.02
NEXIS	2.54	1.2*	1.42 [†]	0.74 [‡]	1.5 – 2.8

* The insert inner diameter is set to 1.20 cm, following Mikellides *et al.*’s work [60, 107, 109]. Later work by Goebel and Katz [42] suggests an insert diameter of 1.27 cm.

[†] The outer diameter for the NEXIS cathode is deduced from insert thickness data retrieved from [60] and [107].

[‡] Measured from plots in [107].

2.9.1 Siegfried and Wilbur’s noble gas cathode

We consider the cathode with an orifice diameter of $d_o = 0.76$ mm, running on xenon at a mass flow rate of 92 mA (1.28 sccm of xenon, or 0.13 mg/s). We vary the input

discharge current from 1 to 5 A, and compare the output of the two recreated insert models to experimental data.

Required inputs The heat loss term necessary for both recreated insert models is obtained from [65]:

$$\dot{q}_{th} = 2(526T_c - 3.99 \times 10^5)L_{\text{emit}}r_c. \quad (2.136)$$

Siegfried and Wilbur assume a value of 0.8 eV for the electron temperature in the insert [65]. We use this value in all of the calculations that require an insert electron temperature. We have also used the total inelastic cross-section data given in [65] for the calculation of the energy-exchange mean free path to avoid calculating a new value of the proportionality constant between λ_{pr} and L_{emit} .

Goebel and Katz’s insert model requires insert wall temperature, emission length, and plasma potential. We use experimental data available in [65]. The neutral gas temperature is set equal to twice the measured wall temperature.

Siegfried notes that the work function of the R500-coated tantalum insert is unknown, and assumes a value of 2.25 eV. We use this value for our calculations. We set the orifice neutral temperature to 0.4 eV for Mandell and Katz’s orifice model and for that of Mizrahi *et al.*. The free parameter δ in Mizrahi *et al.*’s orifice model is set to 0.2 for this cathode.

Comparison Results for the insert and orifice models are shown in Figures 2.12 and 2.13, respectively.

Our re-implementation of Siegfried and Wilbur’s model is able to recreate their original results. The curvature changes observed on both implementations originate from the total inelastic cross-section for xenon that appears in the emission length calculation. Goebel and Katz’s insert model overestimates the plasma density in the insert region by a factor of 5, though the model is very sensitive to the input plasma

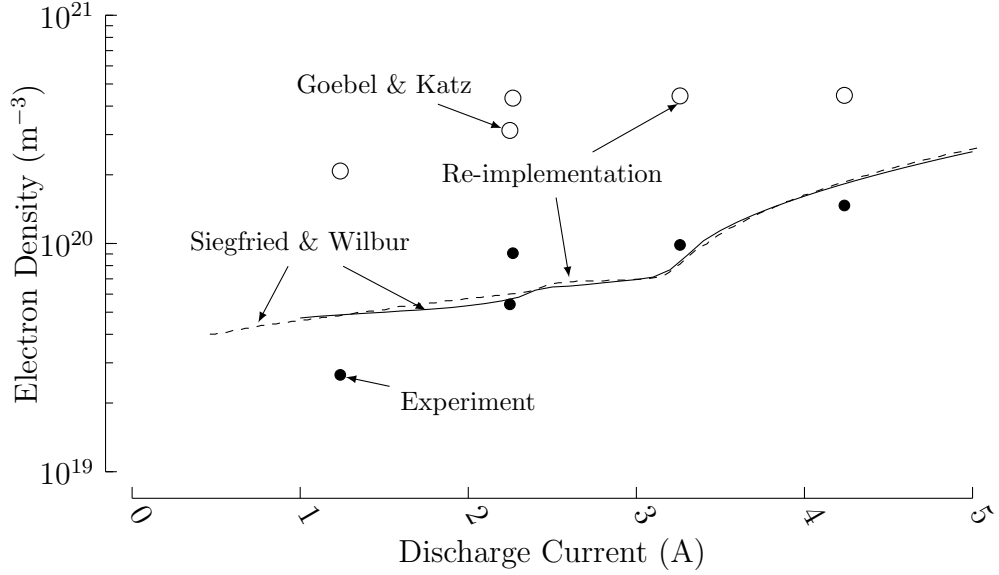


Figure 2.12: Comparison of cathode insert models for Siegfried and Wilbur’s xenon cathode. Experimental data and original model results are from [65].

potential, emission length, and estimated heat loss. No error bounds are provided for these values.

The orifice models yield consistent results for the plasma density. Both Goebel and Katz’s and Mizrahi *et al.*’s results for the electron temperature are insensitive to the discharge current, with Goebel and Katz’s estimate being the largest value consistent with the assumptions of their model. Mandell and Katz’s model returns a substantially larger ionization fraction as compared to the other models. However, without experimental data for the orifice, it is difficult to determine which model is the most accurate.

2.9.2 NSTAR discharge cathode

We computed averaged quantities for the NSTAR discharge cathode operating at the mass flow rates specified by the “TH8” and “TH15” operational conditions. TH8 and TH15 differ both in terms of mass flow rate and discharge current as shown in Table 2.2.

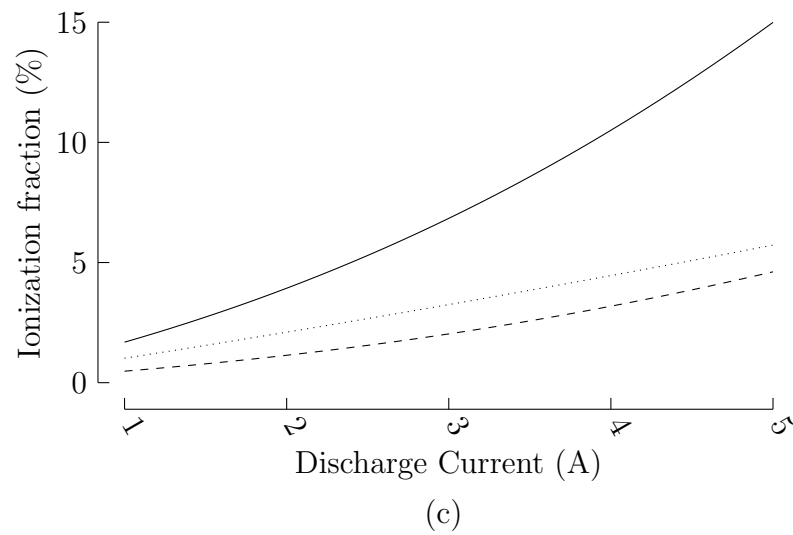
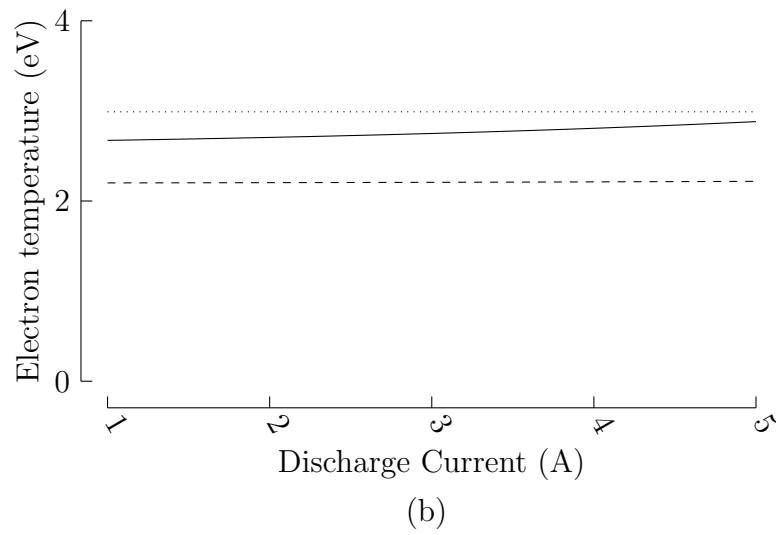
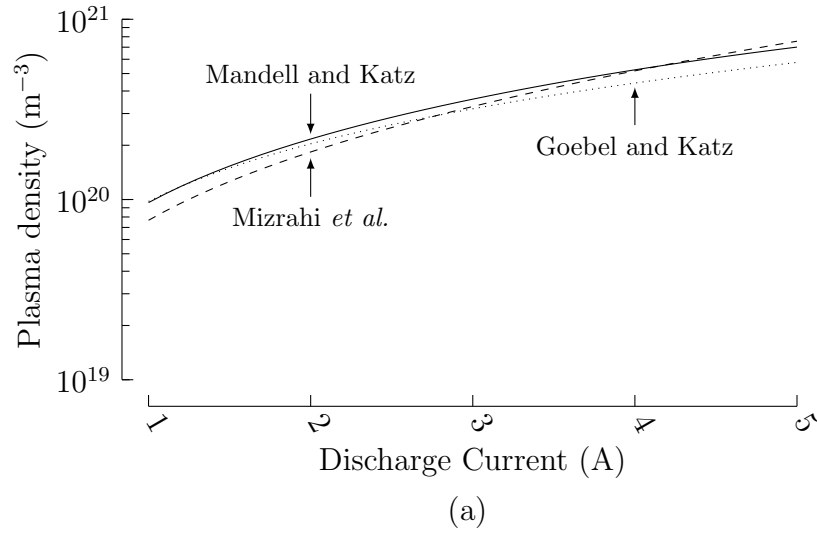


Figure 2.13: Comparison of cathode orifice models for Siegfried and Wilbur's xenon cathode.

Required inputs We computed the average electron temperature and plasma potential in the insert region from experimental data obtained from [111]. The heat loss term necessary for the insert models is taken to be a constant value of 13 W. This figure is taken from the results of the application of the thermal model IROrCa2D on the NSTAR cathode [106]. Though the application point for [106] ($I_d = 12$ A, $\dot{m} = 4.25$ sccm) differs from the two considered operational points, we follow [42] and use this value for all operating conditions. The operating conditions and required inputs are delineated in Table 2.2.

Table 2.2: Operating conditions and average experimental data required for model input. The definition of the TH8 and TH15 operating points is taken from [108]. The average plasma potentials and electron temperatures are computed from [111] — the reported measurement error is ± 1 V for the potential, and ± 0.5 eV for the electron temperature.

Parameter		TH8	TH15
Operating condition	I_d (A)	8.24	13.3
	\dot{m} (sccm)	2.47	3.7
Experimental data	$\bar{\phi}_p$ (V)	9.2	5.5
	\bar{T}_{eV} (eV)	1.4	1.4

We used a work function equal to 2.06 eV for the insert material. The experimental data for the total pressure reported in [111] is used in Siegfried and Wilbur’s insert model. The orifice models use an assumed insert electron temperature, which is set equal to the average value of 1.4 eV. The neutral gas temperature is assumed to be equal to 0.4 eV. Goebel and Katz indicate that the downstream pressure at the exit plane of the orifice on the NSTAR discharge cathode is approximately 2 Torr [42] (p.466). Using a Poiseuille flow model, we calculated the upstream pressure for the two specified mass flow rates. The resulting values for δ are 0.31 and 0.26 for $\dot{m} = 2.47$ sccm and $\dot{m} = 3.7$ sccm, respectively.

Comparison Insert and orifice results are shown in Tables 2.3 and 2.4, respectively. For low-current conditions, both Siegfried and Wilbur’s and Goebel and Katz’s in-

sert models agree with experimental data. The ionization fraction for Siegfried and Wilbur’s model is three times lower than the experimental value, but it is not clear if this result lies outside of the error bounds. For the high-current condition, Siegfried and Wilbur’s insert model over predicts the plasma potential, a consequence of their neglecting Ohmic heating, return electron current, and assuming $\phi_s = \phi_p$. This model does predict a lower attachment length at higher current and mass flow rate, consistent with experimental observations, and shows great accuracy for the emitter temperature. It is not clear whether the predictive accuracy for the emitter temperature would persist for other operating conditions given the sparsity of experimental data.

We do not have an experimental standard for comparison with the orifice results, though we may be able to identify unreasonable predictions. For example, Mandell and Katz’s orifice model seems to over predict both plasma density and ionization fraction, a possible consequence of the omission of the $5/2$ factor in the plasma power balance. We show in Table 2.4 the impact of this correction to the convective term.

Table 2.3: Results from the insert models applied to the NSTAR discharge cathode. The experimental data is spatially averaged from data reported in [111]. Plasma potential accuracy is ± 1 V, and electron temperature ± 0.5 eV. No information about accuracy of density measurements is reported.

		Siegfried and Wilbur	Goebel and Katz	Experiment (average)
TH8	n_e ($\times 10^{-20}$ m $^{-3}$)	3.3	4.0	3.6
	T_{eV} (eV)	1.4*	1.6	1.4
	ϕ_p (V)	10.0	9.2*	9.2
	ϕ_s (V)	—	5.7	—
	T_c (K)	1,420	—	1,470 [†]
	L_{emit} (mm)	1.9	6.0*	6.0
	α (%)	1.2	3.3	3.7
TH15	n_e ($\times 10^{-20}$ m $^{-3}$)	11.9	2.8	4.7
	T_{eV} (eV)	1.4*	1.5	1.4
	ϕ_p (V)	14.7	5.5*	5.5
	ϕ_s (V)	—	2.8	—
	T_c (K)	1,530	—	1,540 [†]
	L_{emit} (mm)	0.49	6.0*	6.0
	α (%)	1.7	1.8	2.7

* Model input.

[†] Calculated from fits to measured temperature profiles — $T_c = 1191.6I_d^{0.0988}$

Table 2.4: Results from the orifice models applied to the NSTAR discharge cathode.

		Mandell and Katz	Mandell and Katz (with correction)	Mizrahi <i>et al.</i>	Goebel and Katz
TH8	n_e ($\times 10^{-20}$ m $^{-3}$)	5.0	2.3	1.6	2.6
	T_{eV} (eV)	2.8	2.7	2.8	3.1
	α (%)	9.1	3.9	1.7	6.8
TH15	n_e ($\times 10^{-20}$ m $^{-3}$)	13.5	7.6	4.4	6.8
	T_{eV} (eV)	2.7	2.5	2.7	2.9
	α (%)	18.6	9.3	4.2	6.0

2.10 Critical issues

2.10.1 Ionized gas flow

The 0-D models outlined in the preceding sections rely on specific assumptions for the gas flow to compute the total pressure inside the cathode. The calculation of the total pressure has been performed using an empirical relationship [52, 63, 65, 71, 72, 82, 112, 113], an isentropic [69] or isothermal [47, 114] flow approach, Poiseuille flow theory [42, 95, 96], a modification of Poiseuille flow theory [64, 73] to take into account compressibility and molecular flow effects, and an “equivalent temperature” or modified specific gas constant taking into account the ionization fraction [47, 49, 55, 114].

Table 2.5 and Figure 2.14 show the pressure calculated using various flow models, for both the NSTAR discharge cathode and the NEXIS cathode, respectively. The NSTAR and NEXIS dimensions are shown in Table 2.1. A neutral gas temperature of 4,000 K and 3,000 K is assumed for the NSTAR and NEXIS Poiseuille flow calculations, respectively. While the empirical approach from [65] (pp. 127–129) is the only one that predicts any variation in the cathode pressure with discharge current, it clearly does not generalize to other cathodes, and overestimates the pressure in both the NSTAR and NEXIS. Figure 2.14 shows that Domonkos’s model has slightly better performance than the Poiseuille approach on the NEXIS cathode, but still cannot capture the effect of the discharge current. The results for the same model applied to the NSTAR cathode differ by an average value of over 20% from the experimental results. The modified Poiseuille flow model used by Domonkos and Albertoni *et al.* produces acceptable results for the NEXIS, though its accuracy decreases as the mass flow rate increases. We now address the relevant issues for each model of ionized gas flow.

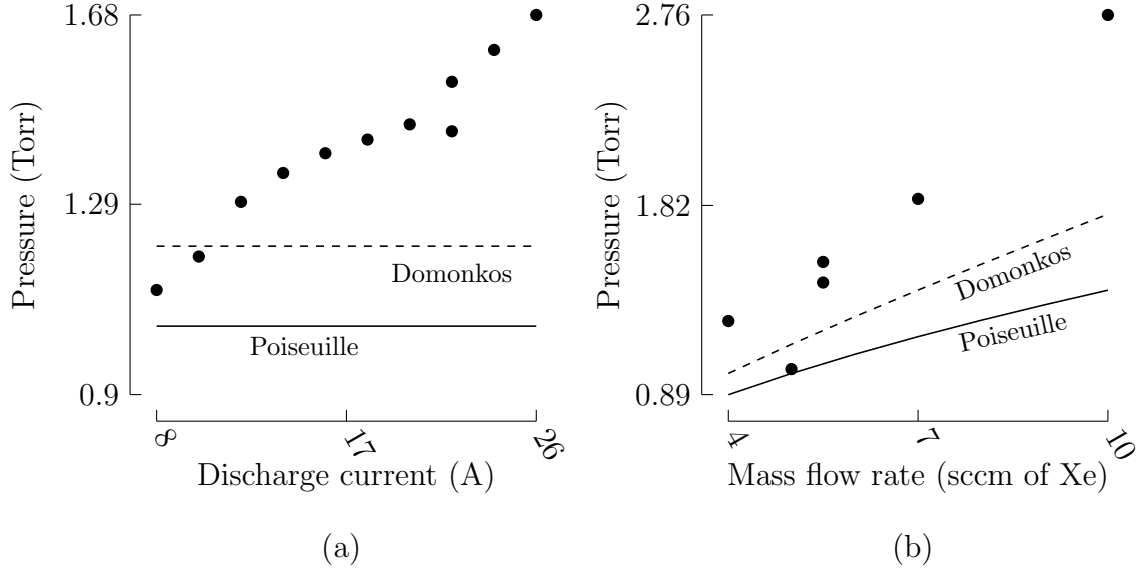


Figure 2.14: Total pressure for two pressure models applied to the NEXIS cathode as functions of (a) discharge current with constant mass flow rate ($\dot{m} = 5.5$ sccm) and (b) mass flow rate with constant discharge current ($I_d = 22$ A). Experimental data from [115, 116].

Empirical correlations The empirical approach suggested by Siegfried and Wilbur [52, 63, 65, 71, 72] for their hollow cathode that operate on mercury, argon, and xenon (later extended by Friedly to a different cathode in [112]) uses a relationship that is based on a single cathode. Similar work by Patterson *et al.* [113] only uses the T6 cathode. The resulting relationships from these approaches cannot be generalized to other cathodes or operating conditions. Friedly [112] suggests that the ion flow rate ingested by the cathode should be added to the total mass flow rate that is used in the empirical relationship. The ions are assumed to go through a double sheath in front of the orifice and recombine in the insert region as neutrals that then exit the orifice. Because Friedly considers that the total flow rate without ion ingestion inside the orifice is that of the supply, the backstreaming ions have to be created through another mechanism outside of the cathode. This approach possibly contradicts conservation of mass.

Table 2.5: Comparison of pressure predictions (in Torr) of multiple flow models applied to the NSTAR cathode. Empirical correlation from [65] (pp.127–129). Experimental data is taken from [117] for TH4, TH8, and TH15, and from [118] for TH12.

Operating condition		Pressure model			Experiment
		Empirical correlation	Poiseuille	Modified Poiseuille	
TH4	$I_d = 5.95$ A $\dot{m} = 2.47$ sccm	5.6	5.7	5.6	4.0
TH8	$I_d = 8.24$ A $\dot{m} = 2.47$ sccm	7.1	5.7	5.6	4.6
TH12	$I_d = 9.9$ A $\dot{m} = 2.81$ sccm	9.4	6.0	6.1	5.9
TH15	$I_d = 13.3$ A $\dot{m} = 3.7$ sccm	15.9	6.8	7.1	8.1

A more general correlation is necessary for an empirical approach to produce accurate results. We also note that these formulations assume scaling that conforms to isentropic flow conditions.

Isentropic flow The isentropic flow model of [69] relies on the assumptions that the flow is choked at the outlet plane, the flow rate is sufficient to ensure continuum flow in the orifice region, and that both viscous losses and heat addition due to Joule heating are negligible. Similar assumptions are made in [114] and in [47] for an isothermal flow. The choked-flow assumption is justified as long as the ratio of backing (stagnation) pressure P_0 to vacuum background pressure P_b satisfies:

$$\frac{P_0}{P_b} > G = \left(\frac{\gamma + 1}{2} \right)^{\gamma/(\gamma-1)}, \quad (2.137)$$

where γ is the ratio of heat capacities. This condition is met for all cathodes operating in vacuum. For monatomic propellants, $\gamma = 5/3$ and $G = 2.05$. Because most cathodes operate in a vacuum chamber with $P_b \sim 10^{-5}$ Torr or lower or in the vacuum of space, $P_0/P_b \gg G$.

For most cathodes, however, the continuum assumption in the orifice is not guaranteed to hold. The validity of this assumption can be estimated by computing the Knudsen number, Kn , in the orifice. The Knudsen number is given by:

$$\text{Kn} = \frac{\text{Ma}}{\text{Re}} \sqrt{\frac{\gamma\pi}{2}}, \quad (2.138)$$

where Re and Ma are the Reynolds and Mach numbers, respectively. To compute Kn , we assume that the flow is sonic in the orifice ($\text{Ma} = 1$). The dynamic viscosity for the Reynolds number is calculated using results from Stiel and Thodos [102] for xenon and argon. For mercury vapor, we use the Chapman-Enskog method applied to the Lennard-Jones 12-6 potential with $\sigma = 2.898 \text{ \AA}$ and $\epsilon/k_B = 851.0 \text{ K}$ [119]. This method produces good agreement with experimental data for temperatures less than 1000 K as shown in Figure 2.15. The values are computed using a set of experimental

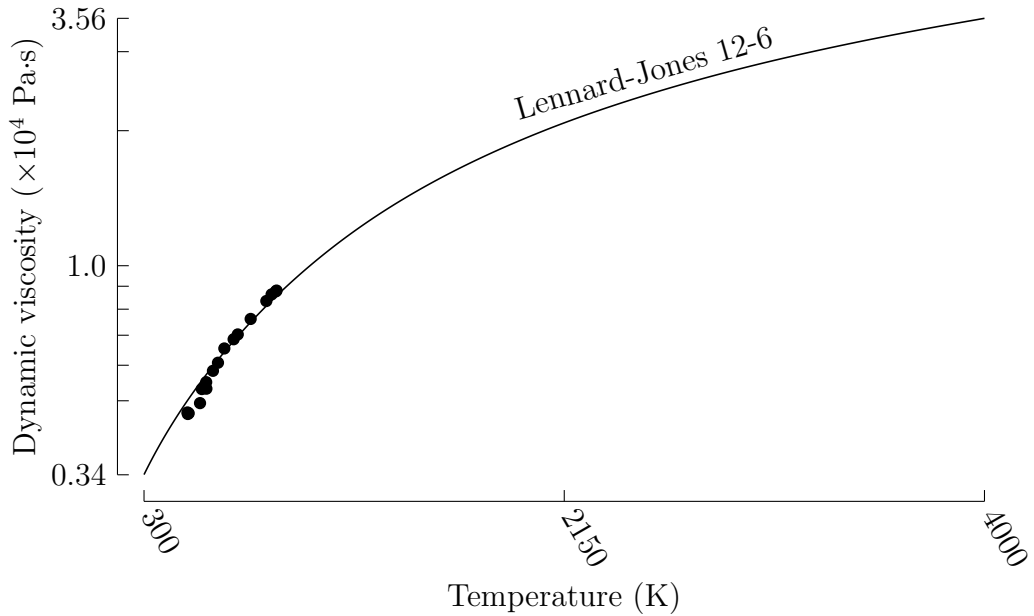


Figure 2.15: Viscosity of mercury vapor computed with the Chapman-Enskog method applied to a Lennard-Jones 12-6 potential. Experimental data from [119].

data from Siegfried and Wilbur's cathode operating on mercury [120] and argon and xenon [65], Friedly's cathode [112], Salhi's xenon and argon cathode [47], Domonkos's

SC012, EK6, and AR3 cathodes [64], the T6 cathode from the Royal Aerospace Establishment [113, 121], the NSTAR and NEXIS cathodes from the Jet Propulsion Laboratory (JPL) [105, 111, 115, 116, 122], and the JPL 1.5 cm cathode [29, 30]. The neutral gas temperature is estimated to be either three times the maximum insert wall temperature [42] (p.465), or 3000 K if wall temperature data is unavailable. Figure 2.16(a) shows the Knudsen number for these cathodes. In all cases, the Knudsen number is in the range $0.01 < \text{Kn} < 10.0$, which indicate that the flow is either in the transition regime from continuum to molecular fluid flow, or molecular.

Poiseuille flow Viscosity has been underlined as an important process for the flow dynamics inside the cathode in 2-D simulations [122]. Computed Reynolds numbers in Figure 2.16(b) indicate that the flow through the cathode is laminar ($\text{Re} \ll 1000$) and that viscous effects are indeed important ($0.1 < \text{Re} < 10$).

The assumptions of a Poiseuille flow seem to be valid in the upstream section of a cathode tube: the flow is incompressible, fully-developed, laminar, and with a no-slip condition at the wall. Poiseuille flow theory, however, is not applicable in the orifice region. In this region, the flow may be laminar and feature a no-slip condition at the wall. However, it becomes compressible and is not fully-developed. Poiseuille flow additionally assumes adiabatic flow, which is not valid in most regions of the cathode. Neglecting Joule heating in the flow is problematic because it prevents the model from capturing any effect of the discharge current. The flow transitions from a low Mach number in the insert region to a sonic condition at the orifice outlet and therefore shows strong compressibility effects. The length over which the flow travels before becoming fully-developed, or “entrance length”, L_{fd} , can be estimated with [123]:

$$L_{fd} \approx 0.06 \text{Re} d_o. \quad (2.139)$$

The range of ratio of L_{fd} to the orifice length L_o is shown in Figure 2.16(c) for various cathodes. For most cathodes the effect of the orifice constriction invalidates the fully-developed-flow assumption over the whole length of the orifice. The Poiseuille flow model also does not take into account plasma effects and therefore fails to capture the true dependency of the total pressure with species and discharge current. The discharge current can change the total pressure significantly, as shown in Figure 2.14(a) for the NEXIS cathode.

Other approaches More complicated theoretical models such as the one proposed by Domonkos in [64, 73] or Albertoni *et al.* in [49, 55] attempt to address some of the aforementioned issues. Domonkos suggests combining Poiseuille flow, a choked flow condition at the orifice outlet, and a correction that takes into account the insert-to-orifice constriction and transition to molecular flow. Albertoni *et al.* [49] introduce the effect of the plasma through the ionization fraction and electron temperature, which are computed as part of the 0-D model. The proposed relationship is used to compute the total static pressure and is valid at the orifice outlet where the author assumes choked flow. This model still relies on Domonkos’s modified Poiseuille flow model to predict the pressure drop across the orifice, and, therefore, suffers from the problems that are associated with the assumptions of a Poiseuille flow in the orifice section. Use of the Poiseuille flow model with choked flow as a downstream boundary condition may also be fundamentally inconsistent, as the average velocity calculated from the linearized pressure gradient is not necessarily equivalent to the (constant) sonic velocity. Without heat addition or viscous contributions, the velocity within the orifice should be assumed constant, as it is a function of only the channel size.

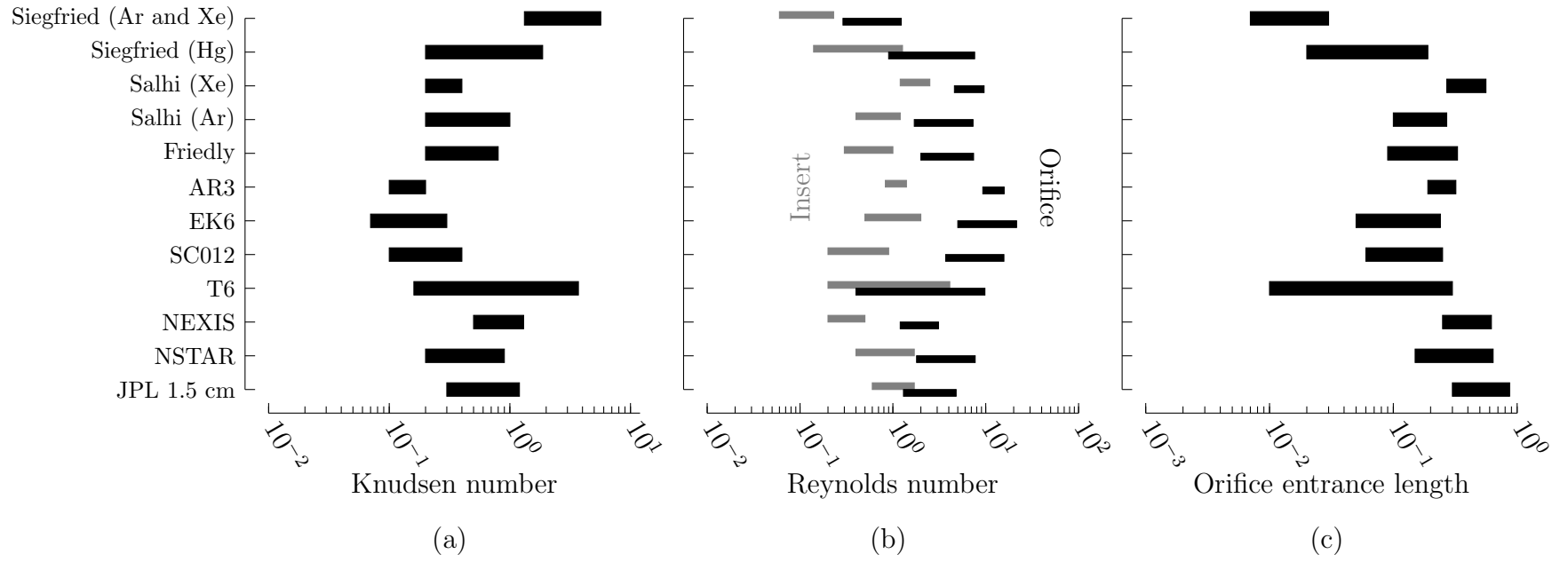


Figure 2.16: Orifice Knudsen number, range of Reynolds number for both insert and orifice, and orifice entrance length (as a fraction of total orifice length).

2.10.2 Flux calculations

The coefficients preceding flux terms in several of the model power balances are used inconsistently, the correct term scalings are given below.

Convection The $5/2T_{eV}I_d$ term that appears in the 0-D plasma volume power balances is a result of the integral form of the energy equation. As shown in Table 2.4, inappropriately rescaling this factor has a significant effect on model results. In steady-state, neglecting viscosity, kinetic-energy terms, and collisions, the energy equation simplifies to:

$$\nabla \cdot \left(\frac{5}{2}T_{eV}n_e e \mathbf{u}_e + \mathbf{q}_e \right) = -en_e \mathbf{E} \mathbf{u}_e, \quad (2.140)$$

where \mathbf{E} is the electric field, \mathbf{u}_e is electron fluid velocity, and \mathbf{q}_e is the heat flux. The first term on the left-hand side corresponds to the convection of energy at the fluid velocity. A direct integration of this term over a 0-D volume along with the application of Gauss's law yields the correct expression for the convected energy.

Random flux A derivation of the average energy of an electron leaving the volume to a surface may be found in [91], Appendix C in [42], or in [60]. The $2T_{eV}$ term stems from the assumed Maxwellian distribution crossing a surface. The average energy is higher than the average energy per particle in the volume because higher-energy particles escape the volume at a greater rate. The average energy is obtained by computing the ratio of the energy flux to the wall to the total particle flux. For a Maxwellian distribution, the total particle flux is given by:

$$\Gamma = \frac{n\bar{c}}{4}, \quad (2.141)$$

where \bar{c} is the distribution-averaged velocity. The energy flux is given by:

$$\Gamma_e = \frac{n\bar{c}}{4}2T_{eV}. \quad (2.142)$$

2.10.3 Sheath considerations

One of the primary reasons that the described models begin to lose accuracy outside of the domain of operating conditions for which they were developed is their handling of the sheath and plasma potential structure. The models generally choose from one of the following idealizations:

- a purely 0-D sheath (no variation in the electron density anywhere),
- a mostly 0-D model with a flat potential structure in the plasma bulk but where an attempt has been made to include some or all of the effects of the pre-sheath, or
- an ambipolar diffusion model.

Flat potential profile In all variants of Siegfried and Wilburs's model and in that of Capacci *et al.*, no attempt was made to account for the variation of plasma density induced by the sheath/pre-sheath. In accordance with a strict 0-D assumption, the plasma density and potential are assumed constant within the entire control volume. The only advantage of this approach is its simplicity. Because of the collisional nature of the plasma and the current densities present within the cathode, it is unlikely that all of the potential drop from the cathode centerline to the emitter surface would be translated into ion bombardment energy or emitted electron energy. This approach artificially decreases the backstreaming electron flux reaching the emitter surfaces, as shown in Figure 2.1, and this term is wrongfully neglected by the authors that use this type of sheath model. This model also causes the over-prediction of the plasma

potential, as the ion bombardment power must increase in order to provide sufficient heating to the insert for self-sustaining operation.

Flat potential profile with pre-sheath In the models of Domonkos and Albertoni *et al.*, the plasma potential is assumed to differ from the sheath potential by $T_e/2$, which is the potential drop due the Bohm condition at the sheath edge. The associated energy term is often neglected (therefore ϕ_s is essentially ϕ_p), with the primary contribution to the model being the modification of the plasma density used to calculate fluxes to the insert surface. This idealization does little to alleviate the issues of the purely 0-D sheath model described above.

Ambipolar diffusion model The model used by Goebel and Katz [42] includes density variation in the radial direction. It is the only implementation of a sheath voltage that is independent of the plasma potential. The diffusion equation solved, however, assumes no variation in the axial direction (consistent with the 0-D approach) and *zero* plasma density at the “wall” of the insert or orifice plasma region. This wall boundary condition is problematic. In this approach, the sheath is assumed to have zero thickness, and, therefore, the sheath edge coincides with the “wall” for the purposes of the ambipolar diffusion model. Depending on the channel geometry and pressure, it may be reasonable to assume that the plasma density is negligible at the sheath edge compared to the bulk plasma density, but for other conditions (especially small diameters and low pressures) this would introduce significant error. We discuss this in greater detail in Section 2.6. This model also leads to the over prediction of the electron temperature, which in turn affects the power balance used to calculate the sheath voltage. As mentioned in [92], this ambipolar diffusion model is also not appropriate for the orifice region plasma.

2.11 Summary

We have reviewed zero-dimensional orificed hollow cathode models developed in the past 40 years that are relevant for electric propulsion applications. Our intent is to provide critical information with regards to the validity and to the consequences of the assumptions made, and the range of applicability of each model. We performed term-by-term comparisons of the physical equations proposed when necessary, re-implemented the models when possible, and compared our implementation to the original authors' calculations. We applied the models to two different cathodes with available experimental data, and found that the models are generally unable to produce good agreement with experiment.

Common points of contention include the modeling of the ionized gas flow through the cathode and the orifice, the calculation of the convection losses, and the representation of the 0-D volume. We argue that the gas flow should be treated with either a general empirical relationship or a three-fluid model. We present calculations for the convection losses, and discuss the different approaches that were used to treat the radial variation of the plasma and sheath potentials inside the cathode. No rigorous treatment of the radial plasma variation has been proposed thus far, though this can be addressed with a combined ambipolar diffusion approach in the bulk plasma along with a sheath model for an emitting boundary.

Including a coupled thermal modelization of the cathode raises the total number of parameters that are required for a complete model. The combination of the plasma model with a thermal one therefore adds another layer of complexity that may hide the effect of underlying plasma processes. We argue that because the temperature gradient of the emitter is typically small [99] the assumption of constant emitter temperature is acceptable. Accurate sheath modeling should then capture the thermally-limited or space-charge-limited operation of the cathode and the corresponding fluxes of particles to the wall.

In the next chapters, we will address some of the shortcomings of the 0-D models that we have uncovered. We will present both an empirical approach and a rigorous fluid approach to the gas flow problem. Sheath modeling, however, is beyond the scope of this work.

Chapter 3

Experimental configuration and data analysis

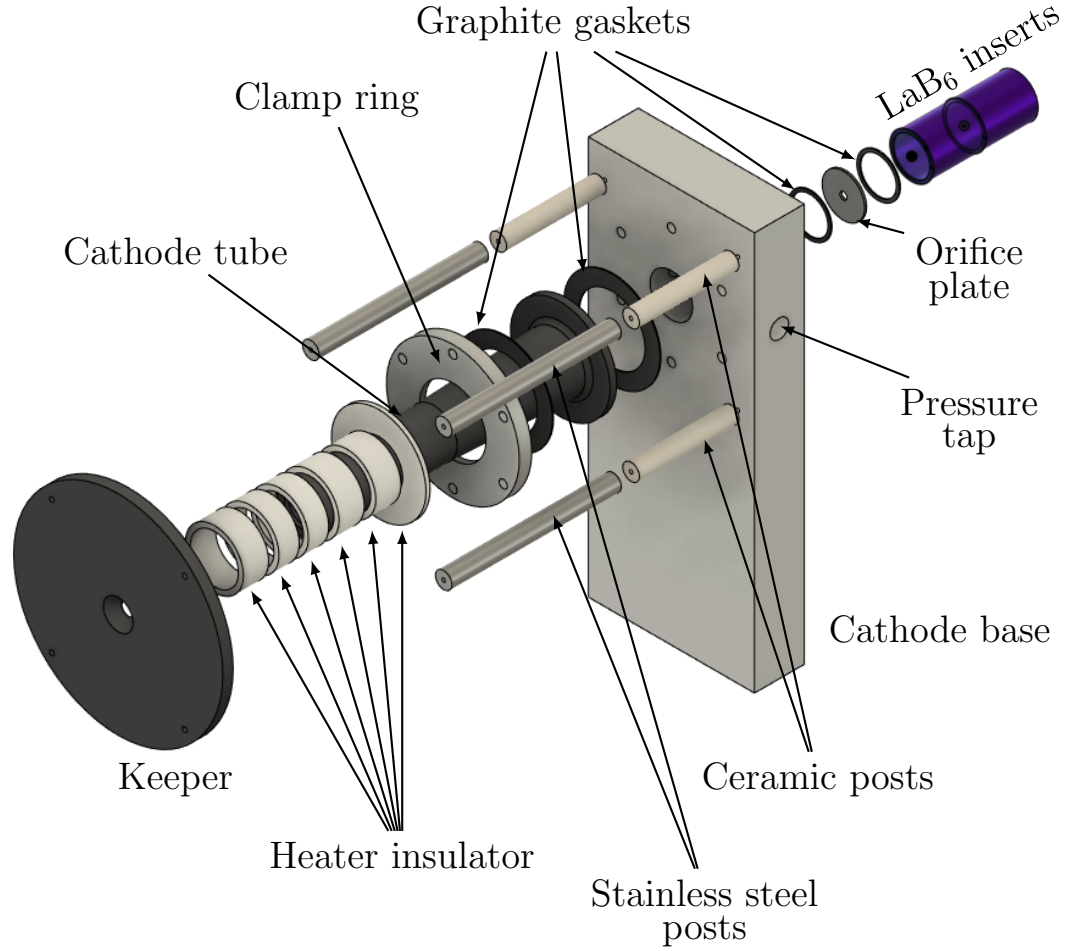
In this chapter, we introduce the experimental configuration to measure the total pressure in a high-discharge-current cathode. We also present the literature data we use in later chapters and the methodology utilized to analyze it.

3.1 Cathode configuration

The Princeton large hollow cathode (PLHC) is a 20 cm long (8-in.) cathode with an inner bore of 3.26 cm (1.284-in.). The cathode material is AXM-5Q POCO graphite. The PLHC features two 2.715 cm inner diameter, 4.02 cm long LaB_6 inserts for a total of 8.04 cm length. The insert is heated via an external graphite heater described in [32]. A heat shield made of multiple layers of 200 μm (0.008-in.) thick grafoil and of 50 μm (0.002-in.) thick molybdenum is used to reduce radiative heat loss. The cathode has a tungsten orifice plate that is 1.5 mm thick and that has a 5.6 mm (7/32-in.) diameter orifice. The cathode is mounted on a block of 253MA stainless steel and is held in place by a clamp ring of the same material. The clamp ring is fastened to the cathode base with 1/4-20 screws. Interfaces between materials are

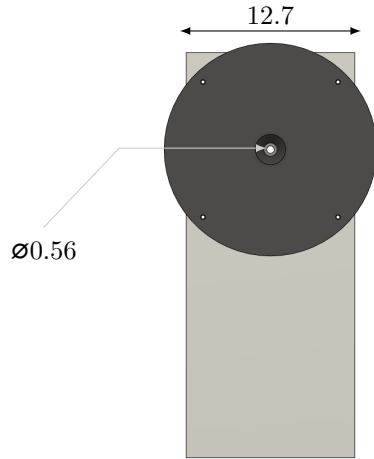
sealed with grafoil gaskets. In front of the cathode is a 6.35 mm (1/4-in.) thick graphite keeper plate with a 9.52 mm (3/8-in.) diameter orifice and a water-cooled, aluminum anode. The keeper plate is held in front of the cathode with a combination of stainless steel and ceramic posts. The keeper is attached to the stainless steel posts with 6/32 screws. The ceramic posts are fastened to the cathode base with 6/32 screws and to the stainless steel post with 6/32 threaded rods.

Gas is inserted in the cathode through a stainless steel Swagelok-to-NPT fitting mounted on the side of the cathode base. A pressure tap is drilled opposite to the gas inlet, in the cathode base. Both NPT connectors are sealed with an anti-seizing compound. The back of cathode base is sealed with a “diagnostics pod” (not used in this work) which is described in [124]. Figure 3.1 shows an exploded view of the cathode assembly (without fasteners) as rendered by a computer-aided design (CAD) software, along with a table showing the materials used for each component. A CAD drawing of the cathode without heater, heat shields, and fasteners can be found in Figure 3.2. A cutaway view is shown in Figure 3.3. A schematic of the experimental setup is shown in Figure 3.4. Figure 3.5(a) shows the physical implementation of the cathode, anode, and heater. The cathode with keeper and heat shielding installed is shown in Figure 3.5(b). Operation of the cathode on argon is shown in Figure 3.6.

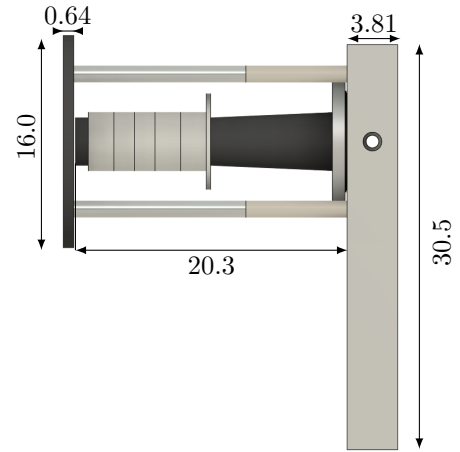


Component	Material
Cathode	AXM-5Q POCO graphite
Keeper	AXM-5Q POCO graphite
Keeper posts	Ceramic and stainless steel
Heater (not shown)	AXM-5Q POCO graphite
Heater electrical insulator	Boron nitride
Orifice plate	Tungsten
Gaskets	Grafoil (graphite)
Inserts	LaB ₆
Cathode base	Stainless steel 253MA
Clamp ring	Stainless steel 253MA

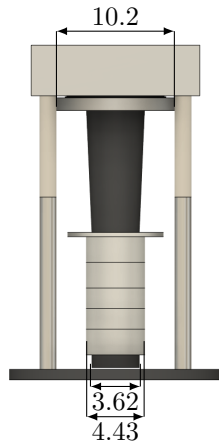
Figure 3.1: Exploded view of the cathode assembly without heater, fasteners, and heat shields.



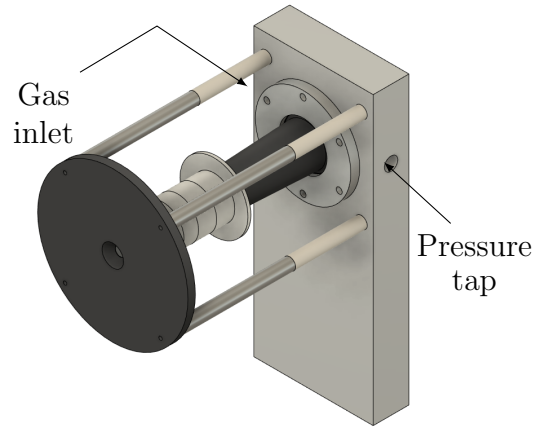
(a) Front view.



(b) Right view.



(c) Top view.



(d) Isometric view. The gas inlet (hidden in this view) is situated opposite of the pressure tap.

Figure 3.2: CAD rendering of the cathode without heater, fasteners, and heat shields. Dimensions are in cm.

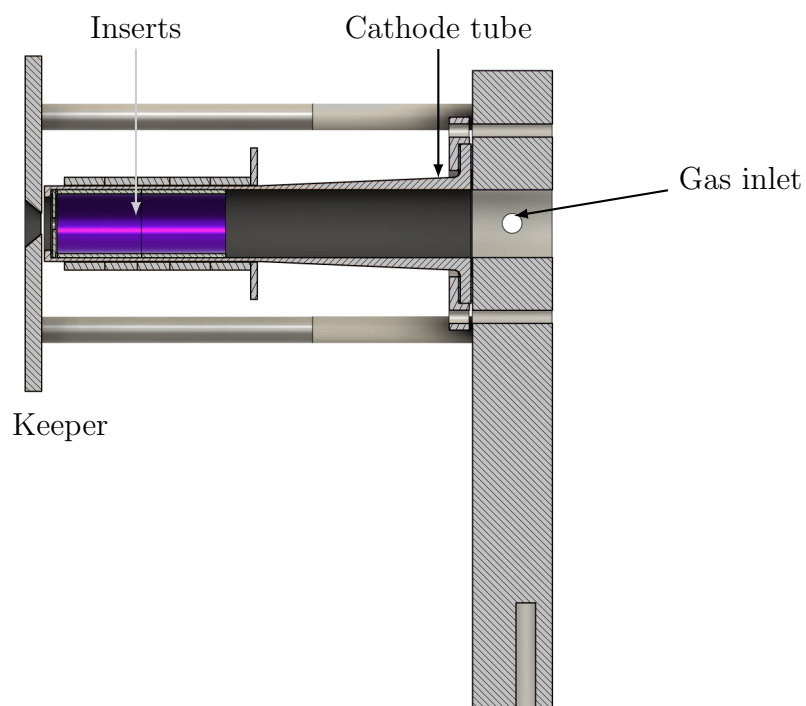


Figure 3.3: Cutaway view of the cathode assembly showing the location of the installed inserts and gas inlet.

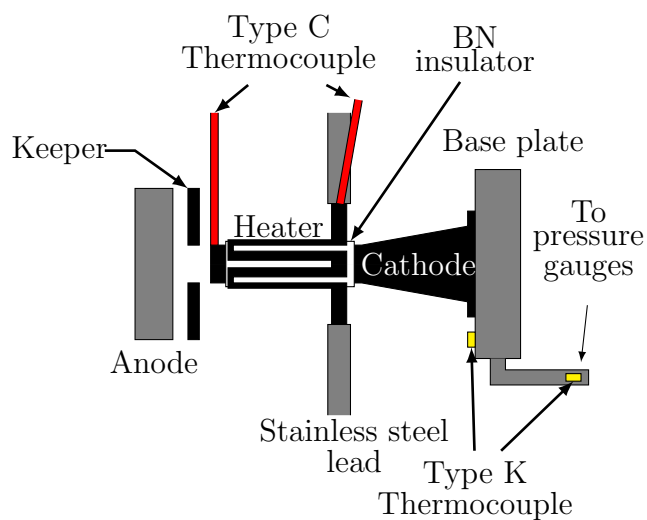
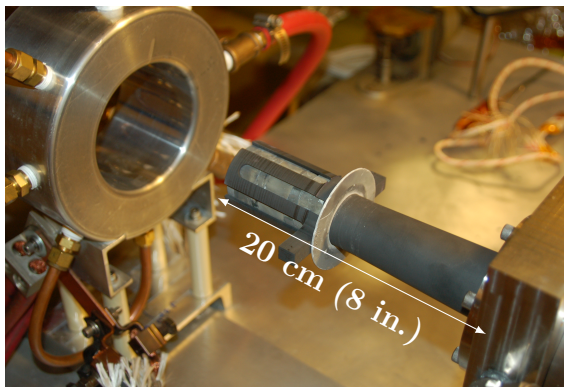


Figure 3.4: Schematic of the cathode apparatus (top view) showing the location of temperature measurements.



(a) Cathode without heat shield.



(b) Cathode with heat shield.

Figure 3.5: Princeton large hollow cathode.

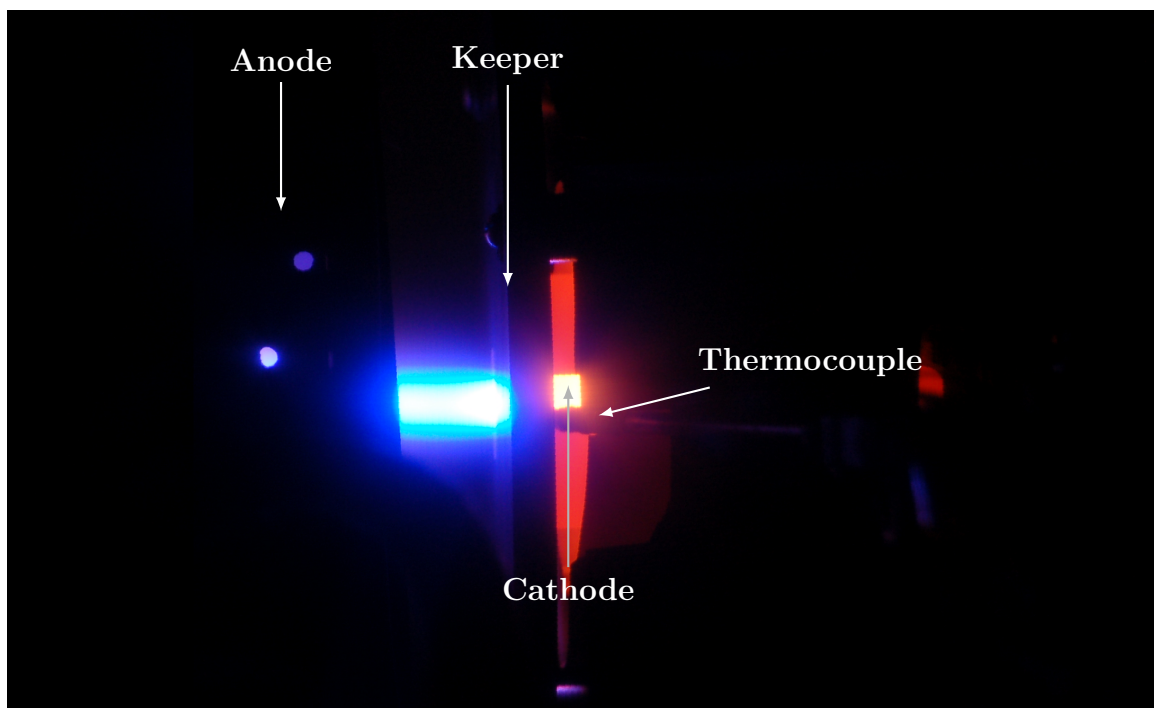


Figure 3.6: Cathode operating on argon at 300 A of discharge current.

3.2 Facilities

3.2.1 Vacuum and feed system

Vacuum system The cathode is installed in a 2 m diameter by 5 m long vacuum vessel (Figure 3.7) evacuated to less than 7×10^{-5} Torr without gas flow, or 2×10^{-4} Torr at the maximum tested flow rate (290 sccm of argon). The background pressure is monitored with an Alcatel ACC1009 pressure gauge. The vacuum cham-

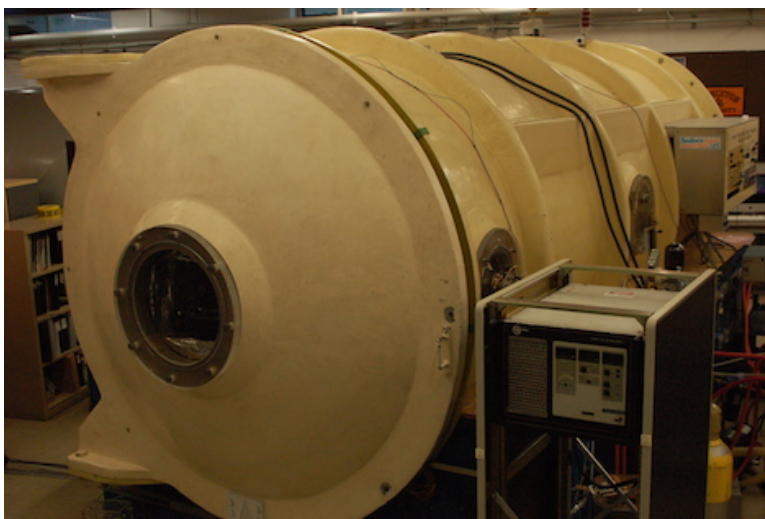


Figure 3.7: Vacuum vessel.

ber is evacuated to high vacuum with a pair of 48-in. CVC diffusion pumps operating with DC-704 diffusion oil. The diffusion pumps are backed by a Leybold-Heraeus air-cooled roots blower and two Stokes 212-H roughing pump. A diagram of the system is shown in Figure 3.8.

Feed system Gas is inserted into the cathode through an Omega FMA-A2304 mass flow controller calibrated for nitrogen with a mass flow ranging from 0 to 200 sccm of nitrogen gas (0–290 sccm of argon gas). The mass flow we report is taken from the controller digital display and corrected for the gas used.

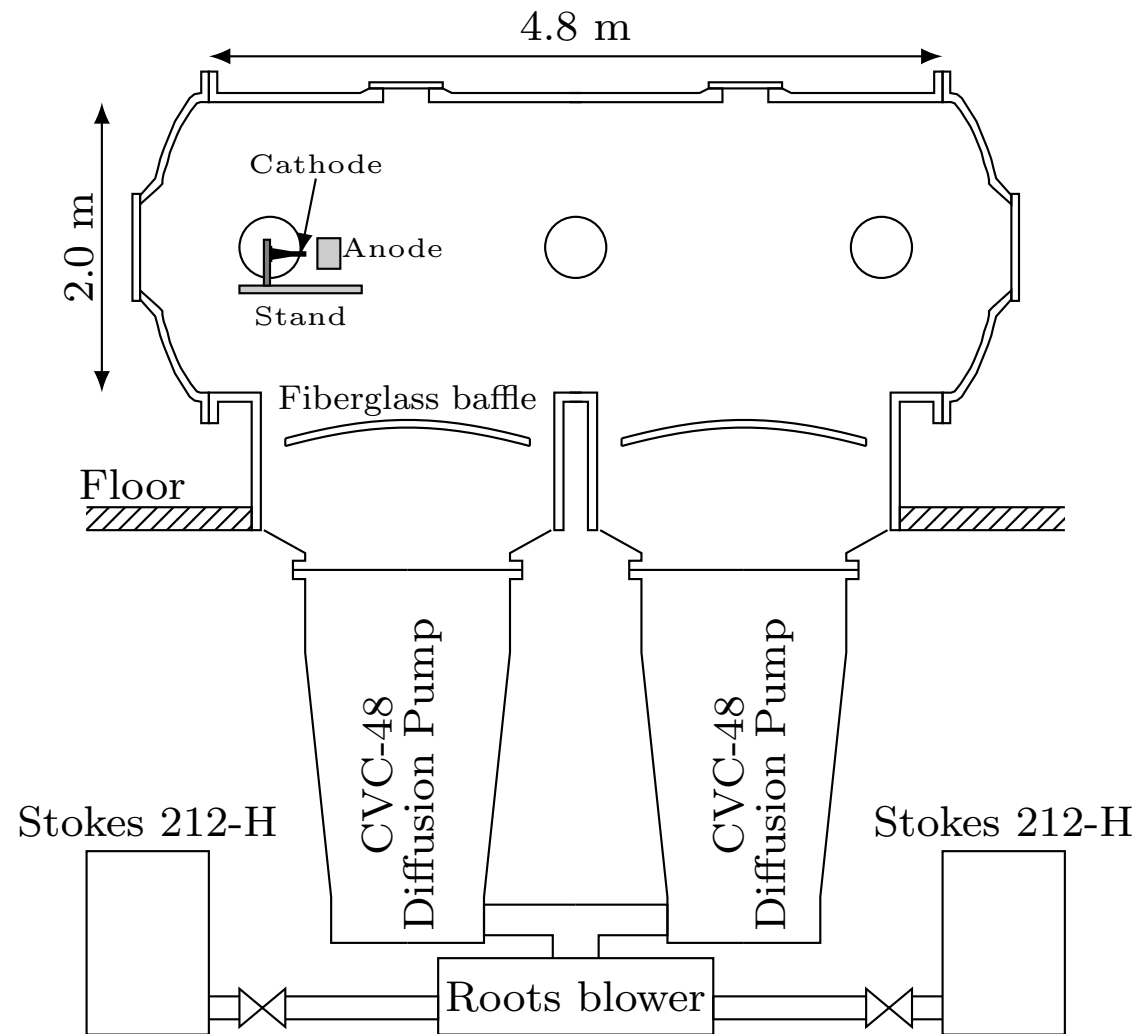


Figure 3.8: Diagram of the vacuum system, inspired by [125]. The pumping system is not to scale.

3.2.2 Electrical system

The graphite heater is powered by a 13.3 kW American Reliance power supply with a maximum output of 32 V or 400 A. In all of our experiments the cathode operates in triode mode (cathode, keeper, anode). The cathode discharge is sustained by a 30 kW Miller SRS-1000-C1 welding power supply configured for a maximum output of 150 V or 500 A. We can also configure the power supply for a maximum output of 80 V or 1,000 A. The total current from the power supply is controlled with a manual dial. An electrical diagram of the setup is shown in Figure 3.9.

The anode and keeper current are provided by the same power supply. Our heater is able to provide enough power to ensure that the ignition voltage falls below the maximum voltage of the 30 kW power supply. A $50\ \Omega$ ballast resistor is used upstream of the keeper to limit the total keeper current to 3 A.

The experimental circuit features current shunts R_c , R_a , R_k , and R_h that are used to measure the current flowing through the cathode, anode, keeper, and heater, respectively. The characteristics of the resistor shunts are shown in Table 3.1.

Table 3.1: Characteristics of the resistor shunts (without temperature derating).

Element	Rated current (A)	Voltage (mV)	Resistance ($m\Omega$)
Cathode*	400/1000	60/75	0.15/0.1875
Anode [†]	400	100	0.25
Heater	400	60	0.15
Keeper	10	100	10.0

* The 400 A cathode shunt is swapped for a 1 kA shunt for operation above 400 A.

[†] The anode shunt is removed for operation above 400 A.

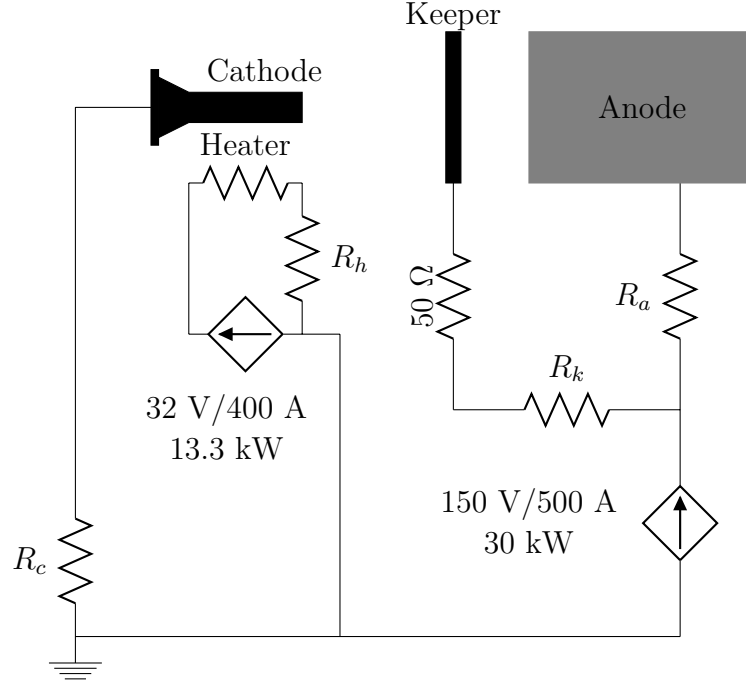


Figure 3.9: Electrical diagram of the experiment.

3.3 Measurement system

3.3.1 Pressure

We measure the total pressure upstream of the cathode with either a Posifa PVC1000 Pirani gauge or with an MKS 622C baratron gauge connected to the stainless steel support block through a 3/8-in. NPT fitting. The pressure tap is located approximately 22 cm (8.75 in.) from the upstream surface of the cathode orifice. The Baratron gauge is situated outside the vacuum tank, another 1.2 m away from the pressure tap.

The housing of the Pirani gauge is water-cooled to keep the gauge below its maximum operating temperature. The temperature of the housing of the Pirani gauge is measured with a K-type thermocouple. The Pirani gauge is powered by a custom-built ultra-precision constant-current power supply (6.7 mA). We show in Appendix E the electrical diagram of this power supply.

The Pirani gauge was calibrated to within ± 0.1 Torr for argon gas with a separate MKS baratron gauge. We calculate the pressure using the measured resistance of the MEMS gauge resistor, corrected for the change in temperature as compared to its calibration temperature ($T_c = 20^\circ\text{C}$). The calibration curve obtained is shown in Figure 3.10.

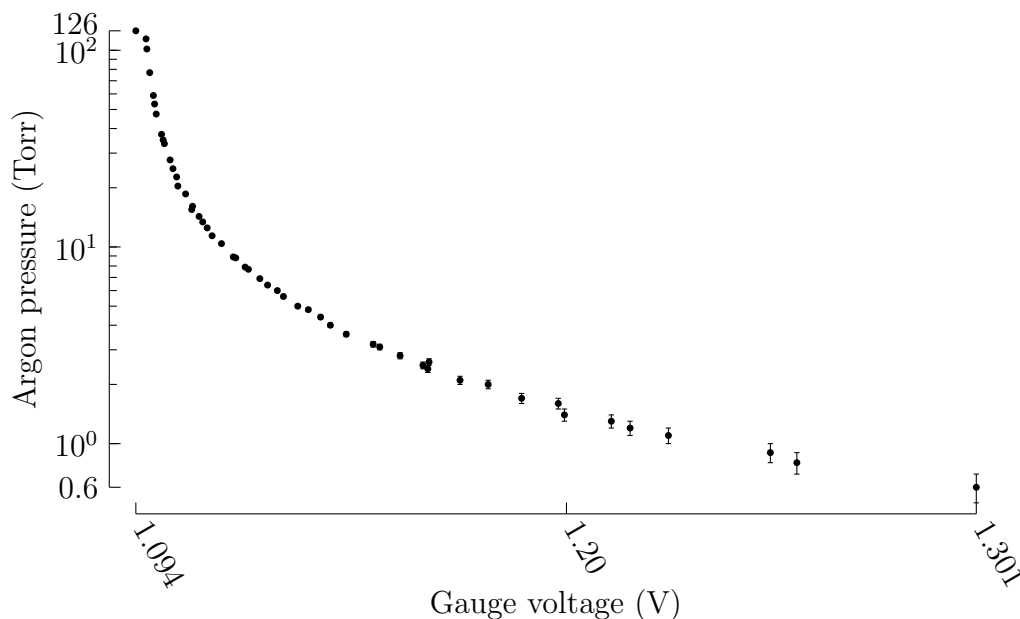


Figure 3.10: Calibration curve for the Pirani gauge.

3.3.2 Temperature

We measure during operation the temperature of the cathode tip and of one of the tabs of the heater with C-type thermocouples that are in direct contact with either surface. K-type thermocouples are used to evaluate the temperature of the stainless steel base and of the housing of the pressure gauge. The location of the temperature measurements is shown in Figure 3.4. The thermocouples are connected to a UWTC Omega wireless transmitter. Each wireless transmitter is powered by one of the galvanically-isolated output of a Voodoo Labs Pedal Power 2 Plus power sup-

ply modified to output 3.6 V. The transmitter data is received at a 1 Hz rate by a UWTC-REC1 Omega receiver connected via USB to a computer.

3.3.3 Data acquisition system

A National Instruments (NI) NI-9206 data acquisition system (DAQ) is used to perform differential voltage measurement across the pressure gauges and current shunts. The NI-9206 is attached to a NI-cDAQ 9274 chassis that is used to communicate via USB to a computer. The voltage difference across each current shunt is amplified by an AD623 instrumentation amplifier before being measured by the DAQ. Special care is taken for the high-side current shunts (keeper and anode); because the operating voltages of both the anode and keeper are higher than that tolerated by our DAQ, we isolate these measurements with an ACPL-790B isolation amplifier. We show in Appendix E the electronics implementation of the isolation and amplification system.

3.4 Additional dataset

We use the electron temperature and plasma density profiles measured for Siegfried's cathode operating with xenon [65], Salhi's cathode [47] operating on xenon at a mass flow rate of 0.5 equivalent-amperes, the NSTAR discharge cathode [111], the NEXIS discharge cathode [60,105], and the JPL 1.5 cm LaB₆ cathode [30]. The total pressure data we use for our empirical analysis and later comparisons are taken from Siegfried and Wilbur's mercury and noble gas cathodes [65,72,120,126], Friedly's cathode [112], Salhi's cathode [47] operating on both argon and xenon, the T6 cathode [113,121], Domonkos's cathodes (AR3, EK6, SC012) [64], the NSTAR discharge cathode [111, 116, 122], the NEXIS cathode [60, 105, 115], the JPL 1.5 cm LaB₆ cathode [29, 30], and our own cathode.

3.5 Data analysis

3.5.1 Attachment length

The experimental attachment length is derived from the measurement of the electron density profile. Because we define the attachment length as the length-scale of the exponential decay of the electron density upstream of the cathode orifice, we fit only the relevant portion of the experimental data with a decaying exponential. We show an example of this approach in Figure 3.11.

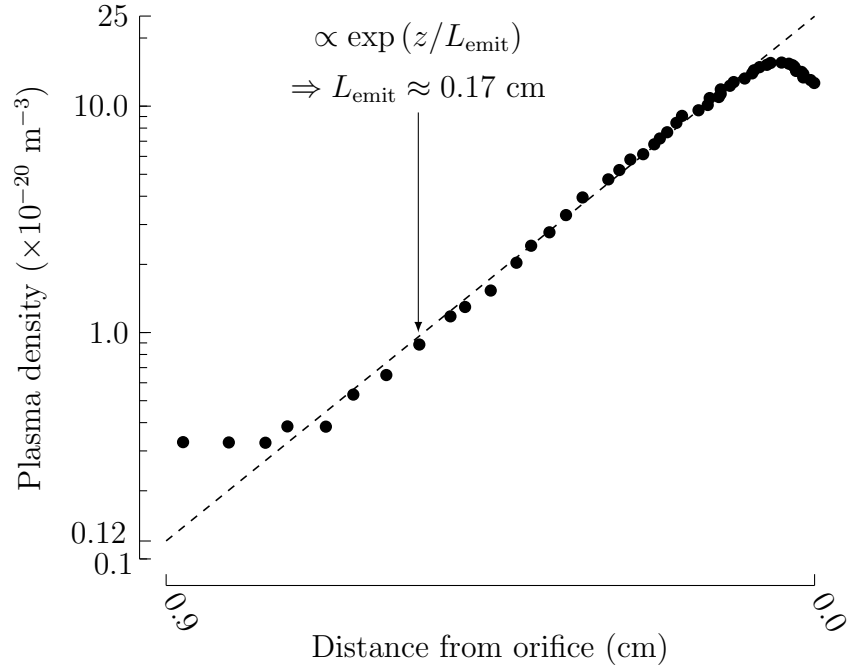


Figure 3.11: Example of the derivation of the attachment length from an electron density profile. Experimental data from [111] for the NSTAR discharge cathode operating at 15 A.

Error analysis The NSTAR, NEXIS, and JPL LaB₆ cathodes share the same experimental setup and diagnostics for which the error in the density measurement was reported [107] to be $\pm 40\%$ ($\sigma_n^2 = 0.04$). For the density measurements taken by Salhi, no experimental uncertainty was reported so we assume the same value of $\pm 40\%$. The error inherent in performing the various steps of the linear regression on the logarithm

of the density must also be estimated to obtain a confidence interval for the derived attachment length. If the density at a given point has a variance of $\bar{n}_e^2 \sigma_n^2$ (where \bar{n}_e is the average density at that point) then its logarithm $Y = \ln n_e$ has a variance of σ_n^2 . We derive this property in Appendix F. For the linear fit of $\ln n_e$ with parameters $\hat{\beta}_0$ and $\hat{\beta}_1$, we have:

$$\hat{Y} = \hat{\beta}_0 + \hat{\beta}_1 \bar{z}. \quad (3.1)$$

The inverse of $\hat{\beta}_1$ is the normalized emission length. The standard error of the slope is [127]:

$$\sigma_\beta^2 = \frac{\sigma_n^2}{\sum_{i=1}^N (\bar{z}_i - \hat{z})^2}, \quad (3.2)$$

where \hat{z} is the average distance from the orifice inlet. If we now assume that $\hat{\beta}_1$ is also normally distributed about the value calculated using the regression procedure, then the emission length has a variance (to first order) of:

$$\sigma_L^2 = \frac{\sigma_\beta^2}{\hat{\beta}_1^2}. \quad (3.3)$$

We also give the derivation for the variance of the inverse of a normally distributed random variable in Appendix F.

3.5.2 Electron temperature

The electron temperature is typically measured as a function of position in the insert region. Because the electron temperature typically varies gradually upstream of the cathode orifice, we use the axial line-average of the experimental data over the entire cathode insert region to obtain a single experimental value. We take the uncertainty of the electron temperature measurements to be ± 0.5 eV, as reported in [107], unless otherwise specified.

3.5.3 Pressure

Pirani gauge resistance Because the resistance of the Pirani gauge varies with operating temperature, it is necessary to adjust the measured voltage V_m for the temperature-induced change in resistance. The measured voltage is given by:

$$V_m = R_{\text{gauge}}(P) I_{dc}, \quad (3.4)$$

where $I_{dc} = 6.667$ mA is the applied current to the gauge. The resistance of the gauge, R_{gauge} , depends on temperature:

$$R_{\text{gauge}} = R_{\text{nom}}(P) (1 + T_{CR} \Delta T), \quad (3.5)$$

where R_{nom} is the nominal resistance at the calibration temperature and given pressure P . ΔT is the temperature change from the calibrated temperature. T_{CR} is the temperature coefficient for the Pirani gauge resistor. We obtain this value from the datasheet for the PVC1000 [128]: $T_{CR} = 0.0025$ 1/K. Using Equation 3.5 in Equation 3.4 gives:

$$V_c(P) = \frac{V_m}{(1 + T_{CR} \Delta T)}, \quad (3.6)$$

where V_c is the calibration voltage: $V_c = R_{\text{nom}} I_{dc}$.

Error analysis We compute ΔT as the average over the time period considered. The standard error of the mean of ΔT , $\epsilon_{\Delta T}$, is used to estimate the error on the pressure:

$$\epsilon_{\Delta T} = \frac{1.96 \sigma_{\Delta T}}{\sqrt{N_{\Delta T}}}, \quad (3.7)$$

where $\sigma_{\Delta T}$ is the standard deviation of the temperature change and $N_{\Delta T}$ the total number of samples. To estimate the error, we first compute the upper and lower

bounds of the temperature change,

$$\Delta T^+ = \Delta T + \epsilon_{\Delta T}, \text{ and} \quad (3.8)$$

$$\Delta T^- = \Delta T - \epsilon_{\Delta T}, \quad (3.9)$$

and use the calibration table to find the upper and lower bounds of the total pressure. If the error is above $\pm 15\%$ we reject the measurement. We note that Equation 3.7 is limited to normally-distributed data. While ΔT may not be normally-distributed, this approach gives us an estimate of the error in pressure.

3.6 Total pressure measurements

Figure 3.12 shows pressure measurements we performed with and without the cathode discharge. Without a plasma, the pressure increases linearly with mass flow rate as is expected from a choked orifice. During operation the pressure increases both with mass flow rate and discharge current, a behavior similar to other cathodes [112, 113, 115]. Measurements performed with the baratron gauge are much more precise than those of the Pirani gauge. This is likely due to the error in the measurement of the temperature of the Pirani gauge.

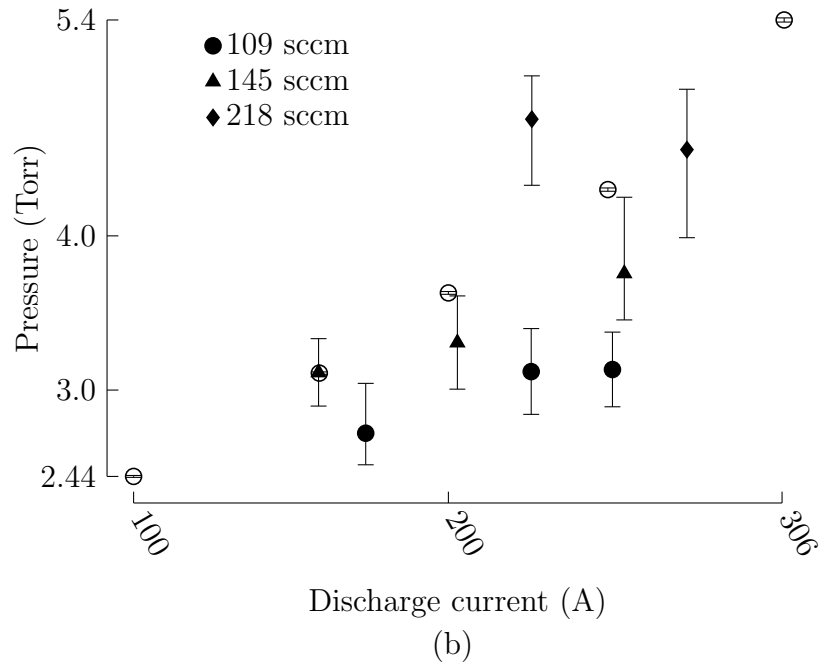
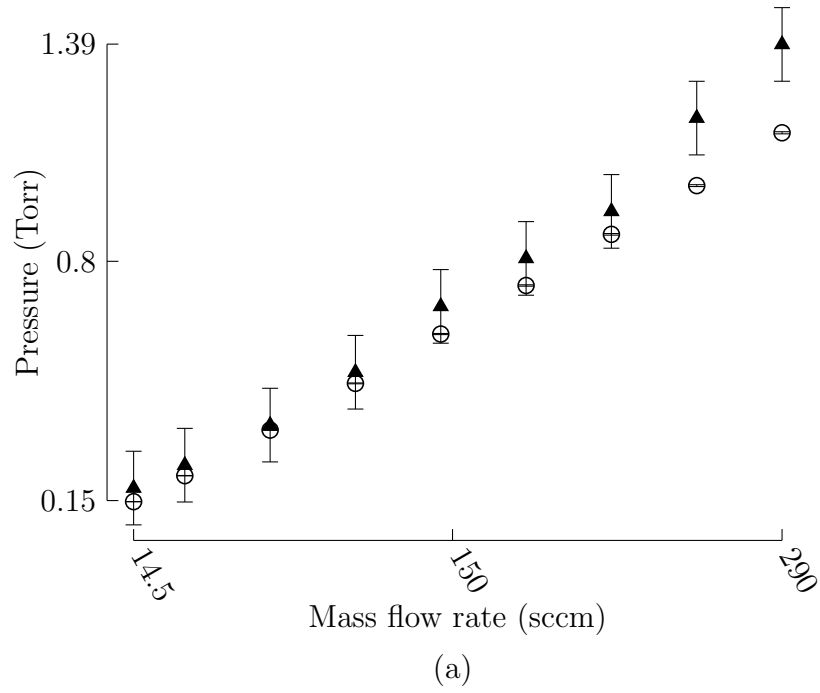


Figure 3.12: Total pressure measurements: (a) with cold gas only (300 K); (b) during cathode operation with argon. Filled and empty markers indicate measurements made with the Pirani and Baratron gauge, respectively.

Chapter 4

Empirical analysis of the total pressure¹

The neutral gas pressure P_n in the cathode affects predicted physical quantities such as the electron temperature and the ratio of sheath-edge plasma density to the average plasma density. The neutral gas pressure can be estimated in both the cathode insert and in the orifice regions from the total pressure and ionization fraction. In this chapter, we only investigate the former.

An analytical description of the flow physics inside the hollow cathode is challenging. The flow features heat addition from Joule heating in the orifice, frozen flow and wall losses due to ionization and plasma sheath fluxes, a transition from incompressible to sonic flow over the length of a short orifice, viscous effects, and a transition to molecular flow. In this chapter, we propose an empirical approach to calculate the total static pressure inside orificed hollow cathodes and to guide the analytical work of the following chapter. We gather experimental data, analyze it using dimensional analysis, and propose a power law for the cathode internal pressure as a function of

¹This chapter is based on work presented in [54]: Taunay, P.-Y. C. R., Wordingham, C. J., and Choueiri, E. Y., “An Empirical Scaling Relationship for the Total Pressure in Hollow Cathodes,” *AIAA Propulsion and Energy Forum*, 2018, AIAA-2018-4428.

the resulting non-dimensional parameters. We compare the empirical relationship to experimental data and perform a statistical analysis to extract the most pertinent non-dimensional variables. We finally discuss their relevance.

4.1 Π -products

Based on observation of the experimental data, we expect the cathode pressure to exhibit dependence on geometry, mass flow rate, discharge current, gas species, gas temperature, and viscosity. We therefore consider a general expression for the pressure in the insert region,

$$P = f(d_o, d_c, L_o, \dot{m}, I_d, M, a, \epsilon_{iz}, \mu, \mu_0), \quad (4.1)$$

where d_o and d_c are the orifice and insert diameters, respectively, L_o the orifice length, I_d the discharge current, \dot{m} the mass flow rate in kg/s, M the atomic mass of the propellant considered, a the speed of sound of the gas of interest, ϵ_{iz} the ionization energy of the species considered in eV, μ the dynamic viscosity in Pa·s, and μ_0 the permeability of vacuum.

There are four physical dimensions (mass, length, time, charge) and 11 parameters. The Buckingham Π theorem [129] indicates that there should be 7 non-dimensional Π -products. We use Ipsen's method [130] to find the Π -products by successively eliminating physical dimensions from Equation 4.1. As opposed to the previous empirical studies [72, 112], the total pressure is not normalized by the gasdynamic pressure ($\sim \dot{m}a/d_o^2$) but by the magnetic pressure ($\sim \mu_0 I_d^2/d_o^2$). Better agreement to a power law fit is obtained using this approach, especially for cathodes operating at higher

discharge currents or lower mass flow rates. We consider the following Π -products:

$$\Pi_1 = \frac{P}{P_{mag}}, \quad (4.2)$$

$$\Pi_2 = \frac{d_o}{d_c}, \quad (4.3)$$

$$\Pi_3 = \frac{d_o}{L_o}, \quad (4.4)$$

$$\Pi_4 = \left(\frac{\dot{m}e}{MI_d} \right)^2 \left(\frac{Md_o}{\mu_0 e^2} \right), \quad (4.5)$$

$$\Pi_5 = \frac{P_{gd}}{P_{mag}}, \quad (4.6)$$

$$\Pi_6 = \left(\frac{P_{\text{ionization}}}{P_{mag}} \right) \left(\frac{L_o}{d_o} \right), \text{ and} \quad (4.7)$$

$$\Pi_7 = \text{Re}, \quad (4.8)$$

where we defined the magnetic pressure, gasdynamic pressure, and ionization pressure as:

$$P_{mag} = \frac{\mu_0 I_d^2}{\pi^2 d_o^2}, \quad (4.9)$$

$$P_{gd} = \frac{4\dot{m}a}{\pi d_o^2}, \text{ and} \quad (4.10)$$

$$P_{\text{ionization}} = \frac{4e\epsilon_{iz}}{\pi d_o^2 L_o}, \quad (4.11)$$

respectively. The derivation of Π -products is shown in Appendix A. We recognize the ratio of total pressure to magnetic pressure in the orifice as the first Π -product. The second and third are geometric aspect ratios. The term $(\dot{m}e/MI_d)$ in the fourth Π -product is the total mass flux divided by the flux of ionized particles. It is related to the ionization fraction. The second half of Π_4 is a function of both mass and orifice diameter, and involves both geometry and gas species. The fifth Π -product is the ratio of gasdynamic to magnetic pressures. The numerator of Π_6 is the ionization

energy density inside the orifice. It is multiplied by the inverse of Π_3 . The seventh Π -product is the Reynolds number and accounts for viscosity effects.

Neutral gas temperature

The neutral gas temperature is necessary to calculate the fluid speed of sound that appears in P_{gd} . It is estimated to be 3 times that of the insert wall temperature, T_c , as suggested in [42] (p.465). For each cathode, we first seek an estimate of the wall temperature based on the available data. For the NSTAR and NEXIS cathodes experimental and numerical fits for the wall temperature in Kelvin are given in [131] and [42] (p.301) as:

$$T_{\text{NSTAR}} [\text{K}] = 1191.6 I_d^{0.0988}, \text{ and} \quad (4.12)$$

$$T_{\text{NEXIS}} [\text{K}] = 1370 + 3.971 \times 10^{-7} I_d^6, \quad (4.13)$$

respectively. Orifice plate temperature is reported in [30] as a function of both mass flow rate and discharge current for the JPL 1.5 cm cathode. A linear fit captures the variation of the data:

$$T_{\text{JPL 1.5 cm}} [^\circ\text{C}] = 1144 + 5.56 I_d. \quad (4.14)$$

We use this fit for the cases reported in [29] as the cathode is identical. Because the geometry of the AR3, EK6, and SC012 cathodes from [64] are similar, we simply use the average value of the available temperature data when no data is available. A similar procedure is performed for Salhi's cathode [47] and Siegfried's cathode operating with noble gases [65], where care is taken to separate the cases with different

orifice sizes and different operating gas:

$$T_{\text{AR3, EK6, SC012}} = 979.7^\circ\text{C}, \quad (4.15)$$

$$T_{\text{Salhi (Ar), } d_o=0.76\text{mm}} = 891.2^\circ\text{C}, \quad (4.16)$$

$$T_{\text{Salhi (Ar), } d_o=1.21\text{mm}} = 998.8^\circ\text{C}, \quad (4.17)$$

$$T_{\text{Salhi (Xe)}} = 991.0^\circ\text{C}, \text{ and} \quad (4.18)$$

$$T_{\text{Siegfried (Xe)}} = 1097.2^\circ\text{C}. \quad (4.19)$$

If no data are available (as is the case of the T6 and our cathode), the temperature is estimated to be that which yields the total discharge current through thermionic emission:

$$I_d = D_{RD} T_c^2 \exp\left(\frac{-e\phi_w}{k_B T_c}\right) 2\pi r_c L_{\text{emit}}, \quad (4.20)$$

where r_c is the insert radius, and L_{emit} is the attachment length. The emission length may be estimated as the insert radius: $L_{\text{emit}} \approx r_c$. The work function and Richardson-Dushman constant are given in Table 1.1.

4.2 Qualitative evidence of a simple scaling relationship

4.2.1 Correlation heatmap

Figure 4.1 shows a heatmap of the correlation matrix of all Π -products. Π_5 , Π_6 , and Π_7 seem to be strongly correlated to Π_1 . Because Π_4 , Π_6 , and Π_7 are only strongly correlated to Π_5 , there may be a combination of those Π -products that reduces to a single relevant independent variable. Because Π_2 and Π_3 only seem correlated to one another, they may also be combined into a single independent variable. This

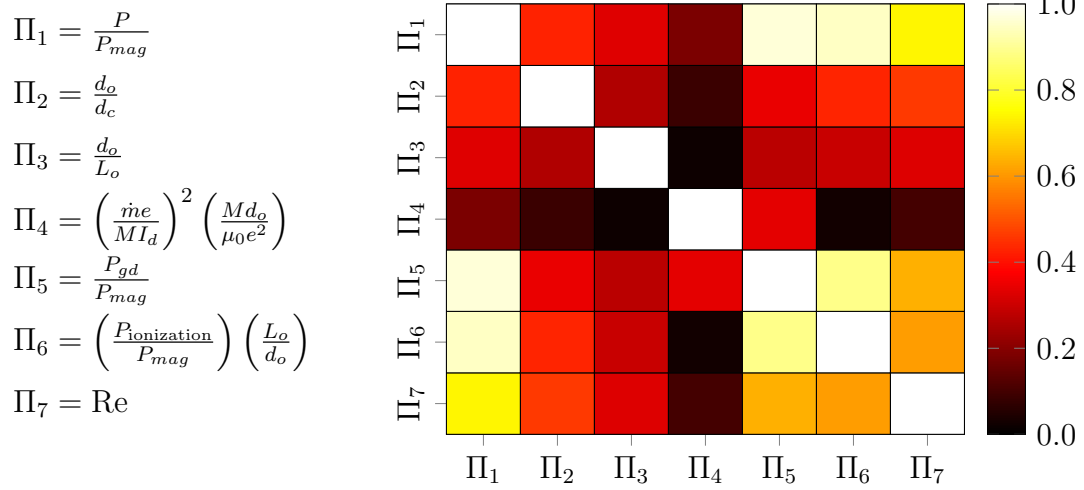


Figure 4.1: Correlation matrix of the Π -products.

analysis indicates that there may be only three relevant independent variables (Π_1 , the combination of Π_4 through Π_7 , and the combination of Π_2 and Π_3).

4.2.2 Principal component analysis

The goal of the Principal Component Analysis (PCA) is to determine the number of relevant variables. PCA calculations are performed with the `scikit-learn` API [132]. Figure 4.2 shows the explained variance as a function of the total number of variables considered. With a single variable the dataset has an explained variance of 0.825, which indicates that it is enough to explain most of the variation. The variance ceases to increase for three or more dimensions which indicates that the total pressure Π -product is not a strong function of three of the other Π -products.

4.2.3 Manifold learning approach

While some of the Π -products clearly show strong correlations (*e.g.*, Π_1 and Π_5) the visualization of the entire dataset is challenging. “Manifold learning” can be used to reduce the dimensionality of a dataset and help with visualization. Qualitatively, this

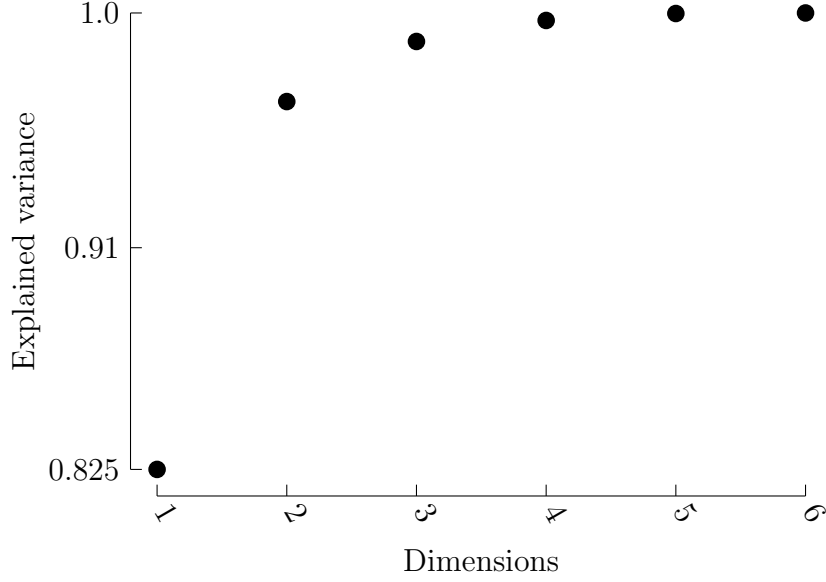


Figure 4.2: Explained variance for the dataset.

technique unfolds the N-dimensional surface on which the dataset exists and projects it onto either a 3-D volume or 2-D plane through a non-linear transform.

We use the Local Linear Embedding (LLE) [133] implemented in the Python library `scikit-learn` [132] to find a simple projection of the 7-D dataset onto a 2-D plane. The LLE seeks to conserve the distance between points that are neighbors in the original dataset. Figure 4.3 shows the results of the embedding as applied to the dataset, with the color map corresponding the logarithm of Π_4 . The LLE is calculated with $k = 14$ neighbors with a reported reconstruction error of 7.3×10^{-7} . Although the embedding cannot be used to retrieve the original relationship between the Π -products, the collapse of the dataset on a 2-D curve with regular coloring by Π_4 indicates that the inherent dimensionality of the dataset is 2.

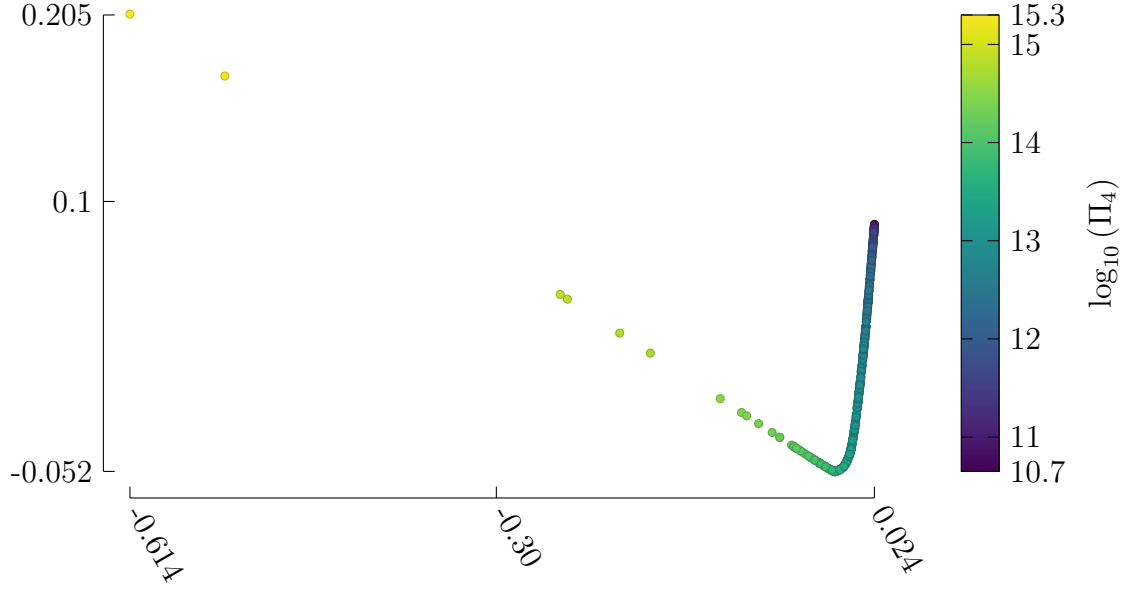


Figure 4.3: Local Linear Embedding applied to the Π -products.

4.3 Power law approach

The Π -products are assumed to have a power law dependency:

$$\Pi_1 = C \prod_{k=2}^7 \Pi_k^{\beta_{k-1}} = \Gamma(\Pi), \quad (4.21)$$

where C is a scaling constant, and the β_{k-1} are exponents to be determined. After applying the logarithm base 10 to both sides of Equation 4.21, we obtain a linear relationship:

$$Y = \beta_0 + \sum_{k=2}^7 \beta_{k-1} X_k, \quad (4.22)$$

where $Y = \log_{10} \Pi_1$, $X_k = \log_{10} \Pi_k$, and $\beta_0 = \log_{10} C$. Equation 4.22 is a linear regression which we fit using a least-squares approach. The least-squares fit yields $\beta = (7.06, 0.79, 0.23, -0.27, 0.82, 0.25, 0.41)$. The corresponding constant for the power law is $C = 1.16 \times 10^7$.

Qualitative analysis The power law fit applied to the experimental data is shown in Figures 4.4(a–c) for the full data set. The data collapse onto a single line, indicating

good agreement with the proposed empirical relationship over a range of five orders of magnitude. Based on the grouping of data by cathode in Figure 4.4(b) and by value of Π_5 in Figure 4.4(c) we can see that as the ratio of the gasdynamic to the magnetic pressure is decreased the data points cluster at the origin of the plot. At the opposite end of the curve, data points corresponding to cathodes with high values of Π_5 are clustered. The cathodes that operate at high current (PLHC, Friedly's cathode, NEXIS) feature a larger magnetic pressure contribution to the total pressure than those that operate at low current (AR3, EK6, SC012). Because the NSTAR, T6, and Salhi's and Siegfried's cathodes have similar dimensions, there is an accumulation of data points at the center of plot.

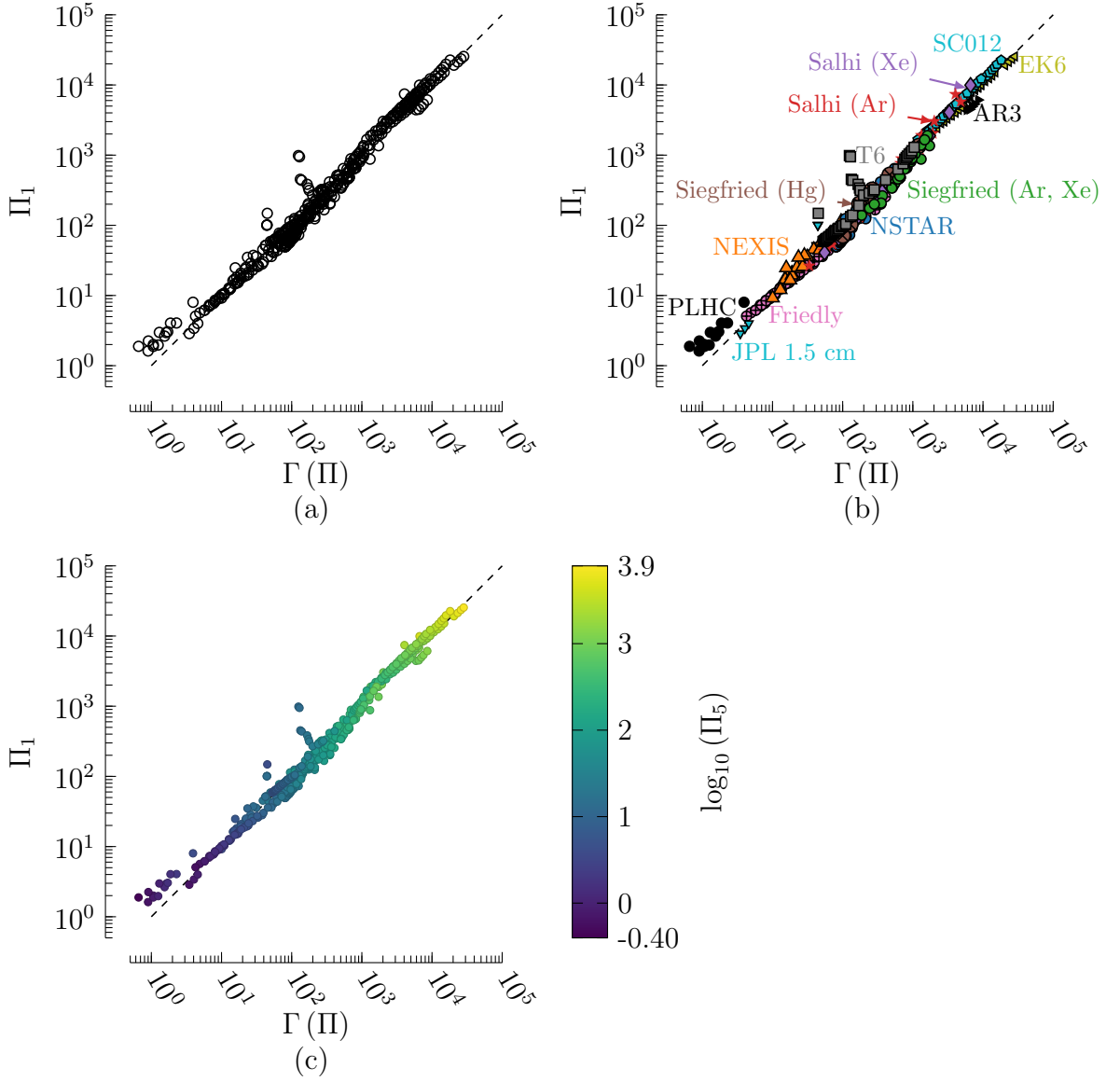


Figure 4.4: Proposed power law (Equation 4.21) applied to the entire data set: $\Gamma(\Pi) = 1.2 \times 10^7 \Pi_2^{0.79} \Pi_3^{0.23} \Pi_4^{-0.27} \Pi_5^{0.82} \Pi_6^{0.25} \Pi_7^{0.41}$. Data from [111, 116, 122] for the NSTAR cathode, [60, 105, 111, 115] for the NEXIS cathode, [47] for Salhi's cathode, [64] for the AR3, EK6, and SC012, [112] for Friedly's cathode, [113, 121] for the T6 cathode, [65, 72, 120, 126] for Siegfried's cathode, and [29, 30] for the JPL 1.5 cm cathode.

Comparison to theoretical models The obtained R-squared and average error for the least-squares fit are equal to 0.98 and 22.7%, respectively. Figure 4.5 shows the error distribution. It indicates that the proposed data fit is mostly within a factor of 1.3 of the experimental data. The aforementioned error analysis can be repeated

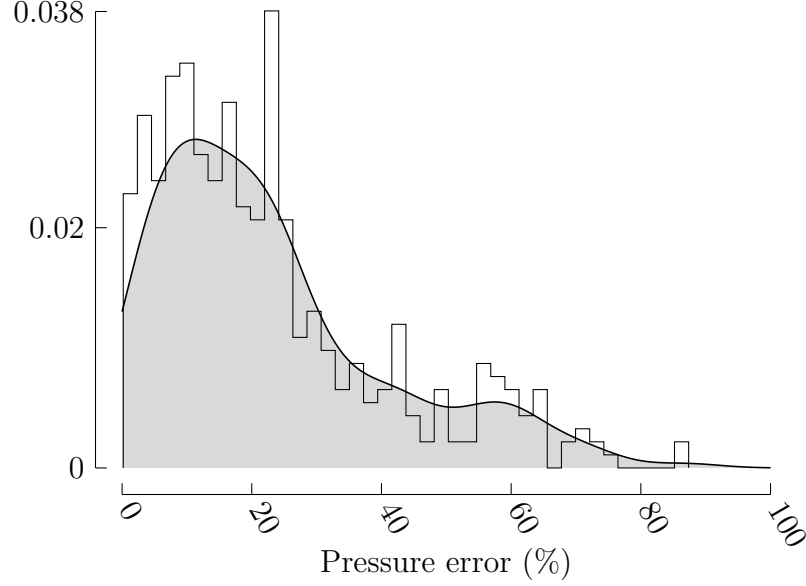


Figure 4.5: Error histogram for the proposed fit (Equation 4.21).

for the isentropic and Poiseuille flow models, as both can be expressed directly in terms of the derived Π -products. The pressure as calculated from an isentropic flow and Poiseuille flow approach depends only on Π_5 , and Π_3 , Π_5 , and Π_7 , respectively:

$$\Pi_1 = C_{\text{iso}} \Pi_5, \quad (4.23)$$

$$\Pi_1 = C_{\text{Poiseuille}} \Pi_3^{-1/2} \Pi_5 \Pi_7^{-1/2}. \quad (4.24)$$

The constants C_{iso} and $C_{\text{Poiseuille}}$ are the respective scaling constants:

$$C_{\text{iso}} = \frac{1}{\gamma} \left(\frac{\gamma + 1}{2} \right)^{(\gamma+1)/(\gamma-1)}, \quad (4.25)$$

$$C_{\text{Poiseuille}} = 4\gamma^{-1/2}. \quad (4.26)$$

Neither approach include a dependency on the plasma quantities and therefore discharge current. The corresponding R-squared value and average errors are shown in Table 4.1. The high values for the R-squared and average error for both the isentropic and Poiseuille flow models indicate that they are not adequate in capturing the variation of the total pressure inside hollow cathodes.

Table 4.1: R-squared value and average error for the studied flow models and empirical relationship.

Flow model or empirical relationship	R^2	Average error (%)
Isentropic	0.82	47.1
Poiseuille	0.82	57.4
Power law	0.98	22.7

4.4 Randomized selection

The randomized selection test consists in rearranging the samples of one Π -product at a time at random, performing a linear regression (Equation 4.22), and calculating both the R-squared value and average error. The randomization of a superfluous Π -product has little to no effect on these metric. The process is repeated 1,000 times to generate statistically significant numbers. The corresponding R-squared and average error resulting from this operation is shown in Table 4.2. We observe that the randomization of Π_3 and Π_6 has the smallest effect on the overall fit. The process can be repeated once these products are discarded. We find that both Π_2 and Π_7 have the next lowest effect on the fit during the second iteration and can also be removed from the fit without introducing large errors. The products that remain are Π_4 and Π_5 , which were shown to be qualitatively important on the correlation map, the LLE, and Figure 4.4(c).

Table 4.2: R-squared value and average error for the linear fit with a randomized Π -product. The data for the unperturbed fit is shown on the “Reference” line.

Perturbed Π -product	Iteration 1		Iteration 2	
	R-squared	Average error (%)	R-squared	Average error (%)
2	0.965	30.0	0.965	29.8
3	0.978	23.6	–	–
4	0.978	24.0	0.936	45.3
5	0.978	24.5	0.482	709.
6	0.979	22.4	–	–
7	0.971	29.9	0.971	30.4
Reference	0.98	22.7	0.978	23.5

Interpretation The four dimensions removed from the original Π -product relationship are Π_2 , Π_3 , Π_6 , and Π_7 . Because most cathodes studied operate with xenon (identical ionization energy) and feature an orifice length which is always close to 1 mm, both L_o and ϵ_{iz} do not show much variation in the dataset. The products that feature both quantities (Π_3 and Π_6) have therefore little to no effect on the overall fit. Both the Reynolds number and cathode aspect ratio are limited to a single order of magnitude: 86% of the computed Reynolds numbers are in the 1–10 range, and all cathode aspect ratios are within the 0.07–0.7 range. More variation in the data is needed for these Π -products to be relevant. The variance is explained by the influence of the plasma (Π_4) and gasdynamic effects (Π_5). Both the gasdynamic and plasma effects are relevant in this context and can describe two mechanisms of pressure change due to a change in mass flow rate, current, or both.

The proposed scaling relationship and analysis is limited by the data on which it relies. The analysis does not extend to cathodes which operate with a much longer orifice or propellant with a lower ionization energy (*e.g.*, lithium). We also note that the relationship spans five orders of magnitude in variation of the non-dimensional variables, and is not able to capture the dominant effects of a given flow regime. Finally, it is likely that the true dependency of the pressure does not follow a power

law. The latter is a simplification that allows for a rapid analysis and development of a pressure estimate.

4.5 Predictive capabilities

For a monatomic gas with $\gamma = 5/3$, the empirical relationship can be re-written in terms of physical quantities to compute the total pressure in Pascals or Torr:

$$P \text{ (Pa)} = 1.28 \times 10^{-8} \frac{I_d^{0.39} T_n^{0.41} \dot{m}^{0.69} \epsilon_{iz}^{0.25}}{L_o^{0.23} M^{0.14} \mu^{0.41} d_c^{0.79} d_o^{1.91}}, \text{ and} \quad (4.27)$$

$$P \text{ (Torr)} = 2.13 \times 10^{-7} \frac{I_d^{0.39} T_n^{0.41} M_a^{0.55} \dot{m}_{\text{sccm}}^{0.69} \epsilon_{iz}^{0.25}}{L_{o,\text{cm}}^{0.23} \mu^{0.41} d_{c,\text{cm}}^{0.79} d_{o,\text{cm}}^{1.91}}, \quad (4.28)$$

where M is the atomic mass of the propellant species in kg and M_a is the atomic mass in atomic mass units. Exponent values with more significant digits are shown in Appendix C for fast pressure calculations.

Figure 4.6 shows the empirical relationship applied to the NEXIS cathode for an assumed gas temperature of 3,000 K. The empirical relationship is capable of capturing the dependence of the cathode internal pressure on discharge current and yields a good approximation of the total pressure. A sensitivity analysis to the gas temperature is shown in Figure 4.7 and reveals that a $\pm 30\%$ change in gas temperature results in a $\pm 12\%$ change in total pressure.

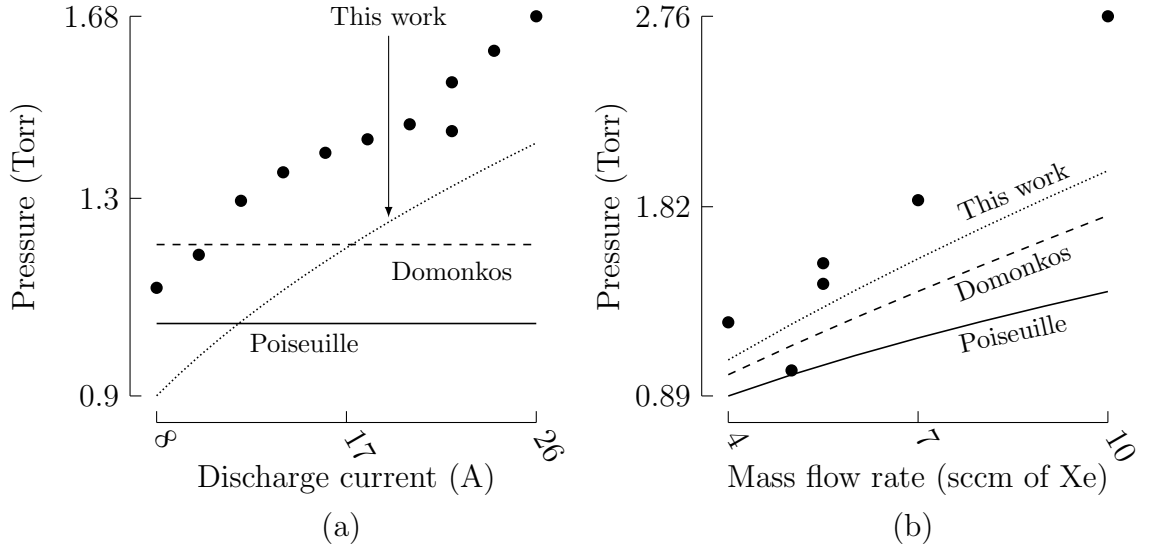


Figure 4.6: Applied power law to the NEXIS cathode for the case of (a) constant mass flow rate of 5.5 sccm, and (b) constant discharge current of 22 A.

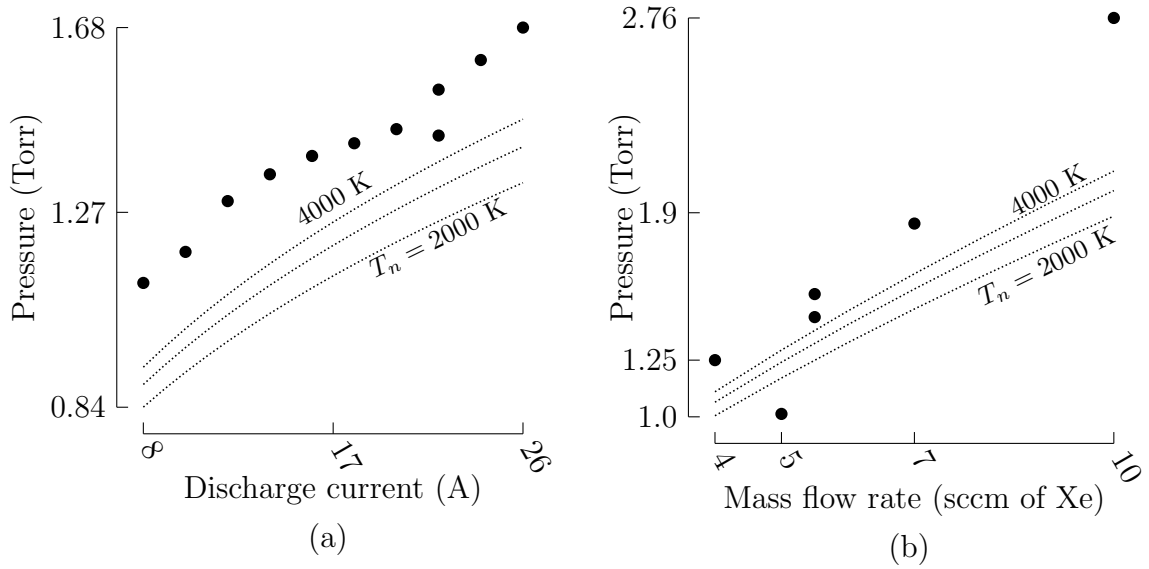


Figure 4.7: Sensitivity of the proposed empirical law to the gas temperature, applied to the NEXIS cathode.

4.6 Summary

We have developed a non-dimensional scaling relationship to calculate the total pressure inside orificed hollow cathodes and compared it to both experimental data for self-consistency and previous modeling attempts. The relationship features good agreement with experimental data and is able to capture the dependency of the pressure with both mass flow rate and discharge current, while theoretical models cannot. It is able to capture the pressure over three orders of magnitude or five orders of magnitude in the non-dimensional space.

Both the uncertainty in the neutral gas temperature and the effect of the feed system (which we do not consider here) may account for some of the discrepancies observed. We do not account for the pressure drop that occurs between the pressure measuring point and the cathode active zone. The pressure measuring point is typically far upstream of the insert plasma and can be sometimes multiple cathode lengths away (see, *e.g.*, [64]). The relationship is therefore representative of ideal experimental conditions in which the pressure is measured right next to the insert plasma.

We have used statistical tools to analyze the relationship and found that the gasdynamic and plasma effects are the most physically relevant. Evaluation of the empirical fit based on the derived Π -products allows for the calculation of the cathode internal pressure over an extremely wide range of operating conditions that could not be captured by a flow model incorporating only a single flow regime.

Chapter 5

Zero-dimensional cathode model¹

As we have shown in Chapter 2, the neutral gas pressure in an orificed hollow cathode affects physical quantities such as the ratio of sheath-edge plasma density to average plasma density and electron temperature, and, therefore, the total lifetime of the insert. If ambipolar diffusion is assumed to be charge-exchange-dominated, the electron temperature depends only on the geometry of the cathode and the neutral gas density (or pressure for a constant temperature) [136]. This assumption is typically valid for orificed hollow cathodes. It is critical to obtain an accurate value of the neutral gas pressure to ensure that the lifetime of the thermionic insert is maximized.

To estimate the neutral gas pressure, both the total pressure and ionization fraction can be used. As discussed in Chapter 2, multiple models exist to estimate the total pressure: empirical relationships, designed for a mercury hollow cathode [52, 63, 65, 71, 72, 112] or based on the available data from the literature (Chapter 4), isentropic [69] or isothermal [47, 114] flow approaches, Poiseuille flow the-

¹This chapter is based on work presented in References

- [134]: Taunay, P.-Y. C. R., Wordingham, C. J., and Choueiri, E. Y., “A 0-D model for orificed hollow cathodes with application to the scaling of total pressure” *AIAA Propulsion and Energy Forum*, 2019, AIAA-2019-4246, and
- [135]: Taunay, P.-Y. C. R., Wordingham, C. J., and Choueiri, E. Y., “The influence of ambipolar diffusion on the attachment length and electron temperature in orificed hollow cathodes” *36th International Electric Propulsion*, 2019, IEPC-2019-426.

ory [42, 95, 96], a modification of Poiseuille flow theory [64, 73], and an “equivalent temperature” or modified specific gas constant taking into account the ionization fraction [47, 49, 55, 114]. The ionization fraction may be estimated through a zero-dimensional model. We have shown in Chapter 2 that the empirical relationships developed in [52, 63, 65, 71, 72, 112] do not generalize to other cathodes and that the assumptions of isentropic, isothermal, or viscous Poiseuille flow are invalid in the flow regime in which cathodes operate. The empirical relationship we proposed in Chapter 4 covers available data from the literature but may not generalize to new designs unless they are similar to cathodes included in the analysis used to derive the relationship. It is also limited by its data-driven approach which does not explain the physical phenomena governing the total pressure in orificed hollow cathodes.

As shown in Chapter 2, existing 0-D cathode models [42, 49, 52, 55, 63–65, 69, 71–73, 75–78, 82, 92, 95, 96, 137, 138] inconsistently treat the sheath and do not address the neutral fluid flow correctly. We have also shown that existing models cannot be applied to cathodes that are different from the design for which they were originally developed. It is therefore not possible to use those models for a wide variety of cathodes and operating conditions. 2-D models also cannot be used for predictive purposes or to formulate scaling laws because they require experimental data and, in the case of fluid models, inconsistently treat the sheath.

To address the critical issues in 0-D and 2-D models, we propose here to use the combination of a two-dimensional charge-exchange-limited ambipolar diffusion model for the electrons, which is solved analytically, and zero-dimensional, volume-averaged, conservation equations for all species (ions, electrons, neutrals) present in the cathode. The two-dimensional charge-exchange-limited ambipolar diffusion model is presented in [136].

In this chapter, we present a theoretical framework to explain the variation of total pressure with mass flow rate, discharge current, cathode geometry, and gas species.

The main assumptions for our analysis are given in the following section. We then delineate the fluid and plasma models. We finally demonstrate that the results of the model agree with experimental data on a variety of cathodes, and use the model to formulate and verify scaling laws in the next chapter.

5.1 Assumptions

We make the following assumptions:

1. In the insert and orifice regions, the plasma is treated as a continuum fluid.
2. The heavy-particle stagnation temperature in both regions is constant and is a free parameter.
3. The flow in the orifice is frozen.
4. The total static pressure is constant in the insert region.
5. The flux of ions to the walls is equal to the Bohm flux and is not modified by the presence of an emitting sheath.
6. The fluid is inviscid.
7. The electron temperature is constant in each region.
8. The electron inertia is negligible compared to that of the heavy species.
9. Inelastic collisions other than direct ionization and ground-state excitation are ignored.
10. Steady-state conditions are reached.

Our first assumption is justified for cathodes with a small orifice-to-insert diameter ratio (*i.e.*, most orificed hollow cathodes). The Knudsen number is generally less than

1 for those cathodes. This assumption is invalid when the flow becomes transitional, such as in the downstream portion of the orifice (see, *e.g.*, Figure 2.16(a)), in cathodes that have an orifice-to-insert diameter ratio close to 1 (*i.e.*, tube cathodes) [139], and in cathodes with a low enough mass flow rate. We will use empirical corrections to compensate for transitional flow effects at the orifice outlet. The second assumption implies that the ion and neutral static temperatures are equal, which is justified for heavy species that have a large cross section for resonant charge exchange (*e.g.*, noble gases). We specify the static temperature in the orifice region and calculate the stagnation temperature under the assumption of an adiabatic flow. It is challenging to experimentally obtain the temperature of the neutral particles or ions in either the insert or orifice regions, and it is therefore difficult to evaluate the validity of the second assumption. However, the model we describe here is not sensitive to the value of the neutral gas temperature in the range of 2,000–4,000 K. This assumption is also used in most cathode models [42, 69, 75–78, 92, 95–97].

Because the mean free path for inelastic electron-neutral collisions is much larger than the orifice size, and because the residency time is smaller than the time between inelastic collisions for neutral particles in the orifice, the assumption of frozen flow (assumption 3) is justified, for typical operating conditions. The ratio of mean free path to orifice length L_o and the ratio of inter-collision time to residency time for the neutrals are given by:

$$\bar{\lambda} = \frac{1}{n_e \sigma (T_{eV}) L_o}, \quad (5.1)$$

and

$$\bar{\tau} = \frac{v_g}{L_o} (n_e \langle \sigma (T_{eV}) v \rangle)^{-1} = \frac{v_g}{v_e} \bar{\lambda}, \quad (5.2)$$

respectively. n_e is the electron density, σ is the inelastic reaction cross section, T_{eV} is the electron temperature in eV, v_g is the local sound speed, and v_e is the electron thermal velocity. Figure 5.1 shows the two ratios for xenon and two orifice aspect

ratios Λ_{or} (orifice length over orifice diameter), where we assume a gas temperature of 2,000 K to calculate the speed of sound. The electron temperature is calculated from the neutral gas density using the ambipolar diffusion model from [136]. The excitation cross section is computed from the sum of all excited states. The mean

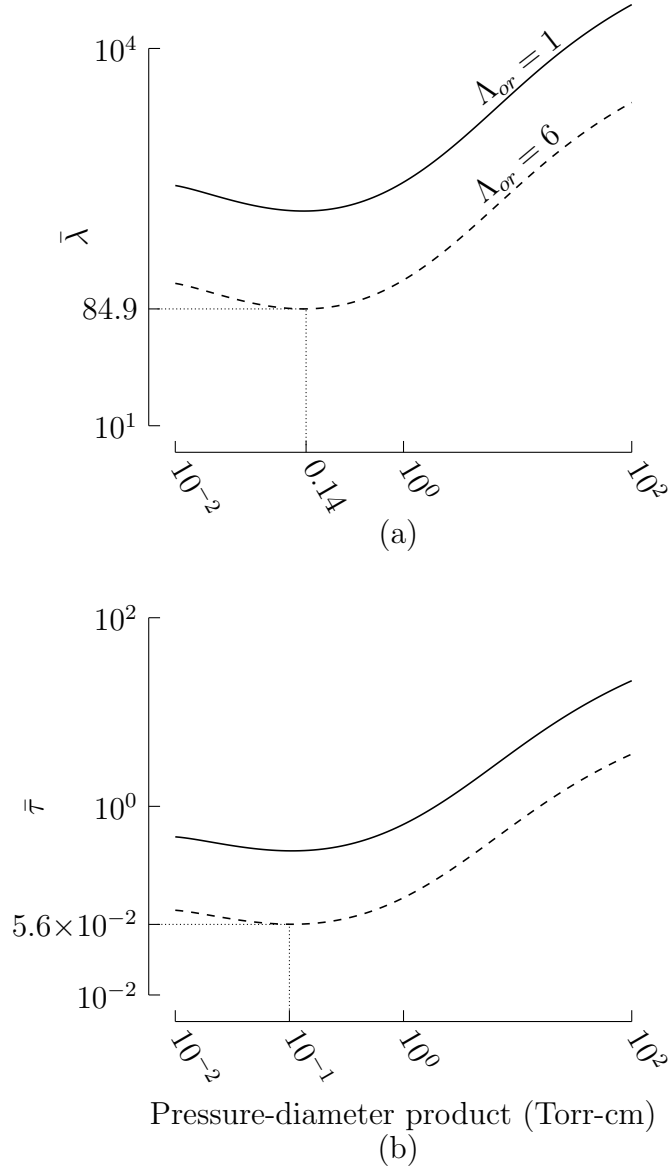


Figure 5.1: Ratio of (a) mean free path to orifice length for total inelastic electron-neutral collisions, (b) inter-collision time to neutral gas residency time.

free path for inelastic collisions is much longer than the orifice length for all neutral densities of interest. As indicated by the variation of the ratio of inter-collision time to

neutral gas residency time, the frozen flow approximation may be challenged for large orifice aspect ratios. The likelihood that a neutral atom undergoes many inelastic collisions before exiting the orifice channel is then very high. In general, however, this approximation allows us to provide a bound on the flow variables.

Assuming a constant total static pressure (assumption 4) in the insert region is justified because pressure gradients are small in the insert region for cathodes with small orifice-to-insert-diameter ratio. We note, however, that pressure gradients occur near the orifice inlet, where the flow is constricted. The flow gains dynamic pressure at the expense of static pressure in this region. The pressure difference between the upstream section and the orifice plate results in an additional force which increases the momentum flux through the orifice [140]. Ignoring this effect should result in an under-prediction of the total pressure.

It is necessary to estimate the flux of ions to the walls to include particle effects in the fluid model. Assuming that ions achieve the Bohm velocity at the edge of an emitting sheath (assumption 5) is not necessarily justified but it is a common assumption to all cathode models. Using the model from [61] it is possible to estimate the modification of the Bohm velocity by an emitting sheath:

$$v_{\text{ion}} = \left(\frac{eT_{eV}}{M} \right)^{1/2} \left(\frac{1 + 2\eta_c J_b}{1 - J_b} \right)^{1/2}, \quad (5.3)$$

where $\eta_c = \phi_s/T_{eV}$ is the normalized sheath voltage, $J_b = j_b/j_e$, where j_b is the emitted beam current and j_e is the electron saturation current:

$$j_e = n_e e \left(\frac{eT_{eV}}{m} \right) (2\eta_c)^{3/2}. \quad (5.4)$$

For cathodes that have a small orifice-to-insert-diameter ratio, the ion current through the sheath is negligible as compared to the emitted electron (beam) and electron saturation currents because of low sheath voltages ($\eta_c \propto 1$) and high plasma densities

(10^{20} – 10^{21} m $^{-3}$) [42]. In this case, the ratio of the beam current to the electron saturation current is typically negligible ($J_b \ll 1$), and, therefore, so is the modification to the Bohm velocity. We note, however, that under certain circumstances, the presence of an emitting sheath may modify the Bohm velocity by up to 20%. We consider in this case that the sheath boundary is situated farther away from the wall at a location where the Bohm velocity is reached. Because the size of the sheath ($\propto \mu\text{m}$) is much smaller than the scale of the system ($\propto \text{cm}$) this increase of the effective sheath size does not affect the diffusion characteristics of the solution.

Neglecting the viscosity (assumption 6) is motivated by the statistical analysis presented in Chapter 4. This study showed that viscous effects on the total pressure are likely negligible as compared to gasdynamic and plasma effects. Viscosity can nonetheless be implemented by considering that most of the viscous losses come from the feed system. Experimental measurements of the pressure data we used are gathered upstream of the insert region (sometimes multiple cathode lengths away, see, *e.g.*, [64]). This means that the viscous pressure drop within the feed system contributes to the measured total pressure. A Poiseuille flow assumption is justified in this section of the feed system: the flow is neutral, isothermal, viscous, laminar, incompressible, fully-developed, and not near a constriction. We use the heavy-particle temperature as the effective gas temperature when estimating the viscous losses in the feed system.

Experimental data [30, 47, 72, 110, 111] suggest that the gradients of the electron temperature in the insert and orifice regions are negligible, which indicates that assumption 7 is appropriate. In effect, this assumption means that the fluid is isothermal in each individual region.

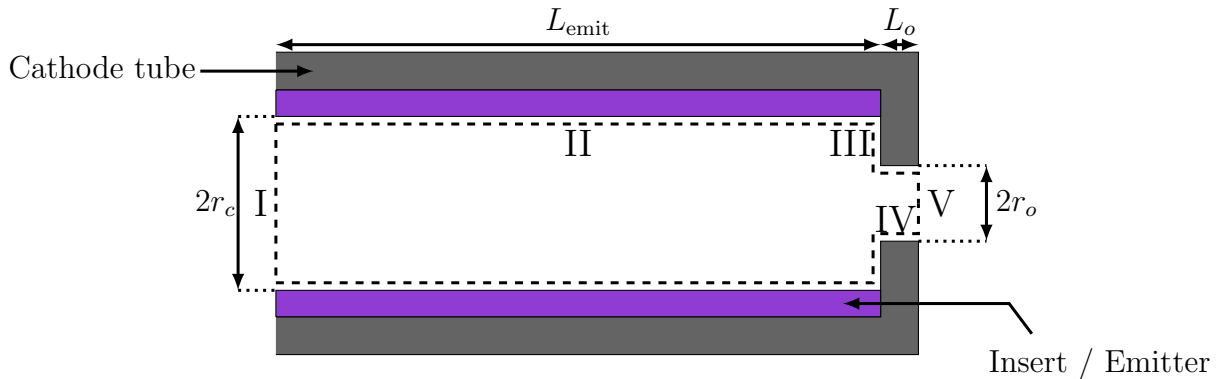


Figure 5.2: Fluid control volume considered in the analysis.

5.2 Fluid model

We use the two-dimensional axisymmetric momentum equations for each species, applied to the geometry shown in Figure 5.2. Boundaries II, III, and IV are chosen to be at the sheath edge. The emission length, L_{emit} , is the length over which the plasma is able to support temperature-limited thermionic emission. We approximate this length with the plasma density decay length scale in the axial direction, as calculated in [136]. The emission length is smaller than the insert length and we consider that the fluid is neutral upstream of the emission zone.

The momentum equations for each species are summed to provide a simpler single-fluid framework. Under the assumptions delineated in the previous section, we obtain:

$$\nabla \cdot (\rho \mathbf{v} \mathbf{v}) + \nabla P = \nabla \cdot \underline{\underline{\beta}}, \quad (5.5)$$

where \mathbf{v} is the mean mass velocity of the combined fluid, ρ its density, and $\underline{\underline{\boldsymbol{\beta}}}$ the magnetic stress tensor. P is the total static pressure. Equation 5.5 may also be written as:

$$\nabla \cdot (Mn_n \mathbf{v}_n \mathbf{v}_n + Mn_e \mathbf{v}_i \mathbf{v}_i) + \nabla P = \nabla \cdot \underline{\underline{\beta}}, \quad (5.6)$$

where the subscripts n , e , and i denote neutral, electron, and ion quantities, respectively. n_x and \mathbf{v}_x are the number density and velocity of the species x , respectively. M is the mass of the heavy particles.

To satisfy conservation of mass, ions return to the control volume as neutrals after having recombined on any of the sheath-facing surfaces (II, III, and IV). The flux of each species is therefore equal in magnitude and opposite in direction:

$$n_n v_n = -n_e^s v_B, \quad (5.7)$$

where n_e^s is the electron density at the sheath edge.

An upper-bound on the magnetic pressure on surfaces III and V can be obtained by considering that the magnetic field $\underline{\mathbf{B}}$ on these surfaces is due only to the current flowing through the orifice, which is assumed to be purely axial. The magnetic field is then purely azimuthal:

$$\underline{\mathbf{B}} = (0, B_\theta, 0)_{(\hat{r}, \hat{\theta}, \hat{z})}. \quad (5.8)$$

The magnetic stress tensor can then be expressed as [141]:

$$\underline{\underline{\beta}} = \begin{bmatrix} -B_\theta^2/2\mu_0 & 0 & 0 \\ 0 & B_\theta^2/2\mu_0 r^2 & 0 \\ 0 & 0 & -B_\theta^2/2\mu_0 \end{bmatrix}, \quad (5.9)$$

where μ_0 is the permeability of vacuum. The azimuthal component of the magnetic field can be estimated by further assuming constant current density in the orifice:

$$B_\theta = \begin{cases} -\frac{\mu_0 I_d}{2\pi r} & \text{if } r > r_o \\ -\frac{\mu_0 I_d}{2\pi r_o^2} r & \text{if } r < r_o \end{cases} \quad (5.10)$$

where r_o is the orifice radius and I_d is the discharge current.

We integrate Equation 5.6 over the volume shown in Figure 5.2, and apply Gauss's theorem. In the z -direction, we obtain:

$$\begin{aligned} & - [\pi r_c^2 P]_{\text{I}} + \pi (r_c^2 - r_o^2) \left[P + Mn_e^s v_B^2 \left(\frac{n_e^s}{n_n} + 1 \right) \right]_{\text{III}} + \pi r_o^2 [\rho v_z^2 + P]_{\text{V}} \\ & = - \frac{\mu_0 I_d^2}{4\pi} \left(\ln \frac{r_c}{r_o} + \frac{1}{4} \right), \end{aligned} \quad (5.11)$$

where r_c is the insert radius and v_z is the fluid velocity on the surface V. To obtain Equation 5.11 we further assumed that

- the upstream momentum is negligible as compared to the static pressure contribution,
- surface quantities other than the magnetic field are constant over their respective surfaces,
- the heavy particles have equal tangential velocity on each surface, and
- the radial velocity of the heavy particles on surface V is much smaller than the axial one.

The third assumption, combined with the flux condition given in Equation 5.7, causes the cross-term in the dyad product to vanish. For example, on surface II, the cross-term resulting from the momentum balance in the axial direction is:

$$S = Mn_e^s v_{i,r} v_{i,z} + Mn_n v_{n,r} v_{n,z}.$$

Because the particle fluxes normal to the wall are equal in magnitude and in opposite direction (Equation 5.7), we have:

$$S = Mn_e^s v_B (v_{i,z} - v_{n,z}).$$

The assumption of equal tangential velocity, motivated by frequent collisions between ions and neutrals, implies that $v_{i,z} = v_{n,z}$ on this surface. The dyad terms then simplify to zero. \square

5.2.1 Outlet (surface V)

The frozen-flow approximation allows us to define the Mach number and specific heat ratio γ . Under this assumption, the flow is choked and becomes sonic at the exit of the orifice because it expands into a vacuum. The flow velocity is therefore given by the local speed of sound a for the combined fluid:

$$v_{z,V} = a = \sqrt{\gamma R_g (T_n + \alpha T_e)}, \quad (5.12)$$

where R_g is the specific gas constant of neutral species, α is the ionization fraction, and T_n and T_e are the neutral and electron temperatures in Kelvin, respectively. This expression can be readily derived for an ideal gas where $a = \sqrt{\gamma P / \rho}$. The ionization fraction is defined as:

$$\alpha = \frac{n_e}{n_e + n_n}. \quad (5.13)$$

Using the conservation of mass, we also have $\pi r_o^2 (\rho v_z)_V = \dot{m}$.

Because the Knudsen number in the orifice, Kn , is within the range of 0.1 – 10 the flow is considered transitional. We therefore estimate the static pressure at the orifice outlet, P_V , with a molecular flow correction. We use a similar framework to [16,142,143]. Under the justifiable assumption that the pressure downstream of the cathode orifice (vacuum vessel pressure) is much smaller than the exit plane pressure, the stagnation pressure P_V^* is given by:

$$P_V^* = \frac{\dot{Q}}{(\theta C_m + (1 - \theta) C_v)}, \quad (5.14)$$

where \dot{Q} is the total throughput and C_m and C_v are the molecular flow and viscous flow aperture conductances, respectively. The linear weight θ is a function of the Knudsen number. The expression proposed in [142] can be written as suggested by [143] and [16]:

$$\theta = \frac{k_\theta \text{Kn}}{k_\theta \text{Kn} + 1}, \quad (5.15)$$

where $k_\theta = 28$. This value of k_θ corresponds to equal weighing of molecular and viscous flows ($\theta \approx 0.5$) when the average pressure in the orifice is equal to the mid-point pressure of the transition range [142]. This corresponds to $\text{Kn} \approx 0.04$. The throughput and the conductance of the orifice aperture for the flow are given by:

$$\dot{Q} = \frac{k_B}{M} T_n \left(\frac{\gamma + 1}{2} \right) \dot{m}, \text{ and} \quad (5.16)$$

$$C_a = \pi r_o^2 \sqrt{\left(\frac{\gamma + 1}{2} \right) \frac{k_B T_n}{2\pi M}}, \quad (5.17)$$

respectively. The $(\gamma + 1)/2$ term comes from the conversion from static to stagnation quantities in the insert region. Because the throughput is referenced to upstream stagnation quantities, the plasma contribution to the sound speed does not appear in \dot{Q} . The molecular and viscous flow conductances are [142, 143]:

$$C_m = C_a \left(\frac{2}{\gamma + 1} \right)^{1/2}, \text{ and} \quad (5.18)$$

$$C_v = \sqrt{2\pi} \left(\gamma \left(\frac{2}{\gamma + 1} \right)^{(\gamma+1)/(\gamma-1)} \right)^{1/2} C_a, \quad (5.19)$$

respectively. The static pressure on surface V is retrieved from the definition of the stagnation pressure at a Mach number of 1:

$$P_{\text{exit}} = P_V = P_V^* \left(\frac{2}{\gamma + 1} \right)^{\gamma/(\gamma-1)}. \quad (5.20)$$

5.2.2 Orifice plate (surface III)

Because we have assumed a constant total pressure in the insert volume, the total static pressure on the orifice plate is equal to that at the inlet: $P_{\text{III}} = P_{\text{I}}$.

5.2.3 Total pressure

We reorganize Equation 5.11 to obtain an expression for the total (static) pressure:

$$P = P_{\text{mag}} + P_{\text{gd}} + P_{\text{mf}} + P_{\text{exit}} \quad (5.21)$$

where P_{mag} , P_{gd} , P_{mf} , P_{exit} are the magnetic pressure on surfaces III and V, gasdynamic pressure contribution, orifice plate momentum flux, and orifice outlet exit pressure, respectively. These quantities are defined as:

$$\begin{aligned} P_{\text{mag}} &= \frac{\mu_0 I_d^2}{4\pi^2 r_o^2} \left(\ln \frac{r_c}{r_o} + \frac{1}{4} \right), \\ P_{\text{gd}} &= \frac{\dot{m}}{\pi r_o^2} \sqrt{\gamma R_g (T_n + \alpha_o T_e)}, \\ P_{\text{mf}} &= \left(\frac{r_c^2}{r_o^2} - 1 \right) e n_e^s T_{eV} \left(1 + \frac{n_e^s}{n_n} \right), \text{ and} \\ P_{\text{exit}} &= P_V^* \left(\frac{2}{\gamma + 1} \right)^{\gamma/(\gamma-1)}, \end{aligned} \quad (5.22)$$

respectively. P_{mf} , n_e^s , and T_{eV} are calculated using insert-region quantities. The speed of sound of the fluid appearing in the gasdynamic pressure is computed with orifice-region quantities. α_o denotes the ionization fraction in the orifice. Equation 5.21 states that the total static pressure upstream of the cathode emission zone is the balance between the particle momentum leaving the volume, the magnetic pressure, and the downstream static pressure.

The total pressure in the absence of plasma effects ($P_{mf} = P_{mag} = 0$) for a continuum flow ($\theta = 0$) is:

$$P = \frac{\dot{m}}{\pi r_o^2} \sqrt{\gamma R_g T_n} \left(1 + \frac{1}{\gamma} \right). \quad (5.23)$$

This expression is different from the one that would be obtained with an isentropic flow relationship:

$$P_{\text{isentropic}} = \frac{\dot{m}}{\pi r_o^2} \sqrt{\gamma R_g T_n} \frac{1}{\gamma} \left(\frac{\gamma + 1}{2} \right)^{\gamma/(\gamma-1)}. \quad (5.24)$$

For a monatomic gas, the constants $(1 + 1/\gamma)$ and $1/\gamma ((\gamma + 1)/2)^{\gamma/(\gamma-1)}$ that appear in Equations 5.23 and 5.24 are equal to 1.6 and 1.23, respectively. The discrepancy comes from the assumption that the static pressure on the orifice plate (surface III) is equal to the upstream total pressure. This assumption of a pressure force on the orifice plate is fundamentally inconsistent with the derivation of isentropic flow relationships, as the use of the momentum balance combined with this assumption over-determines the system of flow equations. In practice, isentropic flow relationships are derived from the energy and continuum equations, with the momentum balance being used to find the total pressure force on the control volume (or the thrust, for nozzle flows). In the absence of a plasma, simple isentropic flow relationships should be directly used to estimate the total pressure inside the cathode.

5.3 Plasma model

To close the system of equations, estimates of the degree of ionization, neutral density, and electron temperature are required for both the insert and orifice regions. In the insert region an estimate of the attachment length, or length over which the plasma is dense enough to support temperature-limited thermionic emission, is also required.

Because the ionization fraction may not be negligible (especially in the orifice region) we do not employ the typical approximation $\alpha \ll 1$; we retain all terms in the resulting equations in both regions. For all of our calculations, the collision frequencies are computed using Maxwellian-averaged collision cross sections.

5.3.1 Electron temperature and attachment length

We employ the method delineated in [136] to calculate the electron temperature in both insert and orifice regions, as well as the attachment length. The method is based on a charge-exchange-limited ambipolar diffusion model of the plasma. Application of this method gives an analytical approximation of the attachment length and the electron temperature in both regions as functions of the neutral-pressure-diameter product only. We define the “attachment length,” more specifically, as the plasma density decay length-scale for the first-order eigenmode of the full 2-D solution in the insert. The insert electron temperature is not sensitive to the neutral gas temperature in that region; we therefore ran the 2-D solution with an assumed neutral gas temperature of 3,000 K in the insert region. The orifice electron temperature as calculated from the method from [136], however, can vary by up to 20% with a change in neutral gas temperature. The solution is therefore calculated with multiple neutral gas temperatures.

We use the following approximations for the insert and orifice electron temperature,

$$T_{eV}^{\text{insert}} = \frac{t_{i,0}}{(n_n k_B T_n (2r_c))^{t_{i,1}}} + t_{i,2}, \quad (5.25)$$

$$T_{eV}^{\text{orifice}} = \frac{t_{o,0}}{(n_n k_B T_n (2r_c))^{t_{o,1}} + t_{o,2}} + t_{o,3}, \quad (5.26)$$

and for the attachment length,

$$L_{\text{emit}} = r_c \left(l_0 + \frac{l_1}{\ln^6(n_n k_B T_n (2r_c) + l_2)} \right), \quad (5.27)$$

respectively. The above expressions were found by inspection of the numerical results. The coefficients $t_{i,k}$, $t_{o,k}$, and l_k for xenon and argon gases are tabulated in Appendix C (Tables C.2 and C.3). In all cases, the pressure-diameter product that appears in the denominator is in Torr-cm.

5.3.2 Insert region

The conservation of charge in the insert region gives the total discharge current I_d as:

$$I_d = I_i + I_{em} - I_r, \quad (5.28)$$

where I_i , I_{em} , and I_r are the ion, thermionic, and random electron currents, respectively. Assuming that all ions created in the volume go to the insert wall, the ion current is either given by its volumetric definition, or by its value at the sheath edge,

$$I_i = en_n n_e \langle \sigma_{iz} v \rangle \pi L_{\text{emit}} r_c^2 = en_e^s v_B 2\pi r_c L_{\text{emit}}, \quad (5.29)$$

where σ_{iz} is the ionization cross section. Using Equation 5.29, we obtain the sheath-edge density:

$$n_e^s = \frac{n_n n_e \langle \sigma_{iz} v \rangle r_c}{2v_B} = \frac{\alpha}{1 - \alpha} \frac{n_n^2 \langle \sigma_{iz} v \rangle r_c}{2v_B}. \quad (5.30)$$

We use this result to define f_s , the ratio between the sheath-edge and the volume-averaged electron density, as a function of volume-averaged quantities:

$$f_s = \frac{n_e^s}{n_e} = \frac{n_n \langle \sigma_{iz} v \rangle r_c}{2v_B}. \quad (5.31)$$

The random electron current can also be expressed in terms of volumetric quantities by using the definition of the sheath-edge density (Equation 5.30):

$$I_r = e \frac{1}{4} \left(\frac{8M}{\pi m} \right)^{1/2} n_n n_e \langle \sigma_{iz} v \rangle \pi L_{\text{emit}} r_c^2 \times \exp(-\phi_s / T_{eV}), \quad (5.32)$$

where m is the mass of the electron and ϕ_s is the sheath potential.

We integrate the electron energy equation over a cylindrical volume of length L_{emit} and radius r_c with the face fluxes estimated using a zeroth-order upwind scheme as suggested in [42] (p.259). We obtain:

$$I_{em} \phi_s + R_p I_d^2 = q_{ex} + I_i \epsilon_{iz} + \frac{5}{2} T_{eV} I_d + (2T_{eV} + \phi_s) I_r, \quad (5.33)$$

where q_{ex} is the total power loss due to radiative transitions from ground-level, ϵ_{iz} is the ionization energy of the species of interest, and R_p is the plasma resistance. The power loss due to radiative transitions from ground level is given by the total excitation rate in the volume multiplied by the average energy of each transition:

$$q_{ex} = e n_e n_n \langle \sigma_{ex} v \rangle \pi L_{\text{emit}} r_c^2 \epsilon_{ex}. \quad (5.34)$$

The excitation cross section in Equation 5.34 is the *total* cross section for all ground-state excitation reactions. The excitation energy is computed as the average of all excitation energies weighted by their respective Maxwellian-averaged reaction rates. The plasma resistance is given by:

$$R_p = \frac{m}{n_e e^2} \frac{L_{\text{emit}}}{\pi r_c^2} (\nu_{ei} + \nu_{en}), \quad (5.35)$$

where ν_{ei} and ν_{en} are the electron-ion and electron-neutral collision frequencies, respectively.

We use the conservation of charge (Equation 5.28) to eliminate the thermionic current terms from the electron energy equation. This removes the dependency of the model on the chosen insert material and assumed wall temperature. The resulting equation is expressed in terms of the ionization fraction and the neutral gas density by replacing the electron density with the definition of the ionization fraction (Equation 5.13). This yields a quadratic expression for the unknown ionization fraction:

$$i_2\alpha^2 + i_1\alpha + i_0 = 0. \quad (5.36)$$

The coefficients i_k are functions of the cathode geometry, neutral gas density, sheath potential, and neutral gas temperature. They are given by:

$$\begin{aligned} i_2 = & en_n^2 \langle \sigma_{iz} v \rangle \pi L_{\text{emit}} r_c^2 \times \left(\epsilon_{iz} + \phi_s + 2T_{eV} \frac{1}{4} \left(\frac{8M}{\pi m} \right)^{1/2} \exp(-\phi_s/T_{eV}) \right) \\ & + en_n^2 \langle \sigma_{ex} v \rangle \pi L_{\text{emit}} r_c^2 \epsilon_{ex} + \frac{mL_{\text{emit}}}{\pi r_c^2 e^2} C_{ei} \ln \Lambda T_{eV}^{-3/2} I_d^2 - I_d \left(\frac{5}{2} T_{eV} - \phi_s \right) \\ & - \frac{mL_{\text{emit}}}{\pi r_c^2 e^2} I_d^2 \langle \sigma_{en} v \rangle, \end{aligned} \quad (5.37)$$

$$i_1 = I_d \left(\frac{5}{2} T_{eV} - \phi_s \right) - \frac{mL_{\text{emit}}}{\pi r_c^2 e^2} C_{ei} \ln \Lambda T_{eV}^{-3/2} I_d^2 + 2 \frac{mL_{\text{emit}}}{\pi r_c^2 e^2} I_d^2 \langle \sigma_{en} v \rangle, \text{ and} \quad (5.38)$$

$$i_0 = - \frac{mL_{\text{emit}}}{\pi r_c^2 e^2} I_d^2 \langle \sigma_{en} v \rangle, \quad (5.39)$$

where $C_{ei} = 2.9 \times 10^{-12}$, and $\ln \Lambda \approx 10$ is the Coulomb logarithm. σ_{en} and σ_{ex} are the electron-neutral cross sections for elastic and excitation collisions, respectively. ϵ_{ex} is the average electron excitation energy. We use data from the Hayashi database [80] as retrieved from the LXCat website [81] for the electron-neutral, ionization, and excitation cross sections.

5.3.3 Orifice region

In the orifice, the energy equation can be considerably simplified by neglecting thermionic emission and electron backstreaming because of the higher sheath voltages due to the lower neutral densities than in the insert region. We again obtain a quadratic equation from the orifice energy balance:

$$o_2\alpha^2 + o_1\alpha + o_0 = 0, \quad (5.40)$$

where the coefficients o_k are:

$$o_2 = en_n^2 \langle \sigma_{iz} v \rangle \pi L_o r_o^2 \epsilon_{iz} + en_n^2 \langle \sigma_{ex} v \rangle \pi L_o r_o^2 \epsilon_{ex} + \frac{mL_o}{\pi r_o^2 e^2} C_{ei} \ln \Lambda T_{eV}^{-3/2} I_d^2 - \frac{mL_o}{\pi r_o^2 e^2} I_d^2 \langle \sigma_{en} v \rangle - \frac{5}{2} I_d (T_{eV} - T_{eV}^{\text{ins}}), \quad (5.41)$$

$$o_1 = \frac{5}{2} I_d (T_{eV} - T_{eV}^{\text{ins}}) - \frac{mL_o}{\pi r_o^2 e^2} C_{ei} \ln \Lambda T_{eV}^{-3/2} I_d^2 + 2 \frac{mL_o}{\pi r_o^2 e^2} I_d^2 \langle \sigma_{en} v \rangle, \text{ and} \quad (5.42)$$

$$o_0 = -\frac{mL_o}{\pi r_o^2 e^2} I_d^2 \langle \sigma_{en} v \rangle. \quad (5.43)$$

L_o is the orifice length and T_{eV}^{ins} is the insert electron temperature.

To obtain a relationship between the ionization fraction and neutral density, we use the conservation of mass applied to the sonic condition at the orifice outlet. This results in a quadratic equation for the ionization fraction,

$$\dot{m} = \pi r_o^2 \frac{1}{1 - \alpha} n_n M \sqrt{\gamma R_g (T_n + \alpha T_e)}. \quad (5.44)$$

Solving this equation and selecting the root for which $\alpha_o < 1$ gives an expression for the ionization fraction,

$$\alpha = 1 + \frac{1}{2\bar{v}} \left(1 - \sqrt{4\bar{v} (1 + \bar{T}) + 1} \right), \quad (5.45)$$

where $\bar{T} = T_n/T_e$ and \bar{v} is given by:

$$\bar{v} = \frac{1}{\gamma R_g T_e} \left(\frac{\dot{m}}{\pi r_o^2 n_n M} \right)^2. \quad (5.46)$$

The orifice energy equation (Equation 5.40) and the solution for the ionization fraction from conservation of mass (Equation 5.45) are combined to obtain a single equation for the unknown neutral density in the orifice.

5.4 Implementation

5.4.1 Algorithm

Both the gas temperature and sheath voltage are free parameters. The expression for the sheath-edge density ratio (Equation 5.31) is used in the pressure balance (Equation 5.21) to form an expression that depends only on α and n_n :

$$P = P_{mag} + P_{gd} + \left(\frac{r_c^2}{r_o^2} - 1 \right) f_s \frac{\alpha_i}{1 - \alpha_i} n_n e T_{eV} \left(1 + \left(\frac{\alpha_i}{1 - \alpha_i} \right) f_s \right) + P_{\text{exit}}. \quad (5.47)$$

To solve this equation, we use the perfect gas law to compute the total static pressure:

$$P = k_B n_n T_n + \frac{\alpha_i}{1 - \alpha_i} n_n e T_{eV} + \frac{\alpha_i}{1 - \alpha_i} n_n k_B T_n. \quad (5.48)$$

Because we have used surface-integrated quantities when deriving the pressure balance, but re-expressed these terms using volume-averaged quantities, there are (at least) two possible choices for the definition of the total static pressure. Assuming constant total pressure in the insert region, we can either use the sheath-edge density or the volumetric value to compute this pressure. We choose the latter option because the sheath-edge terms balance the corresponding ones on the upstream portion, leaving only the pressure contribution on the orifice inlet.

Solving the system of equations resulting from the combination of the pressure balance (Equation 5.47), the perfect gas law (Equation 5.48), and the insert power balance (Equation 5.36) yields the solution for both n_n and α_i . We combine the expressions into a single equation for the unknown neutral density which we then solve using the bisection method to avoid solving the original multivariate nonlinear system. For each proposed insert neutral density and sheath potential, we solve for the ionization fraction in the insert using the insert power balance (Equation 5.36). The insert electron temperature is then obtained using the correlation in Equation 5.25. The orifice neutral density is calculated using the orifice power balance (Equation 5.40), mass continuity (Equation 5.45), and the insert electron temperature. The electron temperature for the orifice is then obtained using Equation 5.26, and the ionization fraction for the orifice is computed with Equation 5.45. Finally, the total pressure results calculated using the momentum balance (Equation 5.47) and the perfect gas law (Equation 5.48) are compared. If both results agree, the algorithm has converged and the solution is reported.

For a given geometry and gas, the orifice quantities depend on the mass flow rate, the discharge current, and the insert neutral density through the insert electron temperature. The orifice quantities can therefore be pre-computed and stored as a lookup table for faster computation. The upper bound for the orifice neutral density can be obtained by imposing the conditions that $\alpha_o > 0$ and that the neutral density in the insert is greater than that in the orifice. We check that both conditions are satisfied for each orifice neutral density found.

5.4.2 Wall temperature

We note that while the emission current has been eliminated from the model equations, the wall temperature may be retrieved from the total emitted current and the conservation of charge (Equation 5.28). The elimination of the emitted current from

the model equations also removes the dependence of the pressure on the choice of emitter material, excluding any indirect dependence due to the temperature of the heavy species. Without the Schottky effect, the total emitted current is given by Richardson-Dushman's law,

$$I_{em} = 2\pi L_{emit} r_c D_{RD} T_c^2 \exp\left(-\frac{e\phi_w}{k_B T_c}\right), \quad (5.49)$$

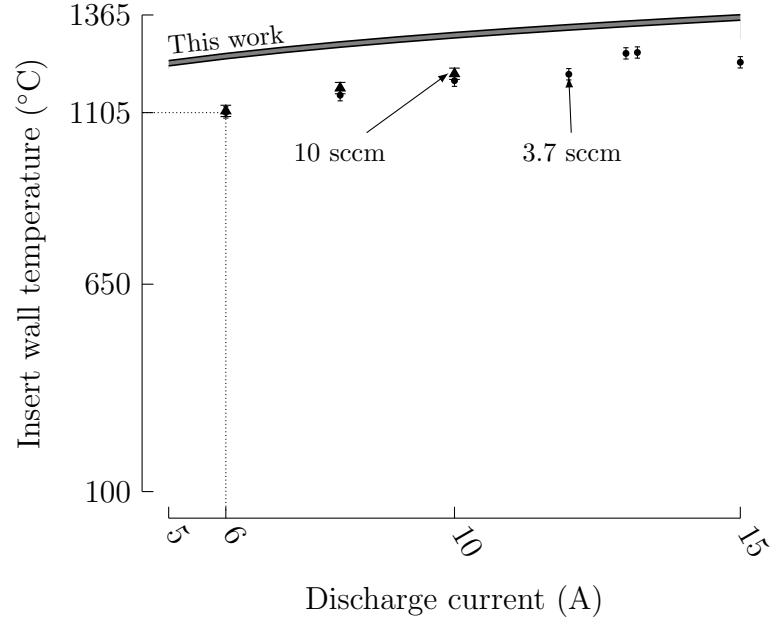
where D_{RD} is the Richardson-Dushman constant, T_c is the emitter temperature, and ϕ_w is the work function. Because we have assumed that the emission length is defined such that the thermionic emission is thermally-limited inside the active zone, the current extracted is not modified by space-charge limitation.

5.4.3 Sheath potential

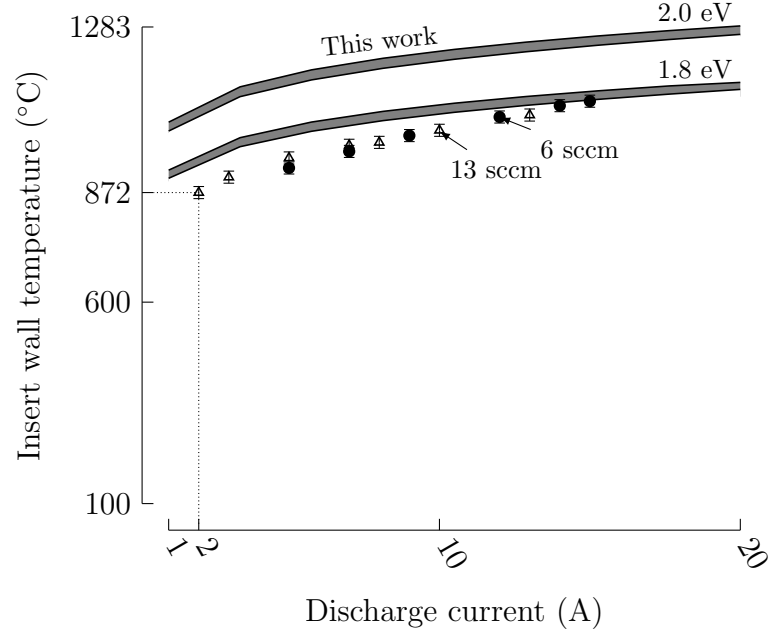
The algorithm may also be used as an indirect method to compute the sheath potential. The total pressure calculated using the pressure balance (Equation 5.47) can be evaluated for multiple sheath potentials, and the intersections of the resulting family of pressure curves with the experimental pressure data can be used to estimate the variation of the sheath voltage over the experimental parameter range.

5.5 Results

We validate in this section the results of our algorithm for multiple cathodes. The dimensions and operating conditions of each cathode are shown in Appendix B (Table B.1). They span a variety of geometries, gases, and operating conditions.



(a)



(b)

Figure 5.3: (a) Peak insert temperature of the NSTAR cathode. (b) Cathode external wall temperature of Salhi's cathode. Experimental data from [116] and [47], respectively. Gray area on the model indicate the minimum and maximum values obtained for the indicated mass flow rates, with sheath voltage and gas temperature with values between 1–10 V and 2000–4000 K, respectively.

5.5.1 Wall temperature

We show in Figure 5.3 a comparison of our model to experimental data of the insert temperature. We applied the algorithm to both Salhi’s cathode operating with argon and to the NSTAR cathode. The cathode wall temperature is reported in [47] and [116], respectively. We took the work function from Table 1.1 (originally from [42], p.252) for the barium-oxide insert installed in the NSTAR cathode. Salhi’s cathode uses a material with an estimated work function of 1.8–2.0 eV [47]. The results from our algorithm are averaged over all of the values tested for the two free parameters. We have computed all quantities with sheath voltages and gas temperatures in the range of 1–10 V and 2000–4000 K, respectively. The algorithm returns values within 10% of the experimental values for both cathodes. We find that the trend of the predicted wall temperature agrees with the experimental data, both with increasing discharge current and mass flow rate.

We also applied the algorithm to Friedly’s cathode [112] with an estimated work function of 2 eV for the insert material (as reported in [72], p.91). We found the calculated results to be within 20% of experimental data, but did not have the same agreement as that of the NSTAR. We note that the temperatures reported by Friedly [112] are that of the exterior of the cathode and are higher than the typical application range of barium-based emitters. We hypothesize that the emitter depleted its coating, especially at higher discharge currents, which would explain the reported high temperatures. The uncertainty in the work function of the material would explain the discrepancy observed between the results of the model and the experimental measurements. We found that the observed trend of the results of the algorithm agrees with experimental results if we assume that the work function is equal to 4.1 eV. This value is within the range of the work function of tantalum (4.0–4.8 eV) [43]. Additionally, the assumptions made in [136] to estimate the emission length become invalid at high discharge currents for this particular cathode. The calculated ion-

ization fraction is indeed large in both the orifice (up to 60%) and in the insert (up to 30%) at high discharge currents and therefore challenges the assumption of charge-exchange-dominated ambipolar diffusion. A possible remedy is to include *all* interactions between particles when considering ambipolar diffusion.

5.5.2 Electron temperature and attachment length

The predicted and experimental attachment length and insert electron temperature are shown in Figure 5.4(a) and Figure 5.4(b), respectively. Results are presented for the JPL’s 1.5 cm LaB₆ hollow cathode [30] and for Salhi’s cathode [47] operating on argon and with an orifice size of 1.21 mm. The insert electron temperature for the JPL’s cathode is reported at the location of peak insert electron density. We use the highest reported values for Salhi’s cathode, close to the peak insert electron density.

We observe in all cases that the trend of decreasing electron temperature with increasing discharge current and mass flow rate is correctly captured. We note, however, that the electron temperature is over-predicted, which is a consequence of an under-prediction of the neutral density and is consistent with an under-predicted neutral gas pressure.

5.5.3 Pressure

We now compare the prediction of the total pressure inside hollow cathodes from existing models to that from ours for the NSTAR, NEXIS, and our own cathode. For the NSTAR cathode we also perform a comparison with results of a 2-D axisymmetric solver from [122]. The results are computed with a gas temperature of 3,000 K and sheath voltages between 1 and 10 V. Results are shown in Figure 5.5. Pressures predicted with both our theoretical model and the empirical correlation from Chapter 4 vary with discharge current and mass flow rate, while other existing models do not. These two approaches yield results that are close to the experimentally measured

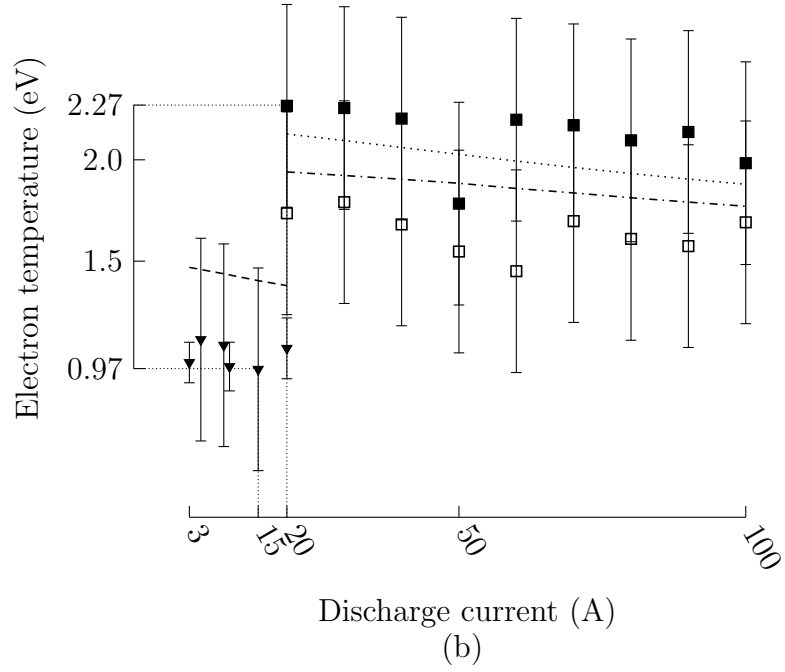
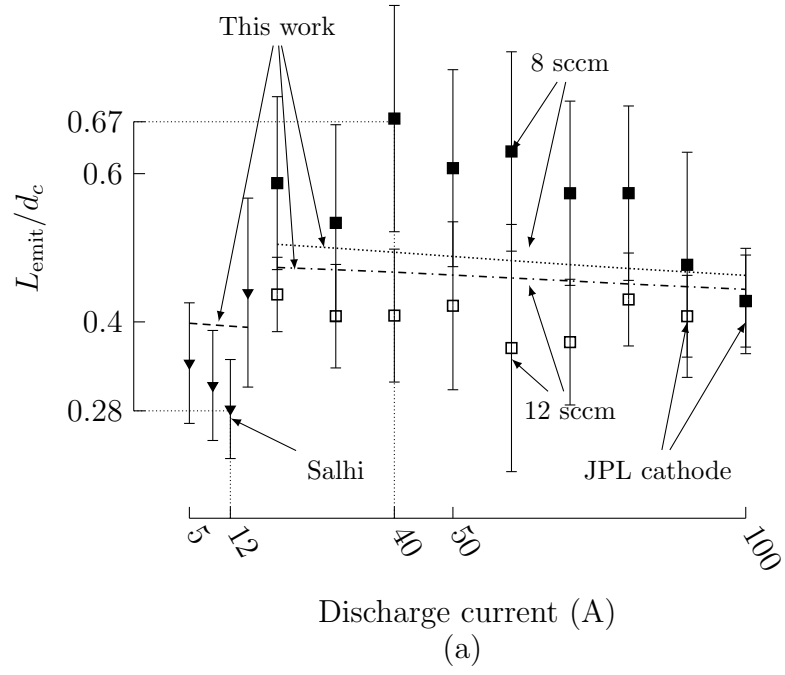


Figure 5.4: (a) Attachment length normalized by the cathode insert diameter and (b) electron temperature as functions of discharge current. Experimental data for the JPL LaB_6 cathode and Salhi's cathode from [30] and [47], respectively.

pressure. Results for the NSTAR are similar to that of the 2-D axisymmetric solver, although the latter uses a discharge current 10% higher than the nominal current of 12 A. For cathodes that reasonably satisfy the model assumptions, the numerical algorithm allows us to bound the pressure for a cathode for which no pressure data are available. The algorithm however overestimates the pressure for our cathode. We hypothesize that:

- the magnetic pressure is overestimated because we did not take into account the net current of charged particles from the insert volume directed towards the orifice plate,
- gas leaks occur through the grafoil seals at graphite/stainless steel interfaces at high temperatures, thus decreasing the experimentally measured pressure, or
- gas leaks occur through the NPT fittings on the feed lines and pressure tap because they are sealed only with anti-seize compound as typical thread sealant compounds would not tolerate the operating temperature of the PLHC.

We note that in all cases, knowledge of the sheath potential is required. The family of curves generated by the model intersect experimental data at different sheath voltages. As mentioned in the previous section, this may be used to compute the sheath voltage from the experimental data.

5.6 Summary

Based on the lessons learned in our review of prior cathode modeling efforts (Chapter 2), we have developed a hybrid model for orificed hollow cathodes and computed volume-averaged plasma quantities for a large variety of cathodes and operating conditions. Good agreement is obtained with both literature data and with experimental

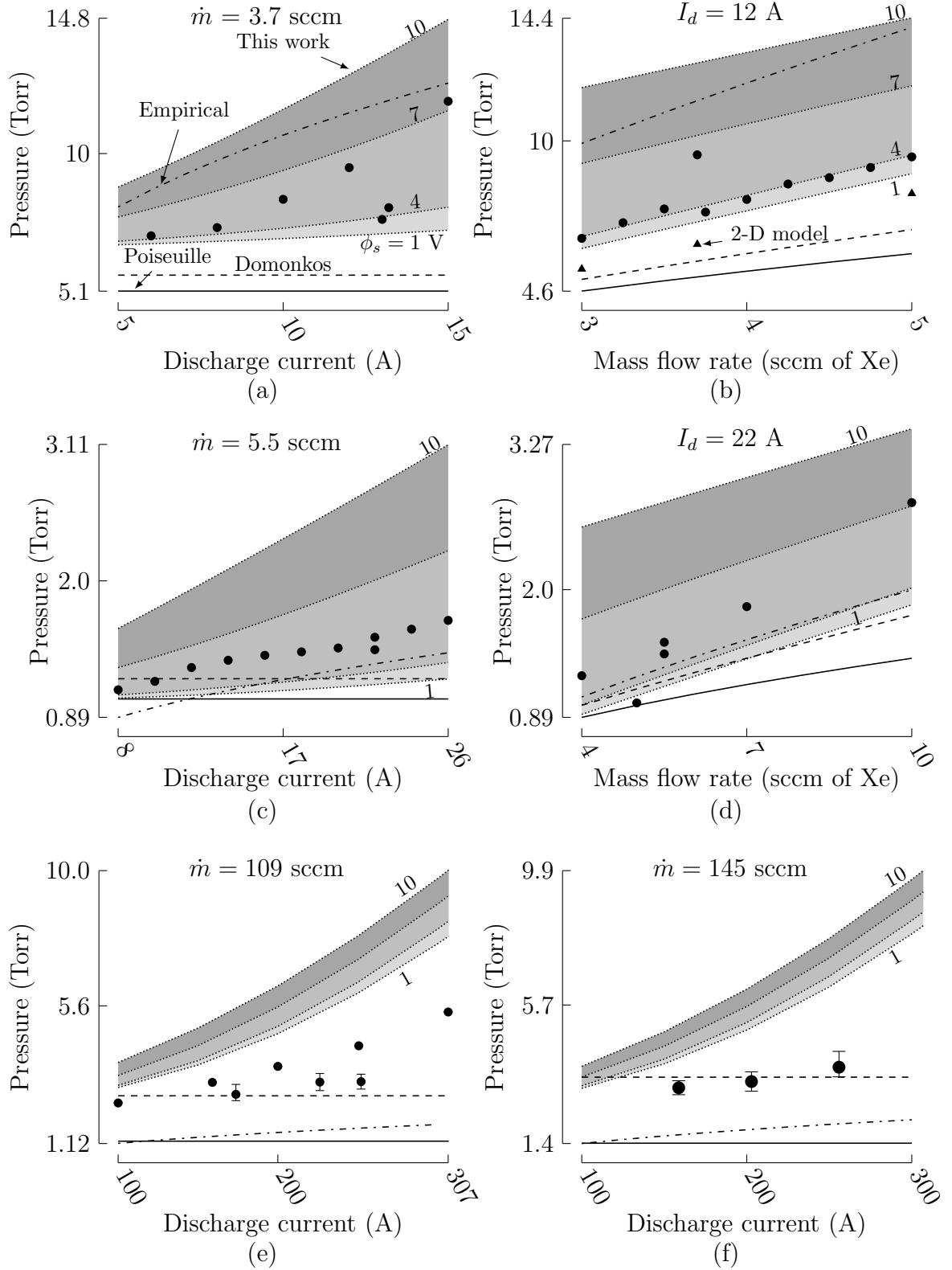


Figure 5.5: Comparison of pressure models used for the calculation of the total pressure inside hollow cathodes. (a,b) NSTAR cathode. Experimental data from [111,116,122]. (c,d) NEXIS cathode. Experimental data from [105,115]. (e,f) PLHC.

pressure data we gathered on our own large hollow cathode running on argon at up to 300 A of discharge current.

We were able to bound both the sheath potential and neutral gas temperature and found that the calculated quantities are not sensitive to these parameters. These two parameters can be self-consistently incorporated into the model through a potential solver and the energy equation for the heavy particles, respectively. The values for the neutral gas temperature remain to be experimentally validated.

This work can be used in conjunction with the charge-exchange-dominated ambipolar diffusion model for the insert region we presented in [136] to find the electron density distribution within a hollow cathode. The model is also a building block for insert performance prediction if coupled to an erosion model for the thermionic material and for cathode performance prediction if coupled to a cathode thermal and plume model. Finally, the proposed model may be used to study scaling laws for hollow cathodes; we perform this analysis in the following chapter.

Chapter 6

Scaling laws¹

We developed and verified a theoretical model for hollow cathodes in the previous chapter. The model is based on a 0-D approach to the conservation of energy and momentum for the combined plasma-neutral fluid and on a 2-D charge-exchange-limited ambipolar diffusion model. We now apply this framework to develop scaling laws for hollow cathodes. We seek to obtain insights into the phenomenological dependence of plasma quantities (total pressure, attachment length, electron temperature) on controlling parameters (cathode geometry, gas species, discharge current, mass flow rate).

6.1 Pressure-diameter product

The experimental measurements we presented in Chapter 3 feature a (total, static) pressure-diameter product in the range of 6.6–14.7 Torr-cm. In general, literature

¹This chapter is based on work presented in References

- [134]: Taunay, P.-Y. C. R., Wordingham, C. J., and Choueiri, E. Y., “A 0-D model for orificed hollow cathodes with application to the scaling of total pressure” *AIAA Propulsion and Energy Forum*, 2019, AIAA-2019-4246, and
- [135]: Taunay, P.-Y. C. R., Wordingham, C. J., and Choueiri, E. Y., “The influence of ambipolar diffusion on the attachment length and electron temperature in orificed hollow cathodes” *36th International Electric Propulsion*, 2019, IEPC-2019-426.

data demonstrate that cathodes operate at a pressure-diameter product near 1 Torr-cm, regardless of gas species used, cathode geometry, mass flow rate, and discharge current. This value has been observed to be a sufficient condition for the efficient operation of tube cathodes on a variety of gases [139, 144]. Similar observations have been made for orificed hollow cathodes that operate with mercury [71], noble gases [145], and hydrogen [146].

We show in Figure 6.1 the statistical distribution of the total pressure-diameter product for a variety of cathodes: Siegfried and Wilbur’s mercury and noble gas cathodes [65, 72, 120, 126], Friedly’s cathode [112], Salhi’s cathode [47] operating on both argon and xenon, the T6 cathode [113, 121], Domonkos’s cathodes (AR3, EK6, SC012) [64], the NSTAR discharge cathode [111, 116, 122], the NEXIS cathode [60, 105, 115], the JPL 1.5 cm LaB₆ cathode [29, 30], and our own cathode. The dataset has 422 points, includes data for argon, xenon, and mercury, and spans operation from low to high current (1–307 A) and mass flow rate (0.5–19.8 sccm of Xe, 3.9–218 sccm of Ar, 0.35–1.4 sccm of Hg). The distribution is shown both as a histogram with 40 bins and as a density function obtained with the Kernel Density Estimation (KDE) technique. We use a Gaussian kernel for the KDE with an optimum bandwidth that is found using a grid search with cross-validation. The KDE method, grid search, and cross-validation are implemented in the Python library `scikit-learn` [132]. Due to the decaying nature of the solutions to the ambipolar diffusion equation, for the very high total pressures (164–609 Torr) measured in cathodes from [64] we expect that the peak plasma density occurs in the orifice as opposed to the insert region. To reflect this, we show in Figure 6.1(b) the pressure-diameter product where we have used the orifice diameter for the cathodes presented in [64] and the insert diameter for all other cathodes. We see that the operation of cathodes is distributed mostly in a region where the pressure-diameter product is 10 Torr-cm or less. The most probable pressure-diameter is 3.7 Torr-cm.

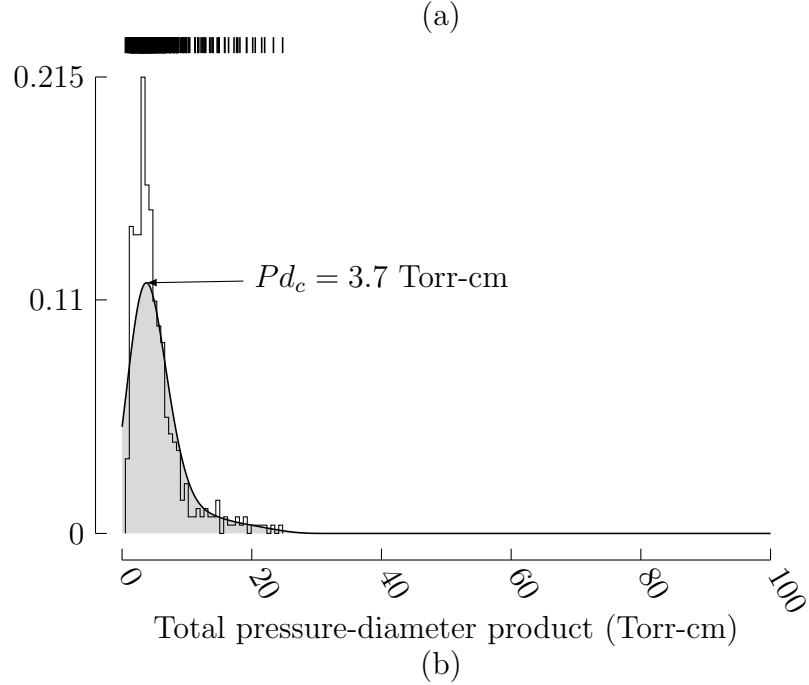
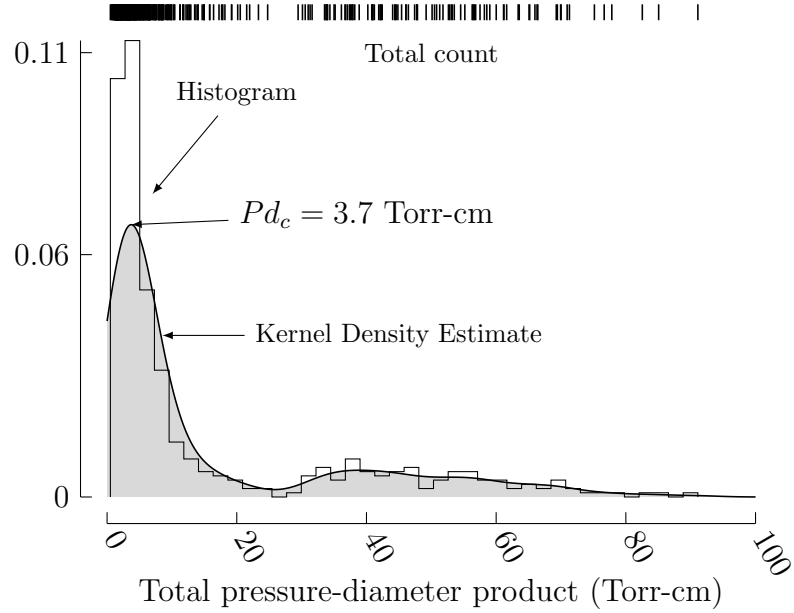


Figure 6.1: Distribution of total pressure-diameter product for a large number of cathodes. (a) Pressure-diameter product calculated using the insert diameter for all cathodes. (b) Pressure-diameter product calculated using the orifice diameter for only those cathodes presented in [64].

6.2 Total pressure

Figure 6.2 shows the variation of the ratio of the measured pressure (P) to the magnetic pressure (P_{mag}) for a variety of cathodes. Both experimental and numerical results are shown. Results are presented as a function of the dimensionless ratio of the discharge current to the mass flow rate (I_d/\dot{m}) where the mass flow rate is expressed in equivalent-amperes. Experimental data suggest that $P/P_{mag} \propto (I_d/\dot{m})^{-r}$ where $1 < r < 2$. The shaded area bounds the results of the range of the free parameters of the numerical algorithm, the neutral gas temperature (T_n) and the sheath voltage (ϕ_s). Both parameters have a range of 2000–4000 K and 1–10 V, respectively. The numerical results capture the decreasing trend within the range of the two free parameters.

6.2.1 Scaling law

We seek to explain the observed trend in the ratio of total pressure to magnetic pressure. We start with the original momentum balance derived in the previous chapter,

$$P = P_{mag} + P_{gd} + P_{mf} + P_{exit}, \quad (6.1)$$

where P_{mag} , P_{gd} , P_{mf} , P_{exit} are the magnetic pressure on orifice plate and orifice outlet surfaces, gasdynamic pressure contribution, orifice plate momentum flux, and orifice

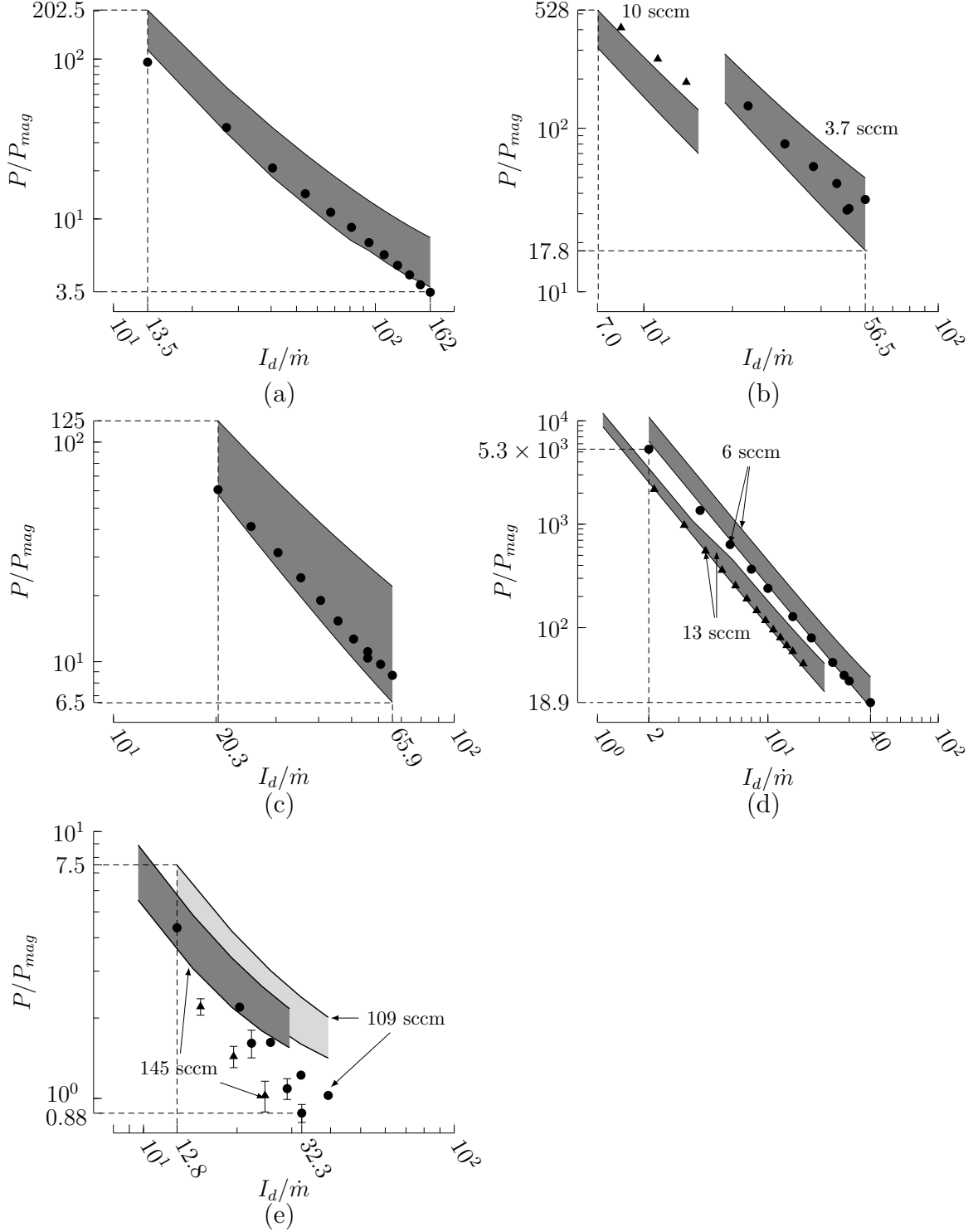


Figure 6.2: Ratio of the total to magnetic pressure (P/P_{mag}) as a function of the ratio of discharge current to mass flow rate (I_d/\dot{m}) for the following cathodes: (a) Friedly's, (b) the NSTAR, (c) the NEXIS, (d) Salhi's operating with argon and an orifice diameter of 1.21 mm, and (e) our own hollow cathode. The shaded area bounds the results of the range of the free parameters of the numerical algorithm.

outlet exit pressure, respectively. These quantities are defined as:

$$P_{mag} = \frac{\mu_0 I_d^2}{4\pi^2 r_o^2} \left(\ln \frac{r_c}{r_o} + \frac{1}{4} \right), \quad (6.2)$$

$$P_{gd} = \frac{\dot{m}}{\pi r_o^2} \sqrt{\gamma R_g (T_n + \alpha_o T_e)}, \quad (6.3)$$

$$P_{mf} = \left(\frac{r_c^2}{r_o^2} - 1 \right) e n_e^s T_{eV} \left(1 + \frac{n_e^s}{n_n} \right), \text{ and} \quad (6.4)$$

$$P_{\text{exit}} = P_V^* \left(\frac{2}{\gamma + 1} \right)^{\gamma/(\gamma-1)}. \quad (6.5)$$

In the above expressions, μ_0 , γ , and R_g denote the permeability of vacuum and the ratio of specific heat and the specific gas constant for the species considered, respectively. The electron temperature is expressed in either Kelvin (T_e) or electron-volt (T_{eV}). Plasma quantities include the sheath-edge electron density (n_e^s), insert neutral gas density (n_n), and orifice ionization fraction (α_o). P_V^* is the total (stagnation) pressure at the orifice outlet.

P_{mf} , n_e^s and T_{eV} are calculated using insert-region quantities. The fluid speed of sound appearing in the gasdynamic pressure is computed with orifice-region quantities. Equation 6.1 can be rewritten as:

$$\begin{aligned} P = P_{mag,\Pi} \times & \left[\left(\frac{1}{4} + \ln \frac{r_c}{r_o} \right) \right. \\ & + 4\pi \left(\frac{\dot{m}_A}{I_d} \right)^2 \left(\frac{M r_o}{\mu_0 e^2} \right) \left(\frac{1}{\pi r_o^3 n_n^o} \right) \left[1 + \frac{F(\gamma)}{\sqrt{1 + \alpha_o T_e/T_n}} \right] \\ & \left. + \frac{P_{mf}}{\mu_0 I_d^2 / (4\pi^2 r_o^2)} \right], \end{aligned} \quad (6.6)$$

where $P_{mag,\Pi}$ is the magnetic pressure as defined in Chapter 4:

$$P_{mag,\Pi} = \frac{\mu_0 I_d^2}{4\pi^2 r_o^2}. \quad (6.7)$$

The mass flow rate \dot{m}_A is in equivalent-amperes, n_n^o is the orifice neutral density, and $F(\gamma)$ is a function of γ only:

$$F(\gamma) = \begin{cases} \frac{1}{\gamma} & \text{if } \theta = 0 \text{ (continuum flow)} \\ \sqrt{2\pi}\gamma^{-1/2} \left(\frac{2}{\gamma+1} \right)^{1/(\gamma-1)} & \text{if } \theta = 1 \text{ (molecular flow)} \end{cases} \quad (6.8)$$

We show in Figure 6.3 the variation with discharge current of (a) the ionization fraction, (b) the quantity $\langle\sigma_{iz}v\rangle T_{eV}^{1/2}$ which appears in the ratio of sheath-edge-to-insert volume electron densities (“sheath-edge ratio”), (c) the orifice neutral density, and (d) the term $\sqrt{1 + \alpha_o T_e/T_n}$ that appears in the above equation. The results are shown for a single illustrative cathode (NSTAR cathode with mass flow rate of 3.7 sccm of Xe) for the given quantity averaged over the entire parameter space (neutral temperature varying from 2,000 K to 4,000 K and sheath voltages between 1 and 10 V). Similar results are obtained with other cathodes.

For a *given mass flow rate*, we can approximate the variation of those quantities with a semi-empirical functional form:

$$\sqrt{1 + \alpha_o T_e/T_n} = C_{s,0} + C_{s,1}I_d + C_{s,2}I_d^2, \quad (6.9)$$

$$\alpha_i = C_\alpha I_d^\eta, \text{ and} \quad (6.10)$$

$$n_n^o = C_{n,0} + C_{n,1}I_d. \quad (6.11)$$

In the region of typical operation of hollow cathodes (pressure-diameter product greater than 1 Torr-cm), the term that appears in the sheath-edge ratio can be given as $\langle\sigma_{iz}v\rangle T_{eV}^{1/2} = C_\sigma (Pd)^2$.

From Equation 6.6 we can now write the ratio of total to magnetic pressure as:

$$\frac{P}{P_{mag}} = 1 + k_1 \left(\frac{\dot{m}_A}{I_d} \right)^2 \frac{1}{1 + C_{n,1}/C_{n,0}I_d} \left(1 + \frac{F(\gamma)}{C_{s,2}I_d^2 + C_{s,1}I_d + C_{s,0}} \right) + k_2 I_d^{\eta-2}, \quad (6.12)$$

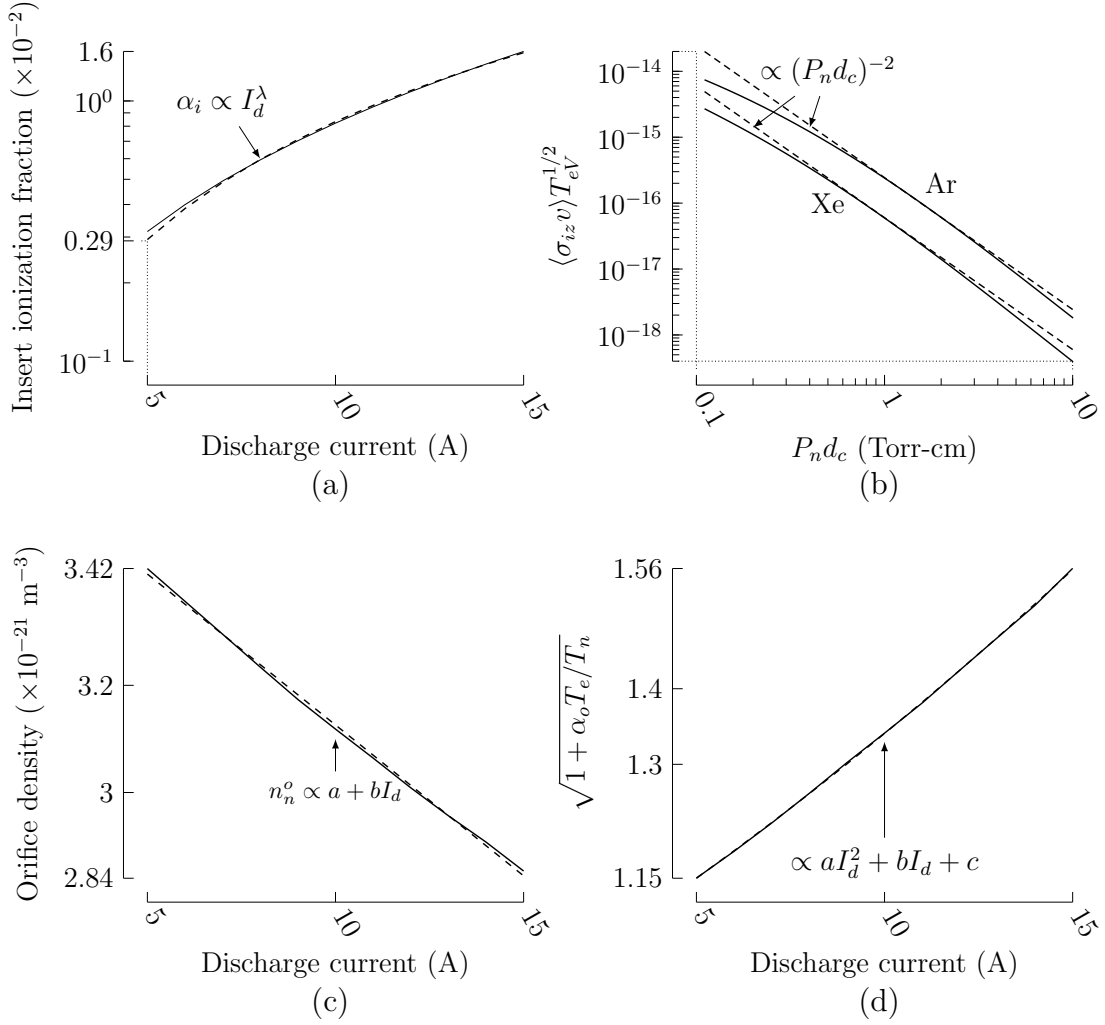


Figure 6.3: Approximation of the quantities that are necessary to find a scaling relationship for the total pressure. (a) Computed insert ionization fraction, (b) term $\langle \sigma_{iz} v \rangle T_e^{1/2}$, (c) computed orifice neutral density, and (d) term $\sqrt{1 + \alpha_o T_e / T_n}$. Results for (a), (c), and (d) are shown for the NSTAR cathode operating at 3.7 scfm only. However, all other cathodes follow similar trends (although fitting values are different).

where the two constants k_1 and k_2 depend on gas, geometry, and chosen value of heavy particle temperature:

$$k_1 = \left(\frac{Mr_o}{\mu_0 e^2} \right) \left(\frac{1}{\pi r_o^3 C_{n,0}} \right) \frac{1}{\frac{1}{4\pi} \left(\frac{1}{4} + \ln \frac{r_c}{r_o} \right)}, \text{ and} \quad (6.13)$$

$$k_2 = \frac{\pi r_o^2 e}{8\mu_0 r_c} \sqrt{\frac{M}{e}} C_\alpha C_\sigma \left(\frac{r_c^2}{r_o^2} - 1 \right) \frac{1}{(k_B T_n)^2} \frac{1}{\frac{1}{4\pi} \left(\frac{1}{4} + \ln \frac{r_c}{r_o} \right)}. \quad (6.14)$$

To obtain k_2 in this form we assumed that both the insert ionization fraction α_i and the sheath-edge ratio f_s are negligible: $\alpha_i \ll 1$ and $f_s \ll 1$. The rational function in the discharge current that arises from the orifice neutral density can always be approximated by a power law in a region where the two functions $1/(1 + C_{n,1}/C_{n,0}I_d)$ and bI_d^δ are reasonably close, where $C_{n,1} < 0$, $|C_{n,1}/C_{n,0}| \ll 1$, and $0 < \delta < 1$. This region can be defined as the values of x , b , and δ such that the Taylor expansion of either function around any point x_0 are equal to the first order or differ only by numerical constant $\epsilon \ll 1$. This in turn means that the gasdynamic term can be rewritten as:

$$\left(\frac{\dot{m}_A}{I_d} \right)^2 \frac{1}{1 + C_{n,1}/C_{n,0}I_d} \propto \left(\frac{\dot{m}_A}{I_d} \right)^{2-\delta} \dot{m}_A^\delta. \quad (6.15)$$

We recognize in the exponent $2 - \delta$ the value r suggested by the experimental data.

We note that the dimensional total pressure can be written as:

$$P = aI_d^2 + b\dot{m}_A^2 G(I_d) + dI_d^\eta, \quad (6.16)$$

where a, b, c, d , and G are found from the above expressions:

$$a = \frac{\mu_0}{4\pi^2 r_o^2} \left(\frac{1}{4} + \ln \frac{r_c}{r_o} \right), \quad (6.17)$$

$$b = \frac{M}{e^2} \frac{1}{(\pi r_o^2)^2 C_{n,0}}, \quad (6.18)$$

$$c = \frac{C_{n,1}}{C_{n,0}}, \quad (6.19)$$

$$d = \frac{e}{8r_c} \sqrt{\frac{M}{e}} C_\alpha C_\sigma \left(\frac{r_c^2}{r_o^2} - 1 \right) \frac{1}{(k_B T_n)^2}, \text{ and} \quad (6.20)$$

$$G(I_d) = \frac{1}{1 + cI_d} \left(1 + \frac{F(\gamma)}{C_{s,0} + C_{s,1}I_d + C_{s,2}I_d^2} \right). \quad (6.21)$$

We recognize in the total pressure scaling (Equation 6.16) the magnetic pressure ($\propto I_d^2$), the gasdynamic pressure ($\propto \dot{m}^2$) modified to take into account the plasma effects ($\propto G(I_d)$) and an additional momentum flux term from the ions that are accelerated towards the orifice plate ($\propto I_d^\eta$). At low current ($I_d \rightarrow 0$) the polynomials with the discharge current terms become constant, the momentum flux term vanishes, and we recover the conservation of momentum for a gas flowing through an orifice plate (under the assumptions delineated in the previous chapter). At high current ($I_d \rightarrow +\infty$) the expression becomes:

$$P = aI_d^2 + b^* \frac{\dot{m}_A^2}{I_d} + dI_d^\eta, \quad (6.22)$$

where $b^* = b/c$. This indicates that the magnetic pressure and momentum flux terms become dominant. In the intermediate range, however, all terms must be kept.

6.2.2 Link to Π -products

The Π -products defined in Chapter 4 can also be used in Equation 6.1:

$$\Pi_1 = \Gamma(\Pi) = \frac{1}{4} - \ln \Pi_2 + \Pi_5 \left(\sqrt{1 + \alpha_o T_e / T_n} + F(\gamma) \right) + \frac{P_{mf}}{P_{mag}}. \quad (6.23)$$

We confirm here that the Π -products we identified as the most relevant for the calculation of the pressure are Π_4 and Π_5 . Π_4 , which is related to the ionization fraction, appears in the orifice plate momentum flux, P_{mf} , because the sheath-edge density is directly proportional to the ionization fraction in the insert. We also verify that the cathode aspect ratio (Π_2) does not have a significant effect on the ratio of total-to-magnetic pressure because (i) it spans only a single order of magnitude (0.07–0.7) and (ii) it appears in a logarithm. The term under the square root can be estimated by considering that

- $0.001 < \alpha_o < 0.1$,
- $1 < T_e < 3$ eV, and
- $2000 < T_n < 4000$ K.

We obtain $1 < \sqrt{1 + \alpha_o T_e / T_n} < 2$. If we further neglect the momentum flux (P_{mf}) the expression simplifies to:

$$\Pi_1 = \frac{1}{4} - \ln \Pi_2 + C \Pi_5, \quad (6.24)$$

where $C \approx 3.43$ (taking the average value for the square-root term and $F(\gamma)$). We show in Figure 6.4 the correlation applied to the entire dataset. Most of the variation is captured by the above relationship. Deviations from the correlation may be explained by the plasma effects that we neglected (Π_4).

6.3 Electron temperature and attachment length

As discussed in Chapter 5, both attachment length and electron temperature are sensitive only to the neutral gas density-insert diameter product for the range of values considered. For a constant heavy particle temperature this corresponds to

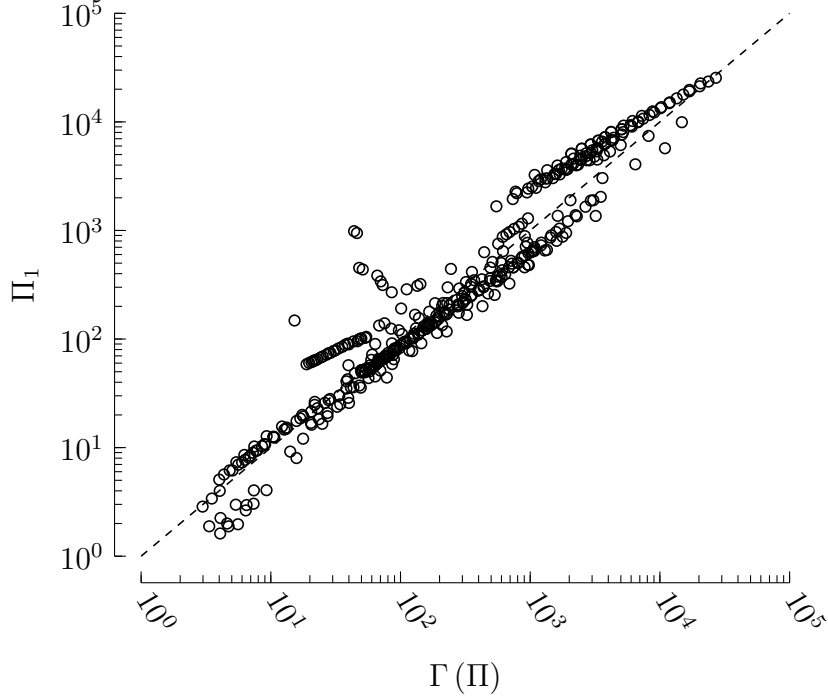


Figure 6.4: Theoretically-derived correlation applied to the entire experimental dataset.

the neutral pressure-diameter product. The following semi-analytical expressions for both electron temperature,

$$T_{eV}^{\text{insert}} = \frac{t_{i,0}}{(P_n d_c)^{t_{i,1}}} + t_{i,2}, \quad (6.25)$$

and attachment length,

$$L_{\text{emit}} = \frac{d_c}{2} \left(l_0 + \frac{l_1}{\ln^6(P_n d_c + l_2)} \right), \quad (6.26)$$

can be obtained by fitting the results of the ambipolar diffusion model as functions of the pressure-diameter product and the ratio of orifice to insert diameter to the functional forms given above. d_c and $P_n = n_n k_B T_n$ are the insert diameter and the neutral gas pressure, respectively. The coefficients $t_{i,k}$ and l_k for xenon and argon gases

are given in Appendix C. In all cases, the pressure-diameter product that appears in the denominator is in Torr-cm.

We show the attachment length and electron temperature as calculated using the ambipolar diffusion model (Equations 6.25 and 6.26) in Figure 6.5. We compare the model results to experimental data extracted from the dataset that we described in Chapter 3. The experimental data is here limited to orificed hollow cathodes operating on xenon gas. Results are shown as a function of the neutral gas pressure-diameter product. The neutral gas pressure for the experimental data is obtained from the 0-D theoretical model. We obtain good agreement between the model and experimental data, which suggests that the model is capable of capturing the appropriate physics.

Figure 6.5(a) shows that the attachment length varies between 0.8 and 1.2 times the cathode insert radius and scales weakly with the pressure-diameter product. As defined, it is insensitive to the orifice diameter, as suggested experimentally [42] (p.267). We also show in Figure 6.5(a) the previous, empirically derived scaling relationship suggested in [49] ($L_{\text{emit}} = K/P$, where K is a constant between 5–15 Pa-m). We plot the results using the neutral gas pressure (as opposed to the total pressure). A similar expression can be derived using the results from the electron transport approach of [52] if one considers sheath voltages less than 8 V for xenon. The corresponding constant is between 0.01–15 Pa-m for ionization fractions between 0.1% and 10% and sheath potentials between 1 and 8 V.

The observed scaling of attachment length cannot be captured by the electron transport phenomena suggested in [52], nor by the purely empirical relationship given in [49] (which does not offer a mechanistic explanation). The results of the ambipolar diffusion model suggest that the observed behavior is governed not by the total static pressure but by the *neutral gas* pressure. When supplied with the neutral gas pressure estimation of the 0-D model, the plasma density decay predicted by

the ambipolar diffusion model appears to account for the variation of the observed attachment length.

6.4 Summary

We have derived and verified scaling laws for the total pressure, attachment length, and electron temperature using the 0-D model presented and verified in the previous chapter. The scaling laws are summarized in Appendix D. Despite neglecting the variation of several properties in the insert region we find good agreement between experimental results gathered from the literature and the scaling laws. This suggests that the ambipolar diffusion model, in combination with the pressure predictions of the zero-dimensional model, captures the relevant physics that govern the scaling of the above quantities. We explore practical applications of these scaling laws in the following chapter.

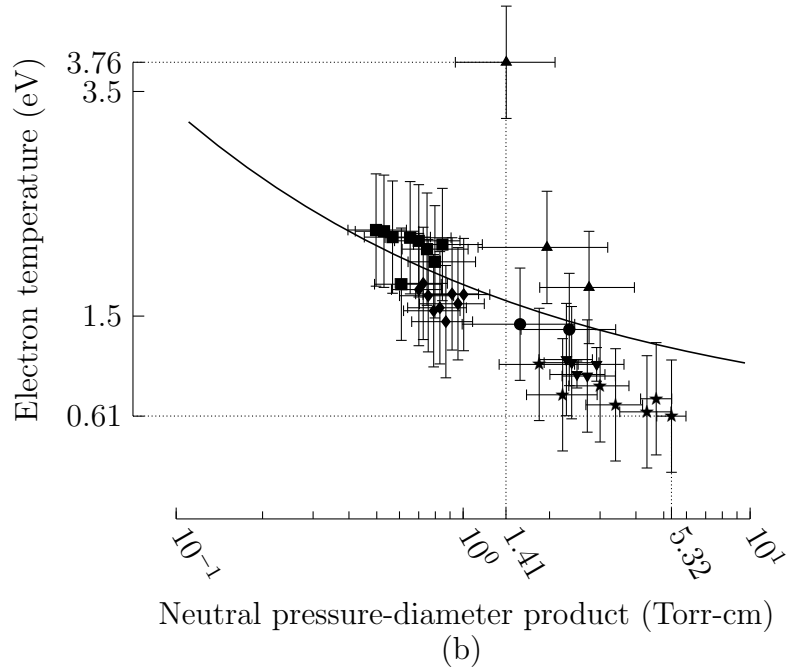
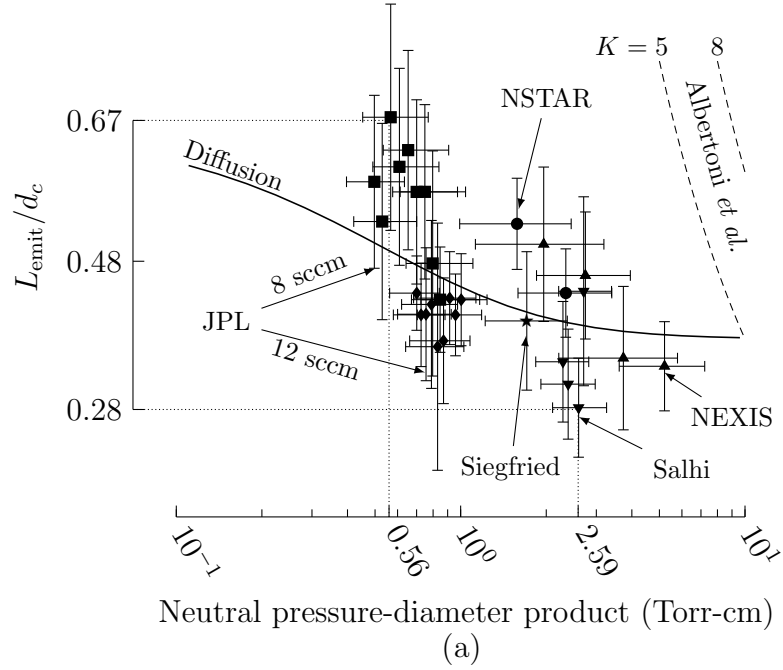


Figure 6.5: (a) Attachment length and (b) electron temperature as functions of the neutral pressure-diameter product ($P_n d_c$). Symbols for (b) are the same as (a). The horizontal error bars bounds the results of the range of the free parameters of the numerical algorithm. Experimental data from [30,47,60,65,110,111]. Scaling law for the attachment length for Albertoni *et al.* from [49] with the corresponding value of K in the range of 5–15 Pa-m.

Chapter 7

Practical applications

7.1 Implications on cathode design

The scaling laws we have derived can be applied to the design of new cathodes. We note that the following suggestions remain to be experimentally confirmed with a new cathode design and are only applicable to orificed, thermionic hollow cathodes that feature a cylindrical and hollow emitter. Other emitter geometries are beyond the scope of this work.

Emitter length Diffusion theory shows that the plasma attachment length is between 0.8–1.2 times the insert radius. This suggests that the emitter length should be equal to the insert radius for efficient use.

Operating envelope The algorithm we described in Chapter 5 can be used to compute the total pressure for a large number of operating conditions. In order to obtain a relationship between the “allowed” mass flow rate and a given geometry, the total pressure may be evaluated by considering only the neutral species for the calculation of the total pressure. The neutral gas temperature is taken to be 2000–4000 K and the orifice ionization fraction is simply zero. As discussed in Chapter 5, the

total pressure may be computed directly from the stagnation pressure (Equations 5.14 through 5.19) when only neutral gas is present. Both molecular and viscous flows can be considered. We can then use the statistically most-likely pressure-diameter product, $Pd_c \sim 3.7$ Torr-cm, to generate an operating envelope for a given cathode. We caution that this estimate does not include any effects that would account for the discharge mode or stability.

We show in Figure 7.1 this approach applied to the NSTAR, NEXIS, and our cathode operating with argon, along with the demonstrated range of mass flow rates. The estimated range of mass flow rates overlaps with the demonstrated range for

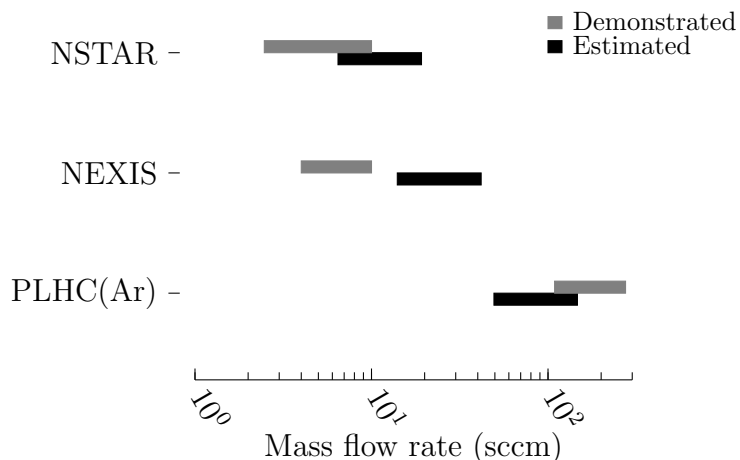


Figure 7.1: Estimated and demonstrated range of mass flow rate for select cathodes.

both the NSTAR and our cathode. The agreement is worse for both the NEXIS and our cathode because they operate at a lower and higher pressure-diameter product than the statistically most-likely one, respectively. Our approach also neglects the discharge current contribution to the total pressure which becomes significant at higher currents. Finally, our cathode typically operates at a much lower temperature than other lanthanum hexaboride cathodes: during operation the cathode tip can be as low as 800°C (the lower operating temperature of our cathode can be explained by its larger emission area).

7.2 Lifetime calculation

The lifetime of a cathode can be quantified using both the scaling relationship for the emission length and an estimate of the neutral pressure. We describe here an iterative procedure to calculate this lifetime.

7.2.1 Evaporation-limited lifetime

For simplicity, we consider material evaporation only from the active zone. The lifetime of the emitter is given by the total time required for the insert diameter to reach its outer diameter by evaporation. The total mass removed during a time period $\Delta t = t^{n+1} - t^n$ is:

$$m_{\text{loss}} = W_n \Delta t A_{em,n} = W_n \Delta t \pi d_{c,n} L_{\text{emit},n}, \quad (7.1)$$

where W_n , $A_{em,n}$, $d_{c,n}$, and $L_{\text{emit},n}$ are the evaporation rate, total emission area, insert diameter, and emission length, at time t^n , respectively. The corresponding volume of material is obtained by dividing the total mass loss by the mass density of the emitter, ρ_{emitter} :

$$V_{\text{loss}} = \frac{m_{\text{loss}}}{\rho_{\text{emitter}}}. \quad (7.2)$$

The volume lost is also given by:

$$V_{\text{loss}} = \frac{\pi}{4} (d_{c,n+1}^2 - d_{c,n}^2). \quad (7.3)$$

Combining Equations 7.2 and 7.3 gives the new insert cathode diameter:

$$d_{c,n+1} = \left(d_{c,n}^2 + \frac{4W_n d_{c,n} \Delta t}{\rho_{\text{emitter}}} \right)^{1/2}. \quad (7.4)$$

We must now estimate the emission length and evaporation rate.

Emission length The emission length is computed from the insert diameter and pressure at time t^n with Equation 5.27. The neutral pressure may be computed with the full 0-D model. Alternatively, the neutral pressure may be estimated with the empirical fit for the *total* pressure (Equation 4.27). Because the estimated neutral pressure is then higher, the emission length ($\propto 1/(P_g d_c)$) is then lower. The corresponding current density, emitter wall temperature, and evaporation rate are consequently higher. This yields a conservative estimate of the evaporation-limited lifetime of the emitter.

Evaporation rate For the target current I_d and current density, the Richardson-Dushman equation may be inverted in order to find the emitter temperature T_c :

$$\frac{I_d}{\pi d_c^n L_{\text{emit}}} = D_{RD} T_c^2 \exp\left(\frac{-e\phi_w}{k_B T_c}\right). \quad (7.5)$$

The evaporation rate is then calculated with the fit to experimental data from [147]:

$$W = \frac{10^{C-B/T_c}}{\sqrt{T_c}}, \quad (7.6)$$

where $C = 13$ and $B = 36850$ K.

Algorithm The initial insert diameter is given by the specified geometry. Once the pressure is estimated (either with the 0-D model or the empirical fit), we compute the emission length, current density, wall temperature, and evaporation rate, and then update the insert diameter with Equation 7.4. The procedure is repeated as long as the insert diameter is smaller than the insert outer diameter ($d_{c,n} < d_{c,\text{outer}}$).

7.2.2 Results

The emission length as defined (density decay length-scale) provides a lower-bound on the actual emission length [136]. As a consequence, the effective emission area is smaller than the physical one, and, therefore, the computed current density is larger than the physical one. This increases the computed temperature and evaporation rate and provides a conservative value of the lifetime. For example, the algorithm applied to the JPL 1.5 cm cathode equipped with a 3 mm orifice diameter predicts a total lifetime of 4.5 kh. This is one order of magnitude lower than the results presented in [29] without material re-deposition.

Despite its limitations, the procedure can be applied to a “generic” cathode in order to obtain qualitative insights. We consider here a LaB₆ cathode operating on xenon, with an orifice length of 1 mm, an insert diameter of 1 cm, and an orifice diameter given by $d_o = \bar{r}d_c$, where $0.01 < \bar{r} < 0.3$. The outer diameter of the insert is 5% larger than its inner diameter. The nominal discharge current and mass flow rate are 25 A and 10 sccm, respectively. Figure 7.2 shows the effect of the ratio of mass flow rate to discharge current and of \bar{r} on the computed lifetime. The mass flow rate (in equivalent-amperes) is normalized by the nominal discharge current, and the computed lifetime is normalized by its maximum value. Increasing both the mass flow rate and the discharge current results in the lowering of the total lifetime, as suggested by Albertoni *et al.* [49]. For a fixed insert diameter, an increase in the orifice diameter yields an increase in the total lifetime.

Both behaviors can be explained through the scaling of the attachment length and pressure. Because of the low ionization fraction in the insert plasma, the neutral gas pressure can be approximated as the total gas pressure. The total pressure increases both as a function of mass flow rate and discharge current, and decreases with increasing orifice diameter (all other quantities fixed). We have from the empirical

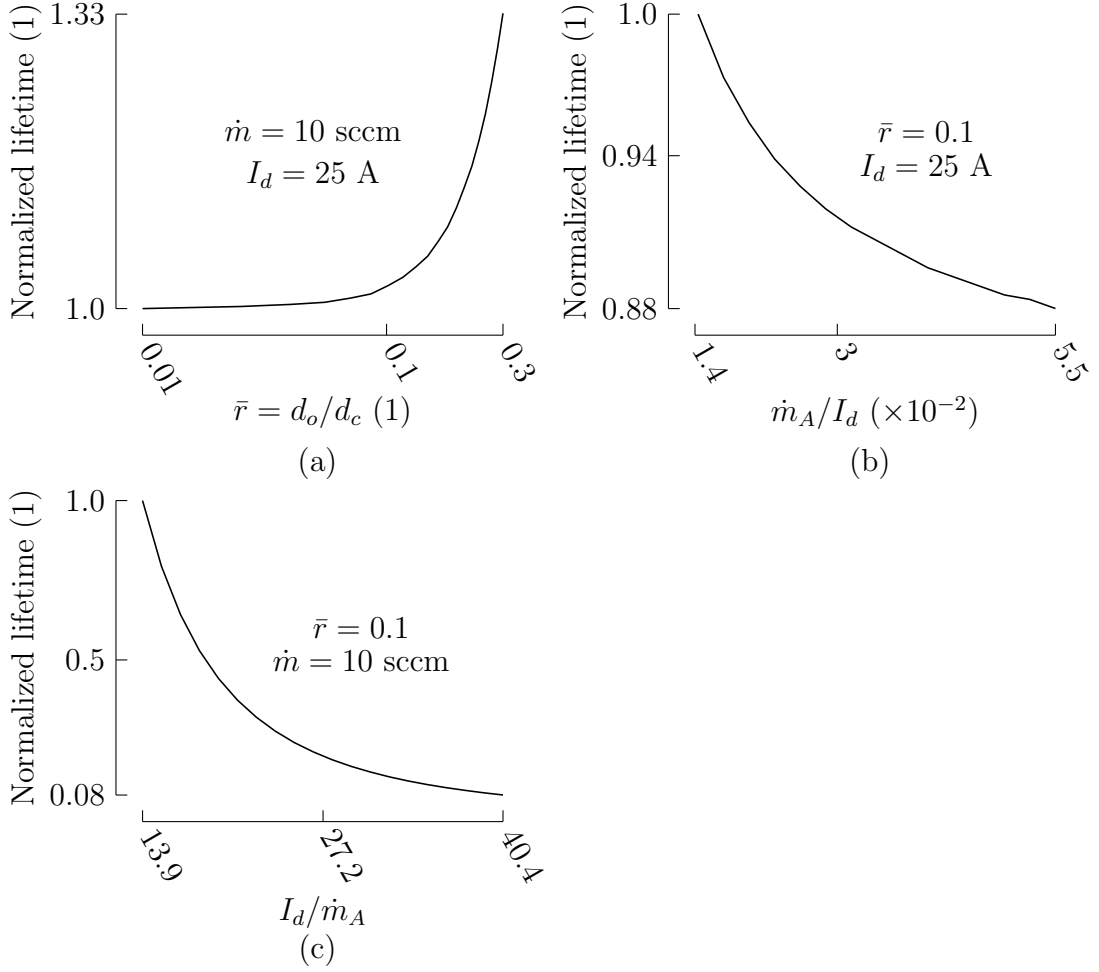


Figure 7.2: Effect of (a) orifice-to-insert diameter ratio, (b) mass flow rate, (c) discharge current on the computed lifetime.

analysis of the total pressure:

$$P \propto \dot{m}^{0.68} I_d^{0.4} d_o^{-1.9}. \quad (7.7)$$

Because the emission length scales inversely with the neutral gas pressure (here considered to be the total gas pressure), an increase in either the mass flow rate or the discharge current yields a lower value of the emission length, and, therefore, a higher current density, wall temperature, and evaporation rate. The increase in evaporation rate results in a decrease in the lifetime of the emitter. An increase in the orifice-to-insert diameter ratio has the opposite effect as it increases the emission length.

Chapter 8

Conclusion

Our goal was to develop tools that inform cathode design. To do so, we sought to quantify, through basic scaling laws derived from a rigorous theoretical model, the variation of insert plasma quantities with controllable parameters and cathode geometry.

The new cathode model we developed to uncover scaling laws addresses some of the critical issues of existing 0-D models. It relies on assumptions that were informed by a dimensional analysis of the experimentally measured total pressure within the cathode. Experimental pressure measurements were taken from the literature and our own, high-current hollow cathode. The model is based on a rigorous approach to the ionized gas flow and considers the three-fluid flow as a single, partially-ionized gas. We applied the model to a large number of cathodes and verified the numerical results by comparing them to experimental measurements. We finally formulated and verified scaling laws based on the results of the theoretical model.

The results of this dissertation are separated into three categories:

- the scaling of total pressure, emission length, and electron temperature inside hollow cathodes,
- the implications of scaling laws on cathode design, and

- the development of tools for cathode design.

8.1 Summary of main findings

8.1.1 Scaling laws

Total pressure The total pressure scales both with the square of the mass flow rate multiplied by a weak function of the discharge current, and with the square of the discharge current. This scaling can be physically interpreted as due to the relative importance of the magnetic pressure and the gasdynamic pressure. Our empirical analysis reveals that the contribution of the gas viscosity to the total pressure is small compared to that of the plasma and gasdynamic effects.

Emission length, electron temperature Both the emission length and electron temperature show an inverse dependency on the neutral pressure-diameter product. The diffusion-dominated nature of the insert plasma can account for the scaling of both quantities.

8.1.2 General design considerations

The scaling laws we uncovered lead to the following “rules of thumb” for cathode design:

- reliable cathode operation is likely if the total pressure-insert diameter product is in the range of 3–4 Torr-cm,
- for effective insert utilization, the length of the insert should be equal to its radius,
- cathode lifetime can be extended by operating at lower mass flow rate and discharge current for a given geometry.

8.1.3 Tools for cathode design

We developed computational tools for the design of new cathodes:

- The theoretical 0-D model may be used as the first-step in the design of a new cathode.
- For fast computations, the combination of the condition that $Pd_c \approx 3\text{--}4$ Torr-cm and the empirical relationship we calculated from experimental data can be used to determine a range of operating conditions for a given geometry and operating gas.
- An estimate of the “allowed” mass flow rate may be calculated with the combination of the total pressure-diameter product and the theoretical expression for the total pressure.

8.2 Future work

8.2.1 Model improvements

The 0-D model we developed relies on two free parameters (sheath potential and neutral gas temperature) that can be bounded. Incorporating those parameters self-consistently most likely requires a full 2-D model of the cathode. This approach is an improvement over a 0-D model and can reveal the true emission length, and, therefore, provide reliable estimates of cathode lifetime for given operating conditions.

Neutral gas temperature To remove the dependency on the neutral gas temperature, the fluid flow must include the neutral energy equation. Removing the semi-empirical correlations for transitional flows is an additional improvement on the flow modelization. It requires an approach that can treat both continuum ($\text{Kn} \ll 1$) and molecular ($\text{Kn} \gg 1$) flows.

Sheath potential A sheath model requires a 2-D approach because the equation to solve for the plasma potential within the cathode is elliptic, and, therefore, requires information on all boundaries simultaneously. A self-consistent sheath model is challenging: the thermionic sheath is not only emitting electrons that modify the boundary potential and electric field, but also current-carrying.

8.2.2 Further verification of scaling laws

Can the scaling laws we have developed be applied to new cathode designs and different gases? A new cathode that is based on the scaling laws and the simple rules we have developed should be developed and tested in order to verify their applicability. We have partially answered this question for the total pressure within high-current cathodes. However, the scaling of emission length and electron temperature within high-current (> 100 A) cathodes remains to be verified with on-axis plasma measurements.

The charge-exchange-dominated nature of the insert plasma for noble gas cathodes is also the case for mercury-fed cathodes because mercury also has a large charge-exchange cross section ($\propto 10^{-18}$ m²) [148–151]. Although hydrogen-fed cathodes also satisfy the pressure-diameter condition, it is unclear if the same physical phenomena govern their operation, as hydrogen features additional excited states (*e.g.*, vibrational modes) and multiple neutral and ion species (H_2 , H , H_2^+ , H^+) that our approach does not take into account. Because iodine gas is now considered for new cathode designs for electric propulsion applications [152–154] it is critical to perform a thorough investigation of the applicability of those scaling laws to molecular propellants.

Appendix A

Π -product derivation

The order in which Ipsen's method is carried yields different Π products. We show here the sequence we used in Chapter 4. We start with Equation 4.1:

$$\underbrace{P}_{\text{kg}\cdot\text{m}^{-1}\cdot\text{s}^{-2}} = f \left(\underbrace{d_o}_{\text{m}}, \underbrace{d_c}_{\text{m}}, \underbrace{L_o}_{\text{m}}, \underbrace{\dot{m}}_{\text{kg}\cdot\text{s}^{-1}}, \underbrace{I_d}_{\text{C}\cdot\text{s}^{-1}}, \underbrace{M}_{\text{kg}}, \underbrace{a}_{\text{m}\cdot\text{s}^{-1}}, \underbrace{e\epsilon_{iz}}_{\text{kg}\cdot\text{m}^2\cdot\text{s}^{-2}}, \underbrace{\mu}_{\text{kg}\cdot\text{m}^{-1}\cdot\text{s}^{-1}}, \underbrace{\mu_0}_{\text{kg}\cdot\text{m}\cdot\text{C}^{-2}} \right). \quad (\text{A.1})$$

We first remove units of length (m) with the orifice diameter, d_o , and obtain both $\Pi_2 = d_o/d_c$ and $\Pi_3 = d_o/L_o$. The leftover units are:

$$\underbrace{Pd_o}_{\text{kg}\cdot\text{s}^{-2}} = f \left(\underbrace{\dot{m}}_{\text{kg}\cdot\text{s}^{-1}}, \underbrace{I_d}_{\text{C}\cdot\text{s}^{-1}}, \underbrace{M}_{\text{kg}}, \underbrace{\frac{a}{d_o}}_{\text{s}^{-1}}, \underbrace{\frac{e\epsilon_{iz}}{d_o^2}}_{\text{kg}\cdot\text{s}^{-2}}, \underbrace{\mu d_o}_{\text{kg}\cdot\text{s}^{-1}}, \underbrace{\frac{\mu_0}{d_o}}_{\text{kg}\cdot\text{C}^{-2}} \right). \quad (\text{A.2})$$

We now remove units of charge (C) and mass (kg) with the ratio $\frac{\mu_0}{d_o}$ and the mass flow rate, \dot{m} , respectively:

$$\underbrace{\frac{Pd_o}{\dot{m}}}_{\text{s}^{-2}} = f \left(\underbrace{\frac{\dot{m}}{M}}_{\text{s}^{-1}}, \underbrace{\frac{\mu_0 I_d^2}{\dot{m} d_o}}_{\text{s}^{-1}}, \underbrace{\frac{a}{d_o}}_{\text{s}^{-1}}, \underbrace{\frac{e\epsilon_{iz}}{\dot{m} d_o^2}}_{\text{s}^{-2}}, \underbrace{\frac{\mu d_o}{\dot{m}}}_{1} \right). \quad (\text{A.3})$$

The orifice Reynolds number is written as

$$\text{Re} = \frac{\rho a d_o}{\mu}. \quad (\text{A.4})$$

By virtue of the continuity equation ($\dot{m} = \rho a \pi r_o^2$), it can be shown that:

$$\text{Re} = \frac{4}{\pi} \frac{\dot{m}}{\mu d_o}. \quad (\text{A.5})$$

The inverse of the dimensionless ratio $\frac{\mu d_o}{\dot{m}}$ is therefore proportional to the Reynolds number. This yields the 7th Π -product: $\Pi_7 = \text{Re}$.

We finally remove units of time (s) using the ratio $\frac{\mu_0 I_d^2}{\dot{m} d_o}$, and re-introduce the dimensionless ratios already formed:

$$\frac{P d_o^2}{\mu_0 I_d^2} = f \left(\frac{d_o}{d_c}, \frac{d_o}{L_o}, \frac{\dot{m}}{M} \frac{\dot{m} d_o}{\mu_0 I_d^2}, \frac{a}{d_o} \frac{\dot{m} d_o}{\mu_0 I_d^2}, \frac{e \epsilon_{iz}}{d_o^2} \frac{d_o}{\mu_0 I_d^2}, \text{Re} \right). \quad (\text{A.6})$$

The Π -products as shown in Chapter 4 are directly obtained from algebraic manipulation of the above equation.

Appendix B

Cathodes reviewed

Table B.1 lists the cathodes and range of operating conditions that we used for this work. For some of the cathodes, we note that operating conditions that are different from the ones reported in Table B.1 exist (*e.g.*, Salhi's cathode also has a 1.27 mm diameter orifice). However, we could not gather relevant experimental data (total pressure, attachment length, electron temperature) for those cases. Because of the difficulty of gathering reliable cathode dimension data, we report all of the possible dimensions in Table B.2. In both tables, the following abbreviations are used:

- *L.*: Length
- *I.D.*: Inner Diameter
- *O.D.*: Outer Diameter

Table B.1: Dimensions and operating conditions of the benchmark cathodes.

Cathode	Dimension (mm)						Species	Mass flow (sccm)	Current (A)	Pressure (Torr)	Refs. for data
	L	Insert I.D.	O.D.	L	Orifice D	Tube D					
Siegfried and Wilbur	25.4	3.9	4.0	1.8	0.76	0.63	Hg	0.35 – 1.42	1.27 – 4.3	1.3 – 6.2	[72, 120, 126]*
		3.8			0.76		Ar, Xe	0.8 – 8.0	1.24 – 4.3	1.8 – 16.6	[65]
Friedly	13.0	4.7	N/A	1.0 [†]	0.74	6.4	Xe	2.51 – 6.41	5.0 – 60.0	5.9 – 52.7	[112]
Salhi	25.4	3.81	5.53	1.24	0.76, 1.21	6.35	Ar	0.5 – 1.24	1.0 – 20.0	4.8 – 25.3	[47]
					1.21		Xe	0.5 – 0.93		6.5 – 14.7	
AR3	25.4	1.22	2.29	0.38	0.13	3.18	Xe	1.40 – 2.40	1.0	250.4 – 345.6	[64]
EK6		1.17		0.71				0.8 – 3.25	0.5 – 1.5	270.2 – 609.4	
SC012		1.8		0.5				0.57 – 2.44		163.7 – 506.1	
T6	20.0	2	5	2	1	7	Xe	0.51 – 11.5	5 – 15	6.4 – 41.1	[113, 121]
NSTAR	25.4	3.8	4.3	0.74	1.02	6.35	Xe	2.47 – 10	5.95 – 15	4.0 – 27.5	[111, 116, 122]
NEXIS	25.4	12.7 [‡]	14.2 [§]	0.74 [¶]	2.5, 2.75, 3.0	15	Xe	4 – 10	4 – 32	0.66 – 2.76	[60, 105, 115]

JPL-1.5cm	25.4	7	13	1.0 [†]	3.8 3, 5	15	Xe	8 – 12 10.5 – 19.8	20 – 100 8.9 – 35.1	1.9 – 2.6 2.4 – 3.4	[30] [29]
PLHC	80.4	27.15	31.2	1.5	5.6	36.2	Ar	109 – 218	100 – 307	2.44 – 5.4	This work

* See [72] pp.17–18 and p.139 for the dimensions and orifice length.

[†] The orifice length is not specified for those cathodes and is set to 1.0 mm.

[‡] We follow later work by Goebel and Katz [42] where the insert diameter is set to 1.27 cm. We note, however, that the insert inner diameter has also been suggested to be equal to 1.20 cm in [60, 107, 109].

[§] The outer diameter for the NEXIS cathode is deduced from insert thickness data retrieved from [60] and [107].

[¶] Measured from plots in [107].

Table B.2: Comprehensive list of dimensions (in mm) of the benchmark cathodes.

Cathode	Insert			Orifice		Tube	Species	Refs.
	L	I.D.	O.D.	L	D	D		
Siegfried	25.4	1.9, 3.8, 3.9	4.0	1.8	0.51, 0.76, 0.79, 0.96	0.63	Ar, Hg, Xe	[52, 65, 69, 71, 72, 120, 126]
Friedly	13.0	4.7, 6.4	N/A	N/A	0.74 – 1.70	6.4, 12.8	Xe	[112]
Salhi	25.4	3.81	5.53	1.24	0.76, 1.21, 1.27	6.35	Ar, Xe	[47]
AR3	25.4	1.22	2.29	0.38	0.13	3.18	Xe	[64]
EK6		1.17		0.71				
SC012		1.8	3.8	0.5		4.8		
T6	20.0	2	5	2	0.75, 1.0, 1.3, 1.6	7	Xe	[113, 121, 155]
NSTAR	25.4	3.8	4.3	0.74	1.02	6.35	Xe	[42, 83, 92, 106–108, 131]
NEXIS	25.0, 25.4	12.0, 12.7	N/A	N/A	1.5, 2.0, 2.5, 2.75, 3.0	15	Xe	[42, 60, 105, 107, 109, 110, 131]
JPL-1.5cm	25.4	7	13	N/A	3, 3.8, 5	15	Xe	[30, 156, 157]
PLHC	80.4	27.15	31.2	1.5	5.6	36.2	Ar	This work

Appendix C

Coefficients for the total pressure, electron temperature, and attachment length

C.1 Total pressure

We give the Π -product exponents with additional digits to ensure accurate computations. Equations for the total pressure (4.27 and D.1) are given below with additional

C	$1.1585377838117006 \times 10^7$
β_1	0.78967753163551446
β_2	0.22577194077376095
β_3	-0.26766913155894489
β_4	0.81622790719254079
β_5	0.25441804916181782
β_6	0.40591950688859579

Table C.1: Π -product exponents and constant.

accuracy:

$$\begin{aligned}
P \text{ (Pa)} &= 1.27554360581865 \times 10^{-8} I_d^{0.394046350409172} T_n^{0.40811395359627} \\
&\times \dot{m}^{0.686809150963247} \epsilon_{iz}^{0.254418049161818} \\
&\times \frac{1}{L_o^{0.225771940773761} M^{0.140444822037326} \mu^{0.405919506888596} d_c^{0.789677531635514} d_o^{1.91255721520008}}
\end{aligned} \tag{C.1}$$

$$\begin{aligned}
P \text{ (Torr)} &= 2.12926144880254 \times 10^{-7} I_d^{0.394046350409172} T_n^{0.40811395359627} M_a^{0.546364328925921} \\
&\times \dot{m}_{\text{sccm}}^{0.686809150963247} \epsilon_{iz}^{0.254418049161818} \\
&\times \frac{1}{L_{o,\text{cm}}^{0.225771940773761} \mu^{0.405919506888596} d_{c,\text{cm}}^{0.789677531635514} d_{o,\text{cm}}^{1.91255721520008}}
\end{aligned} \tag{C.2}$$

C.2 Electron temperature and attachment length

Table C.2: The coefficients used for the insert electron temperature and attachment length correlations (Equations 5.25 and 5.27).

Species	Quantity	Index		
		0	1	2
Xe	T_{eV}	1.3	0.34	0.48
	L_{emit}	0.75	1.0	3.0
Ar	T_{eV}	1.91	0.341	0.945
	L_{emit}	0.86	0.613	1.89

Table C.3: The coefficients used for the orifice electron temperature (Equation 5.26).

Species	Temperature	Index			
		0	1	2	3
Xe	2000 K	1.230	-0.0052	0.313	0.429
	3000 K	1.290	-0.0062	0.337	0.503
	4000 K	1.300	-0.0068	0.365	0.591
Ar	2000 K	1.889	-0.0197	0.287	0.793
	3000 K	1.941	-0.0250	0.320	0.935
	4000 K	1.723	-0.0257	0.401	1.250

Appendix D

Summary of scaling laws

Table D.1 summarizes the scaling laws derived in this work.

Table D.1: List of derived scaling laws.

Scaling law	Derivation
$Pd_c \propto 3.7 \text{ Torr-cm}$	Empirical
$P \text{ (Pa)} = 1.28 \times 10^{-8} \frac{I_d^{0.39} T_n^{0.41} \dot{m}^{0.69} \epsilon_{iz}^{0.25}}{L_d^{0.23} M^{0.14} \mu^{0.41} d_c^{0.79} d_o^{1.91}}$	Empirical
$P \text{ (Torr)} = 2.13 \times 10^{-7} \frac{I_d^{0.39} T_n^{0.41} M_a^{0.55} \dot{m}_{\text{sccm}}^{0.69} \epsilon_{iz}^{0.25}}{L_{o,\text{cm}}^{0.23} \mu^{0.41} d_{c,\text{cm}}^{0.79} d_{o,\text{cm}}^{1.91}},$	Empirical
$P = aI_d^2 + b\dot{m}_A^2 G(I_d) + dI_d^\eta$	Semi-analytical
$T_{eV}^{\text{insert}} = \frac{t_{i,0}}{(P_n d_c)^{t_{i,1}}} + t_{i,2}$	Semi-analytical
$L_{\text{emit}} = \frac{d_c}{2} \left(l_0 + \frac{l_1}{\ln^6(P_n d_c + l_2)} \right)$	Semi-analytical

The coefficients appearing in the semi-analytical form of the total pressure are obtained with Equations 6.17 through 6.21. We repeat them here:

$$a = \frac{\mu_0}{4\pi^2 r_o^2} \left(\frac{1}{4} + \ln \frac{r_c}{r_o} \right), \quad (\text{D.1})$$

$$b = \frac{M}{e^2} \frac{1}{(\pi r_o^2)^2 C_{n,0}}, \quad (\text{D.2})$$

$$c = \frac{C_{n,1}}{C_{n,0}}, \quad (\text{D.3})$$

$$d = \frac{e}{8r_c} \sqrt{\frac{M}{e}} C_\alpha C_\sigma \left(\frac{r_c^2}{r_o^2} - 1 \right) \frac{1}{(k_B T_n)^2}, \text{ and} \quad (\text{D.4})$$

$$G(I_d) = \frac{1}{1 + cI_d} \left(1 + \frac{F(\gamma)}{C_{s,0} + C_{s,1}I_d + C_{s,2}I_d^2} \right). \quad (\text{D.5})$$

The fitting coefficients $C_{s,i}$, $C_{n,i}$, C_α , C_σ are obtained from the results of the 0-D model presented in Chapter 5. The fitting procedure must be repeated for a given cathode and mass flow rate.

The scaling laws for the electron temperature and attachment length are obtained with the results of the ambipolar diffusion model presented in [136]. The values of the parameters t_i and l_i are found in Table C.2.

Appendix E

Associated electronics

E.1 High-voltage, high-current sense board

The differential voltage on each shunt is measured by the NI-DAQ 7206. However, during startup, the anode and keeper voltage is higher than what is tolerated by the DAQ. To ensure the differential voltage on the current shunts can be read by the DAQ we isolate the high-voltage circuit through an HCPL-790 isolation amplifier. Any voltage gain on the low-voltage side is amplified with AD823 instrumentation amplifiers. The -5 V supply necessary for the AD823 is provided by an ICL7660 chip. Figures E.1 and E.2 show the schematic and corresponding board implementation, respectively.

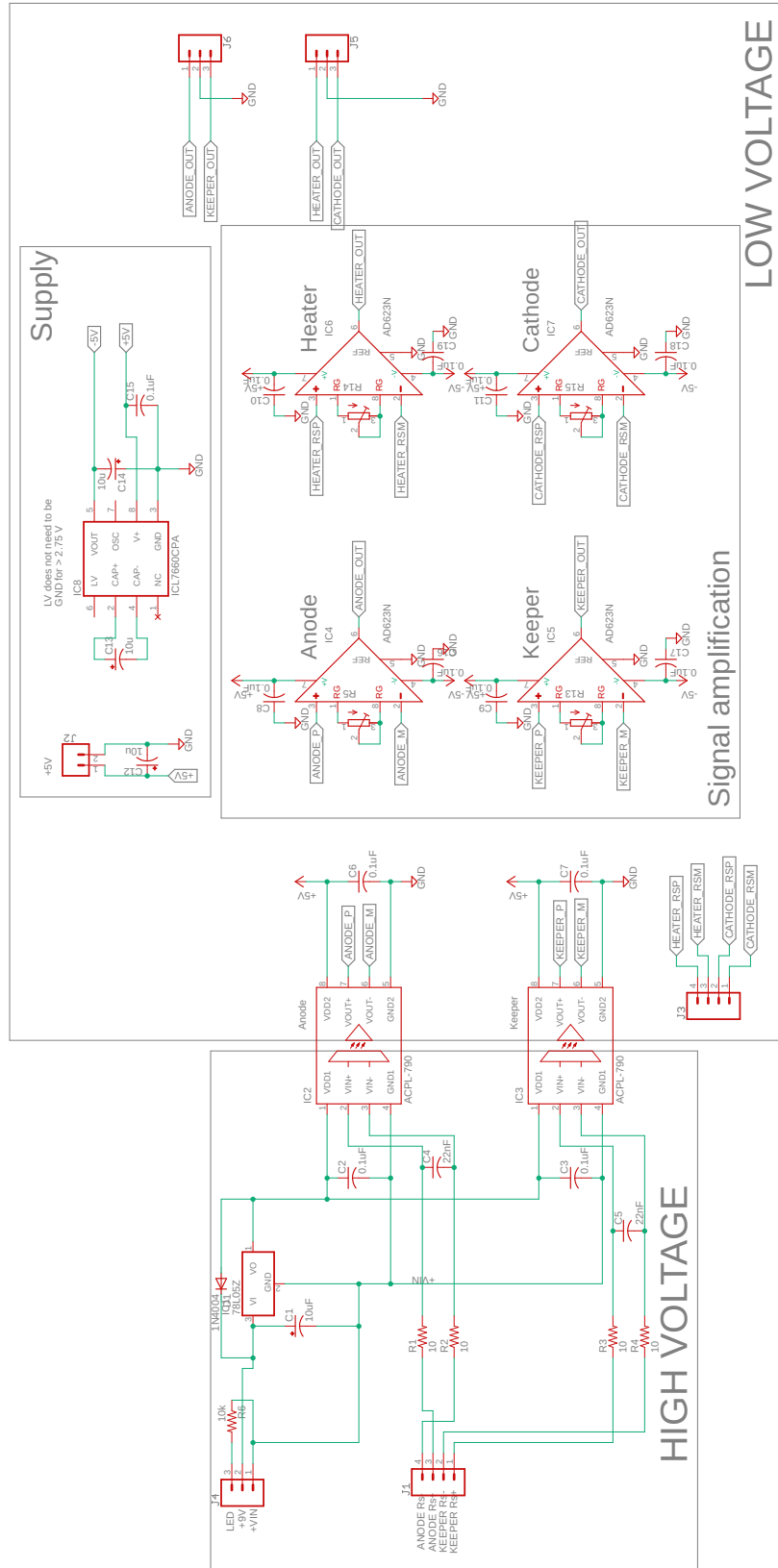


Figure E.1: Schematic of the electronics used to sense current on all shunts.

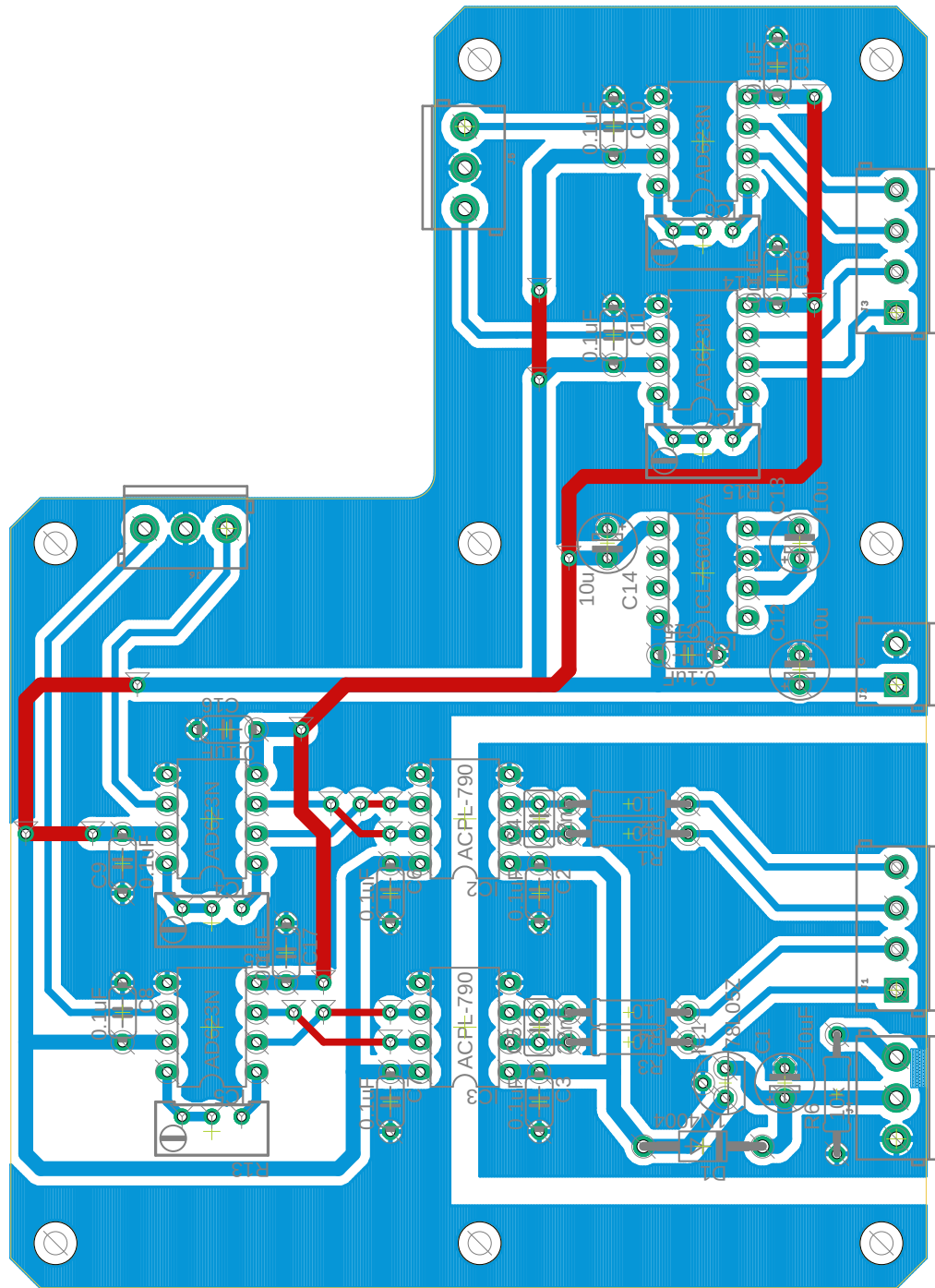


Figure E.2: Shunt board implementation. Red: top PCB layer. Blue: bottom PCB layer.

E.2 Pirani gauge power

The PVC1000 Pirani gauge requires a constant current power supply of 7 mA maximum. Push-pull configurations for constant current are too sensitive to temperature and tend to drift overtime. We use the configuration described in [158]. We use a MAX6250 as a 5 V high-precision reference voltage and an OPA277 operational amplifier. Figures E.3 and E.4 show the schematic and corresponding board implementation, respectively.

We tested the constant current power supply with an input voltage of 8.5 V. The current is measured with a Keithley model 2000 multimeter with 6.5 digits resolution, and verified to be 6.6670 mA.

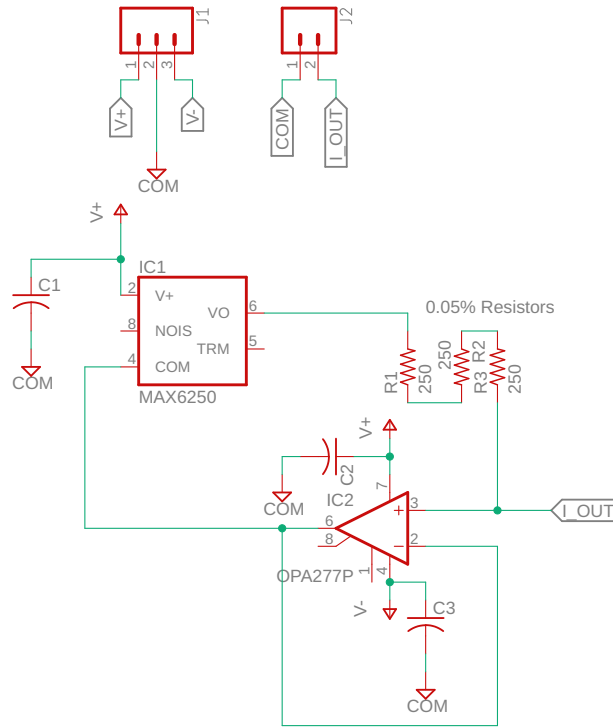


Figure E.3: Schematic of the electronics used to power the PVC1000 Pirani gauge.

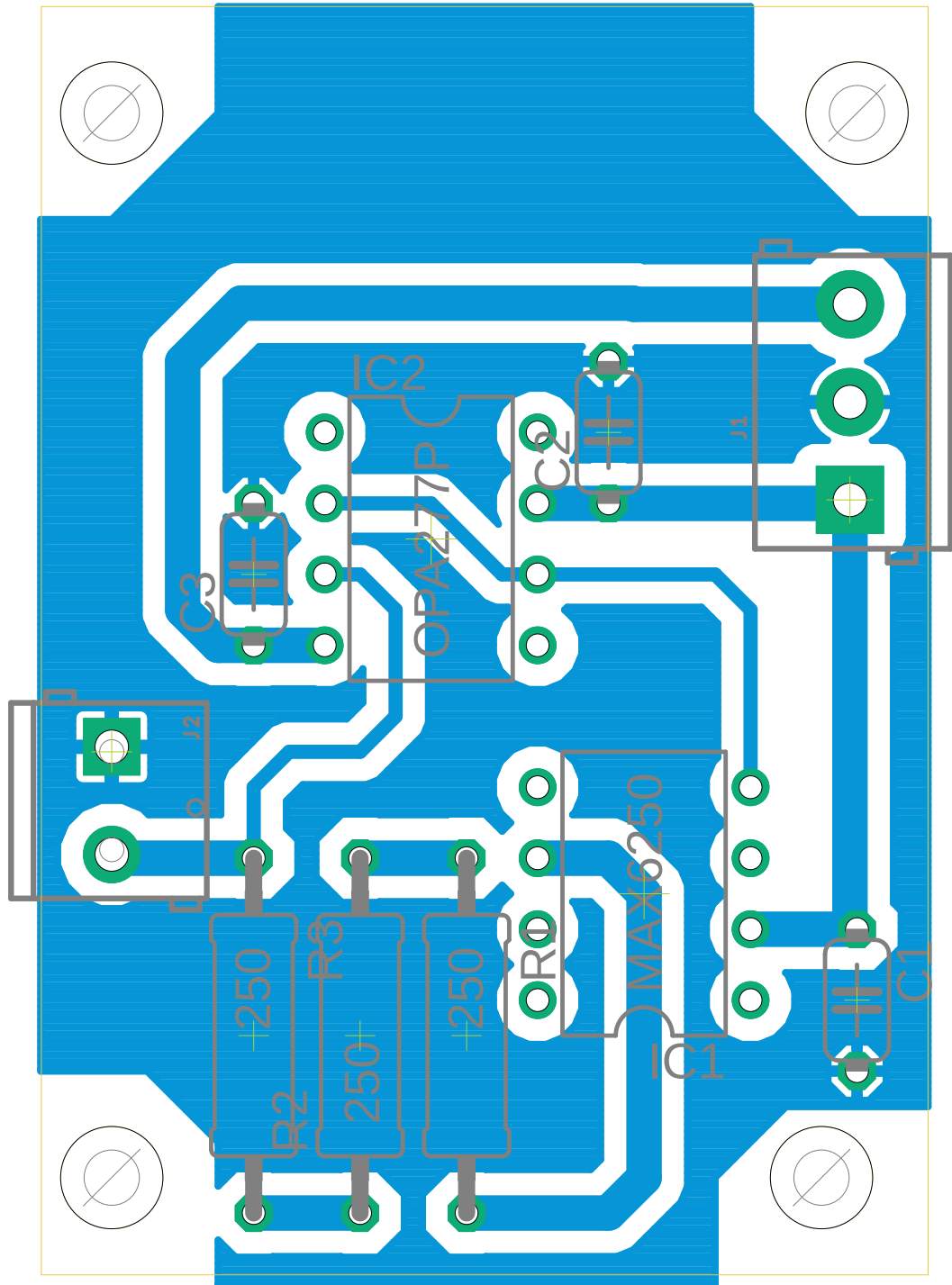


Figure E.4: PVC1000 board implementation. Blue: bottom PCB layer.

Appendix F

Mean and variance of functions of normally-distributed random variable

We compute here the mean and variance of functions of normally-distributed variables and apply those results to the functions $Y = \ln(X)$ and $Y = 1/X$, where X is a normally-distributed random variable.

Theorem 1. *If X is a random variable that follows a normal distribution of mean μ_X and variance σ_X^2 ($X \sim \mathcal{N}(\mu_X, \sigma_X^2)$) and $f : X \mapsto f(X)$ is an arbitrary function then the mean of $f(X)$ is given by*

$$\begin{aligned} \mathbb{E}[f(X)] &= \sum_{n=0}^{N-1} \frac{\sigma_X^{2n} (2n-1)!!}{(2n)!} f^{(2n)}(\mu_X) \\ &+ \mathcal{O}\left(\frac{\sigma_X^{2N} (2N-1)!!}{(2N)!} f^{(2N)}(\mu_X)\right). \end{aligned} \quad (\text{F.1})$$

Proof. The Taylor expansion of $f(X)$ around μ_X is given by

$$\begin{aligned} f(X) &= \sum_{k=0}^{N-1} \frac{1}{k!} f^{(k)}(\mu_X) (X - \mu_X)^k \\ &+ \mathcal{O}\left(\frac{1}{N!} f^{(N)}(\mu_X) (X - \mu_X)^N\right). \end{aligned}$$

The expected value of the sum is the sum of expected values:

$$\begin{aligned} \mathbb{E}[f(X)] &= \sum_{k=0}^{N-1} \frac{1}{k!} f^{(k)}(\mu_X) \mathbb{E}\left[(X - \mu_X)^k\right] \\ &+ \mathcal{O}\left(\frac{1}{N!} f^{(N)}(\mu_X) \mathbb{E}\left[(X - \mu_X)^N\right]\right) \end{aligned}$$

Because $X \sim \mathcal{N}(\mu_X, \sigma_X^2)$ its odd moments are zero:

$$\forall k = 2n + 1, n \in \mathbb{N}, \mathbb{E}\left[(X - \mu_X)^k\right] = 0,$$

and its even moments are given by

$$\forall k = 2n, n \in \mathbb{N}, \mathbb{E}\left[(X - \mu_X)^k\right] = \sigma_X^k (k-1)!!$$

Replacing the k -th order moment with the two previous formulas in the Taylor expansion for the expected value yields the theorem for the expected value of $f(X)$. \square

Theorem 2. *If X is a random variable that follows a normal distribution of mean μ_X and variance σ_X^2 ($X \sim \mathcal{N}(\mu_X, \sigma_X^2)$) and $f : X \mapsto f(X)$ is an arbitrary function then the variance of $f(X)$ is approximated by*

$$\text{Var}[f(X)] \approx \sigma_X^2 (f^1(\mu_X))^2 + \frac{1}{2} (f^2(\mu_X))^2 \sigma_X^4 \quad (\text{F.2})$$

Proof. See [159]. \square

Lemma 1. *If X is a random variable that follows a normal distribution of non-zero mean μ_X and variance σ_X^2 and $\sigma_X/\mu_X \ll 1$, then $Y = \ln X$ can be approximated as a normal distribution of mean $\mu_Y = \ln \mu_X - \sigma_X^2/2$ and variance $\sigma_Y^2 = \sigma_X^2/\mu_X^2$. The truncation error for the mean is equal to $3/4(\sigma_X/\mu_X)^4$.*

Lemma 2. *If X is a random variable that follows a normal distribution of non-zero mean μ_X and variance σ_X^2 and $\sigma_X/\mu_X \ll 1$, then $Y = 1/X$ can be approximated as a normal distribution of mean $\mu_Y = 1/\mu_X (1 + \sigma_X^2/\mu_X^2 + 3\sigma_X^4/\mu_X^4 + 15\sigma_X^6/\mu_X^6)$ and variance $\sigma_Y^2 = \sigma_X^2/\mu_X^4$. The truncation error for the mean is equal to $105\sigma_X^8/\mu_X^9$.*

Proof. This is a direct application of Theorems 1 and 2 where $f(X) = \ln X$ and $f(X) = 1/X$ □

Validity of approximations

Because of the increasing value of the moments of a normal distribution the truncation error of the expected value for both $\ln X$ and $1/X$ grows without bounds. We retain only the first few terms for the above approximations. The approximations are valid as long as $\sigma_X/\mu_X \ll 1$ and μ_X is non-zero.

Bibliography

- [1] Kuo, Y. S., Bunshah, R. F., and Okrent, D., “Hot hollow cathode and its applications in vacuum coating: A concise review,” *Journal of Vacuum Science and Technology A*, Vol. 4, No. 397, 1986.
- [2] Lunk, A., “Plasma activated physical vapour deposition (PAPVD) by hollow cathode arc (HCA),” *Vacuum*, Vol. 41, No. 7–9, 1990, pp. 1965–1967.
- [3] Morgner, H., Neumann, M., Straach, S., and Krug, M., “The hollow cathode: a high-performance tool for plasma-activated deposition,” *Surface and Coatings Technology*, Vol. 108–109, 1998, pp. 513–519.
- [4] Deichuli, P. P., Abdrashitov, G. F., Ivanov, A. A., Kolmogorov, V. V., Mishagin, V. V., Shul’zhenko, G. I., Stupishin, N. V., Beals, D., and Granetz, R., “Ion source with LaB₆ hollow cathode for a diagnostic neutral beam injector,” *Review of Scientific Instruments*, Vol. 77, No. 3, 2006, pp. 03B514.
- [5] Forrester, A. T., Goebel, D. M., and Crow, J. T., “IBIS: A hollow-cathode multipole boundary ion source,” *Applied Physics Letters*, Vol. 33, No. 1, 1978, pp. 11–13.
- [6] Tanaka, S., Morita, H., and Sakuraba, J., “Use of a hollow cathode in a duoPI-Gatron hydrogen ion source,” *Japanese Journal of Applied Physics*, Vol. 19, No. 9, 1980, pp. 1703.
- [7] Brophy, J. R., “NASA’s deep space 1 ion engine,” *Review of Scientific Instruments*, Vol. 73, No. 2, 2002, pp. 1071–1078.
- [8] Szabo, J. J., Pote, B., Tedrake, R., Paintal, S., Byrne, L., Hraby, V. J., Kamhawi, H., and Smith, T., “High throughput 600 watt Hall effect thruster for space exploration,” *52nd AIAA/SAE/ASEE Joint Propulsion Conference & Exhibit*, 2016, AIAA-2016-4830.
- [9] Dodson, C. A., Perez-Grande, D., Jorns, B. A., Goebel, D. M., and Wirz, R. E., “Ion heating measurements on the centerline of a high-current hollow cathode plume,” *Journal of Propulsion and Power*, Vol. 34, No. 5, 2018, pp. 1225–1234.
- [10] Mantenicks, M. A. and Myers, R. M., “Preliminary Test Results of a Hollow Cathode MPD Thruster,” *22nd International Electric Propulsion Conference*, 1991, IEPC-1991-076.

- [11] Ichihara, D., Uno, T., Kataoka, H., Jeong, J., Iwakawa, A., and Sasoh, A., “Ten-ampere-level, applied-field-dominant operation in magnetoplasma-dynamic thrusters,” *Journal of Propulsion and Power*, Vol. 33, No. 2, 2017, pp. 360–369.
- [12] Kasuga, H., Mizutani, K., Ichihara, D., Iwakawa, A., Sasoh, A., Kojima, K., Kimura, T., Kawamata, Y., and Yasui, M., “Ten-Ampere-Level, Direct Current Operation of Applied-Field Magnetoplasma-dynamics (MPD) Thruster using LaB₆ Hollow Cathode,” *35th International Electric Propulsion Conference*, 2017, IEPC-2017-235.
- [13] Coogan, W., *Thrust Scaling in Applied-Field Magnetoplasma-dynamic Thrusters*, Ph.D. thesis, Princeton University, 2018.
- [14] Boxberger, A., Behnke, A., and Herdrich, G., “Current Advances in Optimization of Operative Regimes of Steady State Applied Field MPD Thrusters,” *36th International Electric Propulsion Conference*, 2019, IEPC-2019-585.
- [15] Savitskii, E. M. and Burkhanov, G. S., *Physical Metallurgy of Refractory Metals and Alloys*, Consultants Bureau, 1970, pp. 47–51.
- [16] Cassady, L., *Lithium-fed Arc Multichannel and Single-Channel Hollow Cathode: Experiment and Theory*, Ph.D. thesis, Princeton University, 2006, pp.105–110.
- [17] Goebel, D. M. and Chu, E., “High Current Lanthanum Hexaboride Hollow Cathodes for High Power Hall Thrusters,” *32nd International Electric Propulsion Conference*, 2011, IEPC-2011-053.
- [18] Hofer, R., Randolph, T., Oh, D., Snyder, J., and de Grys, K., “Evaluation of a 4.5 kW Commercial Hall Thruster System for NASA Science Missions,” *42nd AIAA/ASME/SAE/ASEE Joint Propulsion Conference & Exhibit*, 2006, AIAA-2006-4469.
- [19] Brown, D. L., Beal, B. E., and Haas, J. M., “Air Force Research Laboratory High Power Electric Propulsion Technology Development,” *IEEE Aerospace Conference*, 2010.
- [20] Hall, S. J., Jorns, B. J., Gallimore, A. D., Kamhawi, H., Haag, T. W., Mackey, J. A., Gilland, J. H., Peterson, P. Y., and Baird, M., “High-power performance of a 100-kW class nested Hall thruster,” *35th International Electric Propulsion Conference*, 2017, IEPC-2017-228.
- [21] Jorns, B., Gallimore, A. D., Hall, S. J., Peterson, P. Y., Gilland, J. E., Goebel, D. M., Hofer, R., and Mikellides, I., “Update on the Nested Hall Thruster Subsystem for the NextSTEP XR-100 Program,” *AIAA Propulsion and Energy Forum*, 2018, AIAA-2018-4418.

- [22] Shark, S. W., Hall, S. J., Jorns, B., Hofer, R. R., and Goebel, D. M., “High Power Demonstration of a 100 kW Nested Hall Thruster System,” *AIAA Propulsion and Energy*, 2019, AIAA-2019-3809.
- [23] Shastry, R., Herman, D. A., Soulas, G. C., and Patterson, M. J., “Post-test Inspection of NASA’s Evolutionary Xenon Thruster Long-Duration Test Hardware: Discharge and Neutralizer Cathodes,” *52nd AIAA/ASME/SAE/ASEE Joint Propulsion Conference & Exhibit*, 2016, AIAA-2016-4631.
- [24] Polk, J. E., Capece, A. M., and Mikellides, I. G., “Barium Depletion in the NSTAR Discharge Cathode After 30,472 Hours of Operation,” *46th AIAA/ASME/SAE/ASEE Joint Propulsion Conference & Exhibit*, 2010, AIAA-2010-6702.
- [25] Sengupta, A., “Destructive Physical Analysis of Hollow Cathodes from the Deep Space 1 Flight Spare Ion Engine 30,000 Hr Life Test,” *29th International Electric Propulsion Conference*, 2005, IEPC-2005-026.
- [26] Ohkawa, Y., Higuchi, T., Hayakawa, Y., Miyazaki, K., and Nagano, H., “Observation and Analysis of Graphite Hollow Cathode after 45,000-Hour Life Test,” *33rd International Electric Propulsion Conference*, 2013, IEPC-2013-364.
- [27] van Noord, J. L., Kamhawi, H., and McEwen, H. K., “Characterization of a High Current, Long Life Hollow Cathode,” Tech. Rep. TM-214095, NASA, 2006.
- [28] Goebel, D. M. and Chu, E., “High Current Lanthanum Hexaboride Hollow Cathode for High-Power Hall Thrusters,” *Journal of Propulsion and Power*, Vol. 30, No. 1, 2014.
- [29] Becatti, G., Goebel, D. M., Polk, J. E., and Guerrero, P., “Life Evaluation of a Lanthanum Hexaboride Hollow Cathode for High-Power Hall Thruster,” *Journal of Propulsion and Power*, Vol. 34, No. 4, 2017, pp. 893–900.
- [30] Chu, E. and Goebel, D. M., “High-current lanthanum hexaboride hollow cathode for 10-to-50-kW Hall thrusters,” *IEEE Transactions on Plasma Science*, Vol. 40, No. 9, 2012, pp. 2133–2144.
- [31] Chu, E., Goebel, D. M., and Wirz, R. E., “Reduction of Energetic Ion Production in Hollow Cathodes by External Gas Injection,” *Journal of Propulsion and Power*, Vol. 29, No. 5, 2013, pp. 1155–1163.
- [32] Wordingham, C. J., Taunay, P.-Y. C. R., and Choueiri, E. Y., “Multi-kilowatt Class Heaters for Large Hollow Cathodes,” *Review of Scientific Instruments*, Vol. 87, No. 7, 2018.
- [33] Kuznetsov, G., “High temperature cathodes for high current density,” *Nuclear Instruments and Methods in Physics Research*, Vol. 340, 1994, pp. 204–208.

- [34] Kultashev, O. and Djubua, B., “Miniature metal alloy thermionic cathodes,” *Physica Scripta*, Vol. T71, 1997, pp. 127–129.
- [35] Kuznetsov, G. I., “IrCe cathodes for EBIS,” *Journal of Physics: Conference Series*, Vol. 2, 2004, pp. 35–41.
- [36] Kuznetsov, G. I., “Cathodes for electron guns,” *Physica Scripta*, Vol. T71, 2006, pp. 39–45.
- [37] Toda, Y., Matsuishi, S., Hayashi, K., Ueda, K., Kamiya, T., Hirano, M., and Hosono, H., “Field emission of electron anions clathrated in subnanometer-sized cages in $[\text{Ca}_{24}\text{Al}_{28}\text{O}_{64}]^{4+}(\text{e}^{-})_4$,” *Advanced materials*, Vol. 16, No. 8, 2004, pp. 685–689.
- [38] Toda, Y., Yanagi, H., Ikenaga, E., Kim, J. J., Kobata, M., Ueda, S., Kamiya, T., Hirano, M., Kobayashi, K., and Hosono, H., “Work Function of a Room-Temperature, Stable Electride $[\text{Ca}_{24}\text{Al}_{28}\text{O}_{64}]^{4+}(\text{e}^{-})_4$,” *Advanced Materials*, Vol. 19, No. 21, 2007, pp. 3564–3569.
- [39] Rand, L. P., Williams, J., Blakely, J., Beal, B., and Brown, D., “C12A7 Electric Hollow Cathode,” Tech. Rep. AFRL-RQ-ED-TP-2013-047, Colorado State University, 2013.
- [40] Rand, L. P., *A Calcium Aluminate Electride Hollow Cathode*, Ph.d., Colorado State University, 2014.
- [41] Reitemeyer, M., Zschätzsch, D., Holste, K., Chen, L., and J. Klar, P. J., “Applicability of electride materials for hollow cathodes,” *36th International Electric Propulsion Conference*, 2019, IEPC-2019-604.
- [42] Goebel, D. and Katz, I., *Fundamentals of Electric Propulsion: Ion and Hall Thrusters*, John Wiley & Sons, Inc., 2008.
- [43] Rumble, J. R., editor, *CRC handbook of chemistry and physics*, CRC Press/Taylor & Francis, 100th ed., 2019, “Electron Work Function of the Crystalline Elements”, p. 12-102.
- [44] Cronin, J. L., “Practical aspects of modern dispenser cathodes,” *Microwave Journal*, Vol. 22, No. 9, 1979, pp. 57–62.
- [45] Gallagher, H. E., “Poisoning of LaB_6 cathodes,” *Journal of Applied Physics*, Vol. 40, No. 1, 1969, pp. 44–51.
- [46] Kaufman, H. R., “Technology of Electron-Bombardment Ion Thrusters,” *Advances in Electronics and Electron Physics*, Vol. 36, No. C, 1975, pp. 265–373, pp. 363–364.
- [47] Salhi, A., *Theoretical and experimental studies of orificed, hollow cathode operation*, Ph.d., The Ohio State University, 1993.

- [48] Salhi, A. and Turchi, P. J., “Scaling relations for design and operation of orificed-hollow cathodes,” *30th AIAA/ASME/SAE/ASEE Joint Propulsion Conference & Exhibit*, 1994, AIAA-1994-3133.
- [49] Albertoni, R., Pedrini, D., Paganucci, F., and Andrenucci, M., “A Reduced-Order Model for Thermionic Hollow Cathodes,” *IEEE Transactions on Plasma Science*, Vol. 41, No. 7, 2013, pp. 1731–1745.
- [50] Goldston, R. J. and Rutherford, P. H., *Introduction to Plasma Physics*, Taylor and Francis, 1995, p. 119.
- [51] Mitchner, M. and Kruger, C. H. J., *Partially Ionized Gases*, John Wiley and Sons, 1973, p. 149.
- [52] Siegfried, D. E. and Wilbur, P. J., “A model for mercury orificed hollow cathodes - Theory and experiment,” *AIAA Journal*, Vol. 22, No. 10, 1984, pp. 1405–1412.
- [53] Wordingham, C. J., Taunay, P.-Y. C. R., and Choueiri, E. Y., “A Critical Review of Orificed Hollow Cathode Modeling: 0-D Models,” *53rd AIAA/SAE/ASEE Joint Propulsion Conference & Exhibit*, 2017, AIAA-2017-4888.
- [54] Taunay, P.-Y. C. R., Wordingham, C. J., and Choueiri, E. Y., “An Empirical Scaling Relationship for the Total Pressure in Hollow Cathodes,” *AIAA Propulsion and Energy Forum*, 2018, AIAA-2018-4428.
- [55] Albertoni, R., *Cathode Processes in MPD Thrusters*, Ph. d., Universita Degli Studi di Pisa, 2012.
- [56] Mikellides, I. G., Goebel, D. M., Jorns, B. a., Polk, J. E., and Guerrero, P., “Numerical Simulations of the Partially-ionized Gas in a 100-A LaB₆ Hollow Cathode,” *IEEE Transactions on Plasma Science*, Vol. 43, No. 1, 2015, pp. 1–15.
- [57] Sary, G., Garrigues, L., and Boeuf, J.-P., “Hollow cathode modeling: I. A coupled plasma thermal two-dimensional model,” *Plasma Sources Science and Technology*, Vol. 26, No. 5, 2017, pp. 55007.
- [58] Kubota, K., Oshio, Y., Watanabe, H., Cho, S., Ohkawa, Y., and Funaki, I., “Hybrid-PIC Simulation on Plasma Flow of Hollow Cathode,” *34th International Electric Propulsion Conference*, 2015, IEPC-2015-15.
- [59] Cao, S., Ren, J., Tang, H., Zhang, Z., Wang, Y., Cao, J., and Chen, Z., “Numerical simulation of plasma power deposition on hollow cathode walls using particle-in-cell and Monte Carlo collision method,” *Physics of Plasmas*, Vol. 25, No. 10, 2018.

- [60] Mikellides, I. G., Katz, I., Goebel, D. M., and Polk, J. E., “Hollow cathode theory and experiment. II. A two-dimensional theoretical model of the emitter region,” *Journal of Applied Physics*, Vol. 98, 2005.
- [61] Prewett, P. and Allen, J., “The double sheath associated with a hot cathode,” *Proceedings of the Royal Society of London A: Mathematical, Physical and Engineering Sciences*, Vol. 348, The Royal Society of London, 1976, pp. 435–446.
- [62] Lin, T. P. and Eng, G., “Thermionic emission including both space-charge and image forces,” *Journal of Applied Physics*, Vol. 65, No. 8, 1989, pp. 3205–3211.
- [63] Siegfried, D. E. and Wilbur, P. J., “Phenomenological Model Describing Orificed, Hollow Cathode Operation,” *AIAA Journal*, Vol. 21, No. 1, 1983, pp. 5–6.
- [64] Domonkos, M. T., *Evaluation of low-current orificed hollow cathodes*, Ph.d., University of Michigan, 1999.
- [65] Wilbur, P. J., “Advanced Ion Thruster Research,” Tech. Rep. CR-168340, NASA, 1984.
- [66] van der Walt, S., Colbert, C. S., and Varoquaux, G., “The NumPy Array: A Structure for Efficient Numerical Computation,” *Computing in Science & Engineering*, Vol. 13, 2011, pp. 22–30.
- [67] Jones, E., Oliphant, T., Peterson, P., et al., “SciPy: Open source scientific tools for Python,” 2001–, Online.
- [68] More, J. J., Garbow, B. S., and Hillstom, K. E., “User guide for MINPACK-1,” Tech. Rep. ANL-80-74, Argonne National Laboratory, 1980.
- [69] Siegfried, D. E. and Wilbur, P. J., “An investigation of mercury hollow cathode phenomena,” *13th International Electric Propulsion Conference*, 1978.
- [70] Beßling, H., “Theorie der Hochtemperatur-Hohlkathode, ein Modell für den Kathodenmechanismus,” Tech. rep., DFVLR - Institut für Energiewandlung und Elektrische Antriebe, 1976, (In German).
- [71] Siegfried, D. E. and Wilbur, P. J., “Studies on an experimental quartz tube hollow cathode,” *14th International Electric Propulsion Conference*, 1979, AIAA-1979-2056.
- [72] Siegfried, D. E., *A Phenomenological Model for Orificed Hollow Cathodes*, Ph.d., Colorado State University, 1982.
- [73] Domonkos, M. T., “A Particle and Energy Balance Model of the Orificed Hollow Cathode,” *38th AIAA/ASME/SAE/ASEE Joint Propulsion Conference & Exhibit*, 2002, AIAA-2002-4240.
- [74] Peters, R. and Wilbur, P. J., “Double-Ion Production in Mercury Thrusters,” Tech. Rep. CR-135019, NASA, 1976.

- [75] Mandell, M. J. and Katz, I., “Theory of Hollow Cathode Operation in Spot and Plume Modes,” *30th AIAA/ASME/SAE/ASEE Joint Propulsion Conference & Exhibit*, 1994, AIAA-1994-3134.
- [76] Katz, I., Gardner, B., Jongeward, G., Patterson, M., and Myers, R., “A model of plasma contactor behavior in the laboratory,” *34th Aerospace Sciences Meeting & Exhibit*, 1996, AIAA-1996-0484.
- [77] Katz, I., Gardner, B. M., Mandell, M. J., Jongeward, G. A., Patterson, M., and Myers, R. M., “Model of Plasma Contactor Performance,” *Journal of Spacecraft and Rockets*, Vol. 34, No. 6, 1997.
- [78] Katz, I., Mandell, M. J., Patterson, M., and Domonkos, M., “Sensitivity of Hollow Cathode Performance to Design and Operating Parameters,” *35th AIAA/ASME/SAE/ASEE Joint Propulsion Conference & Exhibit*, 1999, AIAA-1999-2576.
- [79] Hayashi, M., “Determination of Electron-Xenon Total Excitation Cross-Sections, from Threshold to 100 eV, From Experimental Values of Townsend’s alpha,” *Journal of Physics D: Applied Physics*, Vol. 16, 1983, pp. 581–589.
- [80] Hayashi, M., “Bibliography of Electron and Photon Cross Sections with Atoms and Molecules Published in the 20th Century - Xenon,” Tech. Rep. NIFS-DATA-79, NIFS, 2003.
- [81] “Hayashi database,” <http://www.lxcat.net>, Retrieved on Jun. 28, 2019.
- [82] Capacci, M., Minucci, M., and Severi, A., “Simple numerical model describing discharge parameters in orificed hollow cathode devices,” *33rd AIAA/ASME/SAE/ASEE Joint Propulsion Conference & Exhibit*, 1997, AIAA-1997-2791.
- [83] Mikellides, I. G., Katz, I., Goebel, D. M., Jameson, K. K., and Polk, J. E., “Wear Mechanisms in Electron Sources for Ion Propulsion, I: Neutralizer Hollow Cathode,” *Journal of Propulsion and Power*, Vol. 24, No. 4, 2008, pp. 855–865.
- [84] Langmuir, I., “The interaction of electron and positive ion space charges in cathode sheaths,” *Physical Review*, Vol. 33, No. 6, 1929, pp. 954–989.
- [85] Raadu, M. A., “The physics of double layers and their role in astrophysics,” *Physics Reports*, Vol. 178, No. 2, 1989, pp. 25–97.
- [86] Wei, R. and Wilbur, P. J., “Space-charge-limited current flow in a spherical double sheath,” *Journal of Applied Physics*, Vol. 60, No. 7, 1986, pp. 2280–2284.
- [87] Korkmaz, O. and Celik, M., “Global numerical model for the assessment of the effect of geometry and operation conditions on insert and orifice region plasmas of a thermionic hollow cathode electron source,” *Contributions to Plasma Physics*, Vol. 54, No. 10, 2014, pp. 838–850.

- [88] Huba, J. D., “NRL Plasma Formulary,” NRL/PU/6790, 2011.
- [89] Williams, G. J., Smith, T. B., Domonkos, M. T., Shand, K. J., Gallimore, A. D., and Drake, R. P., “Laser Induced Fluorescence Characterization of Ions Emitted from Hollow Cathodes,” *35th AIAA/ASME/SAE/ASEE Joint Propulsion Conference & Exhibit*, 1999, AIAA-1999-2862.
- [90] “SIGLO database,” <http://www.lxcat.net>, Retrieved on Jun. 17, 2017.
- [91] Jones, T. J., *Thermionic emission*, Methuin ltd., 1936.
- [92] Katz, I., Anderson, J. R., Polk, J. E., and Brophy, J. R., “One-Dimensional Hollow Cathode Model,” *Journal of Propulsion and Power*, Vol. 19, No. 4, 2003, pp. 595–600.
- [93] Miller, J. S., Pullins, S. H., Levandier, D. J., Chiu, Y. H., and Dressler, R. A., “Xenon charge exchange cross sections for electrostatic thruster models,” *Journal of Applied Physics*, Vol. 91, No. 3, 2002, pp. 984–991.
- [94] Hause, M., Prince, B., and Bemish, R., “Krypton charge exchange cross section for Hall effect thruster models,” *Journal of Applied Physics*, Vol. 113, 2013.
- [95] Mizrahi, J. P., Vekselman, V., Krasik, Y., and Gurovich, V., “0-D Plasma Model for Orificed Hollow Cathodes,” *32nd International Electric Propulsion Conference*, 2011, IEPC-2011-334.
- [96] Mizrahi, J., Vekselman, V., Gurovich, V., and Krasik, Y. E., “Simulation of Plasma Parameters During Hollow Cathodes Operation,” *Journal of Propulsion and Power*, Vol. 28, No. 5, 2012, pp. 1134–1137.
- [97] Katz, I., Anderson, J., Polk, J., and Brophy, J., “A Model of Hollow Cathode Plasma Chemistry,” *38th AIAA/ASME/SAE/ASEE Joint Propulsion Conference & Exhibit*, 2002, AIAA-2002-4241.
- [98] Coletti, M. and Gabriel, S. B., “Insert Temperature Measurements of a 180A Hollow Cathode for the HiPER Project,” *48th AIAA/ASME/SAE/ASEE Joint Propulsion Conference & Exhibit*, 2012, AIAA-2012-4081.
- [99] Polk, J. E., Goebel, D. M., and Guerrero, P., “Thermal Characteristics of a Lanthanum Hexaboride,” *34th International Electric Propulsion Conference*, 2015.
- [100] Krishnan, M., Jahn, R. G., von Jaskowsky, W. F., and Clark, K. E., “Physical processes in hollow cathode discharge,” *AIAA Journal*, Vol. 15, No. 9, 1977, pp. 1217–1223.
- [101] Chang, C. H. and Pfender, E., “Nonequilibrium modeling of low-pressure argon plasma jets; Part I: Laminar flow,” *Plasma Chemistry and Plasma Processing*, Vol. 10, No. 3, 1990, pp. 473–491.

- [102] Stiel, L. I. and Thodos, G., "The Viscosity of Nonpolar Gases at Normal," *A.I.Ch.E. Journal*, Vol. 7, No. 4, 1961, pp. 611–615.
- [103] McQuarrie, D. A., *Statistical Mechanics*, Harper's Chemistry Series, 1976, p. 434.
- [104] Hirschfelder, J. O., Curtiss, C. F., and Bird, R. B., *Molecular Theory of Gases and Liquids*, Wiley, 1954, pp. 1126–1127.
- [105] Goebel, D. M. Jameson, K. K. and Katz, I., "Hollow Cathode and Keeper-Region Plasma Measurements Using Ultra-Fast Miniature Scanning Probes," *40th AIAA/ASME/SAE/ASEE Joint Propulsion Conference & Exhibit*, 2004, AIAA-2004-3430.
- [106] Katz, I., Polk, J. E., Mikellides, I. G., Goebel, D. M., and Hornbeck, S. E., "Combined Plasma and Thermal Hollow Cathode Insert Model," *29th International Electric Propulsion Conference*, 2005, IEPC-2005-228.
- [107] Mikellides, I. G., Katz, I., Goebel, D. M., Polk, J. E., and Jameson, K. K., "Plasma processes inside dispenser hollow cathodes," *Physics of Plasmas*, Vol. 13, 2006.
- [108] Mikellides, I. G., Katz, I., Goebel, D. M., Jameson, K. K., and Polk, J. E., "Wear Mechanisms in Electron Sources for Ion Propulsion, II: Discharge Hollow Cathode," *Journal of Propulsion and Power*, Vol. 24, No. 4, 2008, pp. 866–879.
- [109] Mikellides, I. G., Katz, I., Goebel, D. M., and Polk, J. E., "Model of a Hollow Cathode Insert Plasma," *40th AIAA/ASME/SAE/ASEE Joint Propulsion Conference & Exhibit*, 2004, AIAA-2004-3817.
- [110] Goebel, D. M., Jameson, K. K., Watkins, R. M., Katz, I., and Mikellides, I. G., "Hollow cathode theory and experiment. I. Plasma characterization using fast miniature scanning probes," *Journal of Applied Physics*, Vol. 98, No. 11, 2005.
- [111] Jameson, K. K., Goebel, D. M., and Watkins, R. M., "Hollow Cathode and Keeper-Region Plasma Measurements," *41st AIAA/ASME/SAE/ASEE Joint Propulsion Conference & Exhibit*, 2005, AIAA-2005-3667.
- [112] Friedly, V. J., "Hollow Cathode Operation at High Discharge Currents," 1990, M.Sc.
- [113] Patterson, S. W. and Fearn, D. G., "The Generation of High Energy Ions in Hollow Cathode Discharges," *26th International Electric Propulsion Conference*, 1999, pp. 695–702, IEPC-1999-125.
- [114] Salhi, A. and Turchi, P. J., "Theoretical Modeling of Orificed Hollow Cathode Discharges," *23rd International Electric Propulsion Conference*, 1993, IEPC-1993-024.

- [115] Jameson, K. K., Goebel, D. M., and Watkins, R. M., “Hollow Cathode and Thruster Discharge Chamber Plasma Measurements Using High-Speed Scanning Probes,” *29th International Electric Propulsion Conference*, 2005, IEPC-2005-269.
- [116] Polk, J., Grubisic, A., Taheri, N., Goebel, D. M., and Hornbeck, S. E., “Emitter Temperature Distributions in the NSTAR Discharge Hollow Cathode,” *41st AIAA/ASME/SAE/ASEE Joint Propulsion Conference & Exhibit*, 2005, AIAA-2005-4398.
- [117] Rawlin, V., Sovey, J., Anderson, J., and Polk, J., “NSTAR flight thruster qualification testing,” *34th AIAA/ASME/SAE/ASEE Joint Propulsion Conference & Exhibit*, 1998, AIAA-1998-3936.
- [118] Tighe, W. G., Chien, K.-R., Goebel, D. M., and Longo, R. T., “Hollow Cathode Ignition and Life Model,” *41st AIAA/ASME/SAE/ASEE Joint Propulsion Conference & Exhibit*, 2005, AIAA-2005-3666.
- [119] Epstein, L. F. and Powers, M. D., “Liquid Metals. I. The Viscosity of Mercury Vapor and the Potential Function for Mercury,” *The Journal of Physical Chemistry*, Vol. 57, No. 3, 1953, pp. 336–341.
- [120] Wilbur, P. J., “Ion and Advanced Electric Thruster Research,” Tech. Rep. CR-165253, NASA, 1980.
- [121] Fearn, D. G. and Patterson, S. W., “Characterisation of the high current hollow cathode for the T6 thruster,” *34th AIAA/ASME/SAE/ASEE Joint Propulsion Conference & Exhibit*, 1998, AIAA-1998-3346.
- [122] Mikellides, I. G., “Effects of Viscosity in a Partially Ionized Channel Flow with Thermionic Emission,” *Physics of Plasmas*, Vol. 16, 2009.
- [123] White, F., *Fluid Mechanics, Sixth Edition*, McGraw-Hill Higher Education, 2008, p. 347.
- [124] Brown, J., “Design and Implementation of an Actuated Probe Suite for an Orificed Hollow Cathode,” B.Sc. Thesis, 2018, Princeton University.
- [125] Burton, R. L., Clark, K. E., and Jahn, R. G., “Measured performance of a Multimegawatt MPD Thruster,” *Journal of Spacecraft*, Vol. 20, No. 3, 1983, pp. 299–304.
- [126] Siegfried, D. E. and Wilbur, P. J., “Phenomenological model describing orificed, hollow cathode operation,” *15th International Electric Propulsion Conference*, 1981, AIAA-1981-0746.
- [127] James, G., Witten, D., Hastie, T., and Tibshirani, R., *An Introduction to Statistical Learning*, Springer, 2013, p. 66.

- [128] Posifa Technologies, “PVC1000 Series micro-Pirani vacuum sensors,” 2020, retrieved May 2020.
- [129] Buckingham, E., “On physically similar systems; illustrations of the use of dimensional equations,” *Physical Review*, Vol. 4, 1914, pp. 345–376.
- [130] Ipsen, E. C., *Units, Dimensions, and Dimensionless Numbers*, McGraw-Hill, 1960.
- [131] Goebel, D. M., Katz, I., Polk, J. E., Mikellides, I. G., Jameson, K. K., Liu, T., and Dougherty, R., “Extending Hollow Cathode Life for Electric Propulsion in Long-Term Missions,” *Space Conference & Exhibit*, 2004, AIAA-2004-5911.
- [132] Pedregosa, F., Varoquaux, G., Gramfort, A., Michel, V., Thirion, B., Grisel, O., Blondel, M., Prettenhofer, P., Weiss, R., Dubourg, V., Vanderplas, J., Passos, A., Cournapeau, D., Brucher, M., Perrot, M., and Duchesnay, E., “Scikit-learn: Machine Learning in Python,” *Journal of Machine Learning Research*, Vol. 12, 2011, pp. 2825–2830.
- [133] Roweis, S. T. and Saul, L. K., “Nonlinear Dimensionality Reduction by Locally Linear Embedding,” *Science*, Vol. 290, No. 5500, 2000, pp. 2323–2326.
- [134] Taunay, P.-Y. C. R., Wordingham, C. J., and Choueiri, E. Y., “A 0-D model for orificed hollow cathodes with application to the scaling of total pressure,” *AIAA Propulsion and Energy Forum*, 2019, AIAA-2019-4246.
- [135] Taunay, P.-Y. C. R., Wordingham, C. J., and Choueiri, E. Y., “The influence of ambipolar diffusion on the attachment length and electron temperature in orificed hollow cathodes,” *36th International Electric Propulsion Conference*, 2019, IEPC-2019-426.
- [136] Wordingham, C. J., Taunay, P.-Y. C. R., and Choueiri, E. Y., “Theoretical Prediction of the Dense-Plasma Attachment Length in an Orificed Hollow Cathode,” *35th International Electric Propulsion Conference*, 2017, IEPC-2017-566.
- [137] Pedrini, D., Albertoni, R., Paganucci, F., and Andrenucci, M., “Theoretical Model of a Lanthanum Hexaboride Hollow Cathode,” *IEEE Transactions on Plasma Science*, Vol. 43, No. 1, 2015.
- [138] Pedrini, D., Cannelli, F., Ducci, C., Misuri, T., Paganucci, F., and Andrenucci, M., “Hollow Cathodes Development at SITAEL,” *Space Propulsion*, 2016.
- [139] Delcroix, J.-L. and Trindade, A. R., “Hollow cathode arcs,” *Advances in Electronics and Electron Physics*, Vol. 35, 1974, pp. 87–190.
- [140] Jobson, D. A., “On the flow of a compressible fluid through orifices,” *Proceedings of the Institution of Mechanical Engineers*, Vol. 169, No. 1, 1955, pp. 767–776.
- [141] Jahn, R. G., *Physics of Electric Propulsion*, Dover Publications, 2006, p. 244.

- [142] Santeler, D. J., "Exit loss in viscous tube flow," *Journal of Vacuum Science & Technology A: Vacuum, Surfaces, and Films*, Vol. 4, No. 3, 1986, pp. 348–352.
- [143] Livesey, R. G., *Foundations of Vacuum Science and Technology*, chap. Flow of Gases Through Tubes and Orifices, John Wiley & Sons, Inc, 1998, pp. 135–137.
- [144] Lidsky, L. M., Rothleder, S. D., Rose, D. J., Yoshikawa, S., Michelson, C., and Mackin Jr., R. J., "Highly ionized hollow cathode discharge," *Journal of Applied Physics*, Vol. 33, 1962, pp. 2490–2497.
- [145] Rohrbach, G. and Lunk, A., "Characterization of plasma conditions in a hollow cathode arc evaporation device," *Surface and Coatings Technology*, Vol. 123, 2000, pp. 231–238.
- [146] Tanaka, S., Akiba, M., Arakawa, Y., Horiike, H., and Sakuraba, J., "Reduction of gas flow into a hollow cathode ion source for a neutral beam injector," *Review of Scientific Instruments*, Vol. 53, 1982, pp. 1038–1048.
- [147] Lafferty, J. M., "Boride cathodes," *Journal of Applied Physics*, Vol. 22, No. 1951, 1951, pp. 299–309.
- [148] Rapp, D. and Francis, W. E., "Charge exchange between gaseous ions and atoms," *The Journal of Chemical Physics*, Vol. 37, No. 11, 1962, pp. 2631–2645.
- [149] Kovar, F. R., "Mobility of mercury ions in mercury vapor," *Physical Review*, Vol. 133, No. 3A, 1964, pp. A681.
- [150] Hodgkinson, D. P. and Briggs, J. S., "Resonant charge exchange at low velocities," *Journal of Physics B: Atomic and Molecular Physics*, Vol. 9, No. 2, 1976, pp. 255.
- [151] Smirnov, B. M., "Atomic structure and the resonant charge exchange process," *Physics-Uspekhi*, Vol. 44, No. 3, 2001, pp. 221–253, Fig. 11.
- [152] Thompson, S. J., Farnell, C. C., Farnell, S. C., Williams, D. D., Chandler, J. P., and Williams, J. D., "Evaluation of Iodine Compatible Cathode Configurations," *36th International Electric Propulsion Conference*, 2019, IEPC-2019-768.
- [153] Thompson, S. J., VanGermert, J. J., Farnell, C. C., Farnell, C. C., Farnell, S. C., Hensen, T. J., Ham, R., Williams, D. D., Chandler, J. P., and Williams, J. D., "Development of an Iodine Compatible Hollow Cathode," *AIAA Propulsion and Energy Forum*, 2019, AIAA-2019-3997.
- [154] Taillefer, Z. R., Blandino, J. J., and Szabo, J., "Characterization of a Barium Oxide Cathode Operating on Xenon and Iodine Propellants," *Journal of Propulsion and Power*, 2020.

- [155] Patterson, S. W., Jugroot, M., and Fearn, D. G., “Discharge Initiation in the T6 Thruster Hollow Cathode,” *36th Joint Propulsion Conference*, 2000.
- [156] Goebel, D. M., Watkins, R. M., and Jameson, K. K., “LaB₆ Hollow Cathodes for Ion and Hall Thrusters,” *Journal of Propulsion and Power*, Vol. 23, No. 3, 2007, pp. 552–558.
- [157] Goebel, D. M. and Watkins, R. M., “Compact lanthanum hexaboride hollow cathode,” *Review of Scientific Instruments*, Vol. 81, No. 2010, 2010.
- [158] Stitt, M., “Make a Precision Current Source or Current Sink,” Tech. Rep. 520, Burr-Brown, 1990.
- [159] Anderson, T. V. and Mattson, C. A., “Propagating Skewness and Kurtosis Through Engineering Models for Low-Cost, Meaningful, Nondeterministic design,” *Journal of Mechanical Design*, Vol. 134, 2012, pp. 100911.